Doctoral theses at NTNU, 2018:39

Alisa Lydia Machner

Dolomite calcined clay composite cement – hydration and durability

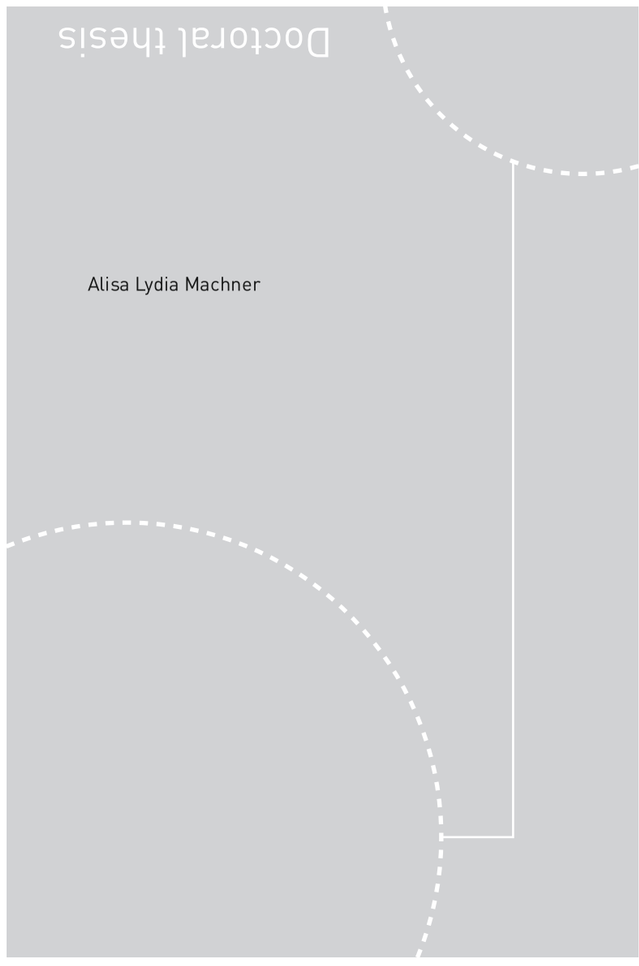

ISBN 978-82-326-2872-8 (printed ver.)
ISBN 978-82-326-2873-5 (electronic ver.)
ISSN 1503-8181

NTNU
Norwegian University of
Science and Technology

NTNU
Norwegian University of Science and Technology
Thesis for the Degree of
Philosophiae Doctor
Faculty of Engineering
Department of Structural Engineering

Doctoral theses at NTNU, 2018:39

NTNU
Norwegian University of
Science and Technology

Alisa Lydia Machner

Dolomite calcined clay composite cement – hydration and durability

Thesis for the Degree of Philosophiae Doctor

Trondheim, February 2018

Norwegian University of Science and Technology
Faculty of Engineering
Department of Structural Engineering

NTNU
Norwegian University of
Science and Technology

NTNU
Norwegian University of Science and Technology

Thesis for the Degree of Philosophiae Doctor

Faculty of Engineering
Department of Structural Engineering

ISBN 978-82-326-2872-8 (printed ver.)
ISBN 978-82-326-2873-5 (electronic ver.)
ISSN 1503-8181

Doctoral theses at NTNU, 2018:39

Printed by NTNU Grafisk senter

Preface

This doctoral thesis was submitted to the Norwegian University of Science and Technology (NTNU) in Trondheim for the degree of Philosophiae Doctor (PhD).

The thesis is the product of an industrial PhD project funded by the Norwegian Research Council (Project number: 241637), the HeidelbergCement Technology Center, and Norcem AS. The project started in November 2014 and ended in October 2017. The candidate was employed at Norcem AS during the project period.

Most of the research was carried out at the Department of Structural Engineering, Faculty of Engineering Science, NTNU, in Trondheim, Norway. Some of the research was carried out at the Research and Development laboratories of the HeidelbergCement Technology Center (Leimen, Germany) and Norcem AS (Brevik, Norway).

The academic supervisors from NTNU were Associate Professor Dr Klaartje De Weerdt as main supervisor, and Professor Dr Mette R. Geiker as co-supervisor. The industrial co-supervisors were Dr Knut O. Kjellsen (Norcem AS, Norway), Dr Maciej Zajac (HeidelbergCement Technology Center, Germany), and Dr Mohsen Ben Haha (HeidelbergCement Technology Center, Germany).

Trondheim, 24.01.2018

Alisa Machner

Acknowledgements

I would like to thank the Norwegian Research Council, HeidelbergCement, and Norcem AS for financing this industrial PhD project and for facilitating the stays at the R&D laboratories of HeidelbergCement and Norcem AS during the project.

I would like to thank Klaartje De Weerdt for the countless meetings and discussions, in which every idea was allowed to be thought, and no question was too stupid to be asked. Thank you for keeping the mood up even when something went not "according to plan" and standing up for me when it was needed. You taught me how to become a researcher and at the same time let me learn my own lessons. I would also like to thank my co-supervisors Mette Geiker, Maciej Zajac, Mohsen Ben Haha, and Knut Kjellsen, for the helpful discussions, their recommendations and help with the experimental set-up, and their thorough comments on the scientific papers to keep the level of our research high.

I would like to thank Tone Østnor for her help in setting up and conducting the experiments. Getting our experimental set-up "Tone-proofed" became an indispensable quality check for me. I also would like to thank Ove Loraas and Steinar Seehuus for their help with setting up and running the chemistry lab in the Department of Structural Engineering. I would like to thank Kristin Høydalsvik, Magnus Rotan, Sergey Khromov, and Ann-Kristin Mjøen for letting me use their laboratories and their quick help in case of problems. Thanks to Arild Monsøy for the high-quality SEM sample preparation. I would also like to thank Markus Bernhard, Tor Magnus Zachariassen, and Sigrun Kjær Bremseth from Nocem AS for their help with the organization of the materials and experiments at Norcem AS. Special thanks belong to Christopher Stabler from HeidelbergCement, without whom I would not have known about this PhD project, and who was reachable also after working hours for all kind of questions not just related to XRD. Thank you as well, to my student assistants Petter Hemstad, Kristine Nøttveit, and Oda Tjeland, who helped me with the experimental work and were a reliable support in the lab. I also would like to thank all my colleagues at the concrete group at the Department of Structural Engineering. I would like to thank Gilles Plusquellec for the very helpful discussions on the C-S-H and every

other question during the project related to chemistry. Guzel and Alessia, you made my time in Trondheim fun and were there whenever I needed to talk to someone.

Last but not least, I would like to thank my family for supporting me in my decision to move to Norway and helping me with the few home-sick moments. Special thanks belong to my father, who started my interest in cement in the very beginning, and to my boyfriend Max, who was there for me after a long working day and made sure I do not forget that there are more important things in the world than cement chemistry.

Abstract

Considerable amounts of CO_2 are emitted during the production of cement. One way to reduce these CO_2 emissions is to replace some of the cement clinker with supplementary cementitious materials (SCMs). A cement containing SCMs is called a composite cement. The use of composite cements has considerably increased over the last few decades and is predicted to continue to do so as the global demand for concrete increases in the future. This will lead to a high demand for SCMs, which in the case of some of the traditionally used SCMs could exceed supply. There is therefore a need to identify potential new SCMs.

The PhD project investigated the possibility of using dolomite in combination with calcined clays as SCMs in Portland composite cements. In this project, metakaolin was used as a model material for industrially available calcined clays. The main objectives of the PhD project were to understand the hydration of Portland composite cements containing dolomite and metakaolin, the resulting phase assemblage, and its stability during carbonation, leaching and chloride exposure. Special focus was put on the hydrate hydrotalcite that was shown to form in composite cements containing dolomite. The compressive strength, phase assemblage, and microstructure of samples, in which various amounts of Portland cement clinker were replaced with either dolomite or with a combination of dolomite and metakaolin, were investigated.

In the first part of the project, the hydration study, two experimental approaches were applied. In the first one, dolomite or limestone were used to replace 0–20%wt of a Portland metakaolin cement. The Portland metakaolin cement represented a mix of Portland cement clinker and metakaolin in the ratio 6:1. It was shown that approximately 10%wt of a Portland metakaolin cement could be replaced with either dolomite or limestone without impairing its compressive strength after curing at temperatures of 20 °C and 38 °C for 28 days and 90 days. The phase assemblages in samples containing limestone or dolomite were generally quite similar, though dolomite was shown to be slightly less reactive than limestone, especially at lower curing temperatures. This lower reactivity resulted in less carbonates delivered from dolomite to form carbonate AFm phases.

In the second experimental approach, various combinations of dolomite and metakaolin were used to replace 40%wt of a Portland cement clinker. After curing for 360 days, especially at elevated temperatures (38 °C and 60 °C), the dolomite in samples with little or no metakaolin content had reacted significantly. The dolomite reaction was shown to consume portlandite and resulted in the formation of hydrotalcite ($Mg_6Al_2(OH)_{18}{\cdot}3(H_2O)$) and calcite:

$$6CaMg(CO_3)_2 + 2Al(OH)_3 + 6Ca(OH)_2 + 3H_2O \rightarrow Mg_6Al_2(OH)_{18}{\cdot}3(H_2O) + 12CaCO_3$$

This reaction was shown to depend on the availability of portlandite in the system. In samples with high metakaolin content, the reactive metakaolin consumed the portlandite before the less reactive dolomite started to react, which limited the dolomite reaction. The pore space and the availability of aluminium were found to play minor roles in limiting the dolomite reaction.

The durability part of the PhD project investigated the stability of the hydrotalcite formed in composite cements containing dolomite. Samples with little or no metakaolin content were selected because they formed the greatest amount of hydrotalcite in the hydration study. It was shown that hydrotalcite can withstand high degrees of leaching and carbonation. After chloride exposure, the formation of a chloride-containing hydrotalcite was observed, which increased the chloride binding of the cement paste samples investigated. With mass balance calculations, it was shown that the chloride-containing hydrotalcite in samples containing dolomite can contribute to the chloride binding of the cement paste to an extent comparable to Friedel's salt in samples containing limestone.

It could be concluded that dolomite performs in a similar way to limestone in cementitious systems with regard to compressive strength and phase stability. The phase assemblages in composite cements containing dolomite and limestone are similar. The reaction of dolomite in systems containing little or no metakaolin was shown to result in the additional formation of hydrotalcite, a stable reaction product in the aggressive environments tested, which is able to take up a significant amount of chloride.

Table of contents

Structure of the doctoral thesis

The thesis consists of two parts. Part I contains a short literature review on the research topics investigated, the objectives and limitations of the thesis, and an overview of the experimental approach. Finally, the main findings and conclusions are summarized.

Part II presents the scientific journal papers, which represent the detailed outcome of the various research questions formulated in Part I.

List of appended papers in Part II

The PhD thesis includes the following scientific journal papers:

I **Portland metakaolin cement containing dolomite or limestone – similarities and differences in phase assemblage and compressive strength**
Alisa Machner, Maciej Zajac, Mohsen Ben Haha, Knut O. Kjellsen, Mette R. Geiker, Klaartje De Weerdt
Construction and Building Materials, 2017, Vol. 157, pp. 214-225

II **Limitations of the hydrotalcite formation in Portland composite cement pastes containing dolomite and metakaolin**
Alisa Machner, Maciej Zajac, Mohsen Ben Haha, Knut O. Kjellsen, Mette R. Geiker, Klaartje De Weerdt
Accepted for publication in Cement and Concrete Research (November 2017)
*D*OI: 10.1016/j.cemconres.2017.11.007

III **Stability of the phase assemblage in Portland composite cements containing dolomite and metakaolin after leaching, carbonation, and chloride exposure**
Alisa Machner, Maciej Zajac, Mohsen Ben Haha, Knut O. Kjellsen, Mette R. Geiker, Klaartje De Weerdt
Revised version submitted to Cement and Concrete Composites (January 2018)

IV **Chloride-binding capacity of hydrotalcite in cement pastes containing dolomite and metakaolin**
Alisa Machner, Maciej Zajac, Mohsen Ben Haha, Knut O. Kjellsen, Mette R. Geiker, Klaartje De Weerdt
Revised version submitted to Cement and Concrete Research (January 2018)

Other publications

Conference proceedings:

Investigation of the products of the dolomite reaction in Portland cement pastes
Alisa Machner, Maciej Zajac, Mohsen Ben Haha, Knut O. Kjellsen, Mette R. Geiker, Klaartje De Weerdt
Proceedings of the XXIII Nordic Concrete Research Symposium, Aalborg (Denmark), August 21th–23rd 2017.

Articles in popular scientific magazines:

Bedre egenskaper med dolomitt i sement
Alisa Machner, Mette R. Geiker, Klaartje De Weerdt, Knut O. Kjellsen
Byggeindustrien, 2017 (Nr. 16), p. 76

Declaration of authorship

Alisa Machner conducted most of the experiments and wrote most of each of the above-listed publications and all other parts of the thesis. The laboratories of the HeidelbergCement Technology Center carried out the characterisation of the clinker (used in Papers I and II), the carbonates, and the metakaolin with XRF and QXRD, and the MIP experiments for Papers I and II. Maciej Zajac (HeidelbergCement Technology Center) performed the thermodynamic modelling in Paper II. Norcem AS carried out the XRF investigation of the cement used in Papers III and IV. Torill Sørlokk (Institute for Geoscience and Petroleum, NTNU) carried out the XRF investigations of the hydrated cement pastes for Paper III.

List of symbols and abbreviations

Cement chemistry shorthand notation used in this thesis:

C = CaO	S = SiO_2	A = Al_2O_3	F = Fe_2O_3
M = MgO	H = H_2O	$\bar{C}$ = CO_2	$\bar{S}$ = SO_3

Shorthand notation of anhydrous phases and hydrates in cementitious systems:

Name	**Shorthand notation / abbreviation**	**Stoichiometric or general formula**
Alite*	C_3S	Ca_3SiO_5
Belite*	C_2S	Ca_2SiO_4
Aluminate*	C_3A	$Ca_3Al_2O_6$
Ferrite$^{\Delta}$	C_4AF	$4CaO{\cdot}Al_2O_3{\cdot}Fe_2O_3$
Calcium silicate hydrate	C-S-H	$xCaO{\cdot}SiO_2{\cdot}yH_2O$ (variable composition)
Portlandite	CH	$Ca(OH)_2$
Monocarbonate	$C_4A\bar{C}H_{11}$ (Mc)	$3CaO{\cdot}Al_2O_3{\cdot}CaCO_3{\cdot}11H_2O$
Hemicarbonate	$C_4A\bar{C}_{0.5}H_{11.5}$ (Hc)	$3CaO{\cdot}Al_2O_3{\cdot}0.5Ca(OH)_2{\cdot}0.5CaCO_3{\cdot}11.5H_2O$
Monosulphate	$C_4A\bar{S}H_{12}$ (Ms)	$3CaO{\cdot}Al_2O_3{\cdot}CaSO_4{\cdot}12H_2O$
Friedel's salt	Fs	$3CaO{\cdot}Al_2O_3{\cdot}CaCl_2{\cdot}10H_2O$
Ettringite	$C_6A\bar{S}_3H_{32}$ (Et)	$3CaO{\cdot}Al_2O_3{\cdot}3CaSO_4{\cdot}32H_2O$
Hydrotalcite†	Ht	$Mg_6Al_2(OH)_{18}{\cdot}3(H_2O)$
Brucite	MH	$Mg(OH)_2$
Hydrogarnet (Si and Fe substituted)	Hg	$Ca_3(Al_xFe_{1-x})_2(SiO_4)_y(OH)_{4(3-y)}$
Gypsum	$C\bar{S}H_2$ (Gyp)	$CaSO_4{\cdot}2H_2O$

** These names refer to impure phases, which contain small quantities of foreign ions to stabilize their crystal structure*

Δ The ferrite phase in Portland cement has a variable composition and is a part of the incomplete solid solution between C_2A and C_2F. C_4AF (Brownmillerite) is one possible phase within this solid solution.

† The name hydrotalcite refers to a hydrotalcite-like phase within the group of layered double hydroxides with the general formula $[M^{2+}_{1-x}M^{3+}_x(OH)_2]^{x+}[A^{m-}]_{x/m}{\cdot}nH_2O$.

Abbreviations used:

PC	Portland cement
SCM	Supplementary cementitious material
w/b ratio	Water-to-binder ratio (on weight basis)
C-S-H	Amorphous calcium silicate hydrate, which is the main hydration product of the silicate clinker phases (C_3S and C_2S). It can also be formed by the pozzolanic reaction of e.g. metakaolin. It has a variable composition and is therefore abbreviated and not given with a stoichiometric formula
AFm	Alumina-ferric monophase, derived from the monosulphate structure by the replacement of SO_4^{2-} with other anions. Replacement of aluminium with iron is possible.
AFt	Alumina-ferric triphase, derived from the ettringite structure by the replacement of SO_4^{2-} with other anions. Replacement of aluminium with iron is possible.
C_l	Portland cement clinker (without addition of gypsum or limestone)
C_i	Portland cement (without addition of limestone)
$D_{(l,n)}$	Dolomite ($CaMg(CO_3)_2$), l: laboratory-grade, n: natural
$L_{(l,n)}$	Limestone ($CaCO_3$), l: laboratory-grade, n: natural
M	Metakaolin ($Al_2Si_2O_7$)
SEM	Scanning electron microscopy
EDS	Energy dispersive spectrometry
BSE	Back-scattered electron (image)
TGA	Thermogravimetric analysis
DTG	Differential thermogravimetry
MS	Mass spectrometry
XRD	X-ray diffraction
QXRD	Quantitative X-ray diffraction
MIP	Mercury intrusion porosimetry
RH	Relative humidity
%wt / wt%	Weight percentage

Part I
Extended Summary

1. Introduction

Concrete, which consists of cement, water, and aggregates, is the most used material in the world besides water and is known to be inexpensive and durable. However, a significant amount of CO_2 is emitted during the production of cement for two main reasons. Firstly, CO_2 is emitted when heating the kiln to a temperature of approx. 1450 °C. This high temperature is needed to form the clinker phases, such as alite, belite, and aluminate, which can react with water and cause the cement paste to set and develop its strength. Secondly, limestone, which is the main raw material for cement production and consists mainly of $CaCO_3$, releases 44%wt of its mass as CO_2 when heated above approx. 800 °C (Damtoft et al., 2008; Huntzinger & Eatmon, 2009; Sonebi et al., 2016).

One way to reduce the CO_2 emissions during cement production is to reduce the clinker factor of the resulting product, which means replacing some of the cement clinker with supplementary cementitious materials (SCMs) (Lothenbach et al., 2011). Cements that include SCMs are called composite cements and are widely used today.

Commonly used SCMs include ground granulated blast furnace slag (GGBFS), fly ash, limestone, or natural pozzolans (e.g. EN 197-1, 2011). However, some of the SCMs traditionally used have limited availability when compared to the global increase in cement demand (Scrivener et al., 2016). Alternative SCMs that are available in sufficient quality and quantity need therefore to be found. These new SCMs should yield a similar or even improved compressive strength and durability of the resulting concrete products compared to the SCMs traditionally used. This project focused on dolomite in combination with calcined clays as new SCMs. In this study, metakaolin was used as a model material for industrially available calcined clays.

2. Objectives and limitations

2.1. Objectives

The main objectives of the PhD project were to understand the hydration mechanisms of composite cements that contain a combination of dolomite and metakaolin and the durability of the phase assemblage formed. The PhD project was divided into two sub-studies, the hydration study and the durability study.

Consequently, the following research questions were formulated:

Within the hydration study:

1 How does the addition of dolomite to a Portland metakaolin cement affect the compressive strength and phase assemblage in comparison to the commonly used limestone?

2 What is the effect of metakaolin on the reaction of dolomite and thereby on the formation of hydrotalcite in composite cements?

Within the durability study:

3 How stable is the hydrotalcite formed in composite cements that contain dolomite during chloride exposure, leaching and carbonation?

4 What is the contribution of the hydrotalcite formed in composite cements that contain dolomite to the chloride binding of the cement paste?

2.2. Limitations

This study used one type of Portland cement clinker ("Standard clinker" produced by Norcem AS at the Brevik plant), which is the most commonly used Portland cement clinker in Norway and is representative for commonly used Portland cement clinkers. Moreover, laboratory-grade metakaolin with a known composition (Metastar501, from Imerys) was used as a model material for industrially available calcined clay. The carbonates used (dolomite and limestone) were either laboratory-grade (from Brenntag) or relatively pure natural carbonates (from Miljøkalk AS). Pure materials were used to isolate their effect on phase assemblage and phase composition.

To accelerate the normally very slow reaction of dolomite, the samples investigated in the PhD project were cured at elevated temperatures of 38 °C or 60 °C, as well as at the commonly used 20 °C. Curing at 38 °C accelerates the reactions in cementitious systems, but does not have a significant effect on the phase stabilities (Lothenbach et al., 2007). However, curing at 60 °C changes the phase stabilities of the hydration phases formed, because phases such as ettringite and monocarbonate are no longer stable (Lothenbach et al., 2007). This introduces limitations on the transferability of the results of the phase assemblage and phase composition at 60 °C to 20 °C.

The quantification of the dolomite reaction by quantitative X-ray diffraction (QXRD) had a relatively high margin of error (approx. 10%), which was caused by the spottiness effects of the dolomite peaks in the diffractograms due to the hardness of the dolomite used. The formation of calcium carbonate during the reaction of dolomite was observed qualitatively, but was not evaluated quantitatively because of the limitations of quantifications with TGA and XRD.

The focus of the PhD project was on understanding the hydration reactions, the resulting phase assemblage, and the durability of Portland composite cements containing dolomite and metakaolin. Optimization of the replacement level and the optimization of the combined replacement of dolomite and metakaolin were beyond the scope of the PhD project. The durability study in the PhD project was limited to the samples with little or no metakaolin present, in which the highest amount of hydrotalcite was detected. Moreover, the durability study experiments were limited to chloride exposure (NaCl, $CaCl_2$), leaching with deionized water, and carbonation. Other aggressive environments, such as sulphate-containing solutions were not investigated. No performance tests were carried out within the PhD project, which limits the discussion on the durability of composite cements containing dolomite and metakaolin to phase stability.

3. Background

3.1. Dolomite and limestone as supplementary cementitious materials

The addition of finely ground limestone to Portland cement has been reported to affect the hydration in several ways. A comprehensive overview of the effect of limestone addition to Portland cement on compressive strength and phase assemblage can be found in (Hawkins et al., 2003). First, there is the physical effect of finely ground limestone, which is also often called the filler effect. The addition of fine limestone to Portland cement provides additional nucleation sites, which facilitate the precipitation of hydrates during the hydration of the cement (Lothenbach et al., 2011). Moreover, in systems where some of the cement clinker is replaced with another material, the water-to-clinker ratio increases when the water-to-solid ratio is kept constant. This increases the degree of cement clinker reaction (Lothenbach et al., 2011). The addition of finely-ground limestone is known to enhance the reaction of alite and therefore of Portland cement (Soroka & Stern, 1976; Péra et al., 1999), and can also shorten the time to nucleate the first C-S-H phase (Nicoleau, 2011; Berodier et al., 2014), and thus accelerates the hydration of the cement. On the other hand, the filler effect is always connected with a dilution effect, because the most reactive part of the system is partially replaced with a less-reactive material (Lothenbach et al., 2011).

Second, and contrary to the earlier understanding that limestone is an inert material, several authors have reported a reaction of limestone added to Portland cement (Matschei et al., 2007b; Lothenbach et al., 2008; Barker & Cory, 1991; Bensted, 1980; Bonavetti et al., 2001; Feldmann et al., 1965; Ingram et al., 1990). Carbonate AFm phases, such as hemicarbonate and monocarbonate, are formed during the reaction of limestone with pure C_3A or C_3A in Portland cement (Bonavetti et al., 2001; Feldmann et al., 1965; Bensted, 1980; Barker & Cory, 1991; Ingram et al., 1990). In the presence of carbonates, these AFm phases are more stable than monosulphate (Matschei et al., 2007a) and as a consequence, the ettringite does not transform to monosulphate after the sulphate source, e.g. gypsum, is depleted. This chemical effect is called “ettringite stabilization” and results in a relative increase in the volume of hydrates and leads to an increase in compressive strength at low replacement levels (Matschei et al., 2007b; Lothenbach et al., 2008).

The scarceness of high-quality limestone in some parts of the world obliges the cement industry to consider alternative supplementary cementitious materials (SCMs) for the production of composite cements. Various other carbonate sources are therefore in the focus of ongoing research, with dolomite rock being one promising alternative. Zajac & Ben Haha observed a similar compressive

strength of samples where 20%wt of the cement clinker was replaced with either limestone or dolomite (Zajac & Ben Haha, 2015). Moreover, Zajac et al. have been able to demonstrate that the effect of ettringite stabilization upon carbonate addition, which has been reported for cements containing limestone, is also valid for cements containing ground dolomite rock (Zajac et al., 2014).

The mineral dolomite is a double salt containing calcium and magnesium with the chemical formula $CaMg(CO_3)_2$ and can, therefore, function as a source of calcium, magnesium, and CO_2. Dolomite is the rock-forming mineral for dolomite rock, and it is not stable in the high-alkaline environment of a cement, where it has been reported to undergo what is known as the dedolomitization reaction (Galí et al., 2001; Garcia et al., 2003; Zhang et al., 2014). In this reaction, dolomite reacts with calcium hydroxide (portlandite) to form calcium carbonate (calcite) and magnesium hydroxide (brucite), see Eq. 1 (Galí et al., 2001; Garcia et al., 2003; Zhang et al., 2014):

$$CaMg(CO_3)_2 + Ca(OH)_2 \rightarrow Mg(OH)_2 + 2CaCO_3 \qquad \text{Eq. 1}$$

It has been shown that in cementitious systems the reaction of dolomite forms products similar to those of hydrated Portland limestone cement, and that the magnesium originating from the dolomite resulted in the formation of a hydrotalcite-like phase (Zajac et al., 2011; Zajac et al., 2014), in the following referred to as hydrotalcite ($Mg_6Al_2(OH)_{18}{\cdot}3(H_2O)$ (Myers et al., 2015)).

The dissolution of dolomite and calcite in various conditions has been studied before (Morse & Arvidson, 2002). Pokrovsky et al. were able to show that the dissolution rate of dolomite is significantly lower than that of limestone at both 25 °C and 60 °C (Pokrovsky et al., 2009). Moreover, the dissolution rates of both decrease with increasing pH (Chou et al., 1989) and increase with increasing temperatures from 25 °C to 60 °C (Pokrovsky et al., 2009). This accords with other authors, who have reported a higher degree of dolomite reaction with increasing temperatures (Galí et al., 2001; Zhang et al., 2014; Zajac et al., 2014).

3.2. Metakaolin as supplementary cementitious material

Intense research on the use of calcined clays as SCMs has been conducted in recent years, due to the scarceness of fly ash and ground granulated blast furnace slag as SCMs in some parts of the world. Clays belong to the mineral group of phyllosilicates (sheet silicates). When they are calcined between 600–900 °C, they lose their interlayer water and their ordered crystal structure. The amorphous

calcination products are called calcined clays and react as pozzolans with the portlandite formed during the cement clinker hydration to form additional C-S-H (Jones, 2002). Among various clays tested, kaolinitic calcined clay, known as metakaolin, showed the highest pozzolanic reactivity (Fernandez et al., 2011).

Some of the alumina provided by the reaction of metakaolin leads to the formation of additional AFm phases (Antoni et al., 2012; Nied et al., 2015; Puerta-Falla et al., 2015) in the same way as shown for the addition of fly ash (De Weerdt et al., 2011; De Weerdt et al., 2010), and some is taken up by the C-S-H phase (L'Hôpital et al., 2015; Dai et al., 2014). Aluminium incorporation in the C-S-H phase can lead to the formation of calcium aluminate silicate hydrate (C-A-S-H) phases, as observed in composite cements containing slag, fly ash or metakaolin (Richardson, 1999; Dai et al., 2014). The addition of large amounts of metakaolin increases not only the aluminium content, but also the silicate chain length in the C-S-H phase (Love et al., 2007). The effect on the chain length has also been reported for other SCMs containing silicon, e.g. silica fume, and is accompanied by a decrease in the Ca/Si ratio of the C-S-H (Gaitero et al., 2008; Justnes, 1998; Rossen et al., 2015). Sevelsted & Skibsted have also demonstrated this effect of increasing silicate chain lengths with decreasing Ca/Si ratios for synthetic C-S-H samples (Sevelsted & Skibsted, 2015).

3.3. The synergetic effect

The positive effect of the "ettringite stabilization" on the compressive strength when carbonates are added to Portland cements (see 3.1) is limited because the amount of alumina available is limited in these cements. However, the effect can be amplified by increasing the aluminium content of the cement, e.g. by using various aluminium-containing SCMs. This effect has previously been demonstrated for samples containing limestone and fly ash (De Weerdt et al., 2010; De Weerdt et al., 2011) and for combinations of limestone and metakaolin (Antoni et al., 2012; Nied et al., 2015; Puerta-Falla et al., 2015). The additional alumina provided by the reaction of metakaolin has been reported to lead to the formation of additional AFm phases and therefore to an increased compressive strength at low replacement levels of limestone. This effect is called the "synergetic effect" and allows a higher replacement level of the cement clinker by combining an aluminium-delivering SCM (metakaolin or fly ash) with a carbonate, without impairing compressive strength.

3.4. Effect on SCMs on the durability of composite cements

The durability of concrete is defined as its ability to withstand weathering action, chemical attack, abrasion, or any other deteriorative process during its service life (ACI CT-16, 2016). The durability of concrete may partly depend on the phase assemblage and composition of the phases present in the hydrated cement. Changes in the chemistry of composite cements containing SCMs may also change their resistance to various exposures. In the following, the deteriorative mechanisms of leaching and carbonation, and the response of the cement paste to exposure to chloride-containing solutions will be described in detail.

3.4.1. Leaching

Leaching is the congruent dissolution (e.g. portlandite) or incongruent dissolution (e.g. C-S-H phase) of hydration phases when they are in long-term contact with water, and it represents one type of possible attack on concrete. Leaching of concrete or cement paste results in a decrease in its pH and a lower concentration of ions in the pore solution. This leads to the decalcification of the system, and therefore to the decomposition of hydrates (Taylor, 1997).

During leaching, the portlandite dissolves and the C-S-H gradually decalcifies until it completely decomposes. The increased average silicate chain lengths of the C-S-H phase (due to the addition of SCMs containing silicon) typically improves resistance to the leaching of calcium (Gaitero et al., 2008; Jain & Neithalath, 2009; Matte V. & Moranville M., 1999).

Hydrotalcite displayed good resistance against leaching in MgO-activated slag binder systems (Jin & Al-Tabbaa, 2014; Jin et al., 2016). Thermodynamic modelling for leaching has also predicted that phases, like hydrotalcite or ettringite, withstand harsh leaching conditions without changes in volume and start decomposing only when the C-S-H has completely decomposed (Feng et al., 2014).

3.4.2. Carbonation

The corrosion of the steel rebars is one of the main deterioration mechanisms of reinforced concrete. It can be initiated by the depassivation of the rebar surface due to a drop in the pH caused by carbonation of the cement paste in concrete. The carbonation of concrete is the reaction of CO_2, which dissolves in the pore solution, with the calcium in the hydrated cement paste to form calcium carbonate ($CaCO_3$) (ACI CT-16, 2016; Taylor, 1997). This reaction causes a drop in the pH of the pore

solution once the portlandite is depleted, a decalcification of the system, and consequently the decomposition of the hydrates. During carbonation, portlandite ($Ca(OH)_2$) reacts with the CO_2 to form $CaCO_3$. Afterwards, the C-S-H phase decalcifies, which leads to an increase in its silicate chain length.

The reduced Ca/Si ratio of the C-S-H phase, as observed in samples containing metakaolin (see 3.2), may increase the resistance to carbonation of these samples. The extent of decalcification has been reported to decrease with decreasing Ca/Si ratios, and was observed to be most pronounced in samples of synthesized C-S-H with a high Ca/Si ratio (Black et al., 2007; Black et al., 2008). Sevelsted & Skibsted confirmed these findings in their study, where they observed an increased amount of calcium carbonate in samples with higher Ca/Si ratios (Sevelsted & Skibsted, 2015). During carbonation, ettringite and AFm phases also decompose to $CaCO_3$, hydrous alumina and, in the case of sulphate-containing hydrates, gypsum (Taylor, 1997).

Hydrotalcite has been reported to be a promising material for application in CO_2-capture technology because of its high CO_2 adsorption capacity (Wang et al., 2011). However, pure synthesised hydrotalcite may differ in composition from hydrotalcite formed in Portland cement-based cementitious systems. This study, therefore, focuses on the stability of hydrotalcite formed by the reaction of dolomite in a Portland composite cement during leaching and carbonation.

3.4.3. Chloride exposure

Another way for the corrosion of the steel rebars in reinforced concrete to initiate is through the presence of chlorides in the vicinity of the steel. The most common sources for chlorides are external, e.g. de-icing salts or seawater. When chlorides penetrate the concrete, some will be free in the pore solution and some will interact with the solids. Understanding chloride binding is therefore of major importance for understanding chloride ingress in concrete and predicting the service life of chloride-exposed reinforced concrete structures.

In Portland cement, chloride ions are bound by physical adsorption to the C-S-H phase or by the formation of chloride-containing AFm phases, e.g. Friedel's salt or Kuzel's salt. The use of SCMs can change the phase assemblage of the hydrated cement paste and thereby its chloride-binding capacity (Arya et al., 1990).

The addition of metakaolin has been shown to improve the chloride-binding capacity of cement paste. This has been explained with reference to the additional alumina provided by the reaction of metakaolin, which results in the formation of additional Friedel's salt (Thomas et al., 2012; Shi et al., 2017). Similar results have been reported for other alumina-delivering SCMs, such as fly ash or ground granulated blast-furnace slags (Arya et al., 1990; Arya & Xu, 1995; Dhir et al., 1997; Ipavec et al., 2013; Ogirigbo & Black, 2017). Moreover, the reaction of metakaolin results in the formation of additional C-S-H, which may also bind additional chlorides.

Hydrotalcite is a mineral in the group of layered double hydroxides (LDHs) containing magnesium and aluminium, with the general formula $[Me^{2+}_{1-x}Me^{3+}_{x}(OH)_2]^{x+}$ $[A^{m-}]_{x/m}\cdot nH_2O$. Its crystal structure can be derived from that of brucite. The main layer consists of metals (here abbreviated with Me), specifically magnesium (Me^{2+}) and aluminium (Me^{3+}) hydroxide octahedra. The substitution of aluminium for magnesium in the main layer charges this layer positively. To maintain electrical neutrality, the interlayer incorporates monovalent or divalent anions (here abbreviated with A) like OH^-, Cl^-, CO_3^{2-} or SO_4^{2-}. Several authors have ascribed the excellent chloride-binding capacity of hydrotalcite to the positive charge of its main layer, which is compensated by the incorporation of anions in its interlayer (Miyata, 1975, 1983; Châtelet et al., 1996; Kayali et al., 2012). In cementitious systems containing slag, hydrotalcite has been predicted to bind even more chlorides than Friedel's salt (Ye et al., 2016). However, divalent ions, like CO_3^{2-} are more easily incorporated than monovalent ions, like Cl^- (Miyata, 1983; Châtelet et al., 1996), so CO_3^{2-} ions are seldom exchanged with chloride ions in synthesized hydrotalcite-like phases, and the presence of carbonate ions consequently reduces the chloride-binding capacity (Châtelet et al., 1996; Ke et al., 2017). A greater amount of aluminium available in the system reduces the Mg/Al ratio of the hydrotalcite (Ben Haha et al., 2012). A higher degree of aluminium substitution increases the positive charge of the main layer. Because the interlayer seeks electrical neutrality, more chlorides are incorporated in the interlayer of hydrotalcite with a lower Mg/Al ratio (Miyata, 1975).

The chloride-binding capacity of cements also depends strongly on the cation associated with the chloride anion. Several authors have reported significantly greater chloride binding when samples were exposed to solutions of $CaCl_2$ or $MgCl_2$ rather than NaCl (Arya et al., 1990; Delagrave et al., 1997; Wowra & Setzer, 1997; Zhu et al., 2012; De Weerdt et al., 2014; De Weerdt et al., 2015; Shi et al., 2017). This can be explained by the deprotonation of the surface silanol groups of C-S-H, which gives the C-S-H a negative surface charge. This negative surface charge causes the adsorption of positively

charged ions (counterions) in the Stern layer of its surface (Wowra & Setzer, 1997). Labbez et al. showed that the adsorption of divalent Ca^{2+} ions on C-S-H in model systems can even reverse the surface charge to positive values (overcompensation) (Labbez et al., 2007). This can lead to an accumulation of negatively charged ions (coions), like Cl^- or OH^-, in the diffuse layer of the C-S-H (Plusquellec & Nonat, 2016). The reversal in the surface charge leading to the accumulation of coions in the diffuse layer has not been observed with monovalent ions, like Na^+ (Wowra & Setzer, 1997).

The drop in the pH observed when $CaCl_2$ is added to cement pastes can be partly explained by the substitution of calcium for hydrogen in the silanol groups, which releases H^+ ions in the pore solution (Wowra & Setzer, 1997; Shi et al., 2017), and partly by the common ion effect of calcium (calcium hydroxide) when increasing amounts of $CaCl_2$ are added to the system (De Weerdt et al., 2015).

4. Experimental approach

Overview of the various materials used:

Table 4-1 gives an overview of the materials used for the various papers of the PhD project. The Portland cement clinker (C_l) was a "Standard" clinker supplied by Norcem AS, ground in a laboratory ball mill until a Blaine specific surface of approx. 400 m^2/kg was reached. No gypsum or other calcium sulphate was added to the clinker (C_l) during grinding (cf. Papers I–II). The neat Portland cement (C_i) supplied by Norcem AS was produced by grinding "Standard" clinker in one of the cement mills of Norcem AS with gypsum added until a Blaine specific surface of approx. 400 m^2/kg was achieved (cf. Papers III–IV). No limestone was added after clinkering to C_l or C_i.

Two different carbonate qualities were used. The laboratory-grade carbonates (L_l and D_l) were supplied by Brenntag (cf. Paper I) and the natural carbonates (L_n and D_n) were supplied by Miljøkalk AS (cf. Papers II–IV). Laboratory-grade metakaolin (M) supplied by Imerys (Metastar501) was used throughout the project.

Table 4-1: Overview of the materials used in this PhD project.

Material	Abbr.	Supplier	Paper I	Paper II	Paper III	Paper IV
Portland cement clinker (no gypsum and no limestone added)	C_l	Norcem AS	X	X		
Portland cement (gypsum added, no limestone added)	C_i	Norcem AS			X	X
Laboratory-grade carbonates	D_l, L_l	Brenntag	X			
Natural carbonates	D_n, L_n	Miljøkalk AS		X	X	X
Laboratory-grade metakaolin	M	Imerys	X	X	X	X

Experimental matrix used for Paper I:

Table 4-2 gives the experimental matrix used for Paper I. The clinker (C_l) and the metakaolin (M) were pre-mixed to a ratio 6:1. Afterwards, 5–20%wt of this Portland metakaolin cement (CM) was replaced with either laboratory-grade dolomite (D_l) or limestone (L_l). A Portland metakaolin cement sample without carbonate addition was used as a reference (100CM). The sulphate content of the binders was adjusted by the addition of 2.85%wt laboratory-grade gypsum to all compositions (not included in Table 4-2). The pastes and mortars were prepared with a w/b ratio of 0.55 and cured sealed at 5 °C, 20 °C, or 38 °C for up to 90 days at 100% RH.

Table 4-2: Experimental matrix for Paper I.

No.	Name of the mix	CM (C_l:M = 6:1)	L_l	D_l
1	100CM	100		
2	95CM5L	95	5	
3	90CM10L	90	10	
4	80CM20L	80	20	
5	95CM5D	95		5
6	90CM10D	90		10
7	80CM20D	80		20

Experimental matrix used for Paper II:

Table 4-3 shows the experimental matrix for Paper II. In this study, 40%wt of the Portland cement clinker (C_l) was replaced by either natural dolomite (D_n) or a combination of dolomite and metakaolin (M). Equivalent samples containing natural limestone (L_n) and a pure Portland cement sample were prepared as references. Laboratory-grade gypsum was added to all compositions to achieve a sulphate content of 2.5%wt per gram of binder (not included in Table 4-3). The pastes were prepared with a w/b ratio of 0.45 and were cured sealed at 20 °C, 38 °C, and 60 °C for up to 360 days at 100% RH. Samples containing 20%wt metakaolin were also prepared with a high w/b ratio of 0.93 or with additional portlandite and/or water.

Table 4-3: Experimental matrix for Paper II.

Name of the mix	C_l	D_n	L_n	M	Add. water	Add. CH	w/b ratio
100C*	100	-	-	-	-	-	0.45
60C40D*	60	40	-	-	-	-	0.45
60C35D5M*	60	35	-	5	-	-	0.45
60C30D10M	60	30	-	10	-	-	0.45
60C25D15M	60	25	-	15	-	-	0.45
60C20D20M	60	20	-	20	-	-	0.45
60C40L*	60	-	40	-	-	-	0.45
60C35L5M*	60	-	35	5	-	-	0.45
60C30L10M	60	-	30	10	-	-	0.45
60C25L15M	60	-	25	15	-	-	0.45
60C20L20M	60	-	20	20	-	-	0.45
60C20D20M w/b 0.45	60	20	-	20	-	-	0.45
60C20D20M w/b 0.93	60	20	-	20	-	-	0.93
60C20D20M + H_2O	60	20	-	20	+30%wt	-	0.45
60C20D20M + CH	60	20	-	20	+30%wt	+30%wt	0.45

* Binder compositions also used for Papers III and IV

Experimental matrix used for Papers III and IV:

For Papers III and IV, the compositions in Table 4-3 marked with * were used, except that these samples were prepared using the Portland cement C_i with a w/b ratio of 0.5. The sulphate content of this cement was adjusted to 3.2%wt, so no additional gypsum was added. Figure 1 gives an overview of the steps taken in the preparation of the samples for Papers III and IV. The pastes were cured sealed immersed in water at 38 °C (only Paper IV) and 60 °C (Papers III and IV) for 3 months. To ensure a high degree of reaction in the samples, they were ground and rehydrated after the first 3 months of the curing time. The samples were first crushed in a jaw crusher and passed through a 1 mm sieve. The particles that did not pass through the sieve after the crushing, were then ground in a rotating disc mill until they also passed through the 1 mm sieve. Finally, 30%wt of additional water was added to the ground pastes. The rehydrated samples were then stored for another 4 months at the respective temperatures (38 °C or 60 °C). After a total of 7 months of curing, the samples were transferred to 20 °C for 2 weeks prior to exposure, which was also carried out at 20 °C. Reference samples, which were not carbonated, leached, or exposed to chloride solutions, were stored for a similar time and were also analysed at the end of the exposure time. It should be noted that the exposed samples were compared with these reference samples, which were kept at 20 °C and either stored sealed (for comparison with the carbonated or leached samples) or exposed to water (for comparison with the samples exposed to a chloride solution).

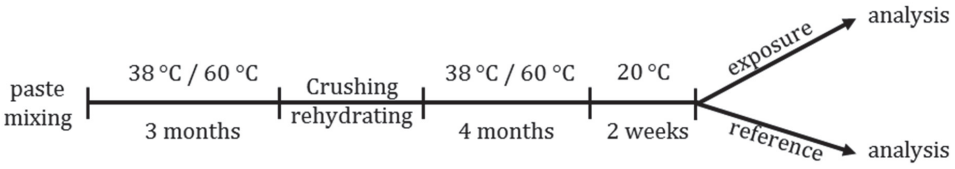

Figure 1: Timeline of the sample preparation for Papers III and IV.

Methods:

Table 4-4 gives an overview of the techniques used for the characterization of the materials in the PhD project. The XRF and QXRD investigations of the clinker C_l, the carbonates, and the metakaolin were carried out by the HeidelbergCement Technology Center laboratory. The Blaine and laser diffraction measurements of these materials were carried out by Alisa Machner at the Norcem AS laboratories. The XRF, Blaine, and laser diffraction measurements of the clinker C_i were carried out by the Norcem AS laboratories.

Table 4-4: Overview of the material characterization methods.

Characterization	Method	Performed
Chemical composition	XRF	HeidelbergCement Technology Center / Norcem AS
Mineralogical composition (For clinker only in Papers I and II)	QXRD	HeidelbergCement Technology Center
Specific surface area	Blaine method	Alisa Machner / Norcem AS
Particle size distribution	Laser diffraction	Alisa Machner / Norcem AS

An overview of the measurement techniques used for the various papers is given in Table 4-5. The papers aimed to answer the research questions listed in 2.1. A detailed description of the method parameters and steps taken in sample preparation for the investigations can be found in the papers appended.

Table 4-5: Overview of the measurement techniques applied for the various papers.

Paper	Title	Techniques used	Research question
I	Portland metakaolin cement containing dolomite or limestone – Similarities and differences in phase assemblage and compressive strength	Compressive strength testing in accordance with EN 196-1, MIP, TGA, XRD, and Thermodynamic modelling	1
II	Limitations of the hydrotalcite formation in Portland composite cement pastes containing dolomite and metakaolin	TGA, XRD, QXRD, SEM-EDS, and MIP	2
III	Stability of the hydrate phase assemblage in Portland composite cements containing dolomite and metakaolin after leaching, carbonation, and chloride exposure	TGA, XRD, SEM-EDS, XRF, TGA-MS, and Thermodynamic modelling	3
IV	Chloride-binding capacity of hydrotalcite in cement pastes containing dolomite and metakaolin	Potentiometric chloride titration, pH measurements, TGA, XRD, SEM-EDS, mass balance calculations, and TGA-MS	4

5. Main findings

Dolomite as an SCM for Portland metakaolin cement – effect on phase assemblage and compressive strength
(Research question 1 – Paper I)

Up to 20%wt of a Portland metakaolin cement was replaced with either dolomite or limestone. Compressive strength, phase assemblage and microstructure were studied on mortar or paste samples prepared with a w/b ratio of 0.55 and cured at 5 °C, 20 °C, or 38 °C for up to 90 days.

It was shown that, for the given hydration time, the addition of dolomite resulted in a phase assemblage similar to the addition of limestone. In both cases, ettringite was stabilized beyond the sulphate depletion point due to the formation of carbonate AFm phases. This shows that either dolomite or limestone can be used to replace up to 10%wt of a Portland metakaolin cement without impairing its compressive strength at 90 days. A strength increase at low replacement levels of dolomite was only visible at 20 °C or 38 °C. This could be explained by dolomite having a lower reactivity than limestone at lower curing temperatures, as indicated by thermodynamic modelling, even though a very fine dolomite was used. However, increasing the curing temperature from 5 °C to 38 °C was shown to increase the reactivity of the dolomite.

The effect of metakaolin on the reaction of dolomite in Portland composite cements
(Research question 2 – Paper II)

40%wt of a Portland cement clinker was replaced by dolomite or a combination of dolomite and metakaolin. Equivalent samples containing limestone instead of dolomite and a pure Portland cement sample were used as references. The paste samples investigated were prepared with a w/b ratio of 0.45 and cured at 20 °C, 38 °C and 60 °C for up to 360 days. Additionally, to investigate the effect of the pore structure, the samples containing 20%wt of dolomite and 20%wt of metakaolin were also prepared with a higher w/b ratio (0.93). To investigate the impact of the availability of portlandite, 30%wt of additional portlandite and or deionized water were added to these metakaolin-rich samples (w/b ratio of 0.45), after a curing time of 1 year and 9 months. The phase assemblage, microstructure and the composition of the hydrotalcite and the C-S-H phase were investigated.

It was shown that significant amounts of dolomite reacted from 90 days on only in samples, which were cured at elevated temperatures and contained little or no metakaolin.

Hydrotalcite was observed in the reaction rims around the dolomite grains, as illustrated in Figure 2. The uniformly grey particles in the SEM-BSE image are unreacted dolomite grains. Around these particles, there is a darker reaction rim filled with hydrotalcite. The shape of the original dolomite grains is still visible, because it is marked with a thin layer of C-S-H precipitated around them, presumably at early ages, which then persisted even after the dolomite started to react at later ages. The reaction of dolomite requires the transport of aluminium into the reaction rims and the transport of calcium and CO_3^{2-} out of the reaction rims. The magnesium from the dolomite stays within the original dolomite grain boundaries.

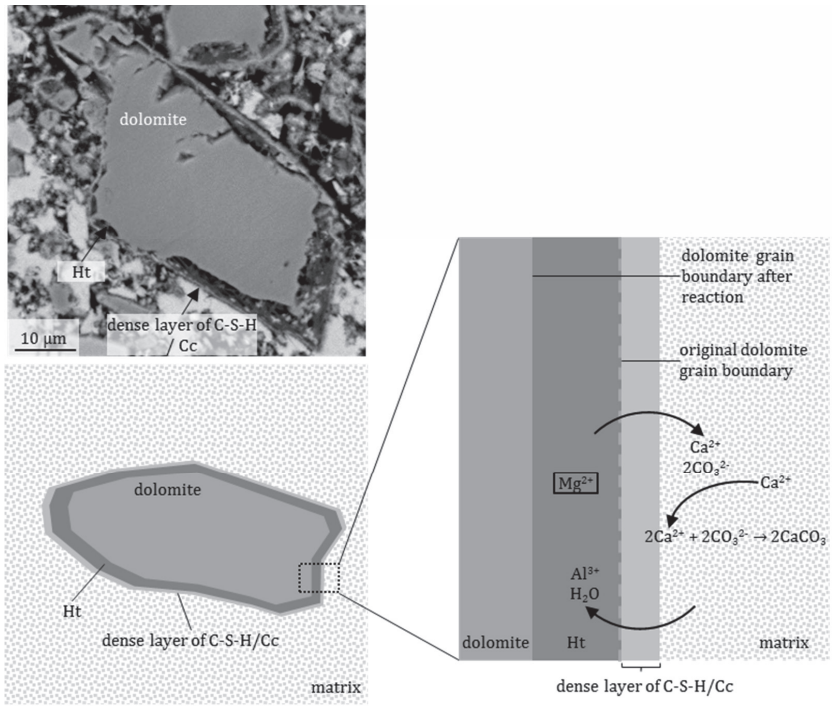

Figure 2: BSE image of a partially reacted dolomite particle in the cement paste and a schematic illustration of the hydrotalcite formation in the reaction rims around the dolomite grains.

Eq. 2 gives the reaction equation of the hydrotalcite formation based on the findings in this study. In this reaction, dolomite reacts with a source of aluminium, here given as $Al(OH)_3$, and portlandite to form hydrotalcite and calcite. Even though hydrotalcite ($Mg_6Al_2(OH)_{18}{\cdot}3(H_2O)$) does not contain

calcium, the formation of hydrotalcite is associated with the consumption of portlandite to form calcite in a way similar to the reported dedolomitization reaction (Eq. 1). The amount of calcite formed was not directly quantified, but is reflected in the formation of carbonate AFm phases (hemicarbonate or monocarbonate). From the XRD and SEM-EDS results, it could be concluded that neither brucite nor M-S-H have formed in significant amounts, and hydrotalcite was assumed to be the main magnesium-containing reaction product.

$$6CaMg(CO_3)_2 + 2Al(OH)_3 + 6Ca(OH)_2 + 3H_2O \rightarrow Mg_6Al_2(OH)_{18}{\cdot}3(H_2O) + 12CaCO_3 \qquad \text{Eq. 2}$$

The limiting factors of hydrotalcite formation were investigated in more detail. It was shown that significant amounts of hydrotalcite only formed in samples containing little or no metakaolin. It seems the supply of aluminium to the system through the reaction of metakaolin did not promote the formation of hydrotalcite, in contrast to what has previously been found for AFm phases.

The addition of metakaolin also influences the system in other ways than solely by providing aluminium. During its pozzolanic reaction, metakaolin consumes portlandite and simultaneously refines the pore structure. The samples prepared with a high w/b ratio did not show a greater degree of dolomite reaction than the samples prepared with the normal w/b ratio. It was concluded that the pore structure refinement does not inhibit the formation of hydrotalcite. In the samples containing 20%wt of metakaolin to which additional portlandite was added, further dolomite reaction was observed. This suggests that the absence of portlandite in high-metakaolin samples is an inhibiting factor for the reaction of dolomite and therefore for the formation of hydrotalcite. Because metakaolin is a very reactive pozzolanic material, it consumes the portlandite in the system before the more slowly reacting dolomite starts to react significantly. This competition between dolomite and metakaolin for portlandite is illustrated in Figure 3. The need for portlandite, and the calcium it contains, can be explained by the difference between dolomite, which contains 2 mol of CO_3^{2-} per mol of dolomite, and calcite, which contains 1 mol of CO_3^{2-} per mol of calcite. To make the magnesium available for the reaction to form hydrotalcite, calcium is needed to accommodate the other carbonate ion from the dolomite, as in the dedolomitization reaction (Eq. 1) in which brucite is formed. The experimental techniques in this study did not enable the determination of the carbonate content of the hydrotalcite. However, provided the hydrotalcite contains less than 1 mol of CO_3^{2-} per mol of hydrotalcite (Miyata, 1975; Rozov et al., 2010; Rozov et al., 2011; Mills et al., 2012; Myers et al., 2015), calcium is needed to accommodate the remaining carbonate ions.

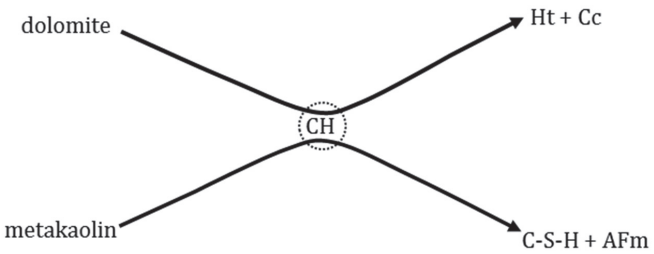

Figure 3: Schematic illustration of the competition for portlandite (CH) between the reaction of dolomite to form hydrotalcite and calcite and the reaction of metakaolin to form additional C-S-H and AFm phases.

Stability of hydrotalcite after carbonation, leaching, and exposure to a chloride-rich solution (Research question 3 – Paper III)

Well-hydrated cement paste samples were investigated, in which 40%wt of the Portland cement has been replaced with dolomite or a combination of dolomite and metakaolin. Equivalent samples containing limestone were used as references. The paste samples cured at 60 °C were ground and rehydrated after the first 3 months of curing. After a total of 7 months of curing, the samples were transferred to 20 °C for two weeks before being carbonated, leached, or exposed to a NaCl solution. The phase assemblage and composition of the hydrotalcite and the C-S-H phase were investigated after exposure. The exposed samples were compared with unexposed reference samples for the carbonated or leached samples, and with samples exposed to water for the samples exposed to a chloride solution.

As expected, it was shown that leaching caused severe decalcification of the C-S-H, and the portlandite and ettringite decomposed. Carbonation resulted in an almost complete decomposition of the C-S-H phase and the consumption of the portlandite as expected. Exposure of the samples to a 2 mol/L chloride solution resulted in the formation of a chloride-containing hydrotalcite. The chloride uptake of the hydrotalcite could also be identified from its chemical composition determined with SEM-EDS and by changes in the peak positions in TGA and XRD. Hydrotalcite seemed to resist both leaching and carbonation, and no change was observed in its Mg/Al ratio. The Mg/Al ratio of the chloride-containing hydrotalcite was similar to the hydrotalcite formed in the reference samples.

Chloride-binding capacity of hydrotalcite in Portland composite cements containing dolomite and metakaolin
(Research question 4 – Paper IV)

Well-hydrated cement paste samples were investigated in which 40%wt of the Portland cement was replaced with dolomite or a combination of dolomite and metakaolin. Equivalent samples containing limestone and a Portland cement sample were used as references. The pastes were originally cured at 38 °C or 60 °C before being transferred to 20 °C for two weeks before exposure to solutions of NaCl or $CaCl_2$, or deionized water. The chloride binding, pH, phase assemblage, and phase composition were investigated.

As shown in Papers I and II, the degree of dolomite reaction and the resulting formation of hydrotalcite can be increased by increasing the curing temperature. The hydrotalcite formed in samples containing dolomite contributed considerably to the chloride binding of these samples. Hydrotalcite in samples exposed to $CaCl_2$ showed a higher chloride uptake than hydrotalcite in samples exposed to NaCl. This might be explained by a decrease in carbonate ion activity when samples are exposed to $CaCl_2$, which might favour the uptake of chlorides over carbonates in the interlayer of hydrotalcite. Mass balance calculations lead to the conclusion that the hydrotalcite formed by the dolomite reaction can contribute to the chloride binding of the cement paste to an extent similar to the Friedel's salt formed in samples containing limestone.

6. Conclusions

The goal of the PhD project was to investigate the possibility of using dolomite instead of limestone as an SCM in combination with an aluminium-delivering SCM, such as metakaolin. In the first part of the PhD project, the reaction of dolomite in a cementitious system was investigated with regard to the compressive strength development, phase assemblage, the composition of the various hydration phases, and the microstructure. In the second part of the PhD project, the durability of the phase assemblage of the composite cements containing metakaolin and/or dolomite was investigated. Special focus was put on the stability of the hydration phases after various aggressive exposures and on the chloride-binding capacity of hydrotalcite.

It was shown that, as a replacement for Portland metakaolin cements, dolomite has similar effects to limestone on the compressive strength and phase assemblage at curing temperatures of 20 °C or 38 °C. Ettringite was stabilized beyond the sulphate depletion point due to the formation of carbonate AFm phases at all curing temperatures and replacement levels of dolomite. However, dolomite was shown to react slowly at low curing temperatures resulting in the formation of hemicarbonate rather than monocarbonate.

In samples where little or no metakaolin was present, dolomite reacted significantly when cured at elevated curing temperatures (38 °C and especially 60 °C) and the formation of hydrotalcite could be observed with XRD, TGA, and SEM-EDS from 90 days on. The significant degree of dolomite reaction in these samples caused the formation of hydrotalcite ($Mg_6Al_2(OH)_{18}{\cdot}3(H_2O)$), which was identified as the main magnesium-containing hydration product. The dolomite reaction was shown to consume portlandite.

The increased availability of aluminium in the system and the refinement of the pore structure due to the addition of metakaolin were found to play minor roles in enhancing or limiting the formation of hydrotalcite. The main limiting factor for the dolomite reaction, and therefore for the formation of hydrotalcite, was found to be the availability of portlandite in the system. This was explained by the competition between dolomite and metakaolin for portlandite. Because metakaolin is a very reactive pozzolanic material, it consumes the portlandite in the system before the more slowly reacting dolomite starts to react significantly.

The hydrotalcite formed in the composite cements was shown to be a stable hydration product, because it did not decompose during leaching or carbonation and it did not change its composition. In the leached or carbonated samples, portlandite could no longer be detected, and the C-S-H had partially decomposed, whereas hydrotalcite could still be observed with TGA, XRD and SEM-EDS after exposure. The results obtained experimentally agreed well with the thermodynamic modelling of the effect of leaching or carbonation on the phase assemblage. Moreover, the exposure to a chloride solution resulted in the formation of a chloride-containing hydrotalcite. The chloride-binding capacity of the hydrotalcite was greater in samples exposed to $CaCl_2$ than in samples exposed to NaCl, probably due to lower carbonate ion activity during $CaCl_2$ exposure. It was shown that the hydrotalcite formed in samples containing dolomite can contribute to the chloride binding of the cement paste to an extent similar to the Friedel's salt formed in samples containing limestone.

It can be concluded that dolomite performs in a similar way to limestone as an SCM in Portland cement-based binder systems with regard to the development of compressive strength and phase assemblage. The main reaction product, hydrotalcite, was shown to remain stable during leaching and carbonation, and to be able to take up significant amounts of chloride.

7. Future research

Optimization of the combined replacement level of Portland cement clinker with dolomite and metakaolin

Investigation of the optimal combination of dolomite and metakaolin as replacement for cement clinker was beyond the scope of this PhD project. However, it has been shown that the addition of metakaolin has an impact on the reaction of dolomite and can even hinder it. Hydrotalcite has been shown to be a stable hydrate and might have a beneficial effect on durability. Consequently, optimization of the partial replacement of cement clinker by dolomite and metakaolin is relevant for the development of any commercial composite cement containing dolomite and metakaolin.

Combination of dolomite with latent hydraulic SCMs or less-reactive calcined clays

Because metakaolin and dolomite compete for portlandite, latent hydraulic SCMs that do not consume portlandite, such as ground granulated blast furnace slag, should be investigated as alternatives to using metakaolin. Another possibility might be the use of less-reactive calcined clays in combination with dolomite. Such blended cements might achieve a higher degree of dolomite reaction even at higher SCM contents.

Other natural carbonate sources

In this study, only relatively pure carbonates were used. Both dolomite and limestone stabilize ettringite in a cementitious system due to the formation of carbonate AFm phases, but they have different rates of reaction and different compositions. Both the higher reactivity of limestone and the hydrotalcite formation from the dolomite reaction can be advantageous for the performance of concrete. Combinations of dolomite and limestone, such as dolomitic limestone or limy dolomite, might therefore be relevant for further research projects to evaluate if their respective advantages can be coupled in a synergetic way.

Stability of chloride-containing hydrotalcite

The hydrotalcite formed in composite cements containing dolomite showed a high chloride-binding capacity. However, the stability of this chloride-containing hydrotalcite should be investigated with regard to its ability to retain the chlorides in its crystal structure, e.g. during leaching or carbonation.

Stability of dolomite in metakaolin-rich samples

The durability study in this PhD project focused on the stability of the hydration products formed in Portland composite cements containing dolomite and metakaolin. It was therefore limited to the samples in which the highest degree of dolomite reaction and consequently the most hydrotalcite were detected. Dolomite did not react in the samples with large amounts of added metakaolin. However, the addition of portlandite and water to these samples triggered the dolomite reaction and the formation of hydrotalcite. This indicates that the exposure of a metakaolin-rich cement to aggressive environments might potentially lead to further dolomite reaction. A durability study on samples containing large amounts of metakaolin should therefore be conducted to elucidate the stability of the phase assemblage in the metakaolin-rich samples under various other exposure conditions.

Performance testing

This PhD project investigated the stability of hydrotalcite and its ability to bind chlorides. However, to document how composite cements containing dolomite and metakaolin perform in concrete exposed to various aggressive environments, suitable performance tests should be carried out.

8. References

ACI CT-16 (2016). *ACI Concrete Terminology*. Farmington Hills, MI: American Concrete Institute.

Antoni, M., Rossen, J., Martirena, F., & Scrivener, K. L. (2012). Cement substitution by a combination of metakaolin and limestone. *Cement and Concrete Research*, *42*(12), 1579–1589.

Arya, C., Buenfeld, N. R., & Newman, J. B. (1990). Factors influencing chloride-binding in concrete. *Cement and Concrete Research*, *20*(2), 291–300.

Arya, C., & Xu, Y. (1995). Effect of cement type on chloride binding and corrosion of steel in concrete. *Cement and Concrete Research*, *25*(4), 893–902.

Barker, A. P., & Cory, H. P. (1991). The early hydration of limestone-filled cements. In R. N. Swamy (Ed.), *Blended Cements in Construction* (pp. 107–124). Sheffield, UK: Taylor & Francis.

Ben Haha, M., Lothenbach, B., Le Saout, G., & Winnefeld, F. (2012). Influence of slag chemistry on the hydration of alkali-activated blast-furnace slag – Part II: Effect of Al_2O_3. *Cement and Concrete Research*, *42*(1), 74–83.

Bensted, J. (1980). Some hydration investigations involving Portland cement - effect of calcium carbonate substitution of gypsum. *World Cement Technology*, *11*(8), 395–406.

Berodier, E., Scrivener, K., & Scherer, G. (2014). Understanding the Filler Effect on the Nucleation and Growth of C-S-H. *Journal of the American Ceramic Society*, *97*(12), 3764–3773.

Black, L., Breen, C., Yarwood, J., Garbev, K., Stemmermann, P., & Gasharova, B. (2007). Structural Features of C-S-H(I) and Its Carbonation in Air – A Raman Spectroscopic Study. Part II: Carbonated Phases. *Journal of the American Ceramic Society*, *90*(3), 908–917.

Black, L., Garbev, K., & Gee, I. (2008). Surface carbonation of synthetic C-S-H samples: A comparison between fresh and aged C-S-H using X-ray photoelectron spectroscopy. *Cement and Concrete Research*, *38*(6), 745–750.

Bonavetti, V. L., Rahhal, V. F., & Irassar, E. F. (2001). Studies on the carboaluminate formation in limestone filler-blended cements. *Cement and Concrete Research*, *31*(6), 853–859.

Châtelet, L., Bottero, J. Y., Yvon, J., & Bouchelaghem, A. (1996). Competition between monovalent and divalent anions for calcined and uncalcined hydrotalcite: anion exchange and adsorption sites. *Colloids and Surfaces A*, *111*(3), 167–175.

Chou, L., Garrels, R. M., & Wollast, R. (1989). Comparative study of the kinetics and mechanisms of dissolution of carbonate minerals. *Chemical Geology*, *78*(3-4), 269–282.

Dai, Z., Tran, T. T., Skibsted, J., & Jennings, H. (2014). Aluminum Incorporation in the C-S-H Phase of White Portland Cement-Metakaolin Blends Studied by ^{27}Al and ^{29}Si MAS NMR Spectroscopy. *Journal of the American Ceramic Society*, *97*(8), 2662–2671.

Damtoft, J. S., Lukasik, J., Herfort, D., Sorrentino, D., & Gartner, E. M. (2008). Sustainable development and climate change initiatives. *Cement and Concrete Research*, *38*(2), 115–127.

De Weerdt, K., Colombo, A., Coppola, L., Justnes, H., & Geiker, M. R. (2015). Impact of the associated cation on chloride binding of Portland cement paste. *Cement and Concrete Research*, *68*, 196–202.

De Weerdt, K., Justnes, H., Kjellsen, K. O., & Sellevold, E. (2010). Fly ash-limestone ternary composite cements: synergetic effect at 28 days. *Nordic Concrete Research*, *42*(2), 51–70.

De Weerdt, K., Kjellsen, K. O., Sellevold, E., & Justnes, H. (2011). Synergy between fly ash and limestone powder in ternary cements. *Cement and Concrete Composites*, *33*(1), 30–38.

De Weerdt, K., Orsáková, D., & Geiker, M. R. (2014). The impact of sulphate and magnesium on chloride binding in Portland cement paste. *Cement and Concrete Research*, *65*, 30–40.

Delagrave, A., Marchand, J., Ollivier, J.-P., Julien, S., & Hazrati, K. (1997). Chloride Binding Capacity of Various Hydrated Cement Paste Systems. *Advanced Cement Based Materials*, *6*(1), 28–35.
Dhir, R. K., El-Mohr, M. A. K., & Dyer, T. D. (1997). Developing chloride resisting concrete using PFA. *Cement and Concrete Research*, *27*(11), 1633–1639.
EN 197-1 (2011). *Cement, Part I: Composition, specifications and conformity criteria for common cements*. Brussels: European Committee for Standardization.
Feldmann, R. F., Ramachandran, V. S., & Sereda, P. J. (1965). Influence of $CaCO_3$ on the Hydration of $3CaO{\cdot}Al_2O_3$. *Journal of the American Ceramic Society*, *48*(1), 25–30.
Feng, P., Miao, C., & Bullard, J. W. (2014). A model of phase stability, microstructure and properties during leaching of portland cement binders. *Cement and Concrete Composites*, *49*, 9–19.
Fernandez, R., Martirena, F., & Scrivener, K. L. (2011). The origin of the pozzolanic activity of calcined clay minerals: A comparison between kaolinite, illite and montmorillonite. *Cement and Concrete Research*, *41*(1), 113–122.
Gaitero, J. J., Campillo, I., & Guerrero, A. (2008). Reduction of the calcium leaching rate of cement paste by addition of silica nanoparticles. *Cement and Concrete Research*, *38*(8-9), 1112–1118.
Galí, S., Ayora, C., Alfonso, P., Tauler, E., & Labrador, M. (2001). Kinetics of dolomite-portlandite reaction: Application to Portland cement concrete. *Cement and Concrete Research*, *31*(6), 933–939.
Garcia, E., Alfonso, P., Labrador, M., & Galí, S. (2003). Dedolomitization in different alkaline media: Application to Portland cement paste. *Cement and Concrete Research*, *33*(9), 1443–1448.
Hawkins, P., Tennis, P. D., & Detwiler, R.J. (2003). The Use of Limestone in Portland Cement: A State-of-the-Art Review. *Portland Cement Association*.
Huntzinger, D. N., & Eatmon, T. D. (2009). A life-cycle assessment of Portland cement manufacturing: Comparing the traditional process with alternative technologies. *Journal of Cleaner Production*, *17*(7), 668–675.
Ingram, K., Polusny, M., Daugherty, K., & Rowe, W. (1990). Carboaluminate reactions as influenced by limestone additions. In P. Klieger, & R. D. Hooton (Eds.), *Carbonate Additions to Cement: ASTM STP 1064* (pp. 14–23). Philadelphia, PA: American Society for Testing and Materials.
Ipavec, A., Vuk, T., Gabrovšek, R., & Kaučič, V. (2013). Chloride binding into hydrated blended cements: The influence of limestone and alkalinity. *Cement and Concrete Research*, *48*, 74–85.
Jain, J., & Neithalath, N. (2009). Analysis of calcium leaching behavior of plain and modified cement pastes in pure water. *Cement and Concrete Composites*, *31*(3), 176–185.
Jin, F., & Al-Tabbaa, A. (2014). Evaluation of novel reactive MgO activated slag binder for the immobilisation of lead and zinc. *Chemosphere*, *117*, 285–294.
Jin, F., Wang, F., & Al-Tabbaa, A. (2016). Three-year performance of in-situ solidified/stabilised soil using novel MgO-bearing binders. *Chemosphere*, *144*, 681–688.
Jones, T. R. (2002). Metakaolin as a pozzolanic addition to concrete. In J. Bensted, & P. Barnes (Eds.), *Structure and Performance of cements* (pp. 372–398). New York: Taylor & Francis.
Justnes, H. (1998). Kinetics of Reaction in Cementitious Pastes Containing Silica Fume as Studied by ^{29}Si MAS NMR. In P. Colombet, H. Zanni, A. R. Grimmer, & P. Sozzani (Eds.), *Nuclear Magnetic Resonance Spectroscopy of Cement-Based Materials* (pp. 245–268). Berlin, Heidelberg: Springer Berlin Heidelberg.
Kayali, O., Khan, M. S. H., & Sharfuddin Ahmed, M. (2012). The role of hydrotalcite in chloride binding and corrosion protection in concretes with ground granulated blast furnace slag. *Cement and Concrete Composites*, *34*(8), 936–945.

Ke, X., Bernal, S. A., & Provis, J. L. (2017). Uptake of chloride and carbonate by Mg-Al and Ca-Al layered double hydroxides in simulated pore solutions of alkali-activated slag cement. *Cement and Concrete Research*, *100*, 1–13.

L'Hôpital, E., Lothenbach, B., Le Saout, G., Kulik, D. A., & Scrivener, K. L. (2015). Incorporation of aluminium in calcium-silicate-hydrates. *Cement and Concrete Research*, *75*, 91–103.

Labbez, C., Nonat, A., Pochard, I., & Jönsson, B. (2007). Experimental and theoretical evidence of overcharging of calcium silicate hydrate. *Journal of Colloid and Interface Science*, *309*(2), 303–307.

Lothenbach, B., Le Saout, G., Gallucci, E., & Scrivener, K. L. (2008). Influence of limestone on the hydration of Portland cements. *Cement and Concrete Research*, *38*(6), 848–860.

Lothenbach, B., Scrivener, K. L., & Hooton, R. D. (2011). Supplementary cementitious materials. *Cement and Concrete Research*, *41*(12), 1244–1256.

Lothenbach, B., Winnefeld, F., Alder, C., Wieland, E., & Lunk, P. (2007). Effect of temperature on the pore solution, microstructure and hydration products of Portland cement pastes. *Cement and Concrete Research*, *37*(4), 483–491.

Love, C. A., Richardson, I. G., & Brough, A. R. (2007). Composition and structure of C–S–H in white Portland cement–20% metakaolin pastes hydrated at 25 °C. *Cement and Concrete Research*, *37*(2), 109–117.

Matschei, T., Lothenbach, B., & Glasser, F. P. (2007a). The AFm phase in Portland cement. *Cement and Concrete Research*, *37*(2), 118–130.

Matschei, T., Lothenbach, B., & Glasser, F. P. (2007b). The role of calcium carbonate in cement hydration. *Cement and Concrete Research*, *37*(4), 551–558.

Matte V., & Moranville M. (1999). Durability of Reactive Powder Composites: influence of silica fume on the leaching properties of very low water/binder pastes. *Cement and Concrete Composites*, *21*(1), 1–9.

Mills, S. J., Christy, A. G., Génin, J.-M. R., Kameda, T., & Colombo, F. (2012). Nomenclature of the hydrotalcite supergroup: Natural layered double hydroxides. *Mineralogical Magazine*, *76*(5), 1289–1336.

Miyata, S. (1975). The Syntheses of Hydrotalcite-Like Compounds and Their Structures and Physico-Chemical Properties I: The Systems Mg^{2+}-Al^{3+}-NO_3^-, Mg^{2+}-Al^{3+}-Cl^-, Mg^{2+}-Al^{3+}-ClO_4^-, Ni^{2+}-Al^{3+}-Cl^- and Zn^{2+}-Al^{3+}-Cl^-. *Clays and Clay Minerals*, *23*(5), 369–375.

Miyata, S. (1983). Anion-Exchange Properties of Hydrotalcite-Like Compounds. *Clays and Clay Minerals*, *31*(4), 305–311.

Morse, J. W., & Arvidson, R. S. (2002). The dissolution kinetics of major sedimentary carbonate minerals. *Earth-Science Reviews*, *58*(1–2), 51–84.

Myers, R. J., Lothenbach, B., Bernal, S. A., & Provis, J. L. (2015). Thermodynamic modelling of alkali-activated slag cements. *Applied Geochemistry*, *61*, 233–247.

Nicoleau, L. (2011). Accelerated growth of calcium silicate hydrates: Experiments and simulations. *Cement and Concrete Research*, *41*(12), 1339–1348.

Nied, D., Stabler, C., & Zajac, M. (2015). Assessing the synergistic effect of limestone and metakaolin. In K. L. Scrivener, & A. Favier (Eds.), *Calcined Clays for Sustainable Concrete: Proceedings of the 1st International Conference on Calcined Clays for Sustainable Concrete* (pp. 245–251).

Ogirigbo, O. R., & Black, L. (2017). Chloride binding and diffusion in slag blends: Influence of slag composition and temperature. *Construction and Building Materials*, *149*, 816–825.

Péra, J., Husson, S., & Guilhot, B. (1999). Influence of finely ground limestone on cement hydration. *Cement and Concrete Composites*, *21*(2), 99–105.

Plusquellec, G., & Nonat, A. (2016). Interactions between calcium silicate hydrate (C-S-H) and calcium chloride, bromide and nitrate. *Cement and Concrete Research*, *90*, 89–96.
Pokrovsky, O. S., Golubev, S. V., Schott, J., & Castillo, A. (2009). Calcite, dolomite and magnesite dissolution kinetics in aqueous solutions at acid to circumneutral pH, 25 to 150 °C and 1 to 55 atm pCO_2: New constraints on CO_2 sequestration in sedimentary basins. *Chemical Geology*, *265*(1–2), 20–32.
Puerta-Falla, G., Balonis, M., Le Saout, G., Neithalath, N., & Sant, G. (2015). The Influence of Metakaolin on Limestone Reactivity in Cementitious Materials. In K. L. Scrivener, & A. Favier (Eds.), *Calcined Clays for Sustainable Concrete: Proceedings of the 1st International Conference on Calcined Clays for Sustainable Concrete* (pp. 11–19).
Richardson, I. G. (1999). The nature of C-S-H in hardened cements. *Cement and Concrete Research*, *29*(8), 1131–1147.
Rossen, J. E., Lothenbach, B., & Scrivener, K. L. (2015). Composition of C–S–H in pastes with increasing levels of silica fume addition. *Cement and Concrete Research*, *75*, 14–22.
Rozov, K., Berner, U., Taviot-Gueho, C., Leroux, F., Renaudin, G., Kulik, D., & Diamond, L. W. (2010). Synthesis and characterization of the LDH hydrotalcite–pyroaurite solid-solution series. *Cement and Concrete Research*, *40*(8), 1248–1254.
Rozov, K. B., Berner, U., Kulik, D. A., & Diamond, L. W. (2011). Solubility and thermodynamic properties of carbonate-bearing hydrotalcite–pyroaurite solid solutions with a 3:1 Mg/(Al+Fe) mole ratio. *Clays and Clay Minerals*, *59*(3), 215–232.
Scrivener, K. L., Vanderley, M. J., & Gartner, E. M. (2016). *Eco-efficient cements: Potential, economically viable solutions for a low-CO_2 cement-based materials industry*. Paris: United Nations Environment Program – Building and Climate Initiative (UNEP-SBCI).
Sevelsted, T. F., & Skibsted, J. (2015). Carbonation of C–S–H and C–A–S–H samples studied by ^{13}C, ^{27}Al and ^{29}Si MAS NMR spectroscopy. *Cement and Concrete Research*, *71*, 56–65.
Shi, Z., Geiker, M. R., De Weerdt, K., Østnor, T. A., Lothenbach, B., Winnefeld, F., & Skibsted, J. (2017). Role of calcium on chloride binding in hydrated Portland cement–metakaolin–limestone blends. *Cement and Concrete Research*, *95*, 205–216.
Sonebi, M., Ammar, Y., & Diederich, P. (2016). Sustainability of cement, concrete and cement replacement materials in construction. In J. M. Khatib (Ed.), *Sustainability of Construction Materials* (pp. 371–396): Elsevier.
Soroka, I., & Stern, N. (1976). Calcareous fillers and the compressive strength of Portland cement. *Cement and Concrete Research*, *6*(3), 367–376.
Taylor, H. F. W. (1997). *Cement Chemistry, 2nd ed.* London: Telford.
Thomas, M.D.A., Hooton, R. D., Scott, A., & Zibara, H. (2012). The effect of supplementary cementitious materials on chloride binding in hardened cement paste. *Cement and Concrete Research*, *42*(1), 1–7.
Wang, Q., Wu, Z., Tay, H. H., Chen, L., Liu, Y., Chang, J., Zhong, Z., Luo, J., & Borgna, A. (2011). High temperature adsorption of CO_2 on Mg–Al hydrotalcite: Effect of the charge compensating anions and the synthesis pH. *Catalysis Today*, *164*(1), 198–203.
Wowra, O., & Setzer, M. J. (1997). Sorption of chlorides on hydrated cement and C_3S pastes. In M. J. Setzer, & R. Auberg (Eds.), *Frost Resistance of Concrete* (pp. 147–153). London: E & FN Spon.
Ye, H., Jin, X., Chen, W., Fu, C., & Jin, N. (2016). Prediction of chloride binding isotherms for blended cements. *Computers and Concrete*, *17*(5), 655–672.
Zajac, M., & Ben Haha, M. (2015). Hydration of limestone and dolomite cement. In *Proceedings of the 14th International Congress on the Chemistry of Cement*.

Zajac, M., Bremseth, S. K., Whitehead, M., & Ben Haha, M. (2014). Effect of $CaMg(CO_3)_2$ on hydrate assemblages and mechanical properties of hydrated cement pastes at 40 °C and 60 °C. *Cement and Concrete Research*, *65*, 21–29.

Zajac, M., Dienemann, W., & Bolte, G. (2011). Comparative experimental and virtual investigations of the influence of calcium and magnesium carbonates on reacting cement. In *Proceedings of the 13th International Congress on the Chemistry of Cement, Madrid*.

Zhang, X., Glasser, F. P., & Scrivener, K. L. (2014). Reaction kinetics of dolomite and portlandite. *Cement and Concrete Research*, *66*, 11–18.

Zhu, Q., Jiang, L., Chen, Y., Xu, J., & Mo, L. (2012). Effect of chloride salt type on chloride binding behavior of concrete. *Construction and Building Materials*, *37*, 512–517.

Part II
Appended papers

Paper I

Portland metakaolin cement containing dolomite or limestone – Similarities and differences in phase assemblage and compressive strength

Machner, A., Zajac, M., Ben Haha, M., Kjellsen, K.O., Geiker, M.R., De Weerdt, K.
Construction and Building Materials, 2017, Vol. 157, 214-225
DOI: 10.1016/j.conbuildmat.2017.09.056

Construction and Building Materials 157 (2017) 214–225

Contents lists available at ScienceDirect

Construction and Building Materials

journal homepage: www.elsevier.com/locate/conbuildmat

Portland metakaolin cement containing dolomite or limestone – Similarities and differences in phase assemblage and compressive strength

Alisa Machner [a,c,*], Maciej Zajac [b], Mohsen Ben Haha [b], Knut O. Kjellsen [c], Mette R. Geiker [a], Klaartje De Weerdt [a]

[a] NTNU Department of Structural Engineering, Richard Birkelandsvei 1A, Trondheim 7491, Norway
[b] Heidelberg Technology Center GmbH, Oberklammweg 2-4, Leimen 69181, Germany
[c] Norcem AS, R&D Department, Setreveien 2, Brevik 3991, Norway

HIGHLIGHTS

- Dolomite can replace up to 10% of cement without impairing strength at 20 °C or 38 °C.
- Carbonates delivered by either dolomite or limestone additions stabilize ettringite.
- The reactivity of dolomite can be increased by elevating the curing temperature.
- Limestone and dolomite additions yield similar compressive strength at 20 °C or 38 °C.

ARTICLE INFO

Article history:
Received 7 June 2017
Received in revised form 10 September 2017
Accepted 13 September 2017

Keywords:
Curing temperature
Blended cements
Ettringite stabilization
Rate of reaction
Thermodynamic modelling

ABSTRACT

The scarceness of high-quality limestone obliges the cement industry to consider alternative supplementary cementitious materials (SCMs) for the production of blended cements. This study investigated the potential usage of dolomite instead of limestone as an addition to Portland metakaolin cement by measuring the development of the compressive strength and phase assemblages at 5 °C, 20 °C or 38 °C. Laboratory grade materials were used to identify potential differences in the impact of the carbonate on the phase assemblages. As with limestone, a strength increase was observed when dolomite is added at temperatures >5 °C due to the formation of additional carbonate AFm phases and the stabilization of ettringite. Differences were observed in the amount and type of the carbonate AFm and AFt phases formed. Thermodynamic modelling in combination with the experimental results indicate that the dolomite and limestone affect Portland metakaolin cement in a similar way, with the reactivity being the major difference between the two carbonate sources. This indicates that with regard to the strength development up to 90 days dolomite can be used instead of limestone to replace parts of a Portland metakaolin cement.

1. Introduction

There are several ways to minimize the effect of cement production on our climate, one of which is to use supplementary cementitious materials (SCMs) [1]. Limestone is widely used as an SCM. According to the European standard EN197-1, it can replace up to 5%wt clinker in CEM I Portland cements and up to 35%wt in CEM II Portland-limestone cements [2].

The addition of finely ground limestone to Portland cement affects the hydration in two ways. First, there is the physical effect of finely ground limestone, which is also often called the filler effect. The addition of fine materials to Portland cement provides additional nucleation sites, which facilitate the formation of hydrates during the hydration of the cement. Moreover, in systems where parts of the cement are replaced by another material, the water-to-cement ratio increases when the water-to-solid ratio is kept constant. This increases the reaction degree of the cement. The addition of finely-ground limestone is known to enhance the reaction of alite and therefore of Portland cement [3,4], and can also shorten the time necessary to nucleate the first C-S-H phase

* Corresponding author at: NTNU Department of Structural Engineering, Richard Birkelandsvei 1A, Trondheim 7491, Norway.
E-mail address: alisa.machner@ntnu.no (A. Machner).

https://doi.org/10.1016/j.conbuildmat.2017.09.056
0950-0618/

[5], which accelerates the hydration of the cement. However, the filler effect is also always connected with a dilution effect, because the most reactive part of the system is replaced with a less-reactive material.

Second, and contrary to earlier understanding that limestone is an inert material, several authors have reported a reaction of limestone when added to Portland cement [6,7]. Carbonate AFm phases, such as hemicarbonate and monocarbonate, are formed during the reaction of limestone with pure C_3A or C_3A in Portland cement [8–12]. In the presence of carbonates, these AFm phases are more stable than monosulphate [13]. Consequently, the ettringite does not transform to monosulphate after the sulphate source, e.g. gypsum, is depleted. This chemical effect is called ettringite stabilization and results in a relative increase in the volume of hydrates and leads to an increase in compressive strength at low replacement levels [6,7]. A comprehensive overview of the effect of limestone addition to Portland cement on compressive strength and phase assemblage can be found in [14].

The high-grade limestone required by EN197-1 [2] is not sufficiently available in all parts of the world, so various other carbonate sources are in the focus of ongoing research, with dolomite rock being one promising alternative. Schöne et al. [15] observed similar compressive strength results from cements where 23%wt was replaced with either limestone or dolomite. Moreover, Zajac et al. were able to demonstrate that the effect of ettringite stabilization upon carbonate addition, which has been known for cements containing limestone, is also valid for cements containing ground dolomite rock [16].

The mineral dolomite, which is petrogenetic for dolomite rock, is not stable in the high-alkaline environment of a cement and has been reported to undergo what is known as the dedolomitization reaction [17,18]. In this reaction, dolomite reacts with calcium hydroxide (portlandite) to form calcium carbonate (calcite) and magnesium hydroxide (brucite). However, it has been shown that, in cementitious systems where other ions (Al, Si) are present, the reaction of dolomite produces products similar to those of hydrating Portland limestone cement and hydrotalcite [16,19].

The dissolution of dolomite and calcite in various conditions has been studied before [20]. Pokrovsky et al. were able to show that the dissolution rate of dolomite is significantly smaller than that of limestone at both 25 °C and 60 °C [21]. Moreover, the dissolution rates of both decrease with increasing pH [22] and increase with increasing temperatures from 25 °C to 60 °C [21]. This accords with other authors, who have reported a higher degree of reaction of dolomite with increasing temperatures [19,23].

The positive effect of adding carbonate to ordinary Portland cements is limited because the amount of alumina available is limited in these cements. However, the effect can be amplified by increasing the aluminium content of the cement by using various aluminium-containing SCMs. This synergetic effect has previously been demonstrated for samples containing limestone and fly ash [24,25] and for combinations of limestone and metakaolin [26–28].

In the present study, we used a calcined clay-containing Portland composite cement with a cement-to-metakaolin ratio of 6:1 to ensure an aluminium-rich cement, referred to in the following as Portland metakaolin cement (CM). We investigated the phase assemblage development of this Portland metakaolin cement with various levels of carbonate addition, either pure dolomite or limestone, in pastes over hydration periods of up to 90 days. We also measured the compressive strength of mortar samples with the same compositions. To investigate the effect of curing at different temperatures, samples were cured at 5 °C and 38 °C as well as the usual 20 °C.

2. Experimental

2.1. Materials

The materials used for this study were Portland cement clinker (C, from Norcem), and laboratory-grade dolomite (D, Magnesia 4179 from Brenntag), limestone (L, Magnesia 4491 from Brenntag) metakaolin (M, Metastar501 from Imerys) and gypsum ($, $CaSO_4 \cdot 2H_2O$, from Merck). The cement clinker was ground in a laboratory ball mill until a Blaine surface area of approx. 400 m^2/kg was achieved. The other materials were used as received. All materials were characterized by means of XRF (Table 1), QXRD (Tables 2and 3), Blaine specific surface area (Table 1), and laser diffraction (Fig. 1). Laboratory-grade materials were used to make it possible to investigate the effect of dolomite without calcite impurities. The dolomite used was synthesized by precipitation, which is why it has a much finer particle size distribution than the limestone used.

The experimental matrix is given in Table 4. The reference 100CM represents a model composite cement consisting of Portland cement clinker and metakaolin with the mass ratio of 6:1. Levels of 5, 10 or 20%wt of the composite cement were replaced by either limestone or dolomite. To ensure a sufficient sulphate content in the samples, 2.85%wt of laboratory-grade gypsum was added to all mixes.

The paste samples were prepared in the laboratory at 20 °C by mixing binder and water with a w/b ratio = 0.55 (due to the high fineness of the materials used) in a Braun MR5550CA high shear mixer. The mixing procedure was: mixing for 30 s, resting for 5 min, and mixing again for 60 s. The pastes were then cast in 12 ml plastic tubes (diameter 23 mm), which were sealed and stored at the various temperatures over water for up to 90 days.

The mortar samples were prepared in accordance with EN 196-1 [29], except that the w/b ratio had to be increased to 0.55 due to the high fineness of the materials used. After 1 day in a climate chamber (20 °C, >90% RH) the prisms (40 × 40 × 160 mm) were demoulded and stored in big tanks immersed in lime water together with other samples at 20 °C until measurement. Additional samples for the other temperatures (5 °C and 38 °C) were prepared in a similar way, except that they were not stored in a climate chamber for the first day, but in their moulds in a closed box over water at their respective temperatures. After 1 day, they were demoulded and stored immersed in lime water at their respective curing temperatures. The samples cured at 38 °C were stored in 20-litre plastic boxes filled with lime water and not in the big tanks as the other samples. The mortar and paste samples were investigated after 1, 28 and 90 days of hydration at 20 °C. The samples cured at 5 °C and 38 °C were investigated after 28 and 90 days.

Table 1
XRF results [%wt] and Blaine specific surface area of the clinker, dolomite, limestone, metakaolin and gypsum used.

Oxide	Clinker	Dolomite	Limestone	Metakaolin	Gypsum
SiO_2	20.6	0.01	0.00	52.18	0.02
Al_2O_3	5.6	0.02	0.00	44.92	0.09
TiO_2	0.29	0.00	0.00	1.14	0.00
MnO	0.05	0.00	0.00	0.00	0.00
Fe_2O_3	3.12	0.00	0.00	0.62	0.00
CaO	63.26	30.32	55.87	0.12	32.66
MgO	2.66	21.59	0.21	0.04	0.06
K_2O	1.23	0.00	0.00	0.18	0.01
Na_2O	0.51	0.00	0.00	0.17	0.02
SO_3	1.37	0.00	0.00	0.14	46.47
P_2O_5	0.09	0.00	0.01	0.07	0.00
LOI	–	47.53	43.73	0.29	20.39
Blaine surface area [m^2/kg]	404	1056	482	897	214
Sum (1050 °C)	**98.78**	**99.52**	**99.82**	**99.87**	**99.72**

Table 2
Mineral composition of the dolomite, limestone, metakaolin and gypsum, determined by Rietveld analysis [%wt]. Amounts given in italics are below the limits of quantification (1%wt). The quantification of mullite is questionable due to its low crystallinity.

Mineral name	Mineral formula	Dolomite	Limestone	Metakaolin	Gypsum
Hydromagnesite	$Mg_3(CO_3)_4(OH)_2{\cdot}4H_2O$	–	–	–	–
Calcite	$CaCO_3$	–	100	–	–
Dolomite	$CaMg(CO3)_2$	100	–	–	–
Gypsum	$CaSO_4{\cdot}2H_2O$	–	–	–	93.7
Bassanite	$CaSO_4{\cdot}0.5H_2O$	–	–	–	6.3
Anatase	TiO_2	–	–	*1.2*	–
Mullite	$Al_6Si_2O_{13}$	–	–	*6.1*	–
Muscovite	$KAl_2Si_3AlO_{10}(OH)_2$	–	–	*0.4*	–
Quartz	SiO_2	–	–	*0.7*	–
Amorphous content	–	–	–	91.6	–

Table 3
Mineralogical composition of the clinker used determined by Rietveld analysis [%wt].

Mineral	%wt
Alite	59.5
α-Belite	1.4
β-Belite	13.9
Σ Belite	15.3
Aluminate (cub.)	5.3
Aluminate (or.)	3.5
Σ Aluminate	8.8
Ferrite	10.0
Periclase	1.5
Free Lime	0.9
Portlandite	1.2
Aphthitalite	2.4
Arcanite	0.5

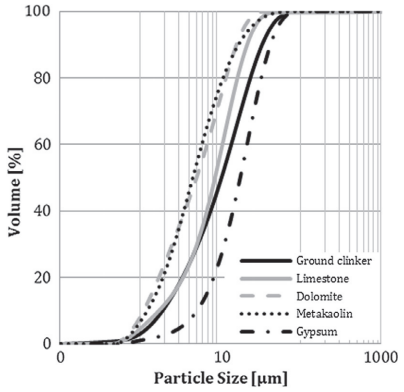

Fig. 1. Particle size distributions of the materials used, determined by laser diffraction.

2.2. Methods

2.2.1. Double solvent exchange

After 1 day (only for samples stored at 20 °C), 28 days, and 90 days, the hydration was stopped by means of double solvent exchange. First, a 6 mm thick slice (diameter: 23 mm) was cut off the cured cement paste sample. The paste was crushed in a porcelain mortar until the whole sample had passed through a 1 mm sieve. The coarsely crushed cement paste was then immersed in 50 ml isopropanol, shaken for 30 seconds, and left to rest for 5 min before the isopropanol was poured off. This isopropanol treatment was performed twice before the sample was transferred to a filtration unit where the isopropanol was filtrated out and the paste was immersed in 10 ml petroleum ether. After 30 s of stirring, the suspension was left to rest for 5 minutes. The sample was then vacuum-filtrated and subsequently dried overnight in a desiccator under a slight vacuum (−0.2 bar) applied using a water pump. All the samples were stored in a desiccator over silica gel and soda lime until measurement. The grinding of the samples to fine powder (<63 µm) was generally performed on the day of measurement.

Table 4
Overview of the experimental matrix. To all mixes, 2.85%wt of laboratory-grade gypsum was added.

No.	Name of the mix	CM (OPC:MK = 6:1)	L	D
1	100CM	100		
2	95CM5L	95	5	
3	90CM10L	90	10	
4	80CM20L	80	20	
5	95CM5D	95		5
6	90CM10D	90		10
7	80CM20D	80		20

2.2.2. TGA

Thermogravimetric analysis (TGA) was performed on all the pastes after the double solvent exchange treatment, drying and grinding. For the TGA measurements, the powders were poured into 600 µl corundum crucibles and stored in a sample changer until measurement (max. 8 h). The weight loss was measured from 40 to 900 °C with a heating rate of 10 °C/min in a Mettler Toledo TGA/DSC3+ device. During the measurement, the measurement cell was purged with 50 ml/min of nitrogen gas. TGA was used to quantify the mass loss due to the loss of bound water (H) and the decomposition of portlandite (CH). The weight loss of the portlandite between approx. 400 °C and 550 °C was determined with a tangential step. The bound water was determined by the difference between the sample weight at 50 °C and approx. 550 °C using a horizontal step. The sample weight at approx. 550 °C was assumed to be the dry binder weight, which would remain constant during the cement hydration. At higher temperatures, the carbonates present in the composite cements would decompose and cause additional mass loss. The equations for the quantification of bound water (H) and portlandite (CH) relative to the dry mass or clinker content (c.f. [30]) are given in Eqs. (1)–(4)

$$H_{dry} = \frac{w_{50} - w_{550}}{w_{550}} \tag{1}$$

$$CH_{dry} = \frac{w_{400} - w_{550}}{w_{550}} \times \frac{74}{18} \tag{2}$$

$$H_{clinker} = \frac{w_{50} - w_{550}}{w_{550}} \times \frac{100}{\%\ clinker} \tag{3}$$

$$CH_{clinker} = \frac{w_{400} - w_{550}}{w_{550}} \times \frac{74}{18} \times \frac{100}{\%\ clinker} \tag{4}$$

The standard deviations of these quantifications were calculated based on three independent measurements of the 100CM sample. For the portlandite quantification, the standard deviation was 0.8%wt and for the bound water content 1.2%wt. This is illustrated as error bars in the figures.

2.2.3. XRD

X-ray diffraction (XRD) analyses were performed on the same pastes as those used for TGA. For the XRD analyses, the powder was loaded into the sample holders by means of front loading and queued in a sample changer until measurement (max. 5 h). A D8 Focus diffractometer from Bruker was used for the measurements with a Bragg-Brentano θ–2θ geometry and a goniometer radius of 200.5 mm. The samples were measured between 5 °2θ and 55 °2θ with a step size of 0.01 °2θ and a sampling time per step of 0.5 s. Cu-Kα radiation with a wavelength of approx. 1.54 Å was used as the X-ray source. The divergence slit was fixed at 0.2 mm and the Soller slits were set to 2.5°. The XRD plots were qualitatively evaluated using DIFFRAC.EVA V4.0 software from Bruker. All observations regarding peak height and shape are only used as an indication, and is used together with the TGA results.

2.2.4. Mercury intrusion porosimetry

To make it possible to study the threshold pore diameter and total porosity of the paste samples with mercury intrusion porosimetry (MIP), a 7 mm slice of the cured cement paste was cut off each sample and coarsely crushed in a porcelain mortar. The crushed samples were then immersed in isopropanol for at least 24 h and then dried in an aerated oven overnight at 40 °C to remove the isopropanol. A Pascal 140/440 porosimeter from Thermo Scientific was used to get the MIP measurements. The first intrusion curve reported from the measurements was used to determine the threshold pore diameter and the pore volume, which equals the total porosity measurable with MIP.

2.2.5. Compressive strength testing

After 1, 28 and 90 days of hydration, the compressive strength of the mortar prisms was determined in accordance with EN 196-1 [29]. For every testing time, two mortar prisms were split in two and the compressive strength of all four resulting specimens was measured. The average and standard deviations of all four results were calculated and plotted in the figures.

2.2.6. Thermodynamic modelling

The Gibbs free energy minimization program GEMS [31,32] was used to model how the hydrate phase assemblages and their volumes depend on the degree of reaction of either dolomite or limestone. The thermodynamic data used from the PSI-GEMS database was supplemented with a cement specific database (CEMDATA14 database) [33–35], which includes solubility products of the solids relevant for cementitious materials. For the C-S-H phase, the CSHQ model proposed by Kulik was used [36]. In the case of hydrogarnets, the solid solution model for Al-Fe siliceous hydrogarnets was used [37]. The effect of the degree of reaction of dolomite or limestone on phase assemblage was investigated. The samples 95CM5D and 95CM5L were used for the geochemical modelling at 20 °C. The composition of the Portland metakaolin cement used as an input for the model was calculated from the XRF results given in Table 1. In this work, we used the same modelling approach as in [38]. However, we assumed the constant hydration degree of clinker and metakaolin to be 100%.

3. Results & general discussion

3.1. Compressive strength

Fig. 2a–c shows the development of the compressive strength of the various compositions investigated for the various curing times and curing temperatures tested.

After 1 day of curing at 20 °C, increasing replacement of CM by either of the carbonates led to slightly decreasing compressive strengths (Fig. 2b). Moreover, there were no notable differences between the samples containing limestone and dolomite. This indicates that any strength increase observed for minor carbonate replacements after 28 or 90 days of curing cannot be caused only by physical filler effects because this should already be visible after 1 day of curing.

Fig. 2b shows that, after 28 and 90 days of curing at 20 °C, the compressive strength increased compared to the 100CM mortar with limestone additions of up to 5%wt and with dolomite additions of up to 10%wt, and decreased again at higher replacement levels. For the 28 d and 90 d samples at 20 °C, the highest overall compressive strength was shown by the 95CM5L sample. It should be noted that at a replacement level of 20%wt the 80CM20D sample showed slightly higher compressive strength than the 80CM20L sample when cured at 20 °C.

The development of the compressive strength changed at the other curing temperatures. At 5 °C (Fig. 2a), the positive effect of limestone addition on compressive strength could be observed for a replacement level of 5%wt. At higher replacement levels, the compressive strength values decreased. The replacement of CM by dolomite resulted in the reduction of the compressive strength at all replacement levels. Moreover, for replacement levels <20%wt, all the samples containing limestone showed higher compressive strength values than the samples containing dolomite. The positive effect of carbonate addition on compressive strength was generally less pronounced and the total compressive strength values were lower for samples cured at 5 °C than for the samples cured at 20 °C.

Fig. 2c shows that, after 28 and 90 days of curing at 38 °C, the compressive strength levels were similar or even lower for samples containing limestone than for samples containing dolomite. At 38 °C, the positive effect of carbonate addition on the compressive strength was only visible for the samples containing dolomite. The samples containing limestone showed no increased compressive strength for any replacement level. However, we cannot report on a possible increase in compressive strength at lower replacement levels than 5%wt. It should be noted, that the differences between samples containing limestone and dolomite were relatively small at 38 °C compared to the differences observed at lower temperatures. The highest compressive strength values were achieved in samples containing 5%wt of dolomite.

3.2. Mercury intrusion porosimetry

Fig. 3a–c shows the development of the threshold diameter and the porosity for the various replacement levels of either dolomite or limestone at the various curing temperatures after 90 days of hydration.

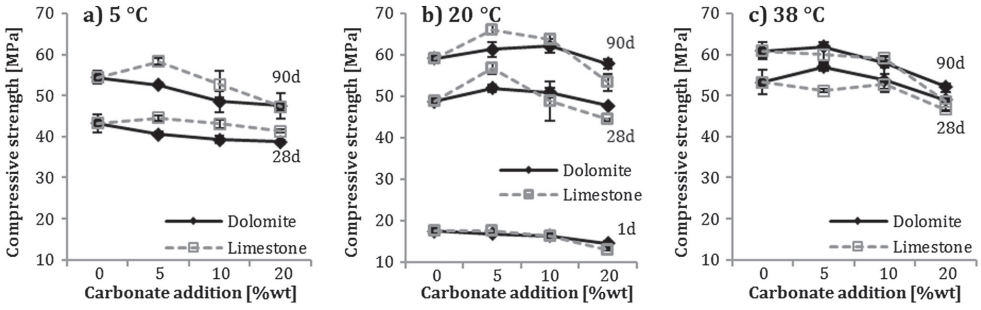

Fig. 2. Development of compressive strength for the different carbonate additions and the reference, for samples cured for up to 90 days at a) 5 °C, b) 20 °C, c) 38 °C.

The results for the samples containing dolomite and limestone are generally very similar. Differences in the particle size distribution of the two carbonate sources seem to have no significant influence on the microstructure of the paste samples.

At 5 °C, the porosity of the samples increased for all replacement levels of dolomite compared to the CM sample. The sample containing 5%wt limestone showed a slightly decreased porosity. At higher replacement levels than 5%wt of limestone, the porosity increased again. The threshold pore diameter decreased for all replacement levels of either dolomite or limestone. The samples containing limestone showed a higher threshold diameter for the 20%wt replacement level than the samples containing dolomite. The reason for this is unclear.

At 20 °C, the trends with increasing replacement levels of either dolomite or limestone are very similar. In both cases, the addition of 5%wt of a carbonate source reduced the porosity slightly. At higher replacement levels, the porosity increased. The threshold diameter increased with every replacement level from 5%wt and upwards compared to the CM sample.

At 38 °C, the results for the threshold diameter are similar to the samples cured at 20 °C, but the porosity of the samples was slightly higher. Moreover, at a replacement level of 5%wt, the porosity decreased for the 95CM5D sample but stayed almost constant for the 95CM5L sample. At higher replacement levels, the porosity of the samples containing dolomite increased. The porosity decreased slightly for the sample containing 10%wt limestone and increased at a replacement level of 20%wt of limestone.

Generally, the MIP results for the samples containing dolomite and limestone correlate well with the compressive strength results (Fig. 2). Samples in which a compressive strength increase was observed for either dolomite or limestone addition compared to the 100CM samples also showed a reduction in the porosity.

3.3. AFm and AFt

3.3.1. XRD

Fig. 4 shows the XRD patterns for the various samples cured at 20 °C after 1, 28 and 90 days.

After 28 and 90 days, the ettringite stabilization effect could be observed in all samples containing carbonates when compared with the 100CM sample regardless of the curing temperature, though 95CM5D did show a minor ettringite peak at 38 °C. The addition of a carbonate source to the system increased the CO_2/SO_3 ratio and this meant the carbonate AFm phases, either monocarbonate (11.7 °2θ) or hemicarbonate (10.8 °2θ), were the stable AFm phases instead of monosulphate (9.9 °2θ). Consequently, ettringite (9.1 °2θ) did not transform to monosulphate after the sulphate depletion.

After 1 day, this effect was less obvious because the ettringite peak in the 100 CM sample was still present. However, samples containing carbonates, especially limestone, showed higher and sharper ettringite peaks than samples without. In addition to the sulphate-containing phases, after 1 day, the limestone samples showed small traces of monocarbonate peaks and samples containing dolomite showed humps of hemicarbonate.

The trends observed for samples cured at 20 °C after 28 and 90 days were similar to each other, and are therefore described together here. The type of carbonate AFm phase changed with the various replacement levels and the different carbonates used. All samples containing limestone showed clear monocarbonate peaks. At replacement levels of 5%wt, broad peaks of hemicarbonate were also detected, but these disappeared at higher replacement levels. The amount of carbonate AFm phases formed at lower replacement levels seemed to be smaller in samples containing dolomite than in samples containing limestone. In the samples containing dolomite, the types of carbonate AFm and their amount changed more gradually with the level of replacement. In samples containing 5%wt of dolomite, broad humps of both hemi- and monocarbonate were detectable. The monocarbonate peak increased in height and became sharper with higher dolomite additions, while the hemicarbonate peak decreased until it disappeared at 20%wt dolomite addition.

The ettringite peak developed in a similar way to the monocarbonate peak in the samples cured at 20 °C. Samples containing limestone generally showed slightly higher and sharper peaks of ettringite than samples containing dolomite. However, the ettringite peaks increased in samples containing dolomite with increasing replacement levels.

The phase assemblages detected for the various binder compositions also varied with the curing temperatures. Fig. 5 shows the XRD plots for the samples cured for 90 days at the various curing temperatures.

At 5 °C the AFm phases detected were the same as at 20 °C, but their peaks seemed slightly higher and sharper at 20 °C than at 5 °C.

At the highest curing temperature (38 °C), the type of carbonate AFm phases detected in samples containing limestone differed from the samples cured at 5 °C and 20 °C. In the 38 °C samples, the monocarbonate peak decreased and hemicarbonate was detected. In the samples containing dolomite, however, hemicarbonate could already be detected at lower curing temperatures, and differences in the phase assemblage are less obvious than in samples containing limestone.

The very sharp and high peak at 9.9 °2θ in the 90CM10D sample cured at 20 °C for 28 days could be due to monosulphate-12H in the light of the peak position. However, in view of the peak shape

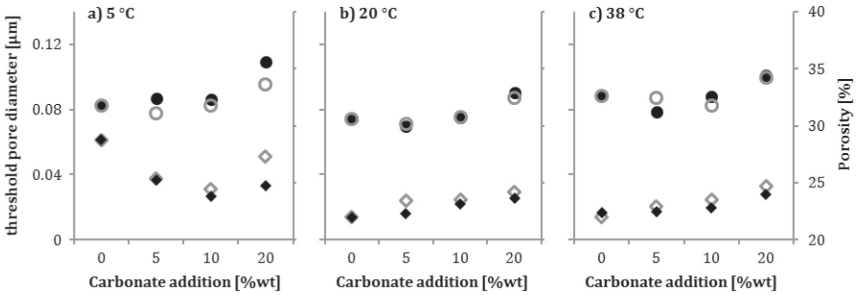

Fig. 3. Development of the threshold pore diameter (*diamonds*) and the total intruded volume (*dots*) for samples containing dolomite (*black filled*) or limestone (*grey hollow*) stored at a) 5 °C, b) 20 °C and c) 38 °C at 90 days.

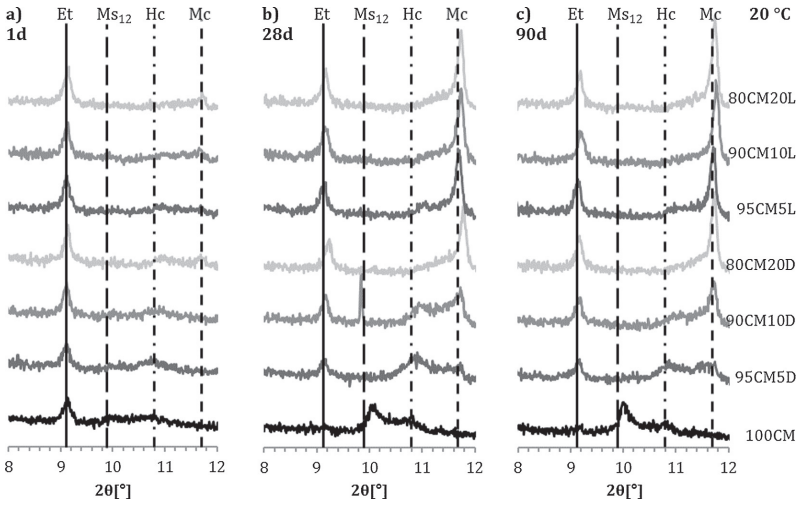

Fig. 4. XRD patterns between 8 °2θ and 12 °2θ for the samples investigated after 1 day, 28 days and 90 days of hydration at 20 °C.

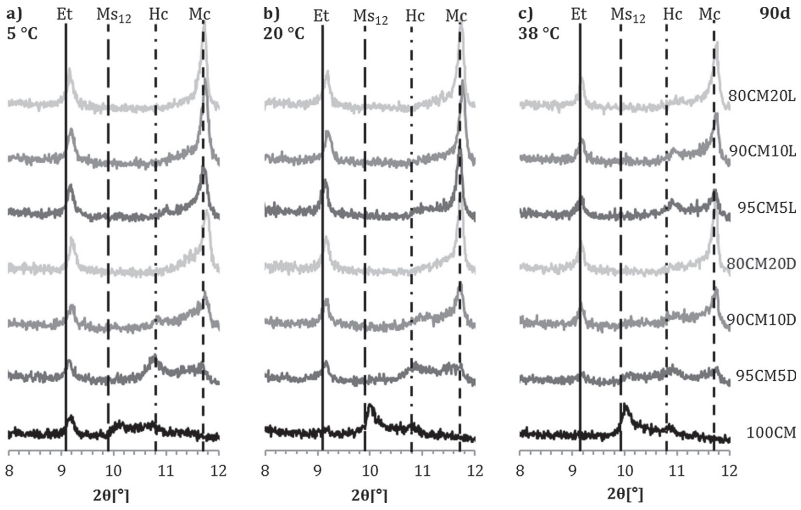

Fig. 5. XRD patterns between 8 °2θ and 12 °2θ for the samples investigated after 90 days of hydration, cured at a) 5 °C, b) 20 °C, c) 38 °C.

and the appearance of carbonate AFm phases in the same sample, it seems more likely to be an artefact of the measurement device. This was confirmed by a second measurement of the sample, which did not show this peak. The origin of this artefact is unknown.

3.3.2. TGA

Figs. 6 and 7 show the derivate curves of the TG signal (DTG curves) for the 100 CM reference and samples where 5%wt or 20%wt of the CM are replaced by a carbonate source at the various curing temperatures.

The DTG graphs can be divided into several sections, in which the decomposition of specific phases can be detected as weight loss. The first peak at around 100 °C is related to the ettringite decomposition and the beginning of C-H-S dehydroxylation. The C-S-H phase decomposes gradually between 40 °C and 600 °C [39] and appears as a polynomial baseline under other peaks in the same temperature range. The region between approx. 150 °C and 400 °C represents the stepwise dehydroxylation of the AFm phases and other lamellar phases, such as hydrotalcite (Ht) [39]. The subsequent sharp peak between approx. 400 °C and 550 °C is related to the decomposition of portlandite (CH). Above 550 °C, carbonates decompose by emitting CO_2 [39].

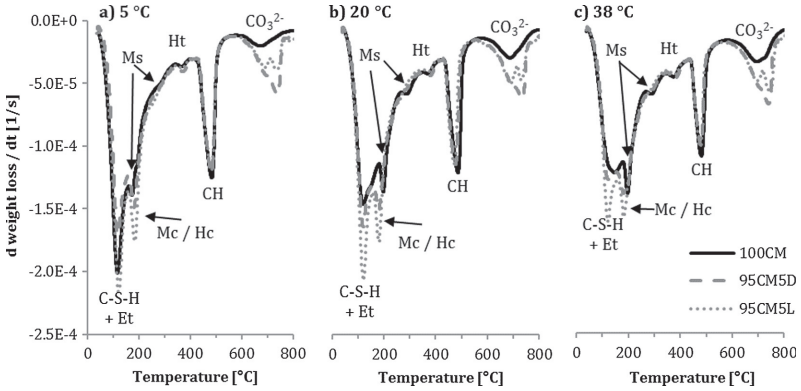

Fig. 6. Differential thermogravimetric (DTG) curves for samples cured for 90 d with a replacement level of 5%wt cured at a) 5 °C, b) 20 °C and c) 38 °C.

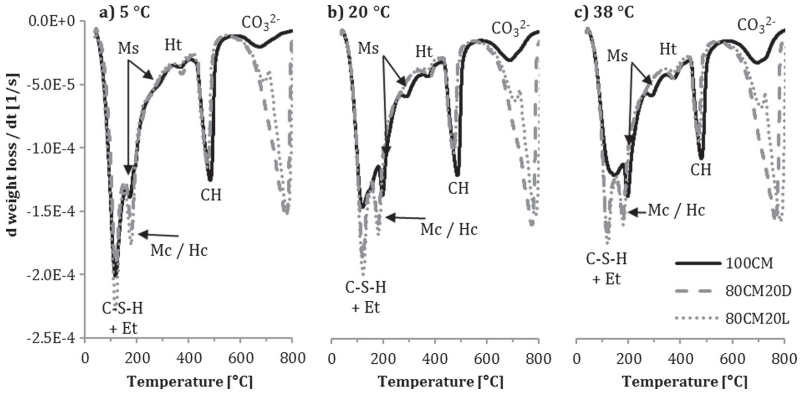

Fig. 7. Differential thermogravimetric (DTG) curves for samples cured for 90 d with a replacement level of 20%wt cured at a) 5 °C, b) 20 °C and c) 38 °C.

Monosulphate is distinguishable from carbonate AFm peaks by its slightly higher decomposition temperature [39]. The trends observed in the XRD results are generally confirmed by TGA. The samples containing limestone show significantly higher carbonate AFm peaks than samples containing dolomite, especially at lower replacement levels. The TGA signal does not enable differentiation between hemicarbonate and monocarbonate. All samples show a weight loss in the temperature region of hydrotalcite (Ht). This weight loss does not increase in samples containing dolomite compared to the equivalent limestone-containing samples or the 100 CM reference. It can potentially be caused by magnesium-containing hydrates formed due to the high magnesium content of the clinker (Table 1). However, no hydrotalcite could be observed with XRD (Figs. 4 and 5), probably due to its poor crystallinity and the small amounts present. A weight loss in this temperature region could also be caused by hydrogarnet or brucite. However, we did not observe any peaks of hydrogarnet nor brucite in our samples with XRD, which are normally quite crystalline and should therefore be visible.

At a replacement level of 5%wt (Fig. 6), the samples containing dolomite and limestone show noticeable differences in the relative quantities of AFm and Aft phases. The samples containing 5%wt of limestone show a higher decomposition peak for the ettringite and carbonate AFm phases than samples containing 5%wt of dolomite. Although this difference is observable at all curing temperatures, its magnitude decreases with increasing curing temperatures.

When 20%wt of the composite cement was replaced with either dolomite or limestone, the DTG curves observed are more alike (Fig. 7) than at the replacement level of 5%wt. The samples containing 20%wt of limestone show only slightly higher decomposition peaks for the carbonate AFm phases and AFt than the samples containing 20%wt of dolomite when cured at 5 °C (Fig. 7a). At the curing temperature of 38 °C, there are no differences between the samples containing 20%wt of dolomite or limestone (Fig. 7c).

3.4. Bound water and portlandite content

The amount of bound water and portlandite content for samples with various replacement levels of either dolomite or limestone and the various curing temperatures are plotted in Figs. 8a) and 9a) relative to the dry binder weight. In Figs. 8b) and 9b) these results are plotted relative to the clinker content.

First, we describe and discuss the results for the samples cured at 20 °C. Any differences in the results for the other curing temperatures are discussed afterwards.

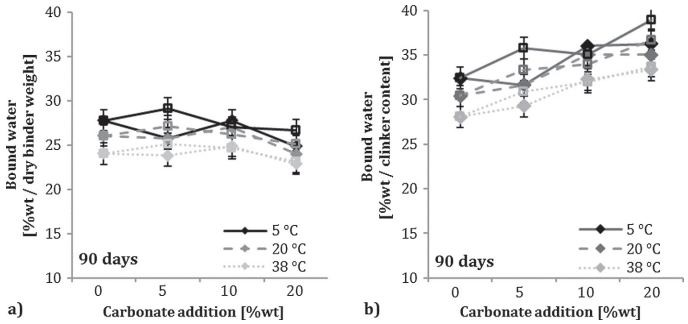

Fig. 8. Amount of the bound water for samples containing dolomite (*filled diamonds*) or limestone (*hollow squares*) and the reference (0%wt carbonate addition) cured for 90 days at 5 °C, 20 °C and 38 °C. The results are normalized to the dry binder weight (a) and the clinker content (b).

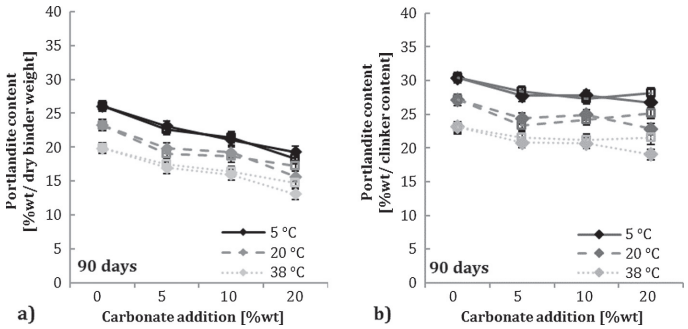

Fig. 9. Amount of portlandite for samples containing dolomite (*filled diamonds*) or limestone (*hollow squares*) and the reference (0%wt carbonate addition) cured for 90 days at 5 °C, 20 °C and 38 °C. The results are normalized to the dry binder weight (a) and the clinker content (b).

In the case of limestone at 5%wt replacement level, the amount of bound water per dry binder weight was higher than the 100CM sample. At higher replacement levels, the amount of bound water decreased again. This is in line with findings reported for the addition of limestone to Portland cement containing fly ash [24,25]. At a replacement level of 5%wt, the amount of bound water increased compared to samples without limestone addition due to the formation of carbonate AFm phases and the stabilization of ettringite, as explained in the introduction. At higher replacement levels, the *dilution effect* of replacing the most reactive part with a less-reactive material resulted in a decrease in the amount of bound water.

In the case of dolomite addition, the increase in bound water normalized to the dry binder weight shifted to higher replacement levels (10%wt) and was less pronounced than with limestone addition.

When the bound water is normalized to the clinker content, dilution effects are erased. The amount of bound water normalized to the clinker content increases for all replacement levels of either dolomite or limestone. This way of plotting depicts the enhancement of the clinker reaction due to the *filler effect* when carbonates are added, as described in the introduction.

The portlandite content normalized to the dry binder weight decreased for all replacement levels of either dolomite or limestone. This can be explained by the *dilution effect* of adding a less-reactive material to the system as explained in the introduction.

When the portlandite content is normalized to the clinker content at 5%wt replacement with either dolomite or limestone, a drop in the values is observed. This drop can probably be explained by the formation of hemicarbonate which consumes portlandite [7,8,13,24,40] and an increased reaction of metakaolin when dolomite or limestone is added [41]. At higher replacement levels than 5%wt, the values slightly increase again in the case of limestone, and again this can be explained by the *filler effect* of adding carbonates to cementitious materials. The enhancement of the clinker reaction produces more portlandite, whereas the enhancement of the metakaolin reaction reduces the portlandite content. Therefore, the observed increase in the portlandite content is only minor, while the increase in bound water is significantly higher.

In the case of dolomite addition, however, the portlandite content normalized to the clinker content continues to decrease even at higher replacement levels. Samples containing dolomite also show an increase in the bound water normalized to the clinker content, so this drop cannot be explained by the dolomite failing to promote the clinker reaction. Moreover, the replacement levels are the same for samples containing dolomite as for samples containing limestone, where a slight increase in the portlandite content is observed. Therefore, the decrease in portlandite content normalized to the clinker content observed in samples containing

dolomite should be due to the reaction of dolomite itself, which is reported to consume portlandite in model systems [17,23]. However, further research on the reaction of dolomite in cementitious systems, where no brucite but carbonate AFm phases or hydrotalcite are formed, is needed to verify this.

The effect of the various curing temperatures is similar in all plots of either bound water or portlandite content. Samples cured at 5 °C show the highest bound water and portlandite content and with increasing curing temperatures, the values decrease. For the portlandite content, this trend can be explained by the enhanced pozzolanic reaction of the metakaolin, which consumes portlandite. This is why the samples cured at the highest temperatures (38 °C) show the lowest portlandite content. The effect on decreasing bound water with increasing curing temperatures has been ascribed to the densification of the C-S-H phase at higher temperatures, which is connected with a decrease in its structural water [42,43]. This decrease in the water content of the C-S-H phase in the samples cured at elevated temperatures affects the bound water content more than a possible enhancement of the clinker hydration.

For the samples containing dolomite or limestone, the results for bound water content and portlandite content were generally quite similar for replacement levels >10%wt. However, when only 5%wt of the Portland metakaolin cement is replaced by dolomite, the bound water content is significantly reduced. This is visible both at the various curing temperatures shown in Fig. 8 and for the various curing times shown in Fig. 10 for 20 °C. Moreover, this difference in bound water content is most obvious in samples cured at low temperatures (5 °C) and decreases with increasing curing temperatures. This correlates with the compressive strength results and the observed phase assemblages, indicating that dolomite has a lower reactivity than limestone.

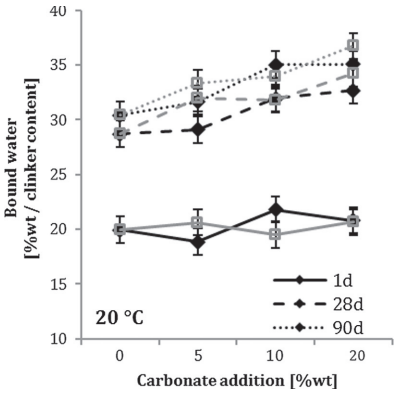

Fig. 10. Amount of bound water for samples with various additions of dolomite *(black diamonds)* or limestone *(grey squares)* and the reference (0%wt carbonate addition) cured for 1 day, 28 days and 90 days at 20 °C normalized to the clinker content.

3.5. Thermodynamic modelling

Thermodynamic modelling was used to confirm the hydrate phase assemblages observed by XRD and TGA and to relate them to the degree of reaction of dolomite or limestone. The effect of the addition of 5%wt of dolomite or limestone was therefore modelled to find the degree of reaction of the two carbonate sources at complete hydration of the clinker and metakaolin.

Fig. 11 shows the modelled phase assemblage for 5%wt of dolomite and limestone addition depending on the degree of reaction of the carbonate source. The figure shows that the addition of 5% wt of either carbonate source results in a similar phase assemblage.

When the carbonate source has not dissolved at all, hydrogarnet, C-S-(A)-H phase, monosulphate, portlandite and hydrotalcite are the stable hydration products. As soon as the carbonate source reacts, hemicarbonate becomes stable and increases in volume as the degree of reaction increases in both cases. Simultaneously with the increase in hemicarbonate, monosulphate decreases and, after approx. 7% of reaction, ettringite becomes stable. At a certain degree of reaction, monocarbonate becomes the stable carbonate

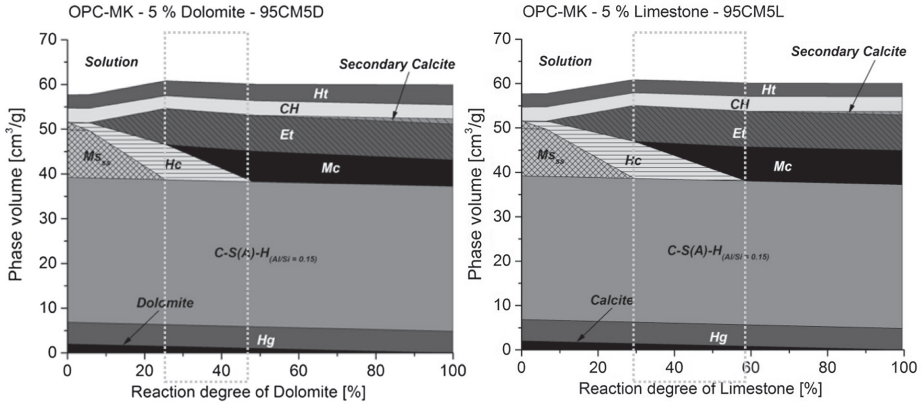

Fig. 11. Effect of the degree of reaction of dolomite or limestone on the phase assemblage of a hydrated Portland metakaolin cement containing 5%wt of one of the carbonate sources. A composition of Portland cement clinker and metakaolin (Table 1) in the ratio 6:1 was used as input for the modelling. The modelled phases dolomite, hydrogrossular (Hg), C-S-(A)-H phase, monosulphate (Ms), hemicarbonate (Hc), monocarbonate (Mc), ettringite (Et), portlandite (CH), hydrotalcite (Ht) and secondary calcite are indicated. The dotted rectangles represent the area of the observed phase assemblage in the 5%wt samples of either dolomite or limestone after 90 days when cured at 20 °C.

AFm phase. Its volume increases simultaneously with the decrease in the volume of hemicarbonate that started the moment monocarbonate became stable.

Differences between dolomite and limestone are only visible in the volume of specific hydrates. In the simulation with dolomite more hydrotalcite is predicted, whereas in the limestone simulation more monocarbonate is predicted. The higher volume for the secondary calcite in the sample containing dolomite than in the sample containing limestone is expected because calcite is a product of the dedolomitization reaction.

4. Discussion of the effect of dolomite addition

4.1. The effect of dolomite addition at 20 °C

The addition of limestone leads to the stabilization of ettringite and the formation of additional carbonate AFm phases [6,7]. The effects on the phase assemblage reported for limestone addition to aluminium-rich cements [24–28] can also be shown for dolomite addition to Portland metakaolin cement. This suggests that the two carbonate sources affect the system in a similar way.

However, the phase assemblage in the samples containing dolomite differed over the various replacement levels from those containing limestone. At a low replacement level (5%wt), there was a difference in the type of carbonate-AFm phases formed. In samples containing dolomite, both hemi- and monocarbonate were formed, while the carbonate-AFm phase formed in samples containing limestone was almost entirely monocarbonate. However, at higher replacement levels, this difference disappeared. In all samples containing 20%wt of either carbonate source, monocarbonate was the main carbonate AFm phase formed.

This could be due to the different rates of reaction of dolomite and limestone. Since limestone is more reactive than dolomite [21], it provides CO_2 to the system faster. After 28 days, sufficient limestone was able to react with the aluminium and form monocarbonate. The lower reactivity of dolomite reduces the CO_2/Al_2O_3 ratio present in the system, which promotes the formation of hemicarbonate over monocarbonate [13]. It should be noted, that the differences in the type of the AFm phase formed are amplified due to the metakaolin content in the composite cement, which is decreasing the CO_2/Al_2O_3 ratio in the system. Moreover, dolomite contains more CO_2 than limestone on a weight basis (Table 1), a slightly smaller amount of dolomite has to react to deliver the same amount of CO_2 to the system and consequently form similar carbonate AFm phases.

The difference in reactivity is indicated by comparing results from the thermodynamic modelling and experimental results for the 95CM5D and 95CM5L samples at 20 °C. Both dolomite and limestone result in the same hydrate phase assemblage at high degrees of reaction with only minor differences in their relative quantity. Consequently, the differences in the phase assemblage observed at low replacement levels must be due to the difference in the degree of reaction present in dolomite and limestone at 28 and 90 days. The areas highlighted in both plots (dotted rectangles) represent the experimentally observed phase assemblage, i.e. the area of hemicarbonate transformation to monocarbonate in these samples. They show that for limestone there is a larger area of influence compared to dolomite, probably indicating a higher degree of reaction. A direct comparison is, however, not possible, due to the similar solubilities of hemi- and monocarbonate [7].

It should be noted that the modelling assumed complete reaction of the clinker and the metakaolin. This is unlikely after 90 days in the experimentally investigated samples, especially in case of the clinker. The impact of this assumption on the results is probably an overestimation of the amount of hydrates formed, this is visible in the high amounts of hydrogarnet predicted by the thermodynamic model, which could not be observed experimentally. The relative stabilities between hemi- and monocarbonate should not be affected because they depend on the degree of reaction of the carbonate source. Moreover, the purpose of these simulations is to compare samples containing dolomite and limestone, and the same assumptions were made in both samples.

Furthermore, it should be noted that the differences in the reactivity of these two materials would probably have been enhanced if dolomite and limestone of the same fineness had been used.

At higher replacement levels of dolomite, more carbonate is available in the system, which increases the CO_2/Al_2O_3 ratio. The higher CO_2/Al_2O_3 ratio led to the formation of monocarbonate in samples containing dolomite at high replacement levels [13]. Consequently, at replacement levels of 20%wt, the carbonate AFm phase assemblages were generally quite similar for samples containing dolomite and limestone, as previously reported by Zajac et al. [19].

At low replacement levels of limestone, only monocarbonate formed despite the considerable metakaolin content of the samples. This suggests fast kinetics of the limestone reaction. We do not think that carbonation due to sample preparation could explain the monocarbonate stabilization because hemicarbonate peaks were observed in the samples containing dolomite.

The addition of dolomite and limestone to calcined-clay containing Portland composite cement affects not only the phase assemblages in a similar way but also the compressive strength development. The addition of dolomite increased the compressive strength up to a replacement level of 10%wt. This effect can be attributed to the above-mentioned effect of ettringite stabilization and the formation of carbonate AFm phases. Ettringite requires more space than monosulphate, so it reduces the porosity of the resulting hydrated cement and increases its compressive strength [6,7]. Because these effects are amplified when sufficient amounts of aluminium are provided to the system [24–28], we used a Portland metakaolin cement instead of a plain Portland cement.

However, there are differences between samples containing dolomite and those containing limestone.

The strength increase due to the carbonate addition was less pronounced for samples containing dolomite than for samples containing limestone. The optimum replacement level with the highest compressive strength was also different for samples containing dolomite and limestone. According to the results reported by De Weerdt et al. [24,25], the optimum addition of limestone to the composite cement is around 5%wt. For the samples containing dolomite, the maximum compressive strength was achieved by 5%wt addition after 28 days and for 10%wt addition after 90 days of hydration.

Moreover, at lower replacement levels, samples containing dolomite showed a lower compressive strength than samples containing limestone. This effect might also be explained by the slower rate of reaction of dolomite. It delivers fewer carbonate ions to the system, so the total amount of carbonate AFm phases and ettringite that can be formed at early ages is smaller. This was confirmed by TGA, which showed that the amount of ettringite and carbonate AFm phases formed at a replacement level of 5%wt was significantly lower in samples containing dolomite than in samples containing limestone. Moreover, the bound water content of samples containing 5%wt of dolomite was lower than in samples containing 5%wt of limestone.

However, these differences were levelled out at higher replacement levels (10%wt). For the highest addition levels tested, dolomite samples showed similar or slightly higher compressive strength values. Such higher compressive strength values for higher replacement levels of dolomite have been reported before [44,45]. The amount of carbonate AFm phases formed and the bound water content were also similar at the high replacement level of 20%wt. It seems, therefore, that adding sufficient amounts

of dolomite to the system can overcome the effect of the lower rate of reaction of dolomite and the accompanying dilution effect of replacing cement with a less reactive material.

The compressive strength results show that relatively high amounts of CM can be replaced by the carbonates without impairing compressive strength. However, in the case of OPC, the addition of >5%wt of carbonates normally results in a drop in compressive strength [24,25]. This can be explained by the fact, that the reaction of metakaolin tends to refine the microstructure of the cement paste [46,47], and therefore might limit itself from further reaction [41]. The addition of either dolomite or limestone provides additional space [16,45] and water, which might allow the metakaolin to react further [41]. This is also visible in our results of the portlandite and bound water content (Figs. 8 and 9). Consequently, more pore space will be filled with additional C-S-H. This effect might be counteracting a strength decrease due to dilution partially and allow relatively high replacement levels without impairing the compressive strength.

It should be noted that the dolomite used was very fine compared to the limestone used. This should be kept in mind when the rate of reaction of the two carbonate sources is discussed on the basis of the present investigation. Differences resulting from the reactivity of dolomite being lower than that of limestone might be greater with natural and coarser dolomite rock [48]. Moreover, the smaller particle size distribution of the dolomite used compared to the limestone used might have affected the compressive strength results due to improved particle packing. However, De Weerdt et al. showed that varying the fineness of limestone additions between 362 m^2/kg and 812 m^2/kg did not significantly affect the compressive strength of Portland fly-ash cements [30]. So although the dolomite used in this study had a fineness of approx. 1056 m^2/kg, we think this would have no significant effect. Lawrence et al. concluded that a compressive strength increase with the addition of fine limestone was due to the enabling of heterogeneous nucleation (filler effect) rather than any particle packing effect [49]. We think this effect is also likely to apply for both dolomite and for the metakaolin [50,51], which was already present in the CM before any carbonate addition.

It can be concluded that the reactions that affect the system when dolomite or limestone is added to Portland metakaolin cement are similar. An apparent strength increase due to the addition of carbonates can only be observed when the carbonates have reacted (28 and 90 days). In these samples, the fine dolomite investigated appears to be able to replace approx. 10%wt of calcined clay-containing composite cement without impairing its compressive strength.

4.2. The effect of dolomite addition at various curing temperatures

The various curing temperatures tested had different effects on the compressive strength development of the composite cement with dolomite addition as opposed to limestone.

At low curing temperatures (5 °C), the dolomite samples show consistently lower compressive strength values than the samples containing limestone at replacement levels <20%wt. This can also be explained by the different rates of reaction of dolomite and limestone, and their differing ability to provide CO_2 to the system. The XRD results show a different phase assemblage, and TGA results show the formation of a smaller amount of AFt and carbonate AFm phases, as described for the 20 °C samples at low replacement levels. These observed differences might explain the overall lower compressive strength of samples containing dolomite compared to those containing limestone.

At each higher level of curing temperature from 5 °C to 38 °C, the differences between samples containing dolomite or limestone decrease. As a result, at 38 °C, and with the exception of the 5%wt replacement level, the dolomite and limestone samples ended up showing similar results in compressive strength for all replacement levels. The increase in strength of dolomite samples at elevated temperatures has been reported previously [19,45] and indicates an enhanced rate of reaction of the dolomite at these temperatures [19,23,45]. So, the lower compressive strength of the samples containing dolomite at some replacement levels seems to be counteracted by increasing the curing temperature.

The phase assemblages of samples containing dolomite and limestone also develop differently with increased curing temperatures. XRD analysis showed that more hemicarbonate was formed at higher temperatures in samples containing limestone. Enhanced metakaolin reaction at higher temperatures reduced the CO_2/Al_2O_3, which favours the formation of hemicarbonate [13]. This increased aluminium content in the pore solution at higher curing temperatures was shown by Deschner et al. for cement containing fly ash [52].

However, the samples containing dolomite did not show significant changes in the hemicarbonate-to-monocarbonate ratio at elevated temperatures (38 °C) compared to the samples cured at 20 °C, because hemicarbonate is already detected at low temperatures. The lower reactivity of dolomite compared to limestone provides a low CO_2/Al_2O_3 ratio at all temperatures, and no phase changes occur when the ratio is lowered even further.

As a result, the phase assemblages for samples containing dolomite and limestone are very similar at elevated temperatures. This was confirmed using TGA, where samples containing dolomite and limestone also showed similar weight losses in the AFt and carbonate AFm temperature range for higher curing temperatures (38 °C).

We can summarize that dolomite and limestone additions to Portland metakaolin cement result in similar compressive strength and similar phase assemblages as long as similar degrees of reaction are achieved. The lower reactivity of dolomite can be counteracted by using increased curing temperatures.

Long-term compressive strength development and questions of durability are possible topics for further research on dolomite as a valid SCM. Moreover, the dolomite used in this study is only one example of a reactive carbonate not covered by EN 197-1 [2]. There are many other carbonate sources which could prove useful as a replacement for pure limestone.

5. Conclusion

Portland metakaolin cement with various replacement levels of up to 20%wt with either dolomite or limestone were investigated with regard to their compressive strength and phase assemblage when cured at 5 °C, 20 °C and 38 °C for up to 90 days.

- Dolomite addition affects Portland metakaolin cement in a similar way to limestone addition. Both result in the formation of additional carbonate AFm phases and ettringite stabilization and either can be used to replace part of the Portland metakaolin cement without impairing its compressive strength at 90 days. At low levels of addition, they can even enhance this strength. In the case of the dolomite, the positive effect was not visible after 90 days of reaction at 5 °C but seemed to be amplified when cured at 38 °C.
- Thermodynamic modelling in combination with experimental determination of phase assemblages indicate a lower degree of reaction for dolomite addition than for limestone when cured at 20 °C for 90 days. This results in a lower ability to deliver CO_2 to the system at 90 days. This was confirmed experimentally by the slight differences in the type and amount of AFm and Aft phases observed at low replacement levels between samples containing dolomite and limestone.

- A similar degree of reaction of dolomite and limestone can be achieved, however, by increasing the curing temperature. At 38 °C the similar phase assemblage and compressive strength indicate a similar degree of reaction.

Acknowledgements

The authors would like to acknowledge the industrial PhD programme of the Norwegian Research Council (Project: 241637) and the Heidelberg Technology Center for their financial support. We are also grateful for the help and assistance of the Norcem AS concrete laboratory with the compressive strength tests.

References

[1] B. Lothenbach, K.L. Scrivener, R.D. Hooton, Supplementary cementitious materials, Cem. Concr. Res 41 (12) (2011) 1244–1256.
[2] EN 197-1, Cement, Part I: Composition, Specifications and Conformity Criteria for Common Cements, European committee for standardization, Brussels, 2011.
[3] J. Péra, S. Husson, B. Guilhot, Influence of finely ground limestone on cement hydration, Cem. Concr. Compos. 21 (2) (1999) 99–105.
[4] I. Soroka, N. Stern, Calcareous fillers and the compressive strength of Portland cement, Cem Concr Res 6 (3) (1976) 367–376.
[5] L. Nicoleau, Accelerated growth of calcium silicate hydrates: Experiments and simulations, Cem. Concr. Res. 41 (12) (2011) 1339–1348.
[6] T. Matschei, B. Lothenbach, F.P. Glasser, The role of calcium carbonate in cement hydration, Cem. Concr. Res. 37 (4) (2007) 551–558.
[7] B. Lothenbach, G. Le Saout, E. Gallucci, K.L. Scrivener, Influence of limestone on the hydration of Portland cements, Cem. Concr. Res. 38 (6) (2008) 848–860.
[8] V.L. Bonavetti, V.F. Rahhal, E.F. Irassar, Studies on the carboaluminate formation in limestone filler-blended cements, Cem. Concr. Res. 31 (6) (2001) 853–859.
[9] R.F. Feldmann, V.S. Ramachandran, P.J. Sereda, Influence of $CaCO_3$ on the Hydration of $3CaO{\cdot}Al_2O_3$, J. Am. Ceram. Soc. 48 (1) (1965) 25–30.
[10] J. Bensted, Some hydration investigations involving Portland cement - effect of calcium carbonate substitution of gypsum, World Cem. Technol. 11 (8) (1980) 395–406.
[11] A.P. Barker, H.P. Cory, The early hydration of limestone-filled cements, in: R.N. Swamy (Ed.), Blended Cements in Construction, Taylor & Francis, Sheffield, UK, 1991, pp. 107–124.
[12] K. Ingram, M. Polusny, K. Daugherty, W. Rowe, Carboaluminate reactions as influenced by limestone additions, in: P. Klieger, R.D. Hooton (Eds.), Carbonate Additions to Cement: ASTM STP 1064, American Society for Testing and Materials, Philadelphia, PA, 1990, pp. 14–23.
[13] T. Matschei, B. Lothenbach, F.P. Glasser, The AFm phase in Portland cement, Cem Concr Res 37 (2) (2007) 118–130.
[14] P. Hawkins, P.D. Tennis, R.J. Detwiler, The Use of Limestone in Portland Cement: A State-of-the-Art Review, Portland Cement Association, 2003.
[15] S. Schöne, W. Dienemann, E. Wagner, Portland Dolomite Cements as Alternative to Portland Limestone Cements, in: Proceedings of the 13th International Congress on the Chemistry of Cement, Madrid, Madrid, 2011.
[16] M. Zajac, W. Dienemann, G. Bolte, Comparative experimental and virtual investigations of the influence of calcium and magnesium carbonates on reacting cement, in: Proceedings of the 13th International Congress on the Chemistry of Cement, Madrid, Madrid, 2011.
[17] S. Galí, C. Ayora, P. Alfonso, E. Tauler, M. Labrador, Kinetics of dolomite-portlandite reaction: Application to Portland cement concrete, Cem. Concr. Res. 31 (6) (2001) 933–939.
[18] E. Garcia, P. Alfonso, M. Labrador, S. Galí, Dedolomitization in different alkaline media: Application to Portland cement paste, Cem. Concr. Res. 33 (9) (2003) 1443–1448.
[19] M. Zajac, S.K. Bremseth, M. Whitehead, M. Ben, Haha, Effect of $CaMg(CO_3)_2$ on hydrate assemblages and mechanical properties of hydrated cement pastes at 40 °C and 60 °C, Cem. Concr. Res. 65 (2014) 21–29.
[20] J.W. Morse, R.S. Arvidson, The dissolution kinetics of major sedimentary carbonate minerals, Earth Sci. Rev. 58 (1–2) (2002) 51–84.
[21] O.S. Pokrovsky, S.V. Golubev, J. Schott, A. Castillo, Calcite, dolomite and magnesite dissolution kinetics in aqueous solutions at acid to circumneutral pH, 25 to 150 °C and 1 to 55 atm pCO_2: new constraints on CO_2 sequestration in sedimentary basins, Chem. Geol. 265 (1–2) (2009) 20–32.
[22] L. Chou, R.M. Garrels, R. Wollast, Comparative study of the kinetics and mechanisms of dissolution of carbonate minerals, Chem. Geol. 78 (3–4) (1989) 269–282.
[23] X. Zhang, F.P. Glasser, K.L. Scrivener, Reaction kinetics of dolomite and portlandite, Cem. Concr. Res. 66 (2014) 11–18.
[24] K. De Weerdt, H. Justnes, K.O. Kjellsen, E. Sellevold, Fly ash-limestone ternary composite cements: synergetic effect at 28 days, Nordic Concr. Res. 42 (2) (2010) 51–70.
[25] K. De Weerdt, K.O. Kjellsen, E. Sellevold, H. Justnes, Synergy between fly ash and limestone powder in ternary cements, Cem. Concr. Compos. 33 (1) (2011) 30–38.
[26] M. Antoni, J. Rossen, F. Martirena, K.L. Scrivener, Cement substitution by a combination of metakaolin and limestone, Cem. Concr. Res. 42 (12) (2012) 1579–1589.
[27] G. Puerta-Falla, M. Balonis, G. Le Saout, N. Neithalath, G. Sant, The Influence of Metakaolin on Limestone Reactivity in Cementitious Materials, in: Calcined Clays for Sustainable Concrete: Proceedings of the 1st International Conference on Calcined Clays for Sustainable Concrete, Lausanne, Switzerland, 2015, pp. 11–19.
[28] D. Nied, C. Stabler, M. Zajac, Assessing the synergistic effect of limestone and metakaolin, in: Calcined Clays for Sustainable Concrete: Proceedings of the 1st International Conference on Calcined Clays for Sustainable Concrete, Lausanne, Switzerland, 2015, pp. 245–251.
[29] EN 196-1, Methods of Testing Cement, PartI: Determination of Strength, European committee for standardization, Brussels, 2005.
[30] K. De Weerdt, E. Sellevold, K.O. Kjellsen, H. Justnes, Fly ash–limestone ternary cements: effect of component fineness, Adv. Cem. Res. 23 (4) (2011) 203–214.
[31] B. Lothenbach, F. Winnefeld, Thermodynamic modelling of the hydration of Portland cement, Cem Concr Res 36 (2) (2006) 209–226.
[32] http://gems.web.psi.ch/.
[33] D.A. Kulik, T. Wagner, S.V. Dmytrieva, G. Kosakowski, F.F. Hingerl, K.V. Chudnenko, U.R. Berner, GEM-Selektor geochemical modeling package: Revised algorithm and GEMS3K numerical kernel for coupled simulation codes, Comput. Geosci. 17 (1) (2012) 1–24.
[34] T. Wagner, D.A. Kulik, F.F. Hingerl, S.V. Dmytrieva, GEM-Selektor geochemical modeling package: TSolMod library and data interface for multicomponent phase models, Can. Mineralogist 50 (5) (2012) 1173–1195.
[35] https://www.empa.ch/de/web/s308/thermodynamic-data.
[36] D.A. Kulik, Improving the structural consistency of C-S-H solid solution thermodynamic models, Cem. Concr. Res. 41 (5) (2011) 477–495.
[37] B.Z. Dilnesa, B. Lothenbach, G. Renaudin, A. Wichser, D. Kulik, Synthesis and characterization of hydrogarnet $Ca_3(Al_xFe_{1-x})_2(SiO_4)_y(OH)_{4(3-y)}$, Cem. Concr. Res. 59 (2014) 96–111.
[38] B. Lothenbach, T. Matschei, G. Möschner, F.P. Glasser, Thermodynamic modelling of the effect of temperature on the hydration and porosity of Portland cement, Cem. Concr. Res. 38 (1) (2008) 1–18.
[39] B. Lothenbach, P. Durdzinski, K. De Weerdt, Thermogravimetric Analysis, in: K. L. Scrivener, R. Snellings, B. Lothenbach (Eds.), A Practical Guide to Microstructural Analysis of Cementitious Materials, CRC Press Taylor & Francis Group, Boca Raton, 2015, pp. 177–211.
[40] H. Hirao, K. Yamada, S. Hoshino, H. Yamashita, The Effect of Limestone Powder Addition on the Optimum Sulfate Levels of Cement Having Various Al2O3 Contents, in: Proceedings of the 12th International Congress on the Chemistry of Cement, Montreal, Montreal, 2007.
[41] W. Kunther, Z. Dai, J. Skibsted, Thermodynamic modeling of hydrated white Portland cement–metakaolin–limestone blends utilizing hydration kinetics from 29Si MAS NMR spectroscopy, Cem. Concr. Res. 86 (2016) 29–41.
[42] E. Gallucci, X. Zhang, K.L. Scrivener, Effect of temperature on the microstructure of calcium silicate hydrate C-S-H, Cem. Concr. Res. 53 (2013) 185–195.
[43] B. Lothenbach, F. Winnefeld, C. Alder, E. Wieland, P. Lunk, Effect of temperature on the pore solution, microstructure and hydration products of Portland cement pastes, Cem. Concr. Res. 37 (4) (2007) 483–491.
[44] O. Mikhailova, G. Yakovlev, I. Maeva, S. Senkov, Effect of Dolomite Limestone Powder on the Compressive Strength of Concrete, Procedia Engineering 57 (2013) 775–780.
[45] J. Xu, D. Lu, S. Zhang, K. Ling, Z. Xu, Pore structures of mortars with dolomite and limestone powders cured at various temperatures, J. Chin. Ceramic Soc. 45 (2) (2017) 268–273.
[46] B. Akcay, M.A. Tasdemir, Investigation of Microstructure Properties and Early Age Behavior of Cementitious Materials Containing Metakaolin, in: CONCREEP 10: Mechanics and Physics of Creep, Shrinkage, and Durability of Concrete and Concrete Structures, Vienna, Austria, American Society of Civil Engineers, Reston, VA, 2015, pp. 1468–1475.
[47] M. Frías, J. Cabrera, Pore size distribution and degree of hydration of metakaolin–cement pastes, Cem. Concr. Res. 30 (4) (2000) 561–569.
[48] T. Knudsen, The dispersion model for hydration of Portland cement - I. General concepts, Cem. Concr. Res. 14 (5) (1984) 622–630.
[49] P. Lawrence, M. Cyr, E. Ringot, Mineral admixtures in mortars effect of type, amount and fineness of fine constituents on compressive strength, Cem. Concr. Res. 35 (6) (2005) 1092–1105.
[50] G. Marchetti, V.F. Rahhal, E.F. Irassar, Influence of packing density and water film thickness on early-age properties of cement pastes with limestone filler and metakaolin, Mater. Struct. 50 (2) (2017). Article: 111.
[51] B. Ilić, V. Radonjanin, M. Malešev, M. Zdujić, A. Mitrović, Study on the addition effect of metakaolin and mechanically activated kaolin on cement strength and microstructure under different curing conditions, Constr. Build Mater. 133 (2017) 243–252.
[52] F. Deschner, B. Lothenbach, F. Winnefeld, J. Neubauer, Effect of temperature on the hydration of Portland cement blended with siliceous fly ash, Cem. Concr. Res. 52 (2013) 169–181.

Paper II

Limitations of the hydrotalcite formation in Portland composite cement pastes containing dolomite and metakaolin

Machner, A., Zajac, M., Ben Haha, M., Kjellsen, K.O., Geiker, M.R., De Weerdt, K.
Accepted for publication in Cement and Concrete Research
DOI: 10.1016/j.cemconres.2017.11.007

ARTICLE IN PRESS

Cement and Concrete Research xxx (xxxx) xxx–xxx

Contents lists available at ScienceDirect

Cement and Concrete Research

journal homepage: www.elsevier.com/locate/cemconres

Limitations of the hydrotalcite formation in Portland composite cement pastes containing dolomite and metakaolin

Alisa Machner[a,b,*], Maciej Zajac[c], Mohsen Ben Haha[c], Knut O. Kjellsen[a], Mette R. Geiker[b], Klaartje De Weerdt[b]

[a] Norcem AS, R&D Department, Setreveien 2, P.O. Box 38, 3991 Brevik, Norway
[b] NTNU Department of Structural Engineering, Richard Birkelandsvei 1A, 7491 Trondheim, Norway
[c] Heidelberg Technology Center GmbH, Oberklammweg 2-4, 69181 Leimen, Germany

ARTICLE INFO

Keywords:
Thermal analysis (B)
X-ray diffraction (B)
$Ca(OH)_2$ (D)
Blended cement (D)
Dedolomitization reaction

ABSTRACT

This study focuses on the reaction of dolomite powder in combination with metakaolin in Portland composite cement pastes. We studied paste samples cured at 20 °C, 38 °C, and 60 °C for up to 1 year. In these systems, the only magnesium-containing hydration phase of dolomite observed was hydrotalcite. Dolomite reacted notably already after 90 days when cured at 60 °C, whereas at lower curing temperatures the reaction was limited. The increased availability of aluminium due to the addition of metakaolin did not contribute to the formation of hydrotalcite. The refined pore space due to the metakaolin addition did not inhibit the hydrotalcite formation. However, the almost total absence of portlandite due to the pozzolanic reaction of the metakaolin inhibited the dolomite reaction, even in pastes with high porosity. Portlandite seems to be the driving force for the reaction as its absence is inhibiting the reaction to take place.

1. Introduction

Supplementary cementitious materials (SCMs) are frequently used as a partial substitute for cement clinker to reduce the emissions caused by cement manufacturing. However, some of the SCMs traditionally used have limited availability when compared to the global increase of cement demand [1]. Therefore, alternative SCMs need to be found that are available in sufficient quantity and show similar or even improved interaction with cement clinker hydration.

Limestone is commonly used as an SCM and, according to the European cement standard EN 197-1, it can replace up to 5 wt% clinker in CEM I Portland cements and up to 35 wt% in CEM II Portland-limestone cements [2]. Due to the additional carbonates, the stable AFm phases which form are hemi- and monocarbonate and not monosulphate. This change in phase stabilities results in the so-called "ettringite stabilization", because the sulphate-containing hydration phase ettringite does not transform to monosulphate when the sulphate sources (e.g. gypsum) are depleted. This stabilization of ettringite beyond sulphate depletion results in a relative increase in the volume of hydrates, a corresponding decrease in porosity, and an increase in compressive strength [3,4].

The limited aluminium content in Portland cements means this effect is somewhat limited [4], but it can be amplified if additional aluminium is provided to the system by adding aluminium-delivering SCMs [5–8]. In this study, we used metakaolin as a model material for industrially available calcined clays supplying silicates and alumina to the system. Metakaolin is also known to be a pozzolanic material. During its pozzolanic reaction, the silicates provided by the metakaolin react with the portlandite formed during the hydration of the Portland cement to produce additional C-S-H [9], and the aluminium provided by the metakaolin reacts with the portlandite to form additional AFm phases [5–8]. Moreover, the aluminium is also partly taken up by the C-S-H [10] and can lead to the formation of calcium aluminate silicate hydrate phases (C-A-S-H phases), as observed in composite cements containing slag, fly ash or metakaolin [11,12].

Because high-grade limestone required by EN 197-1 [2] is not sufficiently available in all parts of the world, various other carbonate sources are in the focus of ongoing research. One possible alternative carbonate source that has been studied is dolomite [13]. This is a double salt consisting of calcium, magnesium and carbonate ions with the formula $CaMg(CO_3)_2$ and can function as a source of CO_2 and magnesium. In the alkaline environment of cement paste, dolomite can undergo a so-called "dedolomitization reaction" [14–16]. In this reaction, dolomite reacts with portlandite to form brucite and calcite. However, Zajac et al. have recently shown that the reaction of dolomite in Portland cement paste results in the formation of a similar phase

* Corresponding author at: NTNU Department of Structural Engineering, Richard Birkelandsvei 1A, 7491 Trondheim, Norway.
E-mail address: alisa.machner@ntnu.no (A. Machner).

https://doi.org/10.1016/j.cemconres.2017.11.007
Received 15 June 2017; Received in revised form 9 November 2017; Accepted 28 November 2017

Please cite this article as: Machner, A., Cement and Concrete Research (2017), https://doi.org/10.1016/j.cemconres.2017.11.007

assemblage to that of limestone addition [17,18]. They further show that the magnesium originating from the dolomite reaction results in the formation of hydrotalcite [17,18] (in the present study given as $Mg_6Al_2(OH)_{18}{\cdot}3(H_2O)$, according to [19]), which can lead to an increase in the compressive strength [17,20].

The present study focuses on the reaction of dolomite powders in combination with metakaolin used as SCM in Portland cement-based pastes. Metakaolin is used as a model material for SCMs that provide Al and Si. The aim was to determine whether dolomite reacts in these Al-rich systems, and what the reaction products are. We also wanted to understand more about the rate-limiting factors of the dolomite reaction in these systems.

We investigated the phase assemblage and microstructure of hydrated cement pastes, in which 40 wt% of Portland cement was replaced by various combinations of dolomite and metakaolin. The pastes were sealed-cured at 20 °C, 38 °C and 60 °C for up to 360 days. Elevated curing temperatures were applied to accelerate the reaction of the dolomite and to be able to study its reaction products. The following techniques were used to characterize phase assemblage and microstructure: XRD, TGA, SEM-EDS and MIP. The phase assemblage was compared with those of a plain Portland cement paste and systems containing limestone so that we could identify the effect of dolomite on the phase assemblage. In addition, a paste with a high w/b ratio, and well-hydrated samples exposed to additional portlandite and or water were prepared to study the impact of increased porosity or additional portlandite on the dolomite reaction.

2. Experimental

2.1. Materials

The mixes investigated in this study were prepared using a Portland cement clinker (C) supplied by Norcem AS, natural dolomite (D) and limestone (L) supplied by Miljøkalk AS, and laboratory-grade metakaolin (M) supplied by Imerys (Metastar501) and gypsum supplied by Merck. The cement clinker was ground in a laboratory ball mill until a Blaine surface area of approx. 400 m^2/kg was achieved. The other materials were used as received. The chemical and mineralogical compositions of all materials were investigated with XRF (Table 1) and QXRD (Table 2 and Table 3). It should be noted that the Portland cement clinker used shows a relatively high alkali content. The particle size distributions of the materials used were determined from the average of 3 independent measurements with laser diffraction (Malvern Mastersizer 2000E) (Fig. 1).

The experimental matrix is given in Table 4. Taking into account the sulphate content of the clinker as determined by XRF, laboratory grade gypsum was added when preparing the mixes to achieve a sulphate content of 2.5 wt%/g of binder in all mixes. This sulphate level was determined by isothermal calorimetry at 20 °C on the sample with the highest metakaolin content. At a sulphate content of 2.5 wt%, the secondary aluminate peak appeared after the silicate peak and thereby the system is assumed to contain sufficient amounts of sulphates. The sulphatation was, however, not checked at the elevated curing temperatures (38 °C and 60 °C). It should be noted that the values in Table 4 do not reflect the actual amounts in the mixes, as they do not include the amount of gypsum added to the system. A pure Portland cement (100C = ground Portland cement clinker + gypsum) was used as a reference. In the other mixes, 40 wt% of the Portland cement clinker was replaced with metakaolin and or dolomite, or limestone. Paste samples were prepared in the laboratory at 20 °C with a w/b ratio of 0.45 for all mixes, and in the case of 60C20D20M, an additional paste sample was also prepared with a w/b ratio of 0.93. The pastes were mixed in a BRAUN MR550CA high-shear mixer (speed 6) and cast in 12 ml plastic tubes (mixing procedure: mixing for 30 s, waiting for 5 min, mixing for 1 min again). The sealed tubes were cured at 100% RH in a sealed box at 20 °C, 38 °C and 60 °C for up to 360 days and up to 400 days in the case of the samples prepared with the various w/b ratio samples. The curing at elevated temperatures (especially 60 °C) was used to accelerate the reaction of dolomite and to be able to study its reaction products.

Additionally, two tubes of the samples with the highest metakaolin content (20 wt%) and the w/b ratio of 0.45 were exposed to additional portlandite and or water after a curing time of 1 year and 9 months (approx. 630 days) at 60 °C. We crushed the samples to a particle size between 1 mm and 0.25 mm and filled them into 45 ml centrifuge tubes. To both samples 30 wt% of deionized water and to one of them additional 30 wt% of portlandite were added. These samples were stored again sealed at 60 °C at 100% RH and investigated after 28 and 90 days.

Table 1
XRF results [wt%] of the clinker, dolomite, limestone, metakaolin, and gypsum used.

Oxide	Clinker	Dolomite	Limestone	Metakaolin	Gypsum
SiO_2	20.6	0.52	0.12	52.18	0.02
Al_2O_3	5.6	0.01	0.06	44.92	0.09
TiO_2	0.29	0.00	0.00	1.14	0.00
MnO	0.05	0.00	0.00	0.00	0.00
Fe_2O_3	3.12	0.04	0.03	0.62	0.00
CaO	63.26	31.52	55.12	0.12	32.66
MgO	2.66	20.14	0.41	0.04	0.06
K_2O	1.23	0.00	0.01	0.18	0.01
Na_2O	0.51	0.00	0.00	0.17	0.02
SO_3	1.37	0.00	0.02	0.14	46.47
P_2O_5	0.09	0.01	0.00	0.07	0.00
LOI	–	46.79	43.57	0.29	20.39
Sum (1050 °C)	98.78	99.03	99.34	99.87	99.72

2.2. Methods

Prior to the investigation of the phase assemblage of the cement pastes using thermogravimetric analysis (TGA) and X-ray diffraction (XRD), the hydration was stopped by double solvent exchange after 28, 90, 208 and 360 days of curing. The samples prepared with the different w/b ratio were stopped after 400 days of curing. For this, a 6 mm thick slice (diameter: 23 mm) was cut off each cured cement paste sample. This slice was crushed in a porcelain mortar until the whole sample had passed through a 1 mm sieve. The coarsely crushed cement paste was then immersed in 50 ml isopropanol, shaken for 30 s, and left to rest for 5 min before the isopropanol was decanted. This isopropanol treatment was performed twice before the sample was transferred to a filtration unit where the isopropanol was filtrated out and the paste was immersed in 10 ml petroleum ether. After 30 s of stirring, the suspension was left to rest for 5 min. The sample was then vacuum-filtrated and subsequently dried. The 28-day-old samples were dried for 15 min in an aerated oven at 40 °C. All other samples were dried overnight in a desiccator under a slight vacuum (− 0.2 bar) applied using a water pump. After drying, the samples were crushed in a porcelain mortar until the whole sample passed through a 63 µm sieve. All samples were stored in a desiccator over silica gel and soda lime until measurement. The well-hydrated samples exposed to additional water and or portlandite were treated similarly with the difference that they have already been crushed at exposure and, due to the additional water, the amounts of isopropanol and petroleum ether were increased to 100 ml and 20 ml respectively. These samples were stopped after 28 and 90 days of exposure and directly prior exposure.

For the TGA measurements, the resulting dry powders were poured into 600 µl corundum crucibles and stored in a sample changer until measurement. The weight loss was measured from 40 °C to 900 °C with a heating rate of 10 °C/min in Mettler Toledo TGA/SDTA851 and TGA/DSC3+ devices. During the measurement, the measurement cell was purged with 50 ml/min of nitrogen gas. Both devices used a similar measurement principle and were operated with the same parameters.

Table 2
Mineral composition of the dolomite, limestone, metakaolin, and gypsum, determined by Rietveld analysis [wt%]. Amounts given in *italics* are below the limits of quantification (1 wt%). Due to the low crystallinity of mullite, its quantification is questionable.

Mineral name	Mineral formula	Dolomite	Limestone	Metakaolin	Gypsum
Calcite	$CaCO_3$	5.8	100	–	–
Dolomite	$CaMg(CO3)_2$	89.9	–	–	–
Gypsum	$CaSO_4{\cdot}2H_2O$	–	–	–	93.7
Bassanite	$CaSO_4{\cdot}0.5H_2O$	–	–	–	6.3
Anatase	TiO_2	–	–	*1.2*	–
Mullite	$Al_6Si_2O_{13}$	–	–	*6.1*	–
Muscovite	$KAl_2Si_3AlO_{10}(OH)_2$	–	–	*0.4*	–
Quartz	SiO_2	*0.4*	–	*0.7*	–
Amorphous content	–	3.9	–	91.6	–

Table 3
Mineralogical composition of the clinker used determined by Rietveld analysis [wt%]. Amounts given in italics are below or close to the limits of detection.

Mineral name	Formula	wt%
Alite	Ca_3SiO_5	59.5
Belite	Ca_2SiO_4	15.3
Aluminate	$Ca_3Al_2O_6$	8.8
Ferrite	$Ca_2(Al,Fe)_2O_5$	10.0
Periclase	MgO	1.5
Free lime	CaO	0.9
Portlandite	$Ca(OH)_2$	*1.2*
Aphthitalite	$K_3Na(SO_4)_2$	*2.4*
Arcanite	K_2SO_4	*0.5*

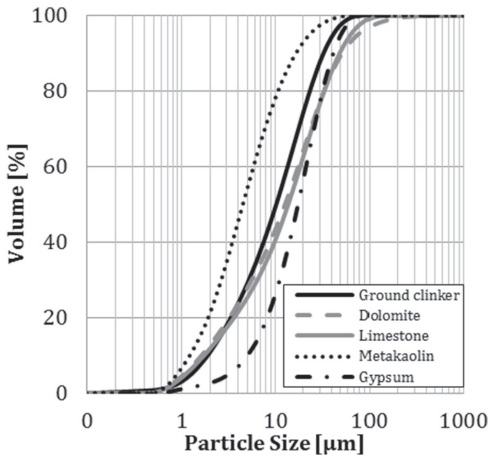

Fig. 1. Particle size distributions of the materials used, determined by laser diffraction.

We therefore assume no significant differences between the results obtained from the two devices.

The derivate curves of the TG signal, the DTG curves, were used to detect phase changes. The DTG curves can be divided into several sections, in which the decomposition of specific phases can be detected as a weight loss. The first peak at around 100 °C is related to the ettringite decomposition and the beginning of the dehydroxylation of the C-S-H phase. C-S-H decomposes gradually between 40 °C and 600 °C [21] and appears as a polynomial baseline under the other peaks. The region between approx. 150 °C and 400 °C represents the stepwise dehydroxylation of the AFm phases (monosulphate, hemi- and monocarbonate) and other lamellar phases, including hydrotalcite (Ht). Consequently, there are several mass loss peaks visible in this temperature range. Hydrotalcite shows two mass loss events, the first at approx. 270 °C and the second at around 400 °C [21]. The subsequent sharp peak between approx. 400 °C and 550 °C is related to the decomposition of portlandite (CH). Above 550 °C carbonates decompose by emitting CO_2.

TGA was used to quantify the mass losses of various hydration phases, such as portlandite and hydrotalcite. The mass loss of a phase in a specific temperature interval can be determined by integration of the derivative curve with subtraction of the background by a linear baseline as described by Lothenbach et al. [21]. The calculated weight losses were then normalized to the sample weight at approx. 550 °C, which was assumed to be the dry binder weight, and remained constant during the cement hydration, or to the original percentage of clinker in the sample (100 wt% or 60 wt%).

For the XRD analyses, the powder was loaded into the sample holders by means of front-loading and stored in a sample changer until measurement. For the measurements, we used a D8 Focus diffractometer from Bruker with a Bragg-Brentano θ–2θ geometry and a goniometer radius of 200.5 mm. The samples were measured between 5°2θ and 55°2θ with a step size of 0.01°2θ and a sampling time of 0.5 s per step. We used Cu-Kα radiation with a wavelength of approx. 1.54 Å as the X-ray source. The XRD plots were qualitatively evaluated with the DIFFRAC.EVA V4.0 software from Bruker by using the PDF4 + database from ICDD and the COD database. For the quantification of the dolomite content in the samples (QXRD), the TOPAS 5 software from Bruker was used combined with the G-Factor Method [22,23], which was applied by using an external quartzite standard. The quartzite was calibrated against a silicon powder from NIST (Standard Reference Material 640d). For the C-S-H phase, the model described by Bergold et al. was used in the refinement [24].

To investigate the phase assemblage and microstructure of the samples with scanning electron microscopy (SEM), a 3 mm slice was cut off the cured cement paste and immersed in isopropanol for min. 1 week. Then the slice was dried, cast in epoxy and polished. In case of the well-hydrated samples exposed to additional water and portlandite, parts of the samples from the double solvent exchange as described above before grinding were used for polishing. We analysed polished and carbon-coated sections of selected paste samples with the SEM. Elemental mapping and point analyses were carried out using a Hitachi S-3400N microscope equipped with an energy dispersive spectrometer (EDS) from Oxford Instruments.

To study the threshold pore entry diameter and total porosity of the paste samples with mercury intrusion porosimetry (MIP), a 7 mm slice was cut off the cured cement paste and coarsely crushed in a porcelain mortar. The crushed samples were then immersed in isopropanol for at least 24 h and then dried in an aerated oven overnight at 40 °C to remove the isopropanol. For the MIP measurements, we used a Pascal 140/440 porosimeter from ThermoFisher Scientific and defined a contact angle of 140°. The first intrusion curve reported from the measurements was used to determine the threshold pore entry diameter and the porosity of the samples. The threshold pore entry diameter was

Table 4
Overview of the experimental matrix, including the original composition, addition of water or portlandite, w/b ratio and curing time of all samples. The times given in brackets represents the time of the samples exposed to portlandite and or water. The sulphate content per gram of binder was set to 2.5 wt% for all mixes [wt%]. It should be noted that the dolomite contains approx. 90% of dolomite (see Table 2).

Name of the mix	C Portland cement clinker	D Dolomite	L Limestone	M Metakaolin	Add. water	Add. CH	w/b ratio	Curing time
100C	100	–	–	–	–	–	0.45	28–360 days
60C40D	60	40	–	–	–	–	0.45	28–360 days
60C35D5M	60	35	–	5	–	–	0.45	28–360 days
60C30D10M	60	30	–	10	–	–	0.45	28–360 days
60C25D15M	60	25	–	15	–	–	0.45	28–360 days
60C20D20M	60	20	–	20	–	–	0.45	28–360 days
60C40L	60	–	40	–	–	–	0.45	28–360 days
60C35L5M	60	–	35	5	–	–	0.45	28–360 days
60C30L10M	60	–	30	10	–	–	0.45	28–360 days
60C25L15M	60	–	25	15	–	–	0.45	28–360 days
60C20L20M	60	–	20	20	–	–	0.45	28–360 days
60C20D20M w/b 0.45	60	20	–	20	–	–	0.45	400 days
60C20D20M w/b 0.93	60	20	–	20	–	–	0.93	400 days
60C20D20M + H_2O	60	20	–	20	+ 30%	–	0.45	630 days (+ 28/90 days)
60C20D20M + CH	60	20	–	20	+ 30%	+ 30%	0.45	630 days (+ 28/90 days)

defined as the intersection of two tangents on the intrusion curve as described in [25]. The porosity as percentage of the sample volume equals the total porosity measurable with MIP and is determined by the maximum of the intrusion curve.

3. Results

3.1. Quantification of the dolomite reaction

3.1.1. QXRD

QXRD was used to quantify the amount of unreacted dolomite in the hydrated cement paste samples. However, the hardness of the dolomite used in this study resulted in coarse dolomite particles in the powder even after grinding and therefore in the vertical exaggeration of one reflex of dolomite in the XRD-patterns (commonly called spottiness-effect). This effect resulted in a relatively large error in the quantification (estimated at approx. 10 %). The results are given as the amount of dolomite determined by QXRD compared to the original amount of dolomite added. The theoretical amount of dolomite added equals the amounts given in Table 4. However, this is not the actual amount of dolomite added, because we also added gypsum to all the samples and the dolomite used contains approx. 90 wt% of dolomite (Table 2).

After 360 days, the amount of dolomite was determined for all the mixes investigated. Fig. 2 shows that the samples cured at 20 °C and 38 °C still contained a high amount of dolomite, close to the actual amount of dolomite added, independently of the sample composition. However, when cured at 60 °C, the samples with low metakaolin contents, especially the sample 60C40D, showed a notable decrease in the amount of dolomite. For samples with a higher metakaolin content, the determined amounts of dolomite were again close to the actual amount of dolomite added.

Fig. 3 shows the amount of dolomite in sample 60C40D over a period of one year. Samples cured at 20 °C and 38 °C showed a similar amount of dolomite, which was close to the actual amount of dolomite added. There is only a slightly increasing trend in the degree of reaction with curing time. For the samples cured at 60 °C, however, the amount of dolomite decreases significantly between 90 and 208 days and stayed rather constant afterwards.

Based on the QXRD results, the degree of dolomite reaction, therefore, seems to depend on the curing temperature, the curing time and the metakaolin addition.

3.1.2. SEM-EDS

Figs. 4 and 5 show the BSE images for the 60C40D and 60C35D5M samples, which showed the lowest amount of dolomite and therefore

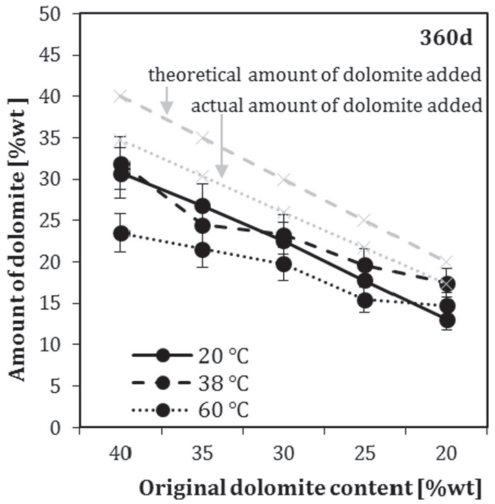

Fig. 2. Amount of dolomite for the various compositions, in wt% compared to the original content of dolomite (theoretical and actual) for samples cured at 20 °C, 38 °C and 60 °C after 360 days.

the highest degree of dolomite reaction with QXRD, cured at 60 °C for 1 year. Fig. 6 shows the BSE image for the 60C20C20M sample, which showed limited dolomite reaction, cured under the same conditions. Alongside the BSE images, the figures show the corresponding elemental maps of magnesium, aluminium, oxygen, calcium and silicon for each sample.

The BSE images show large, uniformly grey particles, which the elemental maps show are rich in Mg and Ca, but poor in Al and Si. These particles are unreacted dolomite grains (up to approx. 70 µm in length). In the samples where dolomite has reacted, a clear reaction rim filled with Mg-rich reaction products can be observed around these grains (Figs. 4 and 5). The shape of the original dolomite grains is still visible in the BSE images, because it is marked with a thin layer of C-S-H precipitated around them, presumably at early ages, which then persisted even after the dolomite started to react at later ages. In addition to the larger, partially reacted dolomite grains in these samples, small fully-reacted dolomite grains can also be observed (some

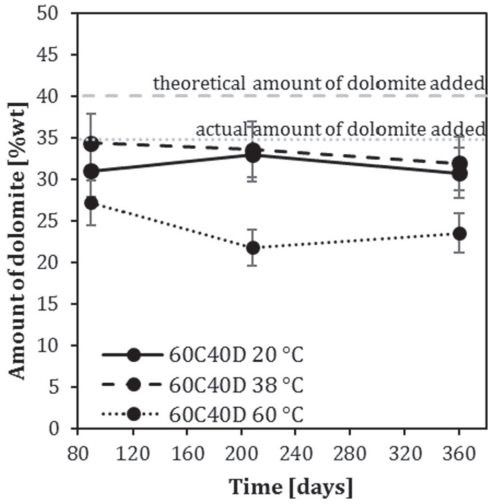

Fig. 3. Amount of dolomite reacted over time, in wt% compared to the original content of dolomite (theoretical and actual) for the sample 60C40D cured at 20 °C, 38 °C and 60 °C.

indicated with arrows). They are completely filled with the Mg-rich reaction product and are surrounded by the C-S-H rim, which indicates the original dolomite grain boundary.

Fig. 7 gives the BSE images for the samples 60C20D20M, which showed limited dolomite reaction under QXRD examination. Here we prepared two samples with the same binder, one with a w/b ratio of 0.45 and the other with a higher w/b ratio, namely 0.93. We did this to investigate the impact of increased porosity on the reaction of dolomite.

As expected, the sample with the high w/b ratio shows considerably more porous microstructure than the sample with the lower w/b ratio (0.45). Moreover, significantly fewer unreacted clinker grains are visible in the high w/b sample than in the low w/b sample. However, the dolomite grains do not show any significant reaction in either case. So we conclude that the higher w/b ratio enhanced the clinker reaction, but was not able to enhance the dolomite reaction.

3.2. Phase assemblage

3.2.1. SEM-EDS

The elemental maps for the 60C40D and 60C35D5M samples cured at 60 °C for 1 year (see Figs. 4 and 5) show that the reaction rims inside the former dolomite grains are rich in magnesium, aluminium and oxygen, but that they do not contain calcium or silicon. This indicates that the product of the dolomite reaction contains magnesium and aluminium and its increased oxygen level indicates that it is a hydrate. Outside the former grain boundaries of the dolomite, no significant amount of magnesium could be detected by elemental mapping. This indicates that the magnesium-containing product of the dolomite reaction formed only within the former grain boundaries, indicating a low mobility of magnesium in the cement matrix, as reported in the literature [1]. Point analyses were performed to further identify the reaction product of the rim inside the former dolomite grains. When the results are plotted as the Mg/Si ration over the Al/Si ratio, the data points describe a linear line for both samples (Fig. 8). This indicates that the reaction product has a fixed Mg/Al ratio (the slope of the line). The small amount of Si present in the analysis originates probably from intermixing with other phases in the analysed volume. The reaction product can therefore be identified as hydrotalcite ($Mg_6Al_2(OH)_{18}{\cdot}3(H_2O)$) [26]. The Mg/Al ratio of the hydrotalcite was approx. 3.2 in sample 60C40D and 2.4 in sample 60C35D5M. In cementitious systems, Mg/Al ratios of approx. 2 are reported [17,26–30]. However, higher Mg/Al ratios are possible as well, as the natural mineral hydrotalcite has a Mg/Al ratio of 3 [31].

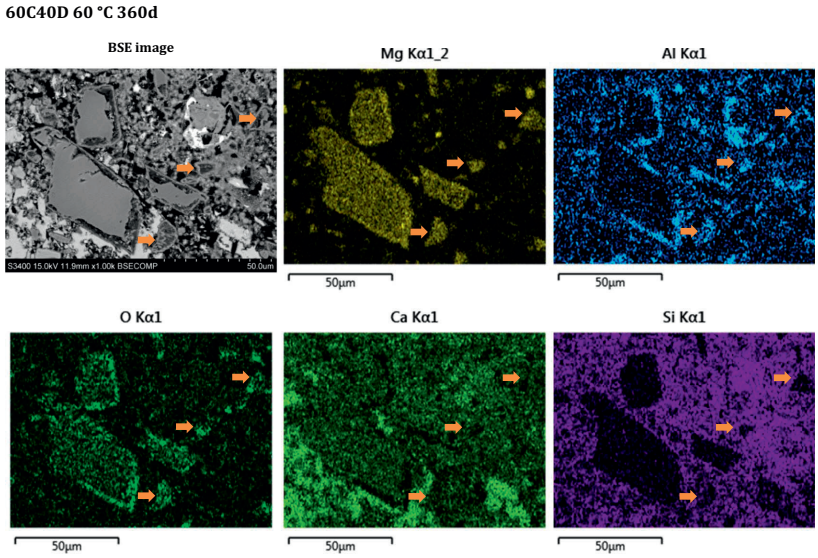

Fig. 4. BSE image and elemental maps of magnesium, aluminium, oxygen, calcium and silicon for the sample 60C40D cured at 60 °C for 360 days. The arrows in the BSE image indicate small fully-reacted dolomite grains.

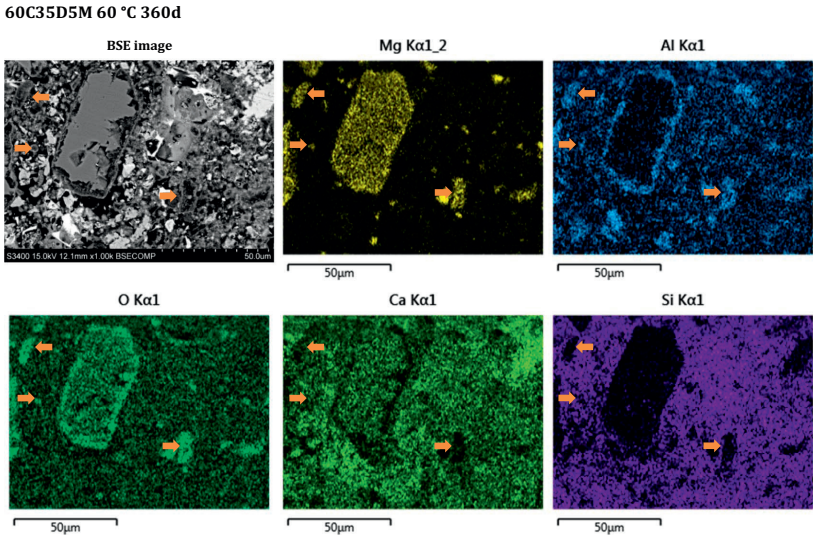

Fig. 5. BSE image and elemental maps of magnesium, aluminium, oxygen, calcium and silicon for the sample 60C35D5M cured at 60 °C for 360 days. The arrows in the BSE image indicate small fully-reacted dolomite grains.

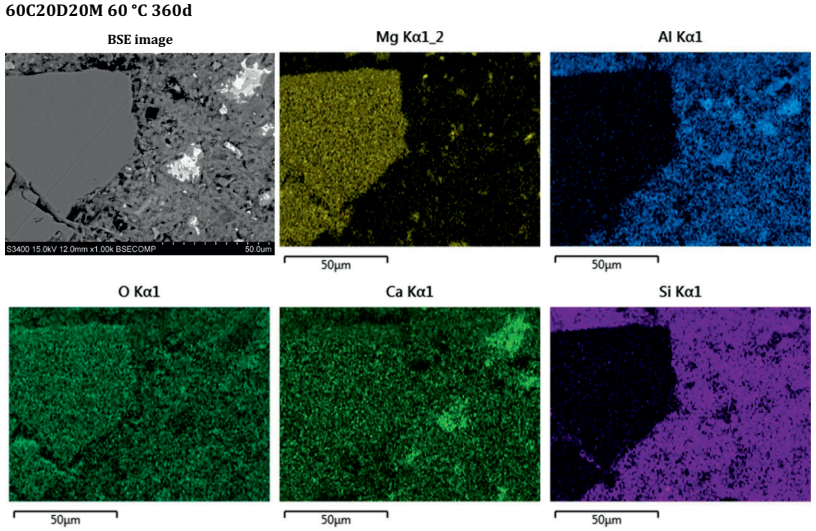

Fig. 6. BSE image and elemental maps of magnesium, aluminium, oxygen, calcium and silicon for the sample 60C20D20M cured at 60 °C for 360 days.

SEM-EDS point analyses also allow us to investigate changes in the C-S-H, e.g. aluminium uptake and changes in the Si/Ca ratio. The dot plots for C-S-H phase of the samples 60C40D, 60C35D5M and 60C20D20M cured at 60 °C are given in Fig. 9. The Al/Si ratio can be determined from the slope of the lower lines, which are framing the C-S-H data clouds. While the addition of 5 wt% metakaolin does not seem to change the C-S-H composition significantly (60C35D5M, Al/Si: 0.04) compared to the 60C40D sample (60C40D, Al/Si = 0), the addition of 20 wt% metakaolin shifted the C-S-H composition to a considerably higher aluminium content (60C20D20M, Al/Si: 0.32). Simultaneously, the Si/Ca ratio is increased as well in this sample.

3.2.2. XRD

The XRD-patterns in the range of 8 to 12°2θ for samples cured for 90, 208 and 360 days at 20 °C are given in Fig. 10, for samples cured at 38 °C in Fig. 11, and for samples cured at 60 °C in Fig. 12. The figures

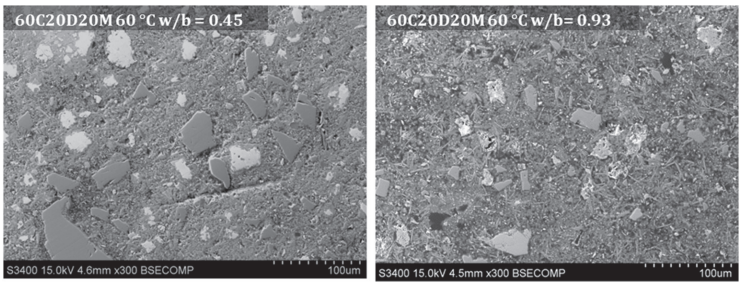

Fig. 7. BSE images of the sample 60C20D20M with w/b ratios of 0.45 and 0.93 cured at 60 °C for 400 days.

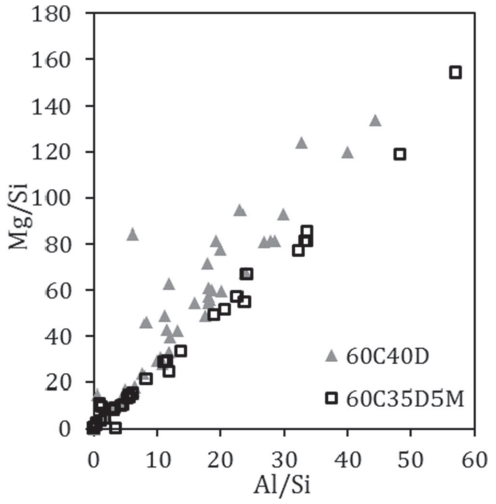

Fig. 8. Mg/Si ratio over the Al/Si ratio for the point analyses of the reaction rims around the dolomite grains of samples cured at 60 °C for 360 days.

indicate the main reflections of ettringite (Et, 9.1°2θ), monosulphate-12H (Ms_{12}, 9.9°2θ), hemicarbonate (Hc, 10.8°2θ), hydrotalcite (Ht, 11.4°2θ) and monocarbonate (Mc, 11.7°2θ). Strätlingite (7.1°2θ) was not detected in any of the samples, irrespective of curing temperature.

For the samples cured at 20 °C, dolomite seems to stabilize the ettringite (Fig. 10), because all the dolomite-containing samples show a clear ettringite peak, but the 100C sample, which contains no dolomite, does not. This is in line with the findings from Zajac et al. [17]. For the 100C sample, the phases observed are monosulphate and some hemicarbonate, the latter possibly formed by carbonation during queuing in the diffractometer. In the 60C40D sample, monocarbonate is the main AFm phase. The sample containing 5 wt% metakaolin (60C35D5M) has a phase composition similar to the 60C40D sample. When the metakaolin content is increased, e.g. from 5 to 20% (60C35D5M to 60C20D20M), small peaks of hemicarbonate are detected as well. This can be explained by the increased aluminium provided by the metakaolin, which lowers the CO_2/Al_2O_3 ratio and leads to the formation of hemicarbonate [32]. However, the hemicarbonate peaks decrease over time due to the slow reaction of the dolomite, which slowly increases the CO_2/Al_2O_3 ratio in the sample which stabilizes monocarbonate over hemicarbonate. Additionally, there is a decrease in the intensity of the AFm peaks in the XRD-pattern. This could be due to increased uptake of Al by C-S-H with increased metakaolin content, as shown by SEM-EDS in Fig. 9, which would leave less aluminium to form AFm phases. Hydrotalcite showed a shoulder on the low-angle side of the monocarbonate peaks at 20 °C but no clear peaks.

The samples cured at 38 °C (Fig. 11) show similar phase assemblages to those of the samples cured at 20 °C. In the 60C40D sample, the monocarbonate observed is partially replaced by hydrotalcite over time. The sample containing 5 wt% metakaolin (60C35D5M) has a similar phase composition to that of the 60C40D sample, but the hydrotalcite appears not as a clear peak, but rather as a shoulder on the monocarbonate peak.

At 60 °C (Fig. 12), the stable phases differ significantly from those at 20 °C and 38 °C. The ettringite peak is not observed because this phase is not stable at 60 °C [33]. The 100C sample does show small peaks of hemicarbonate. The main diffraction peak observed for the 60C40D sample is hydrotalcite, already present from 90 days of hydration on, and no monocarbonate is detected. When 5 wt% of metakaolin is added (60C35D5M), hemicarbonate is observed in addition to the hydrotalcite after 90 days, but it transforms to hydrotalcite at later ages. With metakaolin additions of 10 wt%, monosulphate is detected together with monocarbonate, and only a small hydrotalcite shoulder is observed after 1 year of curing. At higher metakaolin levels, the monocarbonate is replaced by hemicarbonate. Again, this could be due to the additional metakaolin, which provides more Al_2O_3 and reduces the CO_2/Al_2O_3 ratio [32].

Clear peaks of hydrotalcite can only be observed with XRD in samples containing dolomite with a relatively low metakaolin content (< 10 wt%) cured at elevated temperatures (38 °C and especially at 60 °C). When metakaolin additions are high, or when the samples are cued at 20 °C, hydrotalcite was not observable as a peak but as a small shoulder at the low-angle side of the monocarbonate peak.

The hydrotalcite observed using XRD originates from the dolomite reaction because analogue samples containing limestone do not show hydrotalcite-related reflections even after curing for 1 year at 60 °C (Fig. 13). The XRD plots in Fig. 13 also do not show clear peaks of carbonate AFm phases. This can either be explained by the fact that they are not stable, or that they are less crystalline and therefore X-ray amorphous at such a high curing temperature.

Fig. 14 shows the XRD-patterns for 60C20D20M samples prepared with the two different w/b ratios. No hydrotalcite peaks were detected after 400 days of curing. This is in line with the observations from SEM-EDS that a high w/b ratio was not able to enhance the dolomite reaction of the 60C20D20M sample.

3.2.3. TGA

Fig. 15 shows the DTG curves for samples 60C40D and 60C40L after curing for 1 year at 60 °C. Based on the XRD and SEM analysis, we would expect a considerable amount of hydrotalcite to have formed in 60C40D, but not in 60C40L. Hydrotalcite is reported to decompose in two steps during a TGA measurement. The first weight loss related to hydrotalcite is observed at approx. 220 °C and the second weight loss at

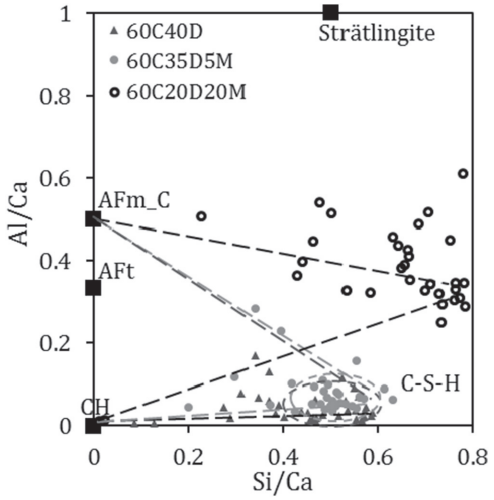

Fig. 9. Al/Ca ratio over the Si/Ca ratio for the point analyses of the matrix of samples cured at 60 °C for 360 days.

approx. 380 °C [21]. These two steps appear as peaks in the DTG curves for the sample 60C40D and are shown in Fig. 15. Moreover, it should be noted that small peaks of AFm phases are detected in the DTG curves of the samples 100C and 60C40L. This confirms the findings with XRD, which indicated that the AFm phases in the samples cured at 60 °C are probably X-ray amorphous.

In Fig. 16 the differences between the samples containing dolomite and limestone with regard to the summed hydrotalcite weight losses of both of its weight loss steps are plotted for the various compositions and curing temperatures. This is done to eliminate the potential impact from Portland cement. The Portland cement used contains significant amounts of magnesium (Table 1) and might also cause a weight loss in the temperature range of hydrotalcite decomposition, as shown in Fig. 15 for the sample 60C40L. So, positive values indicate a higher weight loss in the hydrotalcite temperature range for samples containing dolomite than for those containing limestone. It should be noted that, due to the probability of overlapping weight losses in this temperature interval, the signal recorded might not exclusively originate from the decomposition of hydrotalcite. Taking into account an estimated error of 0.1 wt%, it seems that considerable hydrotalcite formation starts quite late. As Fig. 16 shows, there are no significant differences in the weight losses after 28 days and only a small difference after 90 days between samples containing dolomite and limestone. Only in the 208-day-old and the 360-day-old samples are significantly higher hydrotalcite weight losses detected for samples containing dolomite than for those containing limestone when cured at 60 °C. The highest value is shown by the sample 60C40D after 360 days of hydration. With the addition of metakaolin, the hydrotalcite weight losses decrease. These observed trends are in good agreement with the XRD results, where the formation of hydrotalcite can be detected after 90 days and especially after 208 and 360 days in samples with low metakaolin additions (< 10 wt%), with the sample 60C40D showing the highest hydrotalcite peaks when cured at elevated temperatures (especially 60 °C).

Portlandite dehydrates between approx. 400 °C and 550 °C, and a clear weight loss can be observed in the DTG signal (Fig. 15). Fig. 17 shows the portlandite content of sample mixes containing various amounts of dolomite or limestone at the temperatures investigated. A

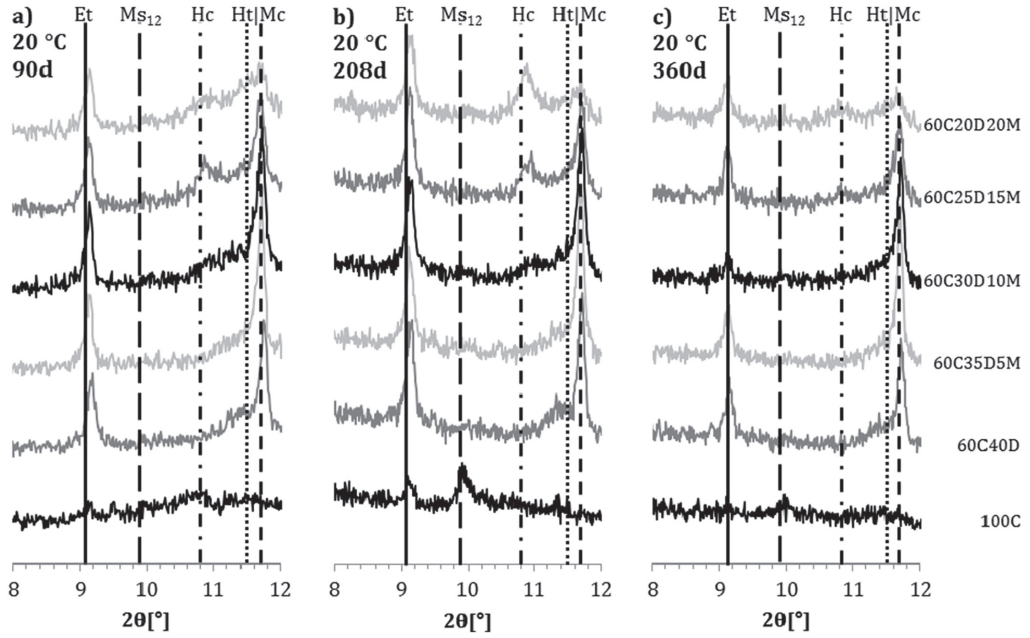

Fig. 10. XRD-patterns of samples containing dolomite and the reference (100C) cured at 20 °C for a) 90 days, b) 208 days and c) 360 days.

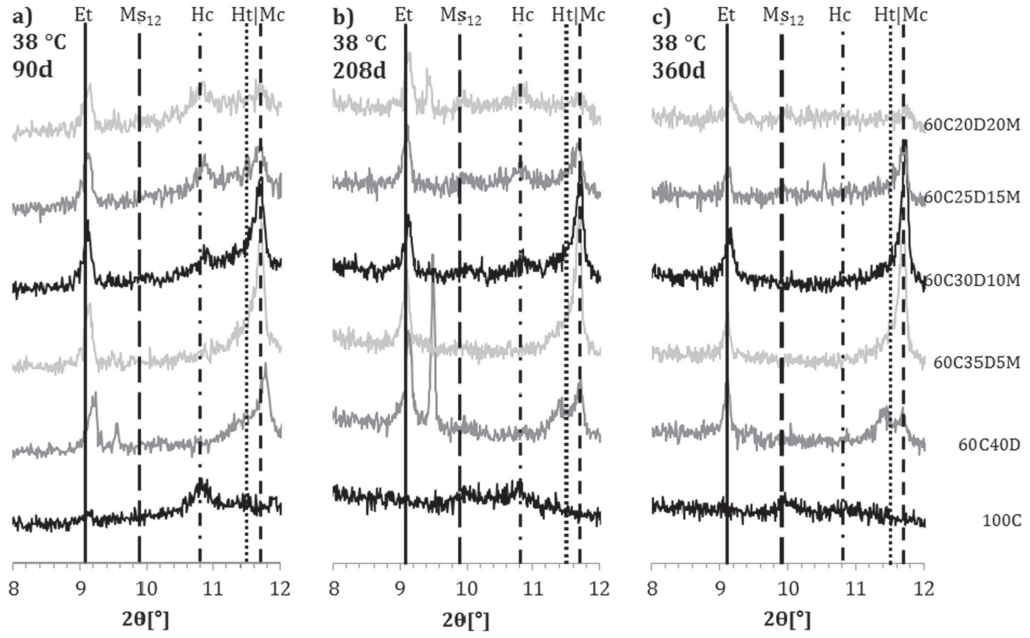

Fig. 11. XRD-patterns of samples containing dolomite and the reference (100C) cured at 38 °C for a) 90 days, b) 208 days and c) 360 days.

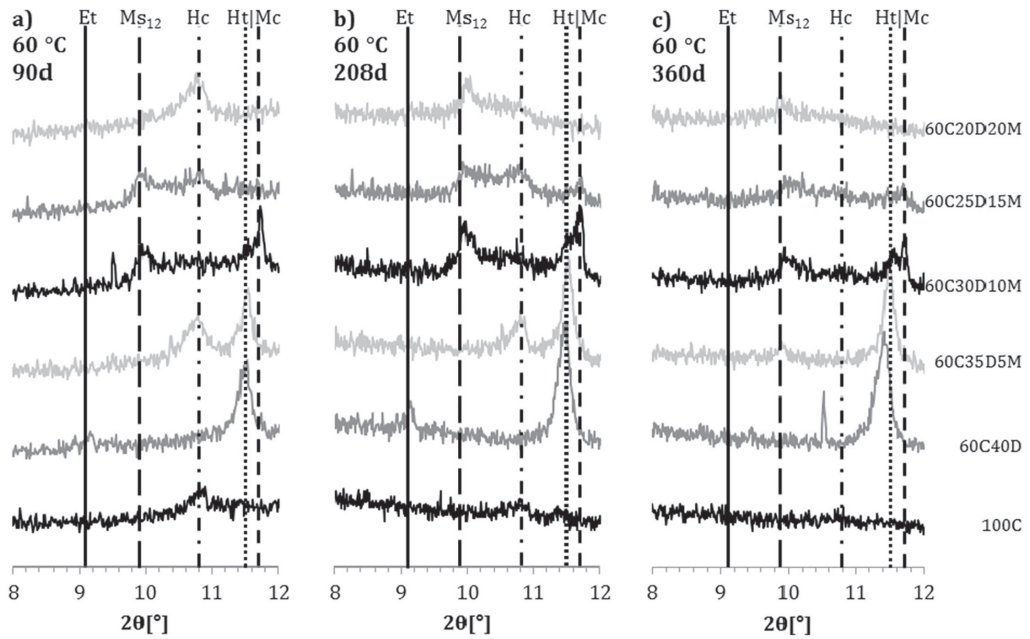

Fig. 12. XRD-patterns of samples containing dolomite and the reference (100C) cured at 60 °C for a) 90 days, b) 208 days and c) 360 days.

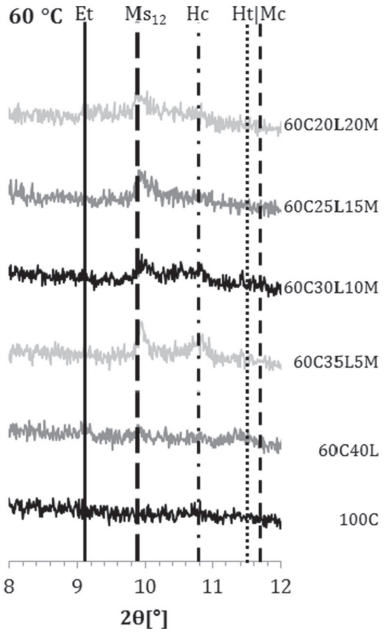

Fig. 13. XRD-patterns of samples containing limestone and the reference (100C) cured at 60 °C for 360 days.

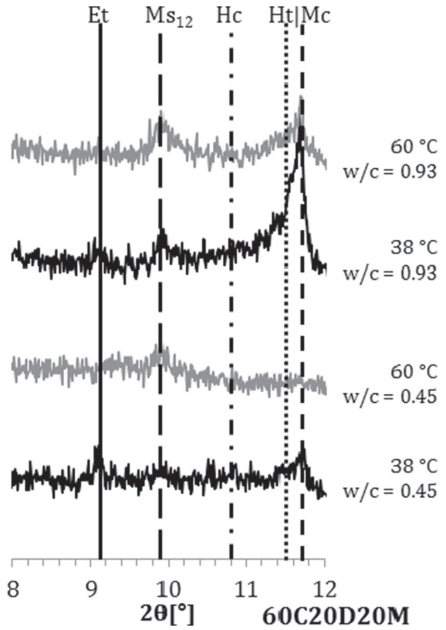

Fig. 14. XRD-patterns of the 60C20D20M samples with a w/b ratio of 0.45 and 0.93, cured at 38 °C and 60 °C for 400 days.

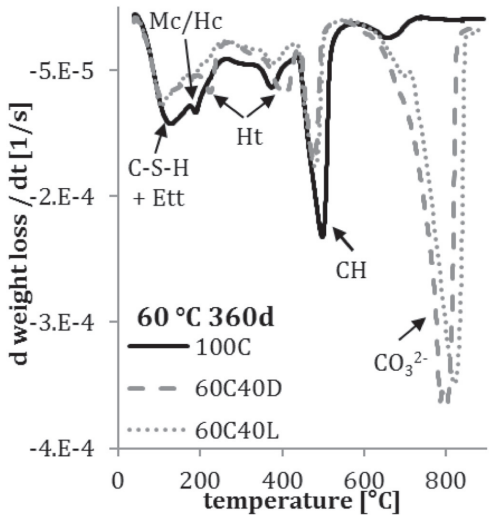

Fig. 15. Differential thermogravimetric (DTG) curves for samples 60C40D, 60C40L and the reference 100C cured at 60 °C for 360 days.

clear reduction can be seen in portlandite with increasing metakaolin content. This is due to the pozzolanic reaction of metakaolin. This reaction is enhanced when the curing temperature is increased. It should be noted that the portlandite content for the samples containing 15 wt% and 20 wt% of metakaolin is similar. This indicates that at metakaolin contents > 10 wt%, its reaction is limited.

Fig. 18 plots the differences in the portlandite content between the samples containing dolomite and limestone (estimated error: 0.5 wt%). Therefore, negative values indicate a lower portlandite content in samples containing dolomite than in those containing limestone. These differences are only visible for compositions where there are also differences in the hydrotalcite weight loss. The sample 60C40D shows significantly lower portlandite content than its limestone equivalent (60C40L) after 208 and 360 days, when cured at 60 °C. This observation indicates that portlandite is consumed during the formation of hydrotalcite from dolomite. This is in-line with descriptions of the reaction of dolomite in the literature [14–16], where the dolomite reaction requires the presence of portlandite.

Fig. 19 shows the portlandite content of the samples 60C20D20M with a w/b ratio of 0.45 and 0.93, both cured at 20 °C, 38 °C and 60 °C for 400 days. In samples with the low w/b ratio, the portlandite content is consumed almost completely when cured at 60 °C, but at lower curing temperatures more portlandite remains. In the samples with the high w/b ratio, the portlandite is completely consumed at all curing temperatures. These results indicate that in the range tested, increasing the w/b ratio enhances the metakaolin reaction.

3.3. MIP

The threshold pore entry diameter and the porosity were estimated from the intrusion curves of the first intrusion cycle of the mercury and are plotted for the various compositions in Fig. 20. Fig. 20 a) shows the results for samples cured at 38 °C for 208 days, Fig. 20 b) for samples cured at 60 °C for 208 days and in Fig. 20 c) for the samples cured at 60 °C for 360 days. The precision of the MIP results was estimated to 20% for the threshold diameter and 1.5% for the porosity according to [34].

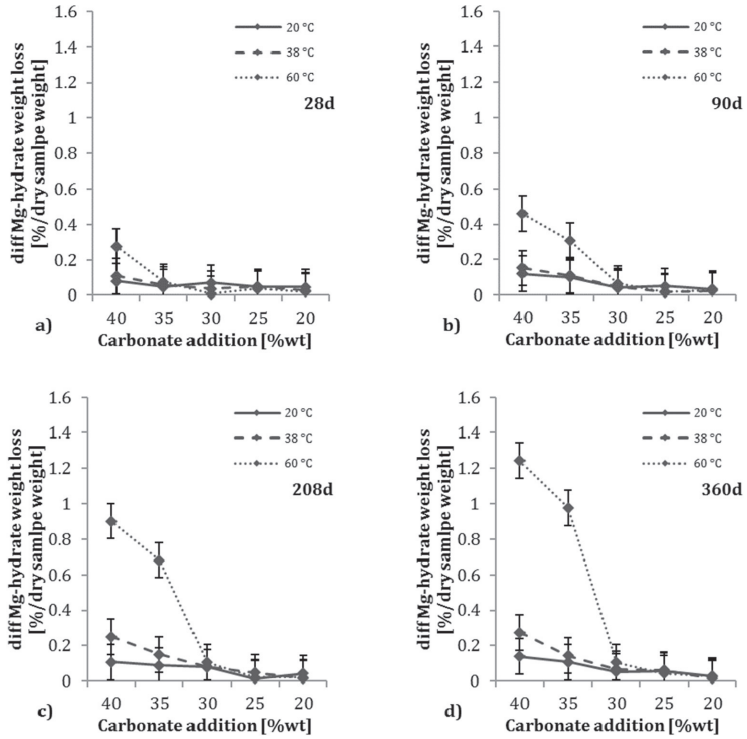

Fig. 16. Development of the difference in Mg-hydrate weight losses between samples containing dolomite and samples containing limestone for the various carbonate additions, cured at 20 °C, 38 °C, and 60 °C for a) 28 days, b) 90 days, c) 208 days, and d) 360 days. It is important to note that, due the broad shape of the peaks and the possible overlapping of weight loss peaks, these weight losses give only an indication about magnesium-containing hydrates decomposing in this temperature region, not necessarily only hydrotalcite.

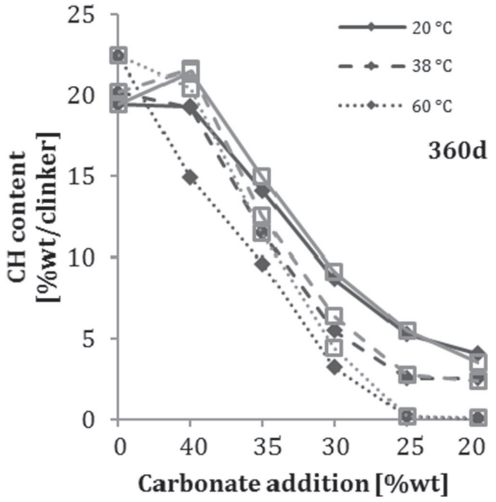

Fig. 17. Development of the portlandite content for the samples containing various amounts of dolomite or limestone in combination with metakaolin and the reference 100C cured at 20 °C, 38 °C and 60 °C for 360 days. Black diamonds indicate the samples containing dolomite and grey squares indicate the samples containing limestone.

Generally, the samples containing dolomite or limestone show similar results. In Fig. 20 b) however, there is a significant difference between the samples containing either 5 wt% of dolomite or limestone, which were cured at 60 °C. In order to elucidate whether this is an effect of hydration or sample preparation, a set of samples cured as well at 60 °C but for 360 days was investigated as well (Fig. 20 c)). After 360 days the samples containing dolomite or limestone show again very similar results. This indicates that the differences observed in Fig. 20 b) are due to sample preparation effects.

If we compare the two curing temperatures (Fig. 20 a & b)), a coarsening effect can be observed at the higher curing temperature. This effect is related to the transformation of ettringite to monosulphate above 48 °C and a densification of the C-S-H phase at elevated temperatures, both resulting in a coarsening of the pore structure [33]. Moreover, an increase in the porosity and the threshold diameter can be observed if we compare the reference 100C with the sample containing 40 wt% of dolomite or limestone at both temperatures. This is in agreement with previous findings [20]. This coarsening effect of added carbonates can be counteracted by the addition of metakaolin, which reduces the threshold diameter as described in the literature [9]. At high metakaolin additions, the threshold pore entry diameter decreases down to values of approx. 0.04 µm for both curing temperatures. The addition of 5 wt% of metakaolin decreases also the porosity compared to the samples only containing dolomite or limestone. However, with additions > 5 wt% metakaolin, there is no further reduction in the porosity.

Fig. 21 shows the threshold pore entry diameter and porosity of the samples prepared with the different w/b ratio of 0.93 or 0.45 cured at 38 °C or 60 °C for 400 days. The threshold diameter and the porosity are

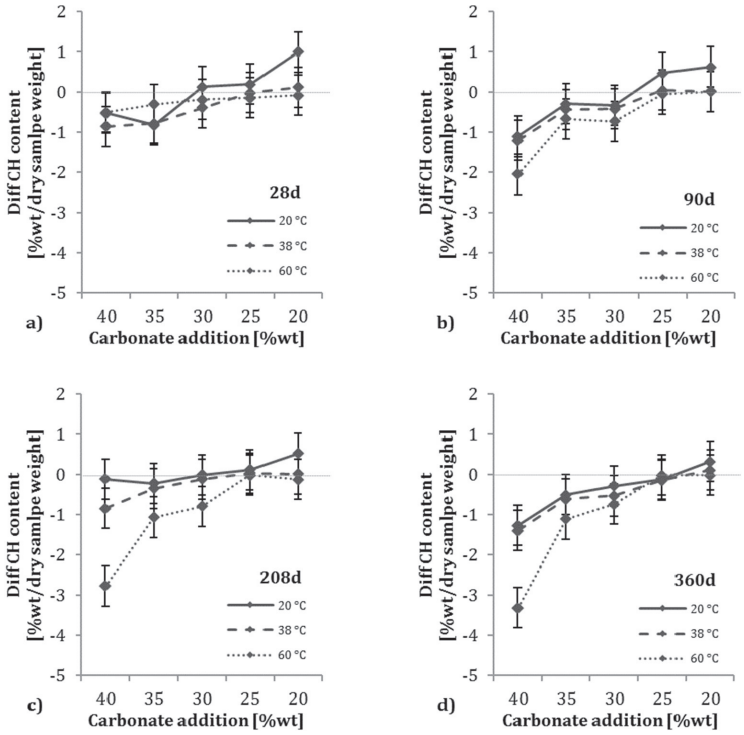

Fig. 18. Development of the difference in the portlandite content between samples containing dolomite and limestone for the various carbonate additions, cured at 20 °C, 38 °C, and 60 °C for a) 28 days, b) 90 days, c) 208 days, and d) 360 days.

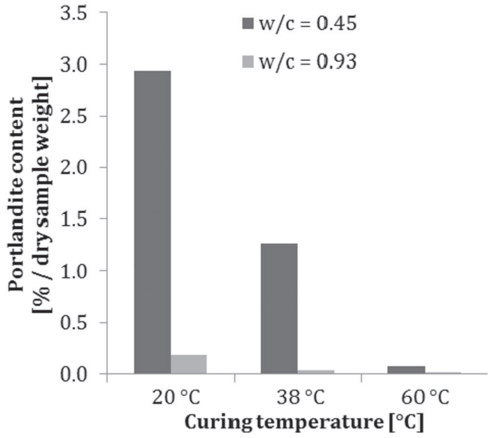

Fig. 19. Portlandite content of samples with a w/b ratio of 0.45 and 0.93 cured at 20 °C, 38 °C and 60 °C for 400 days.

increased for the samples prepared with the high w/b ratio compared to the samples with the low w/b ratio. This coarsening effect of the increased w/b ratio is expected and in good agreement with the microstructural changes between samples with a high or low w/b ratio as observed in the BSE images (Fig. 7). While the threshold diameter is increased for the samples cured at 60 °C compared to 38 °C for both w/b ratios, the porosity is rather similar for the samples cured at 60 °C or 38 °C for both w/b ratios and no considerable increase in porosity can be observed.

3.4. Well-hydrated samples exposed to additional water and or portlandite

Fig. 22 shows the DTG curves of the sample 60C20D20M + H_2O, which was exposed to 30 wt% additional water after 28 and 90 days of exposure at 60 °C, compared to the same sample prior exposure. The sample 60C20D20M + H_2O was used as a reference to the sample 60C20D20M + CH, which was exposed to additional 30 wt% water and 30 wt% portlandite. As the reference samples after 28 and 90 days of exposure show almost completely the same curves as the sample prior exposure, we assume that they were stable during the whole exposure time. Consequently, any phase changes observed in the sample 60C20D20M + CH are due to the addition of portlandite and not due to the addition of water.

Fig. 23 shows the DTG curves of the sample 60C20D20M + CH cured for 28 and 90 days at 60 °C compared to the sample prior exposure. At low temperatures (40–300 °C), the samples exposed to portlandite are shifted upwards compared to the sample prior exposure and show as well a decreased peak in the temperature range of the dolomite decomposition. This can be explained by the dilution effect of the hydrates and the dolomite in the samples where 30 wt% of portlandite was added. Because of this addition, these samples also show a clear peak in the temperature interval of the portlandite decomposition. The two peaks related to the decomposition of hydrotalcite increased with exposure time in the samples exposed to portlandite compared to the

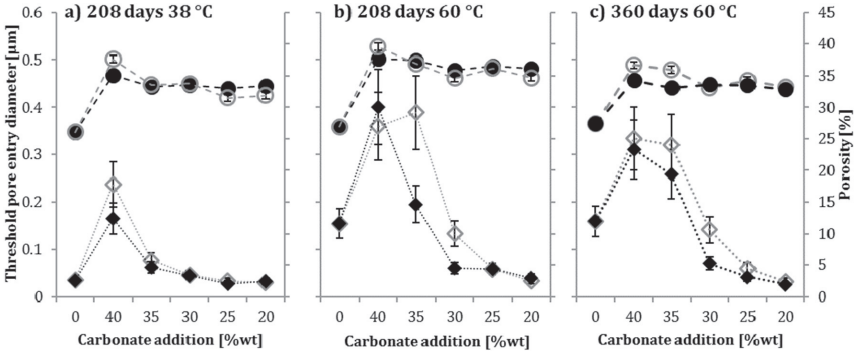

Fig. 20. Development of the threshold pore entry diameter (diamonds) and porosity (dots) for samples containing dolomite (black filled) or limestone (grey hollow) cured for a) 208 days at 38 °C, b) 208 days at 60 °C and c) 360 days at 60 °C.

sample prior exposure. This indicates the formation of hydrotalcite in these samples. The samples exposed to portlandite also show an additional peak in the AFm-temperature region, probably due to the formation of monosulphate. This peak seems to decrease with the exposure time. The increase in the hydrotalcite peak simultaneously with the decrease in the monosulphate peak indicates that due to the reaction of dolomite over time in the samples exposed to portlandite, the monosulphate transforms to hydrotalcite as it is thermodynamically more stable [35].

Fig. 24 shows the XRD-patterns of the samples 60C20D20M + CH and 60C20D20M + H_2O after 90 days of exposure compared to the sample prior exposure. While the sample prior exposure and the reference sample show the same phase assemblage, the sample 60C20D20M + CH shows additional peaks. In this sample, besides the portlandite peak due to the exposure, clear peaks of monosulphate and hydrotalcite are visible. These results are in good correlation with the observations made in the DTG curves of these samples.

4. Discussion

The results of this study show that dolomite can react significantly when added to Portland cement, depending on the curing age, temperature and the metakaolin content of the samples. The reaction products and the limitations of this reaction are discussed in the following.

4.1. What are the products of the dolomite reaction?

The elemental maps obtained from SEM-EDS analysis show that when dolomite reacts magnesium does not move outside the former grain boundary of the dolomite, probably due to a limited mobility of magnesium in high pH environments [1]. So, the magnesium-containing reaction products of dolomite form a reaction rim within the former dolomite grain boundaries. The products in the reaction rim contain magnesium, aluminium and show a higher oxygen content. The high oxygen content indicates that the reaction products are hydrates. No silicon can be found in the rims and the calcium content is less than in the original dolomite grain. The lack of silicon in the rims excludes M-S-H as a reaction product.

EDS point analysis of the reaction rims indicates the presence of hydrotalcite, with a Mg/Al ratio of approx. 2.4–3.2 depending on the metakaolin content of the binder. The formation of hydrotalcite was confirmed by XRD, where peaks of hydrotalcite could be found in samples where significant amounts of dolomite have reacted. XRD did not detect clear peaks of brucite in any samples. TGA analysis seems to indicate that the weight losses in the temperature range of hydrotalcite correlate to the amount of dolomite reacted.

We conclude that hydrotalcite is the only magnesium-containing product of the dolomite reaction and it forms in reaction rims within the former dolomite grains in samples cured at elevated temperatures (60 °C).

TGA and XRD also showed that the addition of dolomite results in the formation of carbonate AFm phases and therefore ettringite

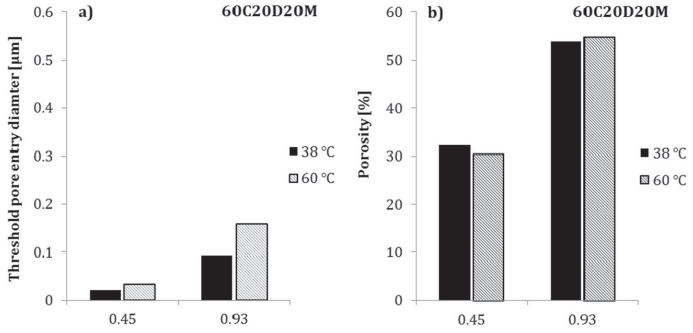

Fig. 21. The threshold pore entry diameter (a) and the porosity (b) for the sample 60C20D20M prepared with a high (0.93) or low (0.45) w/b ratio cured at 38 °C or 60 °C for 400 days.

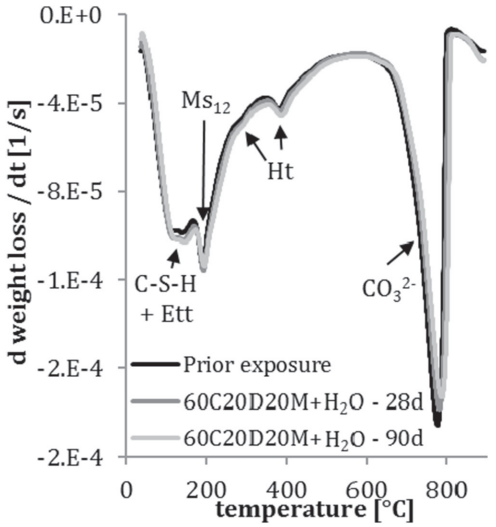

Fig. 22. Differential thermogravimetric (DTG) curves for well-hydrated samples 60C20D20M exposed to 30 wt% additional water for 28 or 90 days at 60 °C and the sample prior exposure.

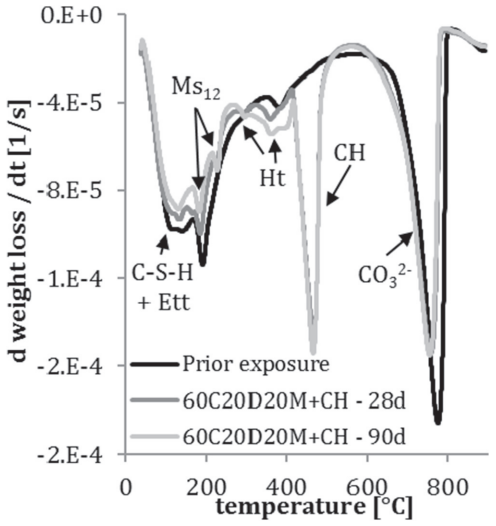

Fig. 23. Differential thermogravimetric (DTG) curves for well-hydrated samples 60C20D20M exposed to 30 wt% additional water and 30 wt% portlandite for 28 or 90 days at 60 °C and the sample prior exposure.

stabilization. This means that the dolomite delivers carbonates to the system, which can form carbonate AFm phases. This is only observable in samples where ettringite is stable, hence in samples cured at 20 °C or 38 °C. Calcite might also be formed due to the reaction of dolomite. XRD detected calcite in the samples, but we could not confirm whether this calcite was formed during the dedolomitization reaction. This is because the dolomite used already contains approx. 6 wt% of calcite, which might partially also participate in the formation of carbonate AFm phases. SEM-EDS cannot differentiate between portlandite and calcite, so the potential replacement of portlandite with calcite during the dolomite reaction cannot be identified.

These findings are in agreement with Zajac et al., who showed that in the presence of other ions dolomite reaction results in the formation of hydrotalcite and carbonate AFm phases, which lead to the stabilization of ettringite [17].

4.2. What limits the hydrotalcite formation?

As described above, hydrotalcite forms slowly over time in samples containing dolomite which have been cured at 60 °C, if they contain < 10 wt% of metakaolin.

To elucidate the possible limitations of the hydrotalcite formation, Eq. (1) gives an idealized reaction based on the observations in this study. In this reaction, dolomite reacts with a source of aluminium, here given as $Al(OH)_3$, and portlandite to form hydrotalcite and calcite. This reaction inside the reaction rims around the dolomite grains is illustrated in Fig. 25. The calcite formed might then precipitate in the matrix or in finely intermixed with the C-S-H in the rim, which indicates the original grain boundary of the dolomite. It might also partially contribute to the formation of hemi- or monocarbonate. The hydrotalcite formation could be chemically limited by any of the reactants given in Eq. (1). Taking into account the refinement of the pore structure due to the metakaolin addition, there might be a physical limitation as well.

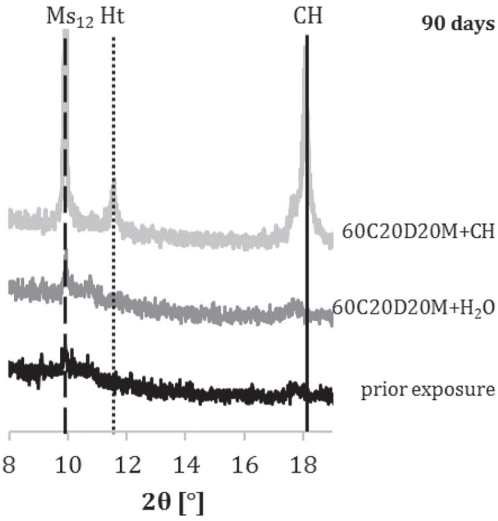

Fig. 24. XRD-patterns of the well-hydrated samples 60C20D20M exposed to 30 wt% of additional portlandite and or water for 90 days at 60 °C and the sample prior exposure.

$$6CaMg(CO_3)_2 + 2Al(OH)_3 + 6Ca(OH)_2 + 9H_2O \rightarrow Mg_6Al_2(OH)_{18}{\cdot}3(H_2O) + 12CaCO_3\ (Hc/Mc) \quad (1)$$

In the following, we discuss the various possible limitations in detail.

4.2.1. Pore space as a physical limitation

The MIP results for the samples cured at 60 °C (Fig. 20) show that while the porosity is not decreased, the threshold diameter is

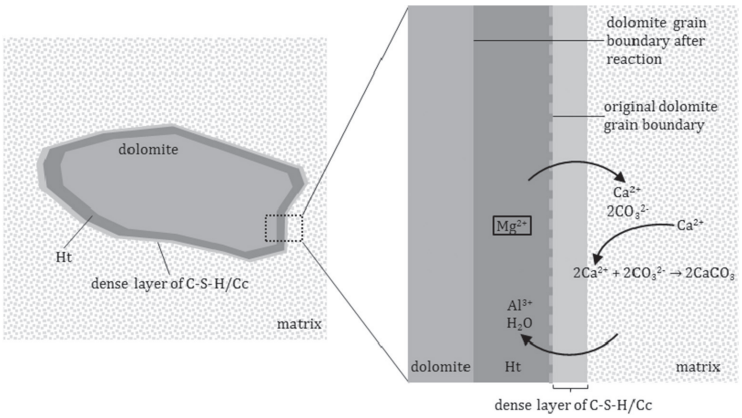

Fig. 25. Schematic illustration of the hydrotalcite formation in the reaction rims around the dolomite grains.

significantly refined with the addition of metakaolin. The threshold pore diameter, which is an important parameter for transport in the pore system [36], is reduced from 0.4 µm, for the samples only containing dolomite but no metakaolin, to 0.04 µm, for the samples with the highest metakaolin content. Durdzinski reported the refinement of the pore structure due to the additions of fine and reactive SCMs to be the major factor for a decreased degree of reaction. This observation was explained with the restricted transport and the hindered crystallization in fine pores compared to coarse pores [34]. This is in agreement with the TGA results, which show a limited further reaction of metakaolin for additions of metakaolin higher than 10 wt% (see Fig. 17). This possible hindrance of further reactions in dense systems has been reported for metakaolin or other SCMs and UHPC previously [34,37,38].

The MIP results also show that curing at 60 °C considerably coarsens the pore structure. So, in addition to the higher reactivity of dolomite at 60 °C than at 38 °C reported before [14–17], the coarser pore structure might also facilitate the ongoing reactions due to the facilitation of transport and crystallization.

To elucidate the effect of the pore space, we prepared samples with high amounts of metakaolin (20 wt%) and a high w/b ratio (0.93). The XRD plots (Fig. 14) show that, despite the coarse pore structure of these samples, no hydrotalcite was formed, and the BSE images also showed that the dolomite did not react (Fig. 7). We, therefore, conclude that the limited pore space in metakaolin-rich samples does not act as a major limitation on the dolomite reaction in the investigated systems.

4.2.2. Aluminium availability

Fig. 25 shows a schematic illustration of the hydrotalcite formation inside the former dolomite grain boundary including the necessary transport of ions. Aluminium is needed for hydrotalcite to form, see Eq. (1) and Fig. 25. The addition of metakaolin to the system provides additional aluminium. Besides the formation of hydrotalcite, this additional aluminium can result in the increased formation of AFm phases shown in XRD (see Fig. 11), and the uptake of aluminium in the C-S-H shown in SEM-EDS (see Fig. 9). Hydrotalcite will win the competition for the aluminium over AFm phases because it is thermodynamically more stable [35], but we cannot reach a conclusion on the competition with the Al-uptake in the C-S-H, due to limited thermodynamic data. When comparing the Al/Si ratios of the C-S-H (Fig. 9) to the Al/Si ratios reported in the literature, we can see that for low metakaolin additions (5 wt%), our values are somewhat lower, and for high metakaolin additions, they are higher than reported in the literature [12]. Our data does therefore not fit the proposed fitting equation by Dai et al. [12]. This might be explained by the formation of hydrotalcite in the samples containing lower amounts of metakaolin, which was shown to reduce the aluminium content of the C-S-H [17]. If aluminium does act as a limiting factor in the hydrotalcite formation reaction, the addition of aluminium through the addition of metakaolin should increase the amount of hydrotalcite formed. A similar effect of additional aluminium has been reported on the formation of carbonate AFm phases [5–8].

However, it was shown that with the addition of 5 wt% of metakaolin there is no increase in the amount of hydrotalcite formed. Consequently, we can conclude that any possible positive effect from the additional aluminium is unable to compensate for the negative effects of metakaolin addition on hydrotalcite formation. We, therefore, conclude that the availability of aluminium does not act as a major limitation on the dolomite reaction in the investigated systems.

4.2.3. Dolomite dissolution

Hydrotalcite is a magnesium-containing hydrate. The availability of magnesium and hence the dissolution of dolomite are required for hydrotalcite to form. This is illustrated in Fig. 25, where the formation of a reaction rim is indicated, which contains the magnesium from the dolomite dissolution. The dissolution of dolomite has been reported to be slow. However, it was shown to be accelerated by increasing the curing temperature from 25 °C to 60 °C [14–17]. This is in good agreement with our results, as we observed an increased reaction degree of dolomite when cured at 60 °C compared to 38 °C or 20 °C. In samples cured at 60 °C with low or no metakaolin content, QXRD showed that significant amounts of dolomite have reacted after 360 days of curing. This also explains the observed hydrotalcite formation only in samples cured at elevated temperatures.

However, only samples with low or no metakaolin addition show significant dolomite reaction and hydrotalcite formation when cured at 60 °C. This indicates that the dissolution of dolomite is additionally limited by another factor besides temperature.

Eq. (1) gives portlandite as one of the reactants for the hydrotalcite formation. Even though hydrotalcite ($Mg_6Al_2(OH)_{18}{\cdot}3(H_2O)$) does not contain calcium, the formation of hydrotalcite is associated with the consumption of portlandite (Fig. 18) to form calcite (as indicated in Fig. 25), similarly to the reported dedolomitization reaction, where brucite is formed [14–16]. To illustrate the consumption of portlandite due to the reaction of dolomite, we plotted the difference in portlandite weight loss between samples containing dolomite and samples containing limestone in Fig. 18. Samples containing dolomite show significantly lower portlandite content than samples containing limestone. This is especially visible at the elevated curing temperatures and low

metakaolin additions, which cause significant dolomite reaction (Fig. 2) and consequent hydrotalcite formation (Fig. 16). The need for portlandite by the reaction of dolomite can be explained by the difference between dolomite, which contains 2 mol CO_3^{2-}/mol dolomite, and calcite, which contains 1 mol of CO_3^{2-}/mol of calcite. Therefore, to make the magnesium available for reaction to hydrotalcite, calcium is needed to compensate for the other carbonate ion from the dolomite, similar as for the dedolomitization reaction in which brucite is formed. The experimental techniques in this study did not allow the differentiation between carbonate-containing hydrotalcite and a carbonate-free hydrotalcite. However, as long as the hydrotalcite contains < 1 mol of CO_3^{2-}/mol of hydrotalcite [19,39–42], additional calcium is needed in the reaction to compensate for the rest of the carbonate ions. This is also indicated in Fig. 25 by the transport of CO_3^{2-} ions out of the reaction rims.

The portlandite availability varies with the metakaolin content. A higher metakaolin content leads to an increased consumption of portlandite due to its pozzolanic reaction, as TGA shows in Fig. 17. As portlandite is also consumed in the reaction of dolomite and the formation of hydrotalcite, it is therefore a possible limitation to this reaction in samples where most or all of the portlandite has already been consumed in the fast pozzolanic reaction of metakaolin.

It was shown from the results of the samples prepared with the various w/b ratios that the higher w/b ratio enhances not only the Portland cement reaction but also the metakaolin reaction. This led to the complete consumption of the portlandite in the system (Fig. 19). Because metakaolin addition refines the pore structure and consumes Portlandite at the same time, these two factors are not completely distinguishable. Because of this, a part of the samples 60C20D20M cured at 60 °C for 1 year and 9 months, were exposed to 30 wt% portlandite and or 30 wt% of additional water for up to 90 days. While the samples, which were exposed only to water, did not change during exposure, the samples exposed to water and portlandite showed the formation of hydrotalcite over time. It can be concluded that in samples, which contain high amounts of metakaolin (20 wt%) and therefore have a refined pore structure, the formation of hydrotalcite can be observed as long as sufficient portlandite is available. This confirms the lack of portlandite as a limiting factor due to the correlation between portlandite consumption and hydrotalcite formation, independently of the pore structure. The refined pore structure in the samples containing high amounts of metakaolin might slow down the reactions but is not inhibiting the formation of hydrotalcite.

5. Conclusion

Cement pastes, in which 40 wt% of Portland cement clinker was replaced by either dolomite or limestone in combination with 0–20 wt % metakaolin, were investigated with regard to their phase assemblage and microstructure. The samples were cured at 20 °C, 38 °C and 60 °C up to 360 days. Additionally, samples with a high w/b ratio (0.93) were prepared and investigated after 400 days of curing and parts of the samples containing 20 wt% of metakaolin were exposed to additional portlandite and or water for up to 90 days. The following conclusions are made based on the investigations:

Within 360 days, significant amounts of the added dolomite react at low metakaolin additions (< 10%) and an elevated curing temperature (60 °C). As a result of the reaction, magnesium and carbonates are supplied to the system. The carbonates originating from the dolomite stabilize ettringite due to the formation of carbonate AFm phases. During the dolomite reaction, portlandite is consumed and hydrotalcite is formed. Hydrotalcite ($Mg_6Al_2(OH)_{18}{\cdot}3(H_2O)$) is the only magnesium-containing reaction product from the dolomite reaction. Neither M-S-H nor brucite were detected in any samples investigated.

To check whether additional aluminium results in additional hydrotalcite formation, up to 20 wt% of metakaolin was added to the system. However, instead of promoting the hydrotalcite formation, the addition of > 5 wt% metakaolin inhibited the dolomite reaction and therefore also the hydrotalcite formation. Thus, aluminium availability is no major limitation for hydrotalcite formation.

The addition of metakaolin influenced the system in more ways than solely providing aluminium. It also consumes portlandite during its pozzolanic reaction and simultaneously refines the pore structure. From the results of the samples containing 20 wt% metakaolin which were exposed to additional portlandite and or water, we can conclude that the pore structure refinement is not inhibiting the formation of hydrotalcite, but might slow reactions down. By investigating the samples with the high w/b ratios, the absence of portlandite in high-metakaolin samples could be confirmed to inhibit the reaction of dolomite and the formation of hydrotalcite independently of any impact from the pore structure.

Acknowledgements

The authors would like to thank the Norwegian Research Council and the Heidelberg Technology Center (industrial PhD programme, project number: 241637) for their financial support.

We are also very grateful for the helpful discussion with Christopher Stabler on the dolomite quantification by XRD Rietveld analysis.

References

[1] K.L. Scrivener, M.J. Vanderley, E.M. Gartner, Eco-efficient Cements: Potential, Economically Viable Solutions for a Low-CO_2 Cement-based Materials Industry, United Nations Environment Program – Building and Climate Initiative (UNEP-SBCI), Paris, 2016.
[2] EN 197-1, Cement, Part I: Composition, specifications and conformity criteria for common cements, European Committee for Standardization, Brussels, 2011.
[3] T. Matschei, B. Lothenbach, F.P. Glasser, The role of calcium carbonate in cement hydration, Cem. Concr. Res. 37 (2007) 551–558.
[4] B. Lothenbach, G. Le Saout, E. Gallucci, K.L. Scrivener, Influence of limestone on the hydration of Portland cements, Cem. Concr. Res. 38 (2008) 848–860.
[5] K. De Weerdt, K.O. Kjellsen, E. Sellevold, H. Justnes, Synergy between fly ash and limestone powder in ternary cements, Cem. Concr. Compos. 33 (2011) 30–38.
[6] M. Antoni, J. Rossen, F. Martirena, K.L. Scrivener, Cement substitution by a combination of metakaolin and limestone, Cem. Concr. Res. 42 (2012) 1579–1589.
[7] D. Nied, C. Stabler, M. Zajac, Assessing the synergistic effect of limestone and metakaolin, in: K.L. Scrivener, A. Favier (Eds.), Calcined Clays for Sustainable Concrete: Proceedings of the 1st International Conference on Calcined Clays for Sustainable Concrete, 2015, pp. 245–251.
[8] G. Puerta-Falla, M. Balonis, G. Le Saout, N. Neithalath, G. Sant, The influence of metakaolin on limestone reactivity in cementitious materials, in: K.L. Scrivener, A. Favier (Eds.), Calcined Clays for Sustainable Concrete: Proceedings of the 1st International Conference on Calcined Clays for Sustainable Concrete, 2015, pp. 11–19.
[9] T.R. Jones, Metakaolin as a pozzolanic addition to concrete, in: J. Bensted, P. Barnes (Eds.), Structure and Performance of Cements, 2nd ed., Taylor & Francis, New York, 2002, pp. 372–398.
[10] E. L'Hôpital, B. Lothenbach, G. Le Saout, D.A. Kulik, K.L. Scrivener, Incorporation of aluminium in calcium-silicate-hydrates, Cem. Concr. Res. 75 (2015) 91–103.
[11] I.G. Richardson, The nature of C-S-H in hardened cements, Cem. Concr. Res. 29 (1999) 1131–1147.
[12] Z. Dai, T.T. Tran, J. Skibsted, H. Jennings, Aluminum incorporation in the C-S-H phase of white Portland cement-metakaolin blends studied by ^{27}Al and ^{29}Si MAS NMR spectroscopy, J. Am. Ceram. Soc. 97 (2014) 2662–2671.
[13] S. Schöne, W. Dienemann, E. Wagner, Portland dolomite cements as alternative to Portland limestone cements, Proceedings of the 13th International Congress on the Chemistry of Cement, Madrid, 2011.
[14] S. Galí, C. Ayora, P. Alfonso, E. Tauler, M. Labrador, Kinetics of dolomite-portlandite reaction: application to Portland cement concrete, Cem. Concr. Res. 31 (2001) 933–939.
[15] E. Garcia, P. Alfonso, M. Labrador, S. Galí, Dedolomitization in different alkaline media: application to Portland cement paste, Cem. Concr. Res. 33 (2003) 1443–1448.
[16] X. Zhang, F.P. Glasser, K.L. Scrivener, Reaction kinetics of dolomite and portlandite, Cem. Concr. Res. 66 (2014) 11–18.
[17] M. Zajac, S.K. Bremseth, M. Whitehead, M. Ben Haha, Effect of $CaMg(CO_3)_2$ on hydrate assemblages and mechanical properties of hydrated cement pastes at 40 °C and 60 °C, Cem. Concr. Res. 65 (2014) 21–29.
[18] M. Zajac, W. Dienemann, G. Bolte, Comparative experimental and virtual investigations of the influence of calcium and magnesium carbonates on reacting cement, Proceedings of the 13th International Congress on the Chemistry of Cement, Madrid, 2011.
[19] R.J. Myers, B. Lothenbach, S.A. Bernal, J.L. Provis, Thermodynamic modelling of alkali-activated slag cements, Appl. Geochem. 61 (2015) 233–247.

[20] J. Xu, D. Lu, S. Zhang, K. Ling, Z. Xu, Pore structures of mortars with dolomite and limestone powders cured at various temperatures, J. Chin. Ceram. Soc. 45 (2017) 268–273.
[21] B. Lothenbach, P. Durdzinski, K. De Weerdt, Thermogravimetric analysis, in: K.L. Scrivener, R. Snellings, B. Lothenbach (Eds.), A Practical Guide to Microstructural Analysis of Cementitious Materials, CRC Press Taylor & Francis Group, Boca Raton, 2015, pp. 177–211.
[22] B.H. O'Connor, M.D. Raven, Application of the Rietveld refinement procedure in assaying powdered mixtures, Powder Diffract. 3 (1988) 2–6.
[23] D. Jansen, F. Goetz-Neunhoeffer, C. Stabler, J. Neubauer, A remastered external standard method applied to the quantification of early OPC hydration, Cem. Concr. Res. 41 (2011) 602–608.
[24] S.T. Bergold, F. Goetz-Neunhoeffer, J. Neubauer, Quantitative analysis of C–S–H in hydrating alite pastes by in-situ XRD, Cem. Concr. Res. 53 (2013) 119–126.
[25] M.M. Canut, M.R. Geiker, Impact of curing on the porosity development of cement pastes with and without slag, Proceedings of the 13th International Congress on the Chemistry of Cement, Madrid, 2011.
[26] M. Ben Haha, B. Lothenbach, G. Le Saout, F. Winnefeld, Influence of slag chemistry on the hydration of alkali-activated blast-furnace slag – part I: effect of MgO, Cem. Concr. Res. 41 (2011) 955–963.
[27] S. Adu-Amankwah, L. Black, M. Zajac, The effect of sulphates on limestone containing composite cements, in: University of Aberdeen (Ed.), 35th Cement and Concrete Science Conference, 2015.
[28] G. Fornasari, R. Glöckler, M. Livi, A. Vaccari, Role of the Mg/Al atomic ratio in hydrotalcite-based catalysts for NOx storage/reduction, Appl. Clay Sci. 29 (2005) 258–266.
[29] S.-D. Wang, Alkali-activated slag: hydration process and development of microstructure, Adv. Cem. Res. 12 (2000) 163–172.
[30] S.-D. Wang, K.L. Scrivener, Hydration products of alkali activated slag cement, Cem. Concr. Res. 25 (1995) 561–571.
[31] R. Allmann, H.P. Jespen, Die Struktur des Hydrotalkitts, Neues Jb. Mineral. Monat. (1969) 544–551.
[32] T. Matschei, B. Lothenbach, F.P. Glasser, The AFm phase in Portland cement, Cem. Concr. Res. 37 (2007) 118–130.
[33] B. Lothenbach, T. Matschei, G. Möschner, F.P. Glasser, Thermodynamic modelling of the effect of temperature on the hydration and porosity of Portland cement, Cem. Concr. Res. 38 (2008) 1–18.
[34] P. Durdzinski, Hydration of Multi-component Cements Containing Cement Clinker, Slag, Calcareous Fly Ash and Limestone, (2016) (Ph.D. Thesis, Lausanne).
[35] M. Zajac, M. Ben Haha, Hydration of limestone and dolomite cement, Proceedings of the 14th International Congress on the Chemistry of Cement, 2015.
[36] Z. Shi, M.R. Geiker, B. Lothenbach, K. de Weerdt, S.F. Garzón, K. Enemark-Rasmussen, J. Skibsted, Friedel's salt profiles from thermogravimetric analysis and thermodynamic modelling of Portland cement-based mortars exposed to sodium chloride solution, Cem. Concr. Compos. 78 (2017) 73–83.
[37] W. Huang, H. Kazemi-Kamyab, W. Sun, K.L. Scrivener, Effect of cement substitution by limestone on the hydration and microstructural development of ultra-high performance concrete (UHPC), Cem. Concr. Compos. 77 (2017) 86–101.
[38] W. Kunther, Z. Dai, J. Skibsted, Thermodynamic modeling of hydrated white Portland cement–metakaolin–limestone blends utilizing hydration kinetics from ^{29}Si MAS NMR spectroscopy, Cem. Concr. Res. 86 (2016) 29–41.
[39] S. Miyata, The syntheses of hydrotalcite-like compounds and their structures and physico-chemical properties I: the systems Mg^{2+}-Al^{3+}-NO_3^-, Mg^{2+}-Al^{3+}-Cl^-, Mg^{2+}-Al^{3+}-ClO_4^-, Ni^{2+}-Al^{3+}-Cl^- and Zn^{2+}-Al^{3+}-Cl^-, Clay Clay Miner. 23 (1975) 369–375.
[40] K. Rozov, U. Berner, C. Taviot-Gueho, F. Leroux, G. Renaudin, D. Kulik, L.W. Diamond, Synthesis and characterization of the LDH hydrotalcite–pyroaurite solid-solution series, Cem. Concr. Res. 40 (2010) 1248–1254.
[41] K.B. Rozov, U. Berner, D.A. Kulik, L.W. Diamond, Solubility and thermodynamic properties of carbonate-bearing hydrotalcite–pyroaurite solid solutions with a 3:1 Mg/(Al + Fe) mole ratio, Clay Clay Miner. 59 (2011) 215–232.
[42] S.J. Mills, A.G. Christy, J.-M.R. Génin, T. Kameda, F. Colombo, Nomenclature of the hydrotalcite supergroup: natural layered double hydroxides, Mineral. Mag. 76 (2012) 1289–1336.

Paper III

Stability of the hydrate phase assemblage in Portland composite cements containing dolomite and metakaolin after leaching, carbonation, and chloride exposure

Machner, A., Zajac, M., Ben Haha, M., Kjellsen, K.O., Geiker, M.R., De Weerdt, K.
Revised version submitted to Cement and Concrete Composites (January 2018)

Stability of the hydrate phase assemblage in Portland composite cements containing dolomite and metakaolin after leaching, carbonation, and chloride exposure

Alisa Machner[1,3,*], Maciej Zajac[2], Mohsen Ben Haha[2], Knut O. Kjellsen[1], Mette R. Geiker[3], Klaartje De Weerdt[3]

[1]Norcem AS, R&D Department, Setreveien 2, P.O. Box 38, 3991 Brevik, Norway
[2]Heidelberg Technology Center GmbH, Oberklammweg 2-4, 69181 Leimen, Germany
[3]NTNU Department of Structural Engineering, Richard Birkelandsvei 1A, 7491 Trondheim, Norway

*Corresponding author: alisa.machner@ntnu.no
+47 45394622
ORCID-ID: 0000-0002-6334-5116

Abstract

To reduce CO_2 emissions during the production of cement and to cope with increasing demands for concrete, and thereby cement, the cement industry needs to identify new supplementary cementitious materials. These new composite cements should provide, among others, a similar or improved durability of the concrete structures. This study investigated the hydrate phase assemblage in Portland cement pastes containing dolomite or a combination of dolomite and metakaolin after leaching, carbonation, and chloride exposure. The phase assemblage and phase compositions of the exposed samples and the unexposed reference samples were investigated using TGA, XRD, and SEM-EDS. The reaction of dolomite in the cement paste resulted in the formation of hydrotalcite. It was found that, unlike most other hydration phases, hydrotalcite can withstand high degrees of leaching and carbonation. When the samples were exposed to a chloride solution, the formation of a chloride-containing hydrotalcite was observed.

Keywords:

Dolomite; Metakaolin; Blended cement; Leaching; Carbonation; Chloride exposure

1. Introduction

There is a need to identify potential new supplementary cementitious materials (SCMs) both to reduce CO_2 emissions during cement production and to cope with increasing demand for concrete and thereby cement. These new composite cements should provide, among others, a similar or improved strength development and durability compared to today's commercial cements. The use of new SCMs might change the chemistry of the cementitious system and therefore change its phase assemblage and its resistance to deterioration. Typical deterioration mechanisms for reinforced concrete include carbonation-induced or chloride-induced corrosion of the reinforcement.

During carbonation, portlandite reacts with the CO_2 dissolved in the pore solution to form $CaCO_3$. Carbonation decomposes ettringite and AFm phases and leads to the formation of $CaCO_3$, hydrous alumina and, in the case of hydrates containing sulphate, gypsum. The C-S-H phase decalcifies gradually and decomposes to amorphous silica and $CaCO_3$ [1]. The decalcification of the C-S-H phase results in an increase in the average silicate chain length and a higher Si/Ca ratio. An increased amount of calcium carbonate has been reported to form in samples with lower Si/Ca ratios and very little change in the average silicate chain length has been reported during the carbonation of the C-S-H with a high initial Si/Ca ratio [2].

When cement paste is exposed to chloride solutions, some of the chlorides will be taken up by the hydrates, while the rest will be freely available for transport in the pore solution. When Portland cement pastes are exposed to NaCl solutions, chlorides will be bound chemically in chloride-containing AFm phases like Friedel's salt or Kuzel's salt. Unlike the exposure to $CaCl_2$ solutions, exposure to NaCl solutions has been reported to result in little or no chloride being physically bound by adsorption on the C-S-H [3–7].

In addition, leaching of the cement paste, another possible deterioration mechanism, causes a drop in the pH of the pore solution and can thereby cause a change in the stability of the phase assemblage. During the leaching of a cement paste, portlandite dissolves and the C-S-H gradually decalcifies until it also decomposes together with ettringite and AFm phases, leaving only hydrous silica, alumina and iron oxide detectable in the residue [1]. However, C-S-H with a higher average silicate chain length due to the addition of SCMs containing silicon typically shows improved resistance to the leaching of calcium [8–10].

The effect on the phase assemblage of replacing 40 wt% clinker with a combination of metakaolin and dolomite or limestone has been reported in an earlier study [11]. It was shown that, depending on curing time and curing temperature, the addition of dolomite in combination with small quantities of metakaolin can lead to the formation of carbonate AFm phases and ettringite as well as a hydrotalcite-like phase (member of the hydrotalcite supergroup [12], in the following simply referred to as hydrotalcite), . The formation of hydrotalcite in Portland composite cements, especially at elevated temperatures (60 °C), has also been reported for other replacement levels of dolomite [13–15].

Hydrotalcite has shown good resistance to leaching in MgO-activated slag binder systems [16,17]. It is also reported to be a promising material for CO_2-capture technology because of its high CO_2 adsorption capacity [18]. Moreover, thermodynamic modelling of leaching has predicted that hydrotalcite will withstand harsher leaching conditions and will decompose only when the C-S-H has completely decomposed [19].

When exposed to a chloride-containing solution, hydrotalcite has been reported to show a high chloride-binding capacity due to its excellent ion exchange properties [20–22]. In cementitious systems containing slag, it has been predicted to bind more chlorides than Friedel's salt [23]. The minerals of the hydrotalcite supergroup belong to the layered double hydroxides, which are defined by the general formula $[Me^{2+}_{1-x}Me^{3+}_{x}(OH)_2]^{x+}$ $[A^{m-}]_{x/m}\cdot nH_2O$. The crystal structure of hydrotalcite can be derived from that of brucite. The main layer consists of metals (here abbreviated with Me), specifically magnesium (Me^{2+}) and aluminium (Me^{3+}) hydroxide octahedra. The substitution of aluminium for magnesium in the main layer charges this layer positively. To maintain electrical neutrality, the interlayer incorporates monovalent or divalent anions (here abbreviated with A), such as OH^-, Cl^-, CO_3^{2-} or SO_4^{2-}.

Previous studies reporting on the stability of hydrotalcite or its chloride-binding capacity focused on pure synthesized hydrotalcite or on hydrotalcite formed in alkali-activated slag binder systems or slag-containing cements. These systems may deviate in pH and composition from Portland-cement-based systems, which will affect the composition and stability of the hydrotalcite formed. Moreover, the chloride-binding capacity of hydrotalcite depends strongly on the presence of carbonate ions in the pore solution [24], because divalent ions, such as carbonates, are favoured in the interlayer of hydrotalcite compared to monovalent ions, such as chlorides [20,21]. The chloride-binding capacity

of hydrotalcite could therefore be reduced for the binder systems investigated in this study, where significant amounts of dolomite are used.

In this study, we investigated the stability of the hydrate phase assemblage formed in dolomite-containing cementitious systems after leaching, carbonation, and chloride exposure with special focus on hydrotalcite. The sample preparation and curing were adapted to ensure the formation of hydrotalcite in the samples investigated [11,13]. Equivalent samples containing limestone instead of dolomite were used as references. The stability of the various hydration phases and their compositions were investigated after exposure using TGA, XRD and SEM-EDS. The results were compared to non-exposed reference samples of the same compositions and to the results of the thermodynamic modelling of one sample composition in this study.

2. Materials & Methods

2.1. Materials and cement paste preparation

For the preparation of the various binder compositions, we used a Portland cement (C) supplied by Norcem AS, to which only gypsum was added during grinding, natural dolomite (D, dolomite content: approx. 90 wt%, for more detailed information see [11]) supplied by Miljøkalk AS, natural limestone (L) supplied by Miljøkalk AS, and laboratory-grade metakaolin (M) supplied by Imerys (Metastar501). Table 1 gives the chemical composition of the materials, determined with X-ray fluorescence (XRF) and their specific surface areas determined using the Blaine method. Figure 1 shows the particle size distributions of the materials, determined using laser diffraction with a Malvern Mastersizer 2000E.

In the samples investigated, 40 wt% of the cement was replaced with dolomite (60C40D) or a combination of dolomite and metakaolin (60C35D5M). Equivalent samples containing limestone instead of dolomite (60C40L, 60C35L5M) were prepared as references. Table 2 gives an overview of the samples investigated in this study.

The pastes were prepared in batches of 540 g with a w/b ratio of 0.5 using a Braun MR 5550CA high-shear mixer (mixing procedure: mixing for 30 s, resting for 5 min, mixing for 60 s). The resulting pastes were poured into 125 mL plastic bottles, which were sealed and stored immersed up to their bottle-necks in water at 60 °C. After 3 months of curing, to ensure a high degree of reaction in the

samples, they were crushed in a jaw crusher and subsequently ground in a rotating disc mill to a particle size < 1 mm. Afterwards, 30 wt% of water was added to the ground pastes, which were then poured into tight and sealed polypropylene bottles (1 L) and stored for another 4 months at 60 °C. After a total of 7 months of curing, the samples were transferred to 20 °C for 2 weeks prior to exposure, which was also carried out at 20 °C. An overview of the sample preparation and curing is given in Table 3. The samples were cured at 60 °C, to accelerate the dolomite reaction and consequently achieve a sufficient reaction degree of dolomite within the curing time, because in a previous study the reaction of dolomite was shown to be very slow at curing temperatures of 20 °C or 38 °C [11].

2.2. Exposure conditions and reference samples

2.2.1. Leaching

50 g of each of the prepared well-hydrated ground cement pastes were poured into a cellulose extraction thimble and loaded into a Soxhlet extraction chamber in a temperature-controlled room at 20 °C. A large volume of deionized water compared to the sample size was slowly dripped onto these samples over time. When the extraction chamber was full (250 mL), it was automatically emptied again. A total of 100 L deionized water was dripped onto the sample (over approx. 6 weeks). The experimental setup was adapted from De Weerdt and Justnes [25].

2.2.2. Carbonation

Approx. 10 g of each of the prepared well-hydrated cement pastes was spread on an evaporating dish (diameter approx. 6 cm) and placed in a carbonation chamber (20 °C, 60% RH, 1% CO_2) for 34 days.

2.2.3. Exposure to chloride solutions

30 g of each of the well-hydrated cement pastes was poured into 45 mL centrifuge tubes. To these samples, 15 mL of a 2 mol/L NaCl solution was added using a volumetric pipette. The solution was prepared with laboratory-grade NaCl supplied by Merck. The samples were stored at 20 °C for at least one month to reach equilibrium. The experimental approach for the chloride exposure of the samples was the same as in [5,6].

2.2.4. Reference samples

Reference samples were prepared for all three types of exposures. The unexposed reference samples for the leached and carbonated samples were stored sealed in a temperature-controlled room at 20 °C. The reference samples for the chloride-exposed samples were prepared by adding 15 mL of deionized water to 30 g of the samples instead of a chloride solution. The XRD and TGA results of the exposed samples were compared with their reference samples, which had been stored for a similar time at 20 °C. As reference samples for the SEM-EDS analyses for all types of exposure, we used the results from an earlier study [11]. In that study, the samples were prepared with a similar cement clinker and the same SCMs, and they were cured sealed at 100% RH for 360 days at 60 °C and were prepared for SEM-EDS in a similar way.

2.3. Analyses after exposure

The samples were analysed before and after leaching, carbonation, or chloride exposure using thermogravimetric analysis (TGA), X-ray diffraction (XRD), and scanning electron microscopy (SEM). Prior to the investigation of the cement pastes, the hydration was stopped by double solvent exchange. For this, approx. 6 g of the coarsely crushed moist cement paste (whether exposed sample or reference sample) was immersed in 100 mL isopropanol, shaken for 30 seconds, and left to rest for 5 min before the isopropanol was decanted. This isopropanol treatment was performed twice, and then the sample was transferred to a filtration unit where the isopropanol was filtrated out and the paste was immersed in 20 mL petroleum ether. After 30 seconds of stirring, the suspension was left to rest for 5 minutes. The sample was then vacuum-filtrated and subsequently dried overnight in a desiccator under a slight vacuum (-0.2 bar) applied using a aspirator pump. For the TGA and XRD analyses, parts of each dried sample were crushed in a porcelain mortar until the whole sample passed through a 63 µm sieve. All samples were stored in a desiccator over silica gel and soda lime until measurement.

The TGA investigations were carried out using a Mettler Toledo TGA/DSC 3+. The 600 µL alumina crucibles were filled with approx. 150 mg of the prepared powder samples. The analysis was performed over the range of 40–900 °C with a heating rate of 10 °C/min. During the analysis, the measurement cell was purged with 50 mL/min N_2 gas. The derivate curves of the TG signal, the DTG curves, were used to detect phase changes. The DTG curves can be divided into several sections as suggested by Lothenbach et al. [26], in which the decomposition of specific phases can be detected as a weight loss. The first peak at around 100 °C is related to the ettringite (Et) decomposition and

the beginning of the dehydroxylation of the C-S-H phase. C-S-H decomposes gradually between 40 °C and 600 °C and appears as a polynomial baseline under the other peaks. Hydrotalcite (Ht) shows two weight loss events: the first at approx. 220 °C and the second at around 400 °C. The subsequent sharp peak between approx. 400 °C and 550 °C is related to the decomposition of portlandite (CH). Above 550 °C, carbonates decompose and emit CO_2.

TGA was also used to quantify the weight losses caused by the decomposition of the hydrotalcite (w_{Ht}, see Eq. 1). This was done by integrating the DTG curve in the specific temperature intervals for hydrotalcite and subtraction of a linear baseline. The resulting area represents the $w_{Ht\text{-}measured}$ in [wt%]. By applying this method the additional weight loss from the decomposition of the C-S-H phase, which appears as a baseline in this temperature region, is excluded as described in [26].

For the leaching experiments, the calculated weight losses from TGA had to be corrected for the loss of material during the leaching ($\Delta w_{leached}$ in [wt%]) as shown in Eq. 2. The $\Delta w_{leached}$ was determined by using XRF to quantify the amount of Fe_2O_3 in the well-hydrated cement pastes before ($Fe_{reference}$) and after leaching ($Fe_{leached}$), assuming that iron was not leached from the sample during exposure. When a certain percentage of the material is lost due to the leaching, the iron is relatively enriched in the leached sample compared to reference sample. From the quantifications of the iron content (see Appendix Table A.1) the loss of material during leaching was calculated to be approx. 30 wt% ±5% relative to the ignited sample weight at 900 °C. This calculation was also done for titanium oxide and led to similar results (see Appendix Table A.1).

The weight loss due to the decomposition of the hydrotalcite was normalized to the ignited weight at approx. 900 °C, which was corrected for the theoretical amount of CO_2 that is lost due to the decomposition of the carbonates (dolomite or limestone) included in the binder ($w_{900} - w_{carbonate}$). $w_{carbonate}$ was determined from the theoretical amount of dolomite or limestone in the samples ($X_{dolomite/limestone}$, which was either 40 wt% or 35 wt%), the molar mass of CO_2 ($M(CO_2)$), and the molar masses of dolomite ($M(CaMg(CO_3)_2)$) or limestone ($M(CaCO_3)$), as shown in Eq 3a) and b). In the case of the samples containing dolomite, the calculated values had to be multiplied by two prior to the normalization to the bound water content (BW) (Eq. 3a) because dolomite contains 2 mol of CO_3^{2-}. An overview of the values for $w_{Ht\text{-}measured}$, w_{900}, and BW for the various samples can be found in the Appendix (Table A.2).

$$w_{Ht} = \frac{w_{Ht-measured}}{w_{900} + w_{carbonate}} \cdot 100 \cdot (1 - \frac{\Delta w_{leached}}{100}) \quad \text{Eq. 1}$$

$$\Delta w_{leached} = 100 - \left(100 \cdot \frac{Fe_{reference}}{Fe_{leached}}\right) \quad \text{Eq. 2}$$

a) $$w_{carbonate,D} = X_{dolomite} \cdot \frac{100}{100 + BW} \cdot \frac{M(CO_2) \cdot 2}{M(CaMg(CO_3)_2)} \quad \text{Eq. 3}$$

b) $$w_{carbonate,L} = X_{limestone} \cdot \frac{100}{100 + BW} \cdot \frac{M(CO_2)}{M(CaCO_3)}$$

For the carbonation experiments, the calculated weight losses for hydrotalcite were also normalized to the sample weight at approx. 900 °C, which was assumed to be the ignited binder weight, eliminating any increased sample weight due to carbonation [27] (Eq. 1). The weight loss originating from the carbonates already present in the binder when the samples were prepared ($w_{carbonate}$) was taken into account (see Eq. 3).

The XRD analyses were carried out using a Bruker AXS D8 focus diffractometer. The diffractometer operates with CuKα radiation in a Bragg-Brentano θ–2θ geometry with a goniometer radius of 200.5 mm and is equipped with a LynxEye detector. The powder samples were front-loaded into the sample holders and queued in the sample changer until measurement. The scans ranged from 5–55 °2θ, with a step size of 0.01 °2θ and a sampling time of 0.5 s per step.

Scanning electron microscopy (SEM) was carried out using a Hitachi S-3400N microscope equipped with energy dispersive X-ray spectroscopy (EDS) from Oxford Instruments. Polished and carbon-coated sections of stopped but not ground samples were investigated. The acceleration voltage was set to 15 keV.

2.4. Thermodynamic modelling

The Gibbs free energy minimization program GEMS [28–31] was used to model changes in the hydrate phase assemblages and their volumes for sample 60C40D during leaching and carbonation exposure. The thermodynamic data from the PSI-GEMS database was supplemented with a cement-specific database (CEMDATA14 database) [32], which includes solubility products of the solids relevant for cementitious materials. For the C-S-H phase, the CSHQ model proposed by Kulik was

used [33]. The modelling of sample 60C40D was carried out for an exposure temperature of 20 °C. The composition of the Portland cement used as an input for the model was calculated from the XRF results (Table 1) by excluding TiO_2, MnO, MgO and P_2O_5 from the results and normalizing the remaining oxides to 100%. The degree of reaction of the Portland cement was assumed to be 90%, and the reaction degree of the dolomite added was assumed to be 10%. Increasing amounts of water for modelling the leaching and increasing amounts of CO_2 for modelling the carbonation were added to the hydrated binder in the model. The formation of the following phases was blocked in the modelling: CA, CA_2, hematite, magnetite, goethite, pyrite, troilite, iron, kaolinite, quartz, zeolites (chabazite), and thaumasite. This was done to prevent the formation of phases, whose formation is kinetically impossible at the conditions (temperature, pressure) of the exposure. For most of the blocked phases, 20 °C and/or the ambient pressure are too low for them to form. For thaumasite, however, this temperature is too high, because its formation has only been reported at temperatures below 20 °C [1].

3. Results

3.1. Phase changes due to sample preparation

Phase changes due to the various stages of sample preparation were monitored. An unexposed reference sample (60C35D5M) was investigated with XRD and TGA after regrinding and rehydration (α-samples), after 2 weeks at 20 °C (β-samples), and after the exposure time (γ-samples). Table 3 gives an overview of the various sample preparation stages and phase assemblage investigations.

Figure 2 shows the DTG curves of sample 60C35D5M at the various stages of sample preparation (α, β, γ). The α and β preparation stages seem only to differ in the weight loss temperature range of the carbonate decomposition. This means that the samples carbonated slightly during preparation and storage. However, a significant increase in the first weight loss interval is observed for both sample compositions between the β and γ preparation stages. Originally, the samples were stored at 60 °C, but the subsequent exposure was at 20 °C. This means that the prolonged curing of the samples at 20 °C caused the formation of additional ettringite, which was not stable at 60 °C. It is therefore important to compare the exposed samples with the γ-references, because they have been stored at 20 °C for the same time (including the exposure time). Phase changes observed between the exposed samples and the γ-reference samples should therefore be due solely to the exposure and not due to changes in phase stabilities caused by the change in curing temperature from 60 °C to 20 °C. In the following, the graphs of the various samples after leaching or carbonation are always compared with

their γ-reference samples for the TGA and XRD results. It should be noted that, for the samples exposed to 2 mol/L NaCl solution, the reference samples were exposed to deionized water for a similar time. The SEM-EDS results (BSE images, elemental maps, and point analyses) are compared with samples from an earlier study, as explained in 2.2.4.

3.2. Phase assemblage of the exposed samples

3.2.1. BSE images and elemental maps

Figure 3 shows the BSE images and elemental maps of magnesium, aluminium, calcium, silicon, oxygen, and chlorine for samples $60C40D_{reference}$, $60C40D_{leached}$, $60C40D_{CO2}$, and $60C40D_{NaCl}$. Sample $60C40D_{reference}$ is from an earlier study and was used as the reference of an unexposed sample. The BSE images and elemental maps for the mix 60C35D5M can be found in the Appendix (Figure A.1).

Figure 3a shows the BSE image and the elemental maps for the unexposed reference sample ($60C40D_{reference}$). The large uniformly grey particles, which are rich in magnesium and calcium, are partially reacted dolomite particles. The shape of the original grain boundaries of the dolomite particles before reaction is still visible due to the thin layer of C-S-H that precipitated around them at early hydration ages, and in the magnesium map. The reaction rims between the unreacted parts of the dolomite particles and their former grain boundaries are filled with hydrates, visible due to the increased oxygen counts in that area. The hydrates inside the reaction rims are rich in aluminium and magnesium, but poor in calcium and silicon, which might indicate that they are filled with hydrotalcite. This will be checked later (see 3.3.1) by SEM-EDS dot plots from measurement points taken inside these reaction rims.

Figure 3b shows that these reaction rims are still visible after leaching this sample, which indicates that hydrotalcite persisted through the leaching procedure applied. Moreover, the portlandite, which is visible due to high calcium counts in the unexposed sample, has vanished in the leached sample.

In contrast to the leached samples, the carbonated samples show relatively large uniformly bright areas within the matrix, which are rich in calcium (Figure 3c). These areas probably consist of calcium carbonate precipitated during carbonation of the calcium-containing phases in the cement paste, such as portlandite or C-S-H. The reaction rims around dolomite probably containing hydrotalcite are also visible in the carbonated samples.

In the samples exposed to a NaCl solution (Figure 3d), the chlorine map shows generally higher counts than in the other samples. Moreover, the reaction rims inside the original grain boundaries of dolomite are also rich in chlorine. This indicates that the hydrotalcite formed in these reaction rims has taken up significant amounts of chlorine.

3.2.2. TGA

Figure 4(a–c) shows the DTG curves of samples 60C40D and 60C35D5M after leaching, carbonation and chloride exposure, and their unexposed reference samples. The two binder compositions show a similar trend and are described together in the following.

The weight losses in the temperature regions of C-S-H and ettringite are significantly lower in the leached samples than in their reference samples (Figure 4a). The peak related to the decomposition of the portlandite has completely disappeared in the leached samples, but the peaks related to the decomposition of the hydrotalcite seem to be higher in the leached samples than in their references.

A significant decrease in the first weight loss interval (up to approx. 200 °C) can also be observed in the carbonated samples compared to their reference samples (Figure 4b), indicating the decomposition of ettringite and C-S-H during carbonation. The small peak in the first temperature interval of the carbonated samples might indicate the dehydration of gypsum. The decomposition of the C-S-H phase is also visible where the whole curve shifts upwards between 40–400 °C. The portlandite peak completely disappears in the carbonated samples. The two peaks related to the decomposition of hydrotalcite seem to be slightly smaller in the carbonated samples than in the reference samples.

Figure 4c shows the DTG curves of samples 60C40D$_{NaCl}$ and 60C35D5M$_{NaCl}$, and their reference samples which were exposed to deionized water. The first weight loss peak related to the decomposition of ettringite and the beginning dehydroxylation of C-S-H is higher in the chloride-exposed sample 60C40D than in its reference. In sample 60C35D5M, the weight loss in this temperature region seems to be unaffected by the chloride exposure. In both samples (60C40D and 60C35D5M), the two peaks related to the decomposition of hydrotalcite were changed by the exposure. The first peak (approx. 220°C) is smaller in sample 60C35D5M, and it has completely vanished in sample 60C40D. The second peak of hydrotalcite (approx. 400 °C) appears at lower temperatures. The portlandite peak is slightly smaller in samples exposed to the NaCl solution than

in their reference samples. In both exposed samples, there are several peaks in the weight loss temperature region of the carbonates, all of which can be related to the emission of CO_2 [34].

To investigate whether the amount of hydrotalcite in the samples changed during leaching or carbonation, we quantified the weight loss related to the decomposition of hydrotalcite. However, small weight losses were also observed in the hydrotalcite temperature regions for the samples containing limestone (see Appendix Figure A.2 and Figure A.3). This indicates that weight losses observed in the samples containing dolomite might not be caused solely by the decomposition of hydrotalcite formed by the reacted of dolomite. We therefore subtracted the weight losses in the samples containing limestone from those containing dolomite, so that we could quantify the hydrate weight loss in these temperature regions due solely to the reaction of dolomite.

Figure 5a shows the quantifications for the two leached samples compared to their unexposed references. The quantifications were normalized to the sample weight loss due to leaching as described in 2.2.4 (Eq. 1–2). Assuming an error of 0.1 wt%, we can see a slight increase in the weight loss of the hydrotalcite in the leached samples compared to their reference samples.

The DTG curves of the carbonated samples (Figure 4b) shifted upwards compared to those of their reference samples, because their initial mass at 40 °C increased during carbonation due to CO_2 binding, so the hydrotalcite weight loss peaks seemed lower in the carbonated samples than in the reference samples. Figure 5b shows the results of these quantifications for the carbonated samples compared to their unexposed references normalized as described in 2.2.4 (Eq. 1), to eliminate the effect of increased sample weight due to carbonation. The results of the hydrotalcite quantification for the carbonated and reference samples of 60C35D5M are very similar and within the assumed error of 0.1%. However, sample 60C40D shows a lower hydrotalcite weight loss in the carbonated sample than the reference.

3.2.3. XRD

Figure 4(d–f) shows the XRD patterns of samples 60C40D and 60C35D5M after leaching, carbonation, and chloride exposure, and their unexposed reference samples. The peak positions of ettringite (Et – 9.1 °2θ), Friedel's salt (Fs – 11.2 °2θ), Ferrite (C_4AF – 12.2 °2θ), hydrogarnet (Htg – 17.4 °2θ), hydrotalcite (Ht – approx. 11.4 °2θ), portlandite (CH – 18.1 °2θ), and brucite (Bru – 18.6 °2θ) are indicated.

Both leached samples show a higher hydrotalcite peak than their reference samples (Figure 4d). This is in good agreement with the results obtained from TGA, where a slightly increased weight loss for the hydrotalcite was measured in the leached samples than in their reference samples. Moreover, no ettringite or portlandite was detected with XRD in either of the leached samples. In sample $60C40D_{leached}$, brucite was detected, and a siliceous hydrogarnet was detected in both samples ($60C40D_{leached}$ and $60C35D5M_{leached}$). These phases seem not to be affected by leaching, because they are visible in both the leached and the reference samples.

No portlandite or ettringite peaks are observed in the carbonated samples (Figure 4e). The brucite peak observed in the reference sample 60C40D has disappeared in the carbonated sample. This might be explained by the carbonation of $Mg(OH)_2$ probably to $MgCO_3$. However, no peaks of $MgCO_3$ were observed with XRD. Generally, the XRD results agree fairly well with the results from TGA. There are no clear changes in the hydrotalcite peak between the carbonated and reference samples of 60C40D and 60C35D5M. In summary, this indicates that hydrotalcite can withstand carbonation.

The XRD patterns of the samples $60C40D_{NaCl}$ and $60C35D5M_{NaCl}$ are shown in Figure 4f alongside their reference samples, which were exposed to deionized water. It can be seen that the phase assemblage was not affected by the exposure to a 2 mol/L NaCl solution. No clear peaks of Friedel's salt can be seen in the samples exposed to NaCl.

Figure 6 shows the XRD patterns of the samples $60C40D_{NaCl}$ and $60C35D5M_{NaCl}$ and their reference samples just in the range of the first hydrotalcite peak (10–12 °2θ). The peak positions of Friedel's salt, hydrotalcite and chloride-containing hydrotalcite (Ht_{Cl} – approx. 11.1–11.3 °2θ) are indicated together with the exact angle of their reflections. The peaks of the hydrotalcite in samples exposed to NaCl have shifted to lower angles compared to those of the hydrotalcite in the reference samples exposed to deionized water.

3.3. Phase composition

3.3.1. Composition of the hydrotalcite

Figure 7 shows the results of the point analyses of the reaction rims around the unreacted dolomite grains in samples 60C40D and 60C35D5M after a) leaching, b) carbonation, and c) chloride exposure. The results of these analyses are plotted as the Mg/Si ratio over the Al/Si ratio.

Most of the points for sample 60C35D5M, and some of the points for sample 60C40D plot along linear lines, which are indicated by dotted lines. This suggests the presence of a reaction product with a fixed Mg/Al ratio, which does not contain significant amounts of silicon. It can, therefore, be identified as hydrotalcite [35,36]. The Mg/Al ratios of the hydrotalcite for the exposed samples and their references are shown by the slope of the dotted lines and are summarized in Table 4.

The Mg/Al ratio is higher for sample 60C40D than for sample 60C35D5M, regardless of the exposure. This difference can be explained by the 5 wt% of metakaolin in sample 60C35D5M, which acts as a source for aluminium and therefore lowers the Mg/Al ratio of the hydrotalcite. This effect has been described for similar binder compositions [11] and for cements containing ground granulated blast furnace slag either in various amounts or with various aluminium contents [37,38].

For the mix 60C40D, there is a bigger spread in the EDS-points of the leached or chloride-exposed samples than in the carbonated sample. In leached or chloride-exposed samples, some of the points spread towards a higher magnesium content. This is due to intermixing with brucite, which is shown by a peak in XRD, both in the reference and in the leached and chloride-exposed 60C40D samples. Intermixing with brucite was not observed for sample $60C40D_{CO2}$, probably because brucite was not stable after carbonation.

Figure 8 shows the results of the point analyses for the samples $60C40D_{NaCl}$ and $60C35D5M_{NaCl}$ and the unexposed reference sample plotted as the Cl/Ca ratio over the Al/Ca ratio. The plots confirm the findings from TGA and XRD that the hydrotalcite in the samples exposed to NaCl contains chlorides, whereas the results from the unexposed reference sample show no chloride uptake in the hydrotalcite.

3.3.2. Composition of the C-S-H phase

We also investigated the composition of the C-S-H in the exposed samples. All graphs show the results from an earlier study [11] as unexposed reference samples with a similar binder composition.

In Figure 9, the results of the point analyses for the leached samples are plotted as the Al/Ca ratio over the Si/Ca ratio. In this graph, the composition of the C-S-H can be determined as shown by the dashed ovals [1]. The C-S-H phase in mature Portland cement pastes usually has a Si/Ca ratio of

approx. 0.5, as shown by the reference samples. This value is significantly lower than the Si/Ca ratio determined in the leached samples in this study, which have a Si/Ca ratio in the range of approx. 1.5–2.0. Moreover, the leached samples showed a less defined C-S-H composition than the reference samples. This is probably due to the decalcification of the C-S-H phase, which causes a significant spread in the results when they are normalized to calcium. It should also be mentioned that the setup applied in this study did not leach the samples homogenously. This inhomogeneity might also cause a spread in the results, as shown previously where the same setup was used [25].

Figure 10 shows the C-S-H composition as the Mg/Si ratio over the Al/Si ratio for the samples $60C40D_{leached}$ and $60C35D5M_{leached}$ compared to their reference samples with similar compositions. This graph shows the Al/Si ratio of the C-S-H as the intersection between the X-axis and the lines described by the data points. The leached samples show similar results to the reference samples, which indicates that the Al/Si ratio of the C-S-H was not affected by the leaching and that the aluminium uptake in the C-S-H was similar in both samples. The slope of the lines in Figure 10 represents the Mg/Al ratio of the matrix. The Mg/Al ratios of the C-S-H are very similar to those of the hydrotalcite listed in Table 4, which indicates that hydrotalcite can also be found finely intermixed with the C-S-H in the matrix.

The C-S-H compositions in the carbonated samples were also measured with SEM-EDS, as shown in Figure 11. Unlike the results for the leached samples, the results of these point analyses do not show a clear composition of the C-S-H phase. Instead, the results spread in two directions: towards lower and higher Si/Ca ratios.

Figure 12 shows the Mg/Si ratio over the Al/Si ratio of the C-S-H of the carbonated samples 60C40D and 60C35D5M compared to the non-carbonated reference samples. Before carbonation, sample 60C35D5M showed a higher Al/Si ratio of the C-S-H due to the metakaolin added in this sample. In contrast to the results from the leached samples (Figure 10), the Al/Si ratio decreased in the carbonated sample 60C35D5M to approximately the same value as for sample 60C40D. Similarly to the leached samples, the Mg/Al ratios of the matrix show very similar results compared to the Mg/Al ratios of the hydrotalcite listed in Table 4, which indicates that hydrotalcite is finely intermixed with the C-S-H in the matrix.

Figure 13 shows the Al/Ca ratio over the Si/Ca ratio of the samples $60C40D_{NaCl}$ and $60C35D5M_{NaCl}$ alongside the results of the unexposed reference samples. The C-S-H in sample 60C35D5M shows a higher Si/Ca ratio than sample 60C40D.

Figure 14 shows the Cl/Al ratio over the Si/Ca ratio for these samples and illustrates the chloride uptake of the C-S-H. The results of the unexposed reference samples plot almost completely on the X-axis, indicating little or no chloride content in these samples, whereas the samples exposed to NaCl show a higher chloride content. This confirms the observations made with the elemental maps in 3.2.1, where sample $60C40D_{NaCl}$ showed generally higher counts of chlorine also in the matrix. This also agrees well with the observations made from Figure 10 and Figure 12, which indicated that hydrotalcite is also finely intermixed with the C-S-H in the matrix.

3.4. Thermodynamic modelling of the phase assemblage during leaching and carbonation

Figure 15 shows the phase assemblage modelled for sample 60C40D in contact with an increasing amount of water. First, the portlandite, and then the ettringite, monocarbonate and C-S-H all decompose. The calcite predicted by the thermodynamic modelling originated from the reaction of dolomite, which we assumed to have a reaction degree of 10%. Ferrihydrite ($Fe_2O_3 \cdot 0.5H_2O$) is predicted due to the decomposition of AFm and AFt phases, which were modelled to contain a certain amount of iron due to the high degree of reaction we assumed for the Portland cement (90%), but it was not observed experimentally. Hydrotalcite seemed to be stable until approx. 28000 L of deionized water had been added. Hydrous silica and aluminium have also been reported in the residue of an extremely leached cement sample [1], but were not predicted by the thermodynamic model. This difference can probably be explained by the modelling, which represents an idealized case leading to the full dissolution of these phases.

Figure 16 shows the phase assemblage modelled for sample 60C40D with increasing amounts of CO_2 added (in grams). First, the portlandite, and then the C-S-H, ettringite and monocarbonate all decompose, and an increasing amount of calcite is formed. As with the leaching model, ferrihydrite is predicted due to the decomposition of the iron-containing AFm and AFt phases. Strätlingite forms as an intermediate state between C-S-H and amorphous silica. The stable phases predicted at high levels of added CO_2 are calcite, ferrihydrite, gypsum, magnesite, natrolite, and gibbsite, but some of these were not observed experimentally. This can be explained either by the small quantities of some

of these phases, which make their identification difficult, or by the fact that our system had not reached equilibrium.

4. Discussion

4.1. Comparison of the results of the thermodynamic modelling with the phase assemblage experimentally observed

In the following, we compare the thermodynamic modelling of the leaching (Figure 15) and carbonation (Figure 16) of sample 60C40D with the phase assemblages experimentally observed (Figure 4). The dashed rectangles drawn in Figure 15 and Figure 16 indicate the areas of the experimentally observed phase assemblages in the thermodynamic modelling. Within the rectangles, all the portlandite has decomposed, and C-S-H and ettringite have started to decompose, while the hydrotalcite is still stable.

The thermodynamic modelling predicted the decomposition of portlandite with increasing amounts of water or CO_2 added to the system. This is in agreement with the phase assemblage experimentally observed in this study, because portlandite was not observed with TGA or XRD after carbonation or leaching. The decomposition of portlandite is caused, in the case of leaching, by its dissolution in the leachate, and, in the case of carbonation, by its reaction with the CO_2 dissolved in the pore solution to form $CaCO_3$ [1].

During carbonation, ettringite is reported to decompose, while hydrous alumina, calcite, and gypsum form instead [1]. This is only partially in agreement with our results. No ettringite peak was observed in the carbonated samples with XRD, but no peak of gypsum was detected either with XRD, and only a small peak of gypsum was observed with TGA. The reason why gypsum was not detected with XRD might be that the gypsum (11.6°2θ) and hydrotalcite (11.4°2θ) peak positions overlapped slightly, or that too little gypsum was formed. During leaching, the thermodynamic model also predicts the dissolution of ettringite. This was confirmed by the experimental results, where no peak of ettringite was observed with XRD and the weight loss of ettringite in TGA was significantly lower in the samples after leaching.

The general shift upwards of the DTG curves after carbonation or leaching indicates the reduced amount of C-S-H, as predicted by the thermodynamic modelling. The thermodynamic modelling

predicted the decomposition of the C-S-H starting when the portlandite has decomposed during the carbonation or leaching of the samples, which is also according to the literature [1].

Hydrotalcite was observed experimentally with XRD and TGA and predicted by the thermodynamic modelling before and after leaching. This confirms the findings of Feng et al. [19]. Hydrotalcite was also observed experimentally in the samples after carbonation. It should be noted that in the thermodynamic model magnesite ($MgCO_3$) is predicted for high amounts of added CO_2, but hydrotalcite has been reported to be able to take up significant amounts of CO_2 and therefore to withstand a high degree of carbonation [18]. The reason for different results in the thermodynamic modelling might be that the hydrotalcite used for the modelling is a hydroxide-hydrotalcite that is not stable at high partial pressures of CO_2, or it might be due to kinetic effects of the transformation of hydrotalcite to $MgCO_3$.

It should be noted that the dashed rectangles in Figure 15 indicate a greater amount of water in the modelling compared to the experimental 100 L. This can be explained by the use of a Soxhlet extractor in our experimental setup. The samples were immersed in a small amount of deionized water for a short time, and then the Soxhlet extractor emptied itself automatically and was slowly filled again. This meant that the samples were not able to reach equilibrium with the total amount of water added. In the modelling, however, increasing amounts of water were added, which were in equilibrium with the solids present. The presence of monocarbonate in the modelling, which was not observed experimentally, can be explained by the sample preparation. The thermodynamic modelling was performed at 20 °C, while the samples were cured at 60 °C for approx. 7 months prior to the exposure at 20 °C. This indicates that due to this high-temperature curing the monocarbonate was not stable in our experimental samples. This is in accordance with the findings from Lothenbach et al., who reported a decreasing amount of monocarbonate in samples cured at such high temperatures [39].

Taking into account the limitations described above, the thermodynamic modelling agreed fairly well with the phase assemblage experimentally observed with XRD and TGA. The thermodynamic model confirms that the hydrotalcite formed by the reaction of dolomite in a cementitious system is a stable hydration product, which can withstand leaching, or carbonation within the range tested.

4.2. Composition of the C-S-H

Because the exposure to a 2 mol/L chloride solution did not change the phase assemblage or the Si/Ca ratio of the C-S-H, these samples can be used to elucidate the effect of metakaolin addition on the composition of the C-S-H. We measured a higher Si/Ca ratio of the C-S-H in samples containing 5 wt% metakaolin than in sample 60C40D. This can be explained by the pozzolanic reaction of metakaolin in sample 60C35D5M, which increases the Si/Ca ratio and the silicate chain length of the C-S-H [40,41]. This has also been reported previously for other silicon-containing SCMs, e.g. silica fume [9,42,43].

Sample 60C35D5M_{NaCl} shows a higher Si/Ca ratio of the C-S-H than the unexposed reference sample from an earlier study [11]. This can be explained by the sample preparation in this study, which resulted in a higher degree of reaction of the cement and metakaolin. The reference samples from an earlier study were cured in sealed tubes for 360 days and probably show a less mature C-S-H phase than the C-S-H in this study.

The increased Si/Ca ratio in the C-S-H in the leached samples indicates a severe decalcification of the C-S-H phase due to the leaching. This effect of leaching on the Si/Ca ratio of the C-S-H is in agreement with previous findings [1,44].

The SEM-EDS point analyses of the C-S-H after carbonation show a spread in the results towards higher and lower Si/Ca ratios (Figure 11). This indicates the presence of calcium carbonate and a silicon-rich phase. A similar observation is reported by Leemann et al. [45]. It can be explained by the gradual decalcification of the C-S-H until it finally decomposes to amorphous silica and $CaCO_3$ [1]. In contrast, Belda Revert et al., who used a similar cement, observed only a decrease in the Si/Ca ratio of the C-S-H due to the fine intermixing of decalcified C-S-H and calcium carbonate [27]. In this study, however, the calcium carbonate precipitated in large lumps, rather than finely intermixed with the C-S-H. The lumps of calcium carbonate can be seen, for example, in a larger picture of the carbonated sample 60C35D5M (see Appendix Figure A.4), where the calcium carbonate (Cc) is indicated with arrows. The large lumps are probably due to the sample preparation in our study. We crushed the samples after 3 months of curing to a grain size <1 mm and added 30 wt% of additional water. These actions were taken in order to maximize the hydration degree of the samples, but they also significantly coarsened the microstructure. This method of sample preparation also changed the transport of CO_2 and H_2O in the samples during exposure.

Moreover, we observed a decrease in the aluminium uptake of the C-S-H for carbonated samples compared to the reference samples, which is in agreement with the results of Belda Revert et al., who observed a decrease in the Al/Ca ratio for C-S-H in carbonated mortar samples containing 30 wt% fly-ash after carbonation [27].

4.3. Quantification of the amount of hydrotalcite in the samples after leaching and carbonation

The fact that sample 60C40D shows a higher weight loss in the temperature region of hydrotalcite in the reference than in the carbonated sample (Figure 5b) might be due to the presence of brucite in the reference sample, which can also result in a weight loss in the temperature region of hydrotalcite. In the carbonated samples, brucite ($Mg(OH)_2$) was not observed with XRD because it probably had reacted to $MgCO_3$ and therefore did not contribute to the weight losses in this temperature region. Brucite and calcite have been reported to be the reaction products of the dedolomitization reaction of dolomite and portlandite [46–48], as shown in Eq. 4.

$$CaMg(CO_3)_2 + Ca(OH)_2 \rightarrow Mg(OH)_2 + 2CaCO_3 \quad \text{Eq. 4}$$

However, in cementitious systems, where other ions are present (e.g. Al), hydrotalcite has been reported to form [11,13–15], as shown in Eq. 5.

$$6CaMg(CO_3)_2 + 2Al(OH)_3 + 6Ca(OH)_2 + 3H_2O \rightarrow Mg_6Al_2(OH)_{18}\cdot 3(H_2O) + 12CaCO_3 \quad \text{Eq. 5}$$

In an earlier study focusing on a similar binder composition, no clear peaks of brucite could be detected [11]. The formation of brucite solely in sample 60C40D in this study might be explained by the sample preparation including the crushing and rehydrating of the samples, which considerably increased the reaction degree of the system and probably also the reaction degree of the dolomite. This would increase the magnesium available in the system. There was no metakaolin in sample 60C40D, so the amount of aluminium in the system is relatively low, which together with the high magnesium content in the sample led to the formation of brucite. No brucite was detected in sample 60C35D5M, because sufficient aluminium was available in this sample containing 5 wt% metakaolin.

In the leached samples, the amount of hydrotalcite quantified with TGA was slightly higher than in the unleached reference samples (Figure 5 a). This could have been an artefact of the low sample weight of the leached samples compared to their references, but the quantifications with TGA were normalized by the XRF results, which would eliminate this effect. Another possible explanation could be the increased dissolution rate of dolomite in solutions at a lower pH [49–52]. Leaching with 100 L of deionized water lowered the pH of the samples to approx. 10.7 according to the modelling results. However, this drop in pH due to leaching is probably not big enough to increase the dissolution rate of dolomite, because significant changes is the dolomite dissolution rate were reported only for pH values < 9 [52].

4.4. Composition of the hydrotalcite

Mg/Al ratios of approx. 2 are commonly reported for hydrotalcite-like phases in cementitious systems [13,35,38,53–56]. However, higher Mg/Al ratios are also possible because the natural mineral hydrotalcite has a Mg/Al ratio of 3 [57]. The high Mg/Al ratios in our study (60C40D:3.2, 60C35D5M: 2.4) might be explained by the relatively pure dolomite (dolomite content approx. 90 wt%) and small metakaolin additions used in our study.

The values of the Mg/Al ratios of the hydrotalcite after the various exposures were similar to the Mg/Al ratios of hydrotalcite formed in unexposed samples of an earlier study [11]. This indicates that the hydrotalcite formed was not only stable during leaching, carbonation, and chloride exposure, but also did not change its composition with regard to its Mg/Al ratio.

The phase assemblage seemed to be only slightly affected by the exposure to a 2 mol/L NaCl solution and was therefore not discussed in detail above. For the hydrotalcite, however, a shift in the peak position was observed with XRD when the samples were exposed to NaCl. This shift to lower angles has been reported previously and can be related to the formation of a chloride-containing hydrotalcite (Ht_{Cl}) [24]. A possible intermixing with Friedel's salt cannot be excluded, because the peaks of the chloride-containing hydrotalcite are slightly asymmetric, which could indicate the presence of small amounts of Friedel's salt. The TGA signal of the hydrotalcite also changed during chloride exposure. These changes in the TGA signal have previously been reported for pure synthesized hydrotalcite [24], but the temperatures of these peaks in the present study differ from those reported by Ke et al. [24], probably because the hydrotalcite in this study was formed in a

cementitious system rather than as a pure phase. The chloride-uptake of the hydrotalcite was confirmed qualitatively by the SEM-EDS investigations (Figure 8).

4.5. Outlook

This study represents a first step in investigating composite cements containing dolomite and metakaolin with regard to durability. The stability in various environments of hydrotalcite, one of the main reaction products of dolomite in Portland cement-based pastes, indicates that its formation can potentially be beneficial for the durability of the resulting concrete. A next step for evaluating the durability would be to conduct suitable performance tests on concrete with this new composite cement compared with today's commercial cements.

5. Conclusions

This study presents a screening of the stability of the hydrate phase assemblage after selected exposures. Well-hydrated cement paste samples in which 40 wt% of the cement was replaced by dolomite or by a combination of dolomite and metakaolin were investigated after carbonation, leaching, and chloride exposure. The exposed samples were compared to unexposed reference samples. From the results obtained, the following conclusions can be drawn:

- Leaching caused severe decalcification of the C-S-H and decomposition of the portlandite and ettringite. The Mg/Al ratio of the hydrotalcite did not change during leaching.
- Carbonation resulted in an almost complete decomposition of the C-S-H phase and ettringite, and the consumption of the portlandite. Hydrotalcite seemed to resist carbonation without changes in its Mg/Al ratio.
- The exposure to a 2 mol/L NaCl solution resulted in the formation of a chloride-containing hydrotalcite. The Mg/Al ratio of the hydrotalcite did not change during exposure to NaCl.

It can be concluded that the hydrotalcite formed in the reaction of dolomite in a Portland composite cement is a stable hydration product in the environments tested.

6. Acknowledgements

The authors would like to thank the industrial PhD programme of the Norwegian Research Council (Project: 241637) and the Heidelberg Technology Center for their financial support. Alisa Machner would also like to thank Tone Østnor from SINTEF and the student assistants Petter Hemstad and Kristine Nøttveit from NTNU for their help with the various exposures and analyses.

7. References

[1] H.F.W. Taylor, Cement Chemistry, 2nd ed., Telford, London, 1997.

[2] T.F. Sevelsted, J. Skibsted, Carbonation of C–S–H and C–A–S–H samples studied by ^{13}C, ^{27}Al and ^{29}Si MAS NMR spectroscopy, Cem Concr Res 71 (2015) 56–65.

[3] Z. Shi, M.R. Geiker, K. De Weerdt, T.A. Østnor, B. Lothenbach, F. Winnefeld, J. Skibsted, Role of calcium on chloride binding in hydrated Portland cement–metakaolin–limestone blends, Cem Concr Res 95 (2017) 205–216.

[4] O. Wowra, M.J. Setzer, Sorption of chlorides on hydrated cement and C_3S pastes, in: M.J. Setzer, R. Auberg (Eds.), Frost Resistance of Concrete, E & FN Spon, London, 1997, pp. 147–153.

[5] K. De Weerdt, A. Colombo, L. Coppola, H. Justnes, M.R. Geiker, Impact of the associated cation on chloride binding of Portland cement paste, Cem Concr Res 68 (2015) 196–202.

[6] K. De Weerdt, D. Orsáková, M.R. Geiker, The impact of sulphate and magnesium on chloride binding in Portland cement paste, Cem Concr Res 65 (2014) 30–40.

[7] A. Delagrave, J. Marchand, J.-P. Ollivier, S. Julien, K. Hazrati, Chloride Binding Capacity of Various Hydrated Cement Paste Systems, Advanced Cement Based Materials 6 (1997) 28–35.

[8] Matte V., Moranville M., Durability of Reactive Powder Composites: influence of silica fume on the leaching properties of very low water/binder pastes, Cement and Concrete Composites 21 (1999) 1–9.

[9] J.J. Gaitero, I. Campillo, A. Guerrero, Reduction of the calcium leaching rate of cement paste by addition of silica nanoparticles, Cem Concr Res 38 (2008) 1112–1118.

[10] J. Jain, N. Neithalath, Analysis of calcium leaching behavior of plain and modified cement pastes in pure water, Cement and Concrete Composites 31 (2009) 176–185.

[11] A. Machner, M. Zajac, M. Ben Haha, K.O. Kjellsen, M.R. Geiker, K. De Weerdt, Limitations of the hydrotalcite formation in Portland composite cement pastes containing dolomite and metakaolin, Manuscript submitted for publication (2017).

[12] S.J. Mills, A.G. Christy, J.-M.R. Génin, T. Kameda, F. Colombo, Nomenclature of the hydrotalcite supergroup: Natural layered double hydroxides, Mineral. Mag. 76 (2012) 1289–1336.

[13] M. Zajac, S.K. Bremseth, M. Whitehead, M. Ben Haha, Effect of $CaMg(CO_3)_2$ on hydrate assemblages and mechanical properties of hydrated cement pastes at 40 °C and 60 °C, Cem Concr Res 65 (2014) 21–29.

[14] M. Zajac, M. Ben Haha, Hydration of limestone and dolomite cement, in: Proceedings of the 14th International Congress on the Chemistry of Cement, 2015.

[15] M. Zajac, W. Dienemann, G. Bolte, Comparative experimental and virtual investigations of the influence of calcium and magnesium carbonates on reacting cement, in: Proceedings of the 13th International Congress on the Chemistry of Cement, Madrid, 2011.

[16] F. Jin, A. Al-Tabbaa, Evaluation of novel reactive MgO activated slag binder for the immobilisation of lead and zinc, Chemosphere 117 (2014) 285–294.

[17] F. Jin, F. Wang, A. Al-Tabbaa, Three-year performance of in-situ solidified/stabilised soil using novel MgO-bearing binders, Chemosphere 144 (2016) 681–688.

[18] Q. Wang, Z. Wu, H.H. Tay, L. Chen, Y. Liu, J. Chang, Z. Zhong, J. Luo, A. Borgna, High temperature adsorption of CO_2 on Mg–Al hydrotalcite: Effect of the charge compensating anions and the synthesis pH, Catalysis Today 164 (2011) 198–203.

[19] P. Feng, C. Miao, J.W. Bullard, A model of phase stability, microstructure and properties during leaching of portland cement binders, Cement and Concrete Composites 49 (2014) 9–19.

[20] S. Miyata, Anion-Exchange Properties of Hydrotalcite-Like Compounds, Clays and Clay Minerals 31 (1983) 305–311.

[21] L. Châtelet, J.Y. Bottero, J. Yvon, A. Bouchelaghem, Competition between monovalent and divalent anions for calcined and uncalcined hydrotalcite: anion exchange and adsorption sites, Colloids and Surfaces A 111 (1996) 167–175.

[22] O. Kayali, M.S.H. Khan, M. Sharfuddin Ahmed, The role of hydrotalcite in chloride binding and corrosion protection in concretes with ground granulated blast furnace slag, Cement and Concrete Composites 34 (2012) 936–945.

[23] H. Ye, X. Jin, W. Chen, C. Fu, N. Jin, Prediction of chloride binding isotherms for blended cements, Computers and Concrete 17 (2016) 655–672.

[24] X. Ke, S.A. Bernal, J.L. Provis, Uptake of chloride and carbonate by Mg-Al and Ca-Al layered double hydroxides in simulated pore solutions of alkali-activated slag cement, Cem Concr Res 100 (2017) 1–13.

[25] K. De Weerdt, H. Justnes, The effect of sea water on the phase assemblage of hydrated cement paste, Cement and Concrete Composites 55 (2015) 215–222.

[26] B. Lothenbach, P. Durdzinski, K. De Weerdt, Thermogravimetric Analysis, in: K.L. Scrivener, R. Snellings, B. Lothenbach (Eds.), A Practical Guide to Microstructural Analysis of Cementitious Materials, CRC Press Taylor & Francis Group, Boca Raton, 2015, pp. 177–211.

[27] A. Belda Revert, K. De Weerdt, K. Hornbostel, M.R. Geiker, Investigation of the effect of partial replacement of Portland cement by fly ash on carbonation using TGA and SEM-EDS, in: O.M. Jensen, K. Kovler, N. de Belie (Eds.), International RILEM Conference on Materials, Systems and

Structures in Civil Engineering: Conference segment on Concrete with Supplementary Cementitious Materials, Rilem Publications S.A.R.L., 2016, pp. 413–422.

[28] D. Kulik, GEM-Selektor v.3.3, available at: http://gems.web.psi.ch/.

[29] B. Lothenbach, F. Winnefeld, Thermodynamic modelling of the hydration of Portland cement, Cem Concr Res 36 (2006) 209–226.

[30] T. Wagner, D.A. Kulik, F.F. Hingerl, S.V. Dmytrieva, GEM-Selektor geochemical modeling package: TSolMod library and data interface for multicomponent phase models, The Canadian Mineralogist 50 (2012) 1173–1195.

[31] D.A. Kulik, T. Wagner, S.V. Dmytrieva, G. Kosakowski, F.F. Hingerl, K.V. Chudnenko, U.R. Berner, GEM-Selektor geochemical modeling package: Revised algorithm and GEMS3K numerical kernel for coupled simulation codes, Comput Geosci 17 (2013) 1–24.

[32] Thermodynamic database, provided by EMPA, available at: https://www.empa.ch/web/s308/thermodynamic-data.

[33] D.A. Kulik, Improving the structural consistency of C-S-H solid solution thermodynamic models, Cem Concr Res 41 (2011) 477–495.

[34] A. Machner, M. Zajac, M. Ben Haha, K.O. Kjellsen, M.R. Geiker, K. De Weerdt, Chloride-binding capacity of hydrotalcite in cement pastes containing dolomite and metakaolin, Manuscript submitted for publication.

[35] M. Ben Haha, B. Lothenbach, G. Le Saout, F. Winnefeld, Influence of slag chemistry on the hydration of alkali-activated blast-furnace slag – Part I: Effect of MgO, Cem Concr Res 41 (2011) 955–963.

[36] A.M. Harrisson, N.B. Winter, H.F.W. Taylor, Microstructure and Microchemistry of Slag Cement Pastes, Mater. Res. Soc. Symp. Proc. 85 (1986) 213–222.

[37] R. Taylor, I.G. Richardson, R.M.D. Brydson, Composition and microstructure of 20-year-old ordinary Portland cement–ground granulated blast-furnace slag blends containing 0 to 100% slag, Cem Concr Res 40 (2010) 971–983.

[38] M. Ben Haha, B. Lothenbach, G. Le Saout, F. Winnefeld, Influence of slag chemistry on the hydration of alkali-activated blast-furnace slag – Part II: Effect of Al_2O_3, Cem Concr Res 42 (2012) 74–83.

[39] B. Lothenbach, F. Winnefeld, C. Alder, E. Wieland, P. Lunk, Effect of temperature on the pore solution, microstructure and hydration products of Portland cement pastes, Cem Concr Res 37 (2007) 483–491.

[40] C.A. Love, I.G. Richardson, A.R. Brough, Composition and structure of C–S–H in white Portland cement–20% metakaolin pastes hydrated at 25 °C, Cem Concr Res 37 (2007) 109–117.

[41] W. Kunther, Z. Dai, J. Skibsted, Thermodynamic modeling of hydrated white Portland cement–metakaolin–limestone blends utilizing hydration kinetics from ^{29}Si MAS NMR spectroscopy, Cem Concr Res 86 (2016) 29–41.

[42] H. Justnes, Kinetics of Reaction in Cementitious Pastes Containing Silica Fume as Studied by ^{29}Si MAS NMR, in: P. Colombet, H. Zanni, A.R. Grimmer, P. Sozzani (Eds.), Nuclear Magnetic Resonance Spectroscopy of Cement-Based Materials, Springer Berlin Heidelberg, Berlin, Heidelberg, 1998, pp. 245–268.

[43] J.E. Rossen, B. Lothenbach, K.L. Scrivener, Composition of C–S–H in pastes with increasing levels of silica fume addition, Cem Concr Res 75 (2015) 14–22.

[44] A. Dauzères, G. Achiedo, D. Nied, E. Bernand, S. Alahrache, B. Lothenbach, Magnesium perturbation in low-pH concretes placed in clayey environment – solid characterizations and modeling, Cem Concr Res 79 (2016) 137–150.

[45] A. Leemann, P. Nygaard, J. Kaufmann, R. Loser, Relation between carbonation resistance, mix design and exposure of mortar and concrete, Cement and Concrete Composites 62 (2015) 33–43.

[46] E. Garcia, P. Alfonso, M. Labrador, S. Galí, Dedolomitization in different alkaline media: Application to Portland cement paste., Cem Concr Res 33 (2003) 1443–1448.

[47] S. Galí, C. Ayora, P. Alfonso, E. Tauler, M. Labrador, Kinetics of dolomite-portlandite reaction: Application to Portland cement concrete, Cem Concr Res 31 (2001) 933–939.

[48] X. Zhang, F.P. Glasser, K.L. Scrivener, Reaction kinetics of dolomite and portlandite, Cem Concr Res 66 (2014) 11–18.

[49] F. Mittermayr, A. Baldermann, C. Baldermann, G.H. Grathoff, D. Klammer, S.J. Köhler, A. Leis, L.N. Warr, M. Dietzel, Environmental controls and reaction pathways of coupled de-dolomitization and thaumasite formation, Cem Concr Res 95 (2017) 282–293.

[50] L. Chou, R.M. Garrels, R. Wollast, Comparative study of the kinetics and mechanisms of dissolution of carbonate minerals, Chemical Geology 78 (1989) 269–282.

[51] O.S. Pokrovsky, S.V. Golubev, J. Schott, A. Castillo, Calcite, dolomite and magnesite dissolution kinetics in aqueous solutions at acid to circumneutral pH, 25 to 150 °C and 1 to 55 atm pCO_2: New constraints on CO_2 sequestration in sedimentary basins, Chemical Geology 265 (2009) 20–32.

[52] J.W. Morse, R.S. Arvidson, The dissolution kinetics of major sedimentary carbonate minerals, Earth-Science Reviews 58 (2002) 51–84.

[53] G. Fornasari, R. Glöckler, M. Livi, A. Vaccari, Role of the Mg/Al atomic ratio in hydrotalcite-based catalysts for NOx storage/reduction, Applied Clay Science 29 (2005) 258–266.

[54] S.-D. Wang, Alkali-activated slag: hydration process and development of microstructure, Advances in Cement Research 12 (2000) 163–172.

[55] S.-D. Wang, K.L. Scrivener, Hydration products of alkali activated slag cement, Cem Concr Res 25 (1995) 561–571.

[56] S. Adu-Amankwah, L. Black, M. Zajac, The effect of sulphates on limestone containing composite cements, in: University of Aberdeen (Ed.), 35th Cement and Concrete Science Conference, 2015.

[57] R. Allmann, H.P. Jespen, Die Struktur des Hydrotalkits, Neues Jahrbuch für Mineralogie (Monatshefte) 12 (1969) 544–551.

8. Tables

Table 1: Chemical composition of the Portland cement, dolomite, limestone and metakaolin used, determined with XRF [wt%] and their Blaine specific surface areas [m^2/kg].

Oxide	**C** Portland cement	**D** Dolomite	**L** Limestone	**M** Metakaolin
SiO_2	19.91	0.52	0.12	52.18
Al_2O_3	5.15	0.01	0.06	44.92
TiO_2	0.282	0.00	0.00	1.14
MnO	0.062	0.00	0.00	0.00
Fe_2O_3	3.42	0.04	0.03	0.62
CaO	62.73	31.52	55.12	0.12
MgO	2.34	20.14	0.41	0.04
K_2O	1.09	0.00	0.01	0.18
Na_2O	0.48	0.00	0.00	0.17
SO_3	3.16	0.00	0.02	0.14
P_2O_5	0.109	0.01	0.00	0.07
LOI	1.07	46.79	43.57	0.29
Sum (1050°C)	**99.80**	**99.03**	**99.34**	**99.87**
Blaine [m^2/kg]	**416**	**340**	**370**	**987**

Table 2: Overview of the various binder compositions investigated [wt%]. The sulphate content of the cement was set to 3.2 wt%.

Name	**C** Portland cement	**D** Dolomite	**L** Limestone	**M** Metakaolin
60C40D	60	40	-	-
60C35D5M	60	35	-	5
60C40L	60	-	40	-
60C35L5M	60	-	35	5

Table 3: Overview of the various sample preparation stages and phase assemblage investigations with XRD and TGA.

Sample preparation stage	**XRD & TGA investigation**
Paste mixing 1st curing at 60°C for 3 months Grinding & re-hydration	
	α
2nd curing at 60°C for 4 months Transferring samples (20°C, 2 weeks)	
	β
Start of exposure (at 20 °C)	
End of exposure	**γ**

Table 4: Mg/Al ratios of the hydrotalcite formed in the samples 60C40D and 60C35D5M after leaching, carbonation, or chloride exposure. As reference, the Mg/Al ratios of the hydrotalcite in samples from an earlier study are given [11].

	Mg/Al	
Exposure	**60C40D**	**60C35D5M**
Reference	3.2	2.4
Leaching	3.0	2.6
Carbonation	3.1	2.4
NaCl	3.2	2.4

9. Figures

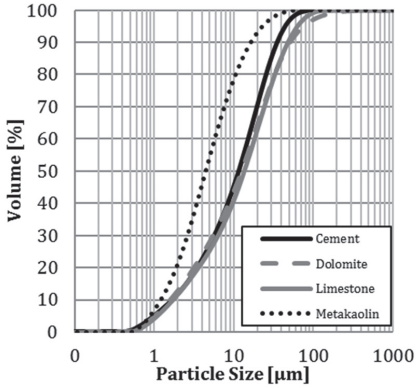

Figure 1: Particle size distributions of the materials used, determined using laser diffraction.

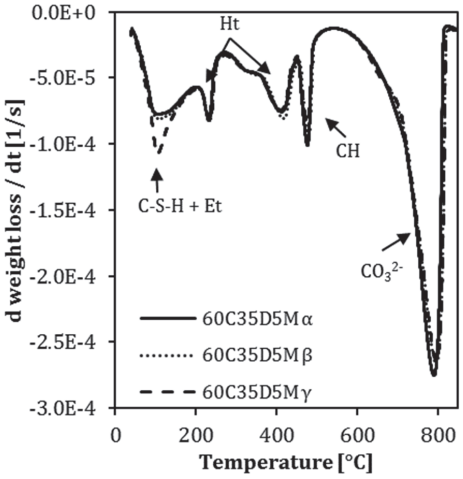

Figure 2: DTG curves of the various stages of sample preparation (α, β, γ, see Table 3) of the reference samples 60C35D5M.

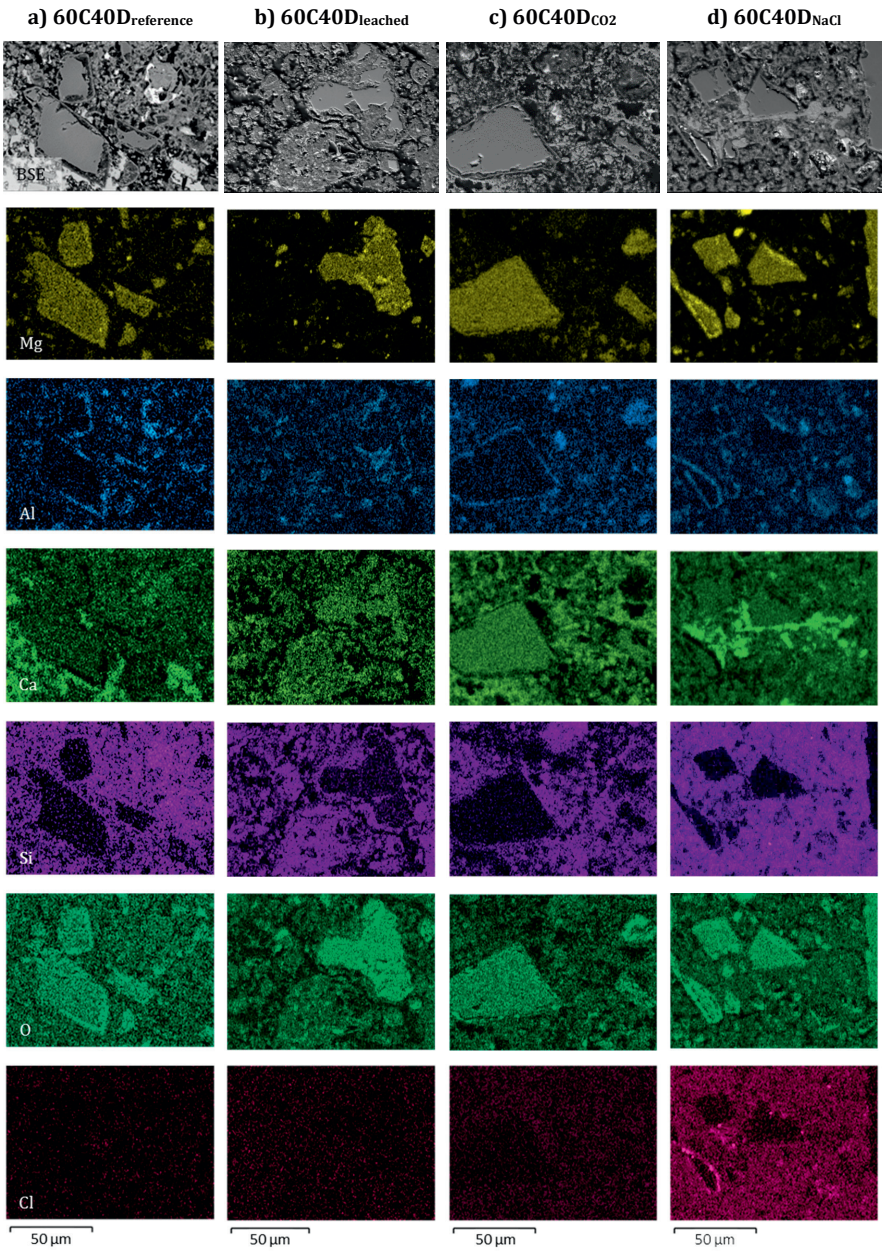

Figure 3: BSE image and elemental maps of magnesium, aluminium, calcium, silicon, oxygen, and chlorine for the samples 60C40D$_{reference}$, 60C40D$_{leached}$, 60C40D$_{CO2}$, and 60C40D$_{NaCl}$. The unexposed reference sample is from an earlier study [11].

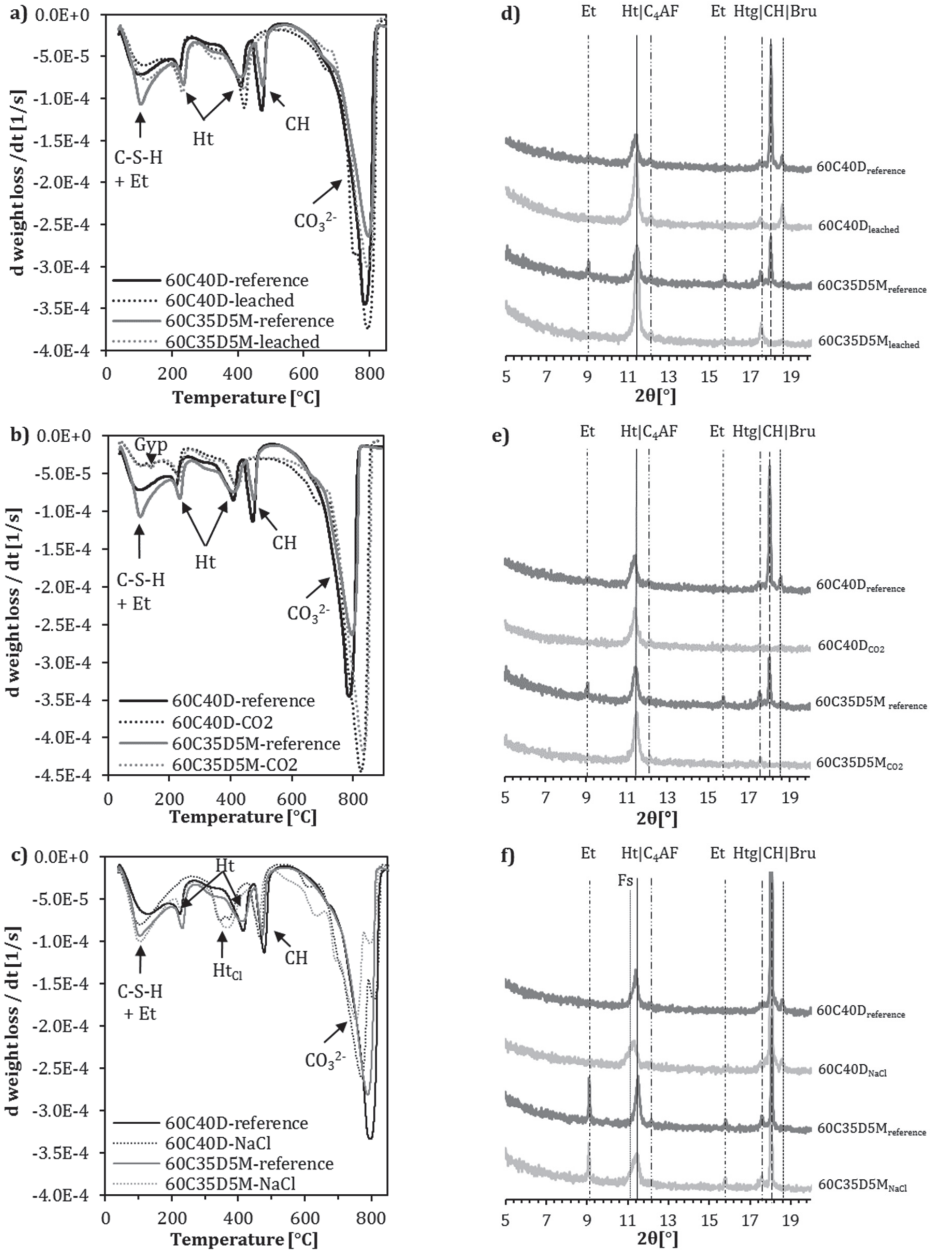

Figure 4: Phase assemblage of the samples 60C40D and 60C35D5M after leaching, carbonation, or chloride exposure determined with TGA (from 40–900 °C) and XRD (shown from 5–19.5 °2θ). The results of unexposed reference samples are also shown. The following abbreviations are used: ettringite (Et), hydrotalcite (Ht), chloride-containing hydrotalcite (Ht_{Cl}), portlandite (CH), carboantes (CO_3^{2-}), Friedel's salt (Fs), ferrite (C_4AF), siliceous hydrogarnet (Htg), brucite (Bru).

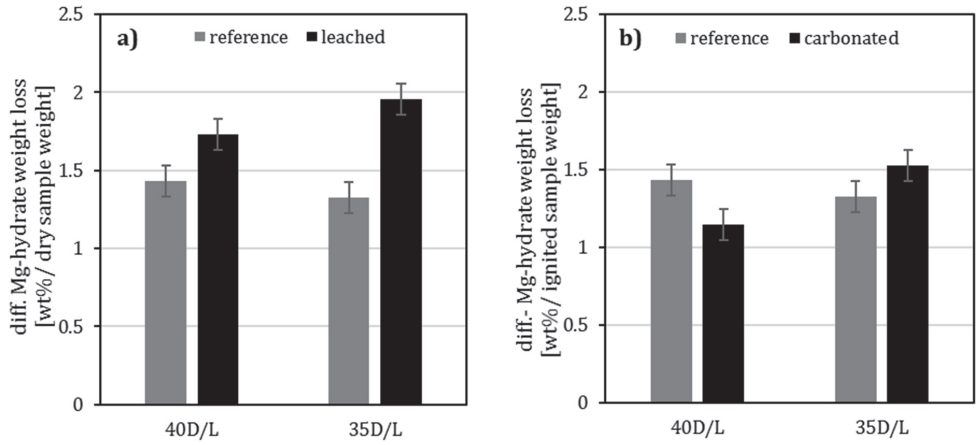

Figure 5: Difference in the weight loss in the hydrotalcite temperature region between samples containing dolomite and limestone in the unexposed reference samples and the exposed samples after a) leaching and b) carbonation.

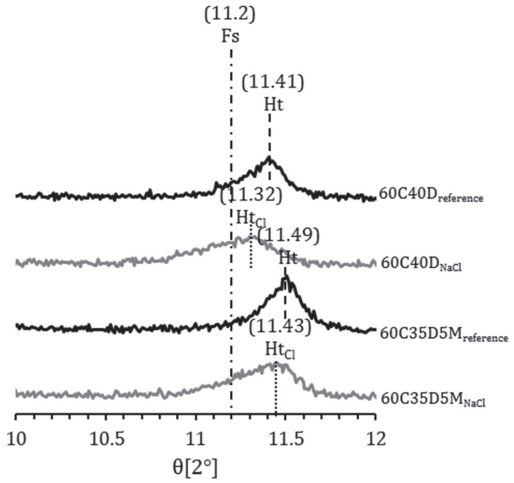

Figure 6: XRD patterns (zoomed in to 10-12 °2θ) of the samples 60C40D$_{NaCl}$, 60C35D5M$_{NaCl}$, and their reference samples exposed to deionized water.

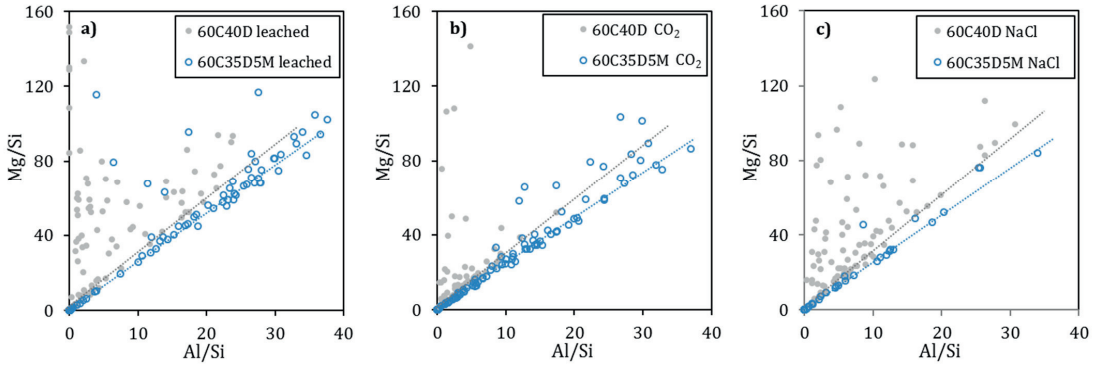

Figure 7: Mg/Si ratio over the Al/Si ratio for the point analyses of the reaction rims around the dolomite grains of samples 60C40D and 60C35D5M after a) leaching, b) carbonation, and c) chloride exposure.

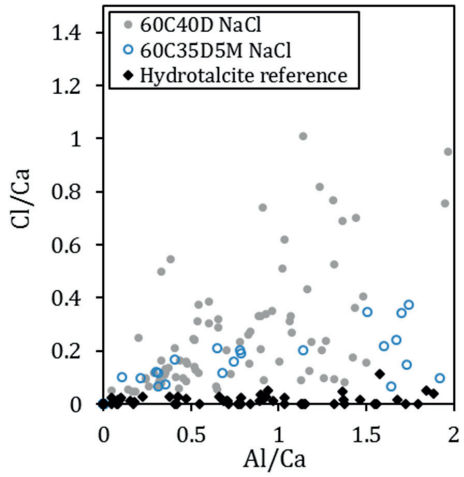

Figure 8: Cl/Ca ratio over the Al/Ca ratio for the point analyses of the reaction rims around the dolomite grains of samples 60C40D$_{NaCl}$ and 60C35D5M$_{NaCl}$ and the unexposed reference sample [11].

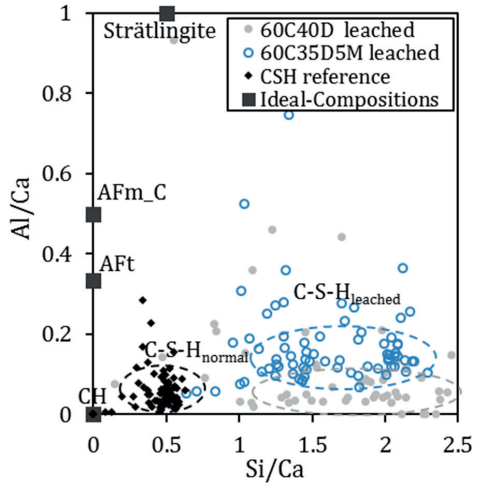

Figure 9: Al/Ca ratio over the Si/Ca ratio for the point analyses of the matrix of the leached samples 60C40D and 60C35D5M. The results of the C-S-H point analyses from an earlier study are shown as a reference for samples that have not been leached [11].

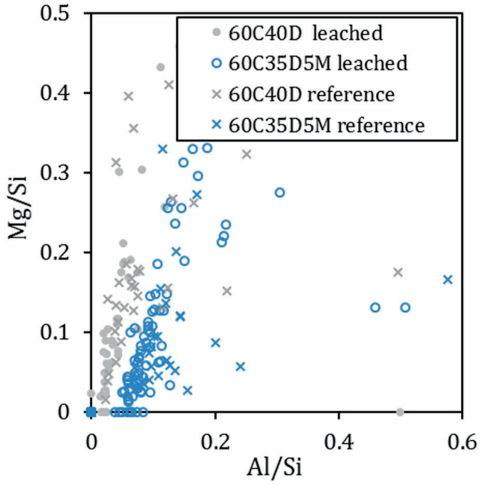

Figure 10: Mg/Si ratio over the Al/Si ratio for the point analyses of the matrix of the leached samples 60C40D and 60C35D5M. The results of the C-S-H point analyses from an earlier study are shown as a reference for samples that have not been leached [11].

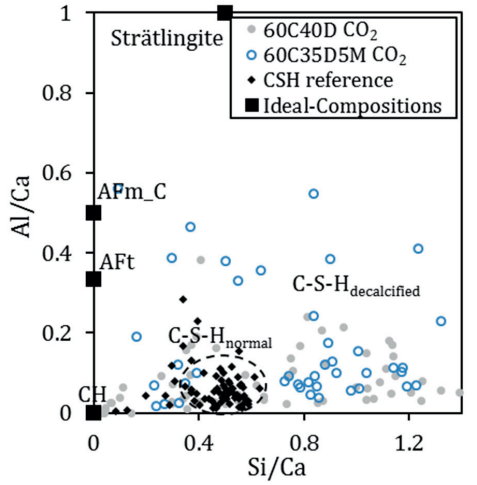

Figure 11: Al/Ca ratio over the Si/Ca ratio for the point analyses of the matrix of the carbonated samples 60C40D and 60C35D5M. The results of the C-S-H point analyses from an earlier study are shown as a reference for samples that have not been carbonated [11].

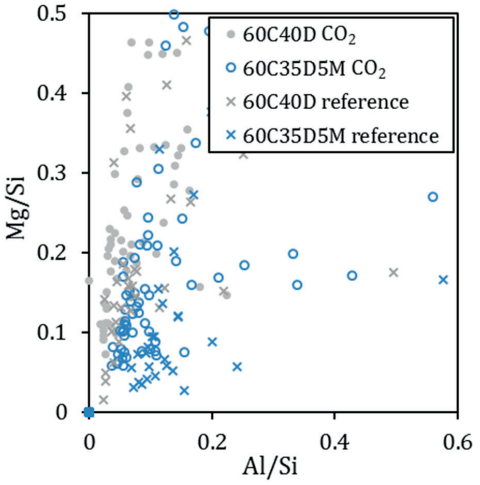

Figure 12: Mg/Si ratio over the Al/Si ratio for the point analyses of the matrix of the carbonated samples 60C40D and 60C35D5M. The results of the C-S-H point analyses from an earlier study are shown as a reference for samples that have not been carbonated [11].

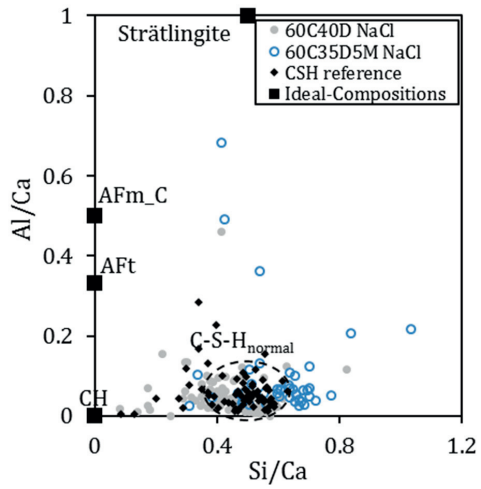

Figure 13: Al/Ca ratio over the Si/Ca ratio for the point analyses of the matrix of the samples 60C40D and 60C35D5M exposed to NaCl. The results of the C-S-H point analyses from an earlier study are shown as a reference for unexposed samples [11]

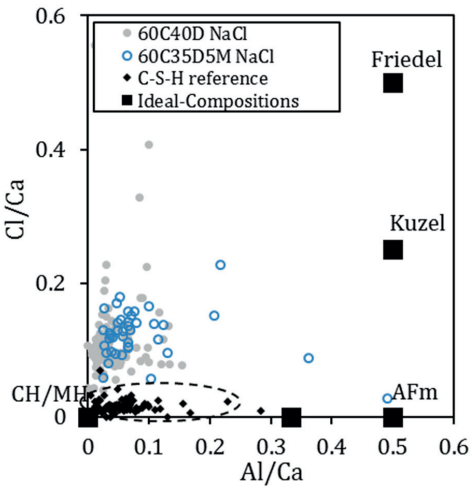

Figure 14: Cl/Ca ratio over the Al/Ca ratio for the point analyses of the matrix of the samples 60C40D and 60C35D5M exposed to NaCl. The results of the C-S-H point analyses from an earlier study are shown as a reference for unexposed samples [11]

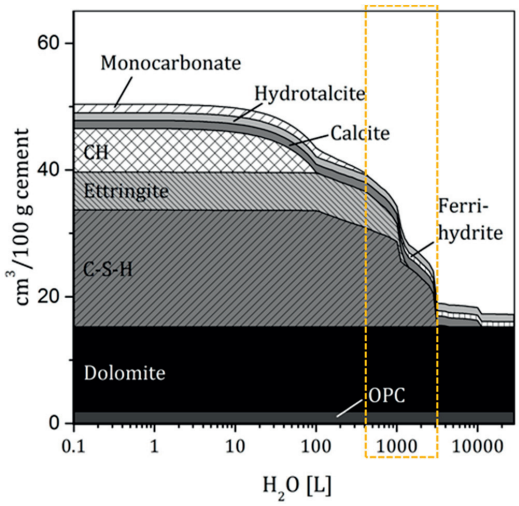

Figure 15: Results of the thermodynamic modelling of the effect of leaching on the phase assemblage in sample 60C40D. The dashed rectangle indicates the phase assemblage experimentally observed with TGA and XRD.

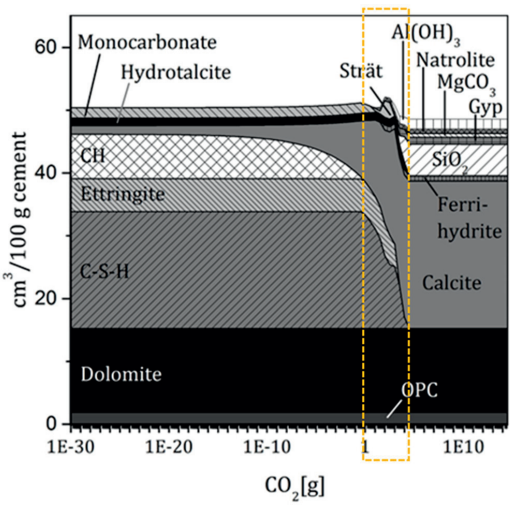

Figure 16: Results of the thermodynamic modelling of the effect of carbonation on the phase assemblage in sample 60C40D. The dashed rectangle indicates the phase assemblage experimentally observed with TGA and XRD

10. Appendix

Table A.1: Ti and Fe contents [wt%] on the ignited weight basis of the various samples determined with XRF and the weight losses of the samples after leaching ($\Delta w_{leached}$) calculated with Eq. 2 [wt%].

		60C40D	60C35D5M	60C40L	60C35L5M	Average
Ti	$Ti_{reference}$	0.14	0.19	0.14	0.19	
	$Ti_{leached}$	0.19	0.29	0.22	0.26	
	$Ti_{reference}/Ti_{leached}$	0.74	0.65	0.66	0.72	
	$\Delta w_{leached}$	**26**	**35**	**34**	**28**	**30±4**
Fe	$Fe_{reference}$	1.70	1.77	1.71	1.74	
	$Fe_{leached}$	2.27	2.83	2.38	2.45	
	$Fe_{reference}/Fe_{leached}$	0.75	0.63	0.72	0.71	
	$\Delta w_{leached}$	**25**	**37**	**28**	**29**	**30±5**

Table A.2: Overview of the $w_{Ht\text{-}measured}$, w_{900}, and BW values of the various samples used for the calculations in Eq. 1 and Eq.3.

Sample	Exposure	$w_{Ht\text{-}measured}$ [wt%]	w_{900} [wt%]	BW [wt%]
60C40D	reference	1.5	67.3	14.2
	leached	2.5	67.8	12.8
	CO_2	1.0	61.6	9.1
60C35D5M	reference	1.4	68.3	15.8
	leached	2.7	65.6	13.7
	CO_2	1.3	63.4	9.7
60C40L	reference	0.3	68.3	13.7
	leached	0.3	66.9	10.2
	CO_2	0.1	62.1	6.2
60C35L5M	reference	0.3	69.7	13.9
	leached	0.4	69.2	11.4
	CO_2	0.1	64.0	7.1

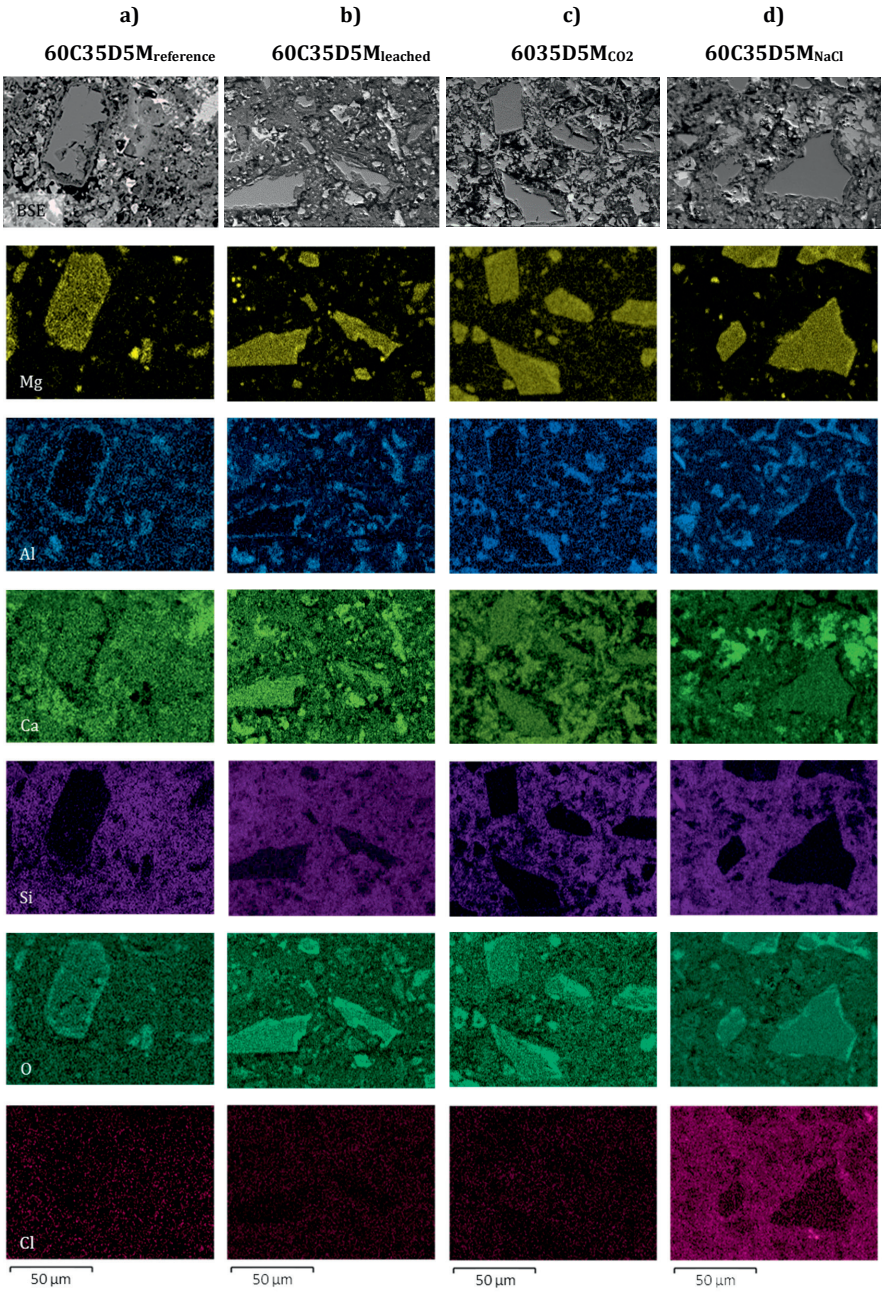

Figure A.1: BSE image and elemental maps of magnesium, aluminium, calcium, silicon, oxygen, and chlorine for the samples 60C35D5M$_{reference}$, 60C35D5M$_{leached}$, 60C35D5M$_{CO2}$, and 60C35D5M$_{NaCl}$. The unexposed reference sample is from an earlier study [11].

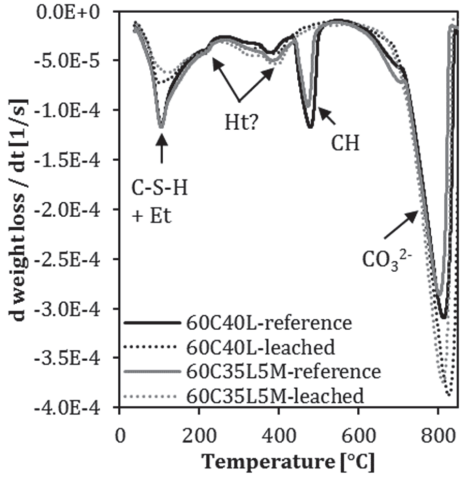

Figure A.2: DTG curves of the samples 60C40L and 60C35L5M after leaching and their unexposed reference samples.

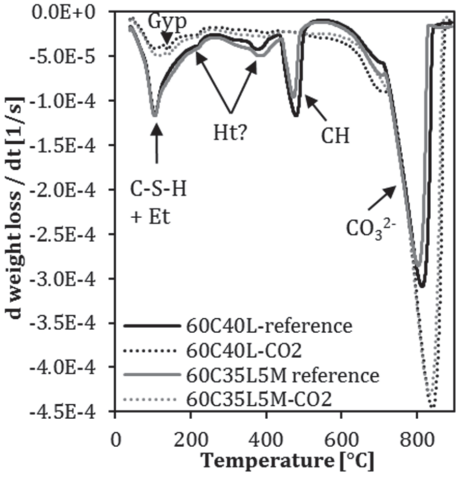

Figure A.3: DTG curves of the samples 60C40L and 60C35L5M after carbonation and their unexposed reference samples.

6035D5M$_{CO2}$

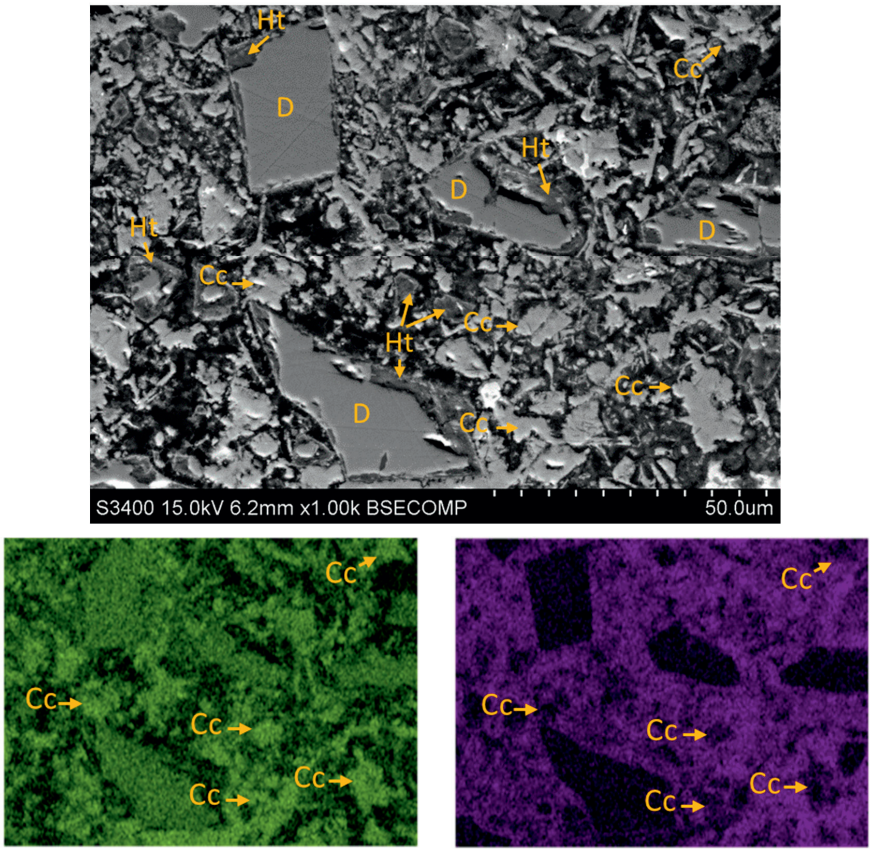

Figure A.4: BSE image and elemental maps of calcium and silicon for sample 60C35D5M CO_2. Areas of dolomite (D), calcite (Cc) and hydrotalcite (Ht) are indicated.

Paper IV

Chloride-binding capacity of hydrotalcite in cement pastes containing dolomite and metakaolin

Machner, A., Zajac, M., Ben Haha, M., Kjellsen, K.O., Geiker, M.R., De Weerdt, K.
Revised version submitted to Cement and Concrete Research (January 2018)

Chloride-binding capacity of hydrotalcite in cement pastes containing dolomite and metakaolin

Alisa Machner[1,2,*], Maciej Zajac[3], Mohsen Ben Haha[3], Knut O. Kjellsen[1], Mette R. Geiker[2], Klaartje De Weerdt[2]

[1]Norcem AS, R&D, Setreveien 2, P.O. Box 38, 3991 Brevik, Norway
[2]NTNU Department of Structural Engineering, Richard Birkelandsvei 1A, 7491 Trondheim, Norway
[3]Heidelberg Technology Center GmbH, Oberklammweg 2-4, 69181 Leimen, Germany

*Corresponding author: alisa.machner@ntnu.no
+47 45394622
ORCID-ID: 0000-0002-6334-5116

ABSTRACT

In this study, we investigated well-hydrated cement pastes containing dolomite and metakaolin cured at 38 °C or 60 °C, which were exposed to NaCl or $CaCl_2$ solutions of various concentrations. We determined the chloride-binding capacity, the phase assemblage and the composition of hydration phases formed. The dolomite reaction led to the formation of hydrotalcite, which contributed considerably to the chloride binding of the pastes. When the samples were exposed to $CaCl_2$, significantly more chlorides were bound in the hydrotalcite than when the samples were exposed to NaCl. It was shown that hydrotalcite contained a similar amount of chloride per mol compared to Friedel's salt when exposed to $CaCl_2$. By mass balance calculations, it was shown that the hydrotalcite formed in the samples containing dolomite can contribute to the chloride binding of the cement pastes to a similar extent as the Friedel's salt formed in the samples containing limestone.

Keywords:

EDX (B), Thermal Analysis (B), X-Ray Diffraction (B), Durability (C), Blended Cement (D)

1 INTRODUCTION

One of the main deterioration mechanisms for reinforced concrete structures is steel reinforcement corrosion. Reinforcement steel in sound concrete is passivated, i.e. does not corrode, due to the high pH of the concrete pore solution. However, in the presence of a sufficient level of chlorides, the steel is de-passivated and corrosion can occur. During the exposure to e.g. sea water or de-icing salts, chlorides ingress through the concrete cover towards the steel. Some chlorides will be free in the pore solution and some will interact with the hydrates in cement paste. In order to estimate the service life of reinforced concrete structures exposed to chlorides, we need to understand the interaction between concrete and chlorides.

Due to the increasing demand for cements and the need to reduce CO_2 emissions during production, new composite cements containing supplementary cementitious materials (SCMs) are being developed. In order to use these cements in reinforced concrete structures exposed to harsh environments such as marine exposure, there is a need to understand how these new binders interact with chlorides. In this study, we used dolomite and a combination of dolomite and metakaolin as SCMs to replace 40%wt of a Portland cement. We investigated the chloride-binding capacity of the hydrate phase assemblage for these new cements.

In an ordinary Portland cement, chloride ions have been reported to be physically adsorbed on the C-S-H phase or chemically bound by the formation of chloride-containing AFm phases, e.g. Friedel's salt ($3CaO{\cdot}Al_2O_3{\cdot}CaCl_2{\cdot}10H_2O$). The use of SCMs can change the phase assemblage of the hydrated cement paste and thereby its chloride-binding capacity [1].

The addition of metakaolin has been shown to improve the chloride-binding capacity of cement paste. This has been explained with reference to the additional alumina provided by the reaction of metakaolin, which results in the formation of additional Friedel's salt [2,3]. Similar results have been reported for other alumina-delivering SCMs, such as fly ash or ground granulated blast-furnace slags (GGBFS) [1,4–7]. Moreover, the reaction of metakaolin results in the formation of additional C-S-H, which may adsorb additional chlorides [8].

The addition of dolomite has been shown, depending on curing temperature, curing time, and metakaolin content, to result in the formation of significant amounts of a hydrotalcite-like phase (in the following referred to simply as hydrotalcite) [9,10]. Hydrotalcite is a mineral in the group of layered double hydroxides (LDHs) containing magnesium and aluminium, with the general formula $[Me^{2+}_{1-x}Me^{3+}_{x}(OH)_2]^{x+}\ [A^{m-}]_{x/m}{\cdot}nH_2O$. Its crystal structure can be derived from that of brucite. The main layer consists of metals (here abbreviated with Me), specifically magnesium

(Me^{2+}) and aluminium (Me^{3+}) hydroxide octahedra. The substitution of aluminium for magnesium in the main layer charges this layer positively. To maintain electrical neutrality, the interlayer incorporates monovalent or divalent anions (here abbreviated with A) , such as OH^-, Cl^-, CO_3^{2-} or SO_4^{2-}.

Several authors observed considerable chloride binding of hydrotalcite, either synthesized as a pure phase [11–13] or formed in GGBFS cement pastes [14,15]. We will investigate chloride binding of hydrotalcite originating from dolomite reaction in composite cements. In this system, the composition of the hydrotalcite differs from the before named studies both by the presence of carbonates or by the Mg/Al ratio of the hydrotalcite. Both factors influence the chloride-binding capacity of hydrotalcite.

Divalent ions, like CO_3^{2-} are more easily incorporated than monovalent ions, like Cl^- [11,12], so CO_3^{2-} ions are seldom exchanged with chloride ions in synthesized hydrotalcite-like phases, and the presence of carbonate ions consequently reduces the chloride-binding capacity [12,13].

A higher degree of aluminium substitution in the main layer, leading to a lower Mg/Al ratio of the hydrotalcite, increases the positive charge of the main layer. Because the interlayer seeks electrical neutrality, more anions, e.g. chlorides, are incorporated in the interlayer of hydrotalcite with a lower Mg/Al ratio [16]. The reduction of the Mg/Al ratio of the hydrotalcite can be caused by the presence of an aluminium-delivering SCM [10,17,18].

Moreover, it was reported that chlorides are also physically adsorbed on the surface of hydrotalcite adsorption [13,15].

The chloride-binding capacity of cements depends strongly on the cation associated with the chloride anion. Several authors have reported significantly greater chloride binding when samples were exposed to solutions of $CaCl_2$ or $MgCl_2$ rather than NaCl [1,3,19–23]. This difference has been largely attributed to the difference in the adsorption of chlorides onto the C-S-H and larger amount Friedel's salt. We will investigate whether the cation also influences the binding capacity of the hydrotalcite.

This study focuses on the impact of the hydrotalcite formed by the reaction of dolomite fines in the cement paste on the chloride binding of composite cement pastes. For this, cement paste samples in which 40%wt of the Portland cement was replaced by dolomite or by a combination of dolomite and metakaolin were investigated. Cement paste samples containing limestone instead of dolomite and a pure Portland cement sample were used as references. In order to be

able to study the effect of hydrotalcite, we needed samples containing sufficient amounts of hydrotalcite. Therefore, we investigates binder compositions containing dolomite and little or no metakaolin and cured at elevated temperatures, which according to an earlier study yielded considerable hydrotalcite formation [10]. Chloride-binding isotherms were experimentally obtained and related to the phase assemblage and phase composition of the solids obtained with XRD, TGA, and SEM-EDS. Additionally, the contribution of hydrotalcite, Friedel's salt, and C-S-H to the chloride binding of the cement pastes was evaluated using a mass balance approach.

2 EXPERIMENTAL

2.1 MATERIALS & SAMPLE PREPARATION

The materials used in this study were Portland cement (C) supplied by Norcem, to which gypsum but no limestone was added during grinding, natural dolomite (D), and natural limestone (L) supplied by Miljøkalk AS, and laboratory-grade metakaolin (M) supplied by Imerys (Metastar501). Table 1 shows the chemical composition, determined by X-ray fluorescence (XRF), of the materials used and their Blaine specific surface area. The particle size distributions of the materials used, determined by laser diffraction (Malvern Mastersizer 2000E), are shown in Figure 1. Table 2 gives an overview of the various sample compositions prepared. We replaced 40%wt of the Portland cement with either dolomite (60C40D) or a combination of 35%wt dolomite and 5%wt metakaolin (60C35D5M). The equivalent samples containing limestone (60C40L and 60C35L5M) and the Portland cement sample (100C) were used as references. Cement pastes were prepared with a w/b ratio of 0.5 for all binder compositions in a high-shear mixer (Braun MR5550CA). The mixing procedure was mixing for 30 s, resting for 5 min and mixing again for 60 s. The resting time of 5 min was chosen to check for false set of the paste. The resulting pastes were cast in 125 mL polyethylene screw-lid bottles, which were sealed with parafilm and stored, immersed up to their bottleneck, in water at 38 °C or 60 °C. After three months of curing, the hydrated cement pastes were removed from the bottles, crushed in a jaw-crusher and then ground in a rotating disc mill to a particle size <1 mm. The crushed cement paste was poured into 1 L screw-lid polypropylene bottles and 30%wt of deionized water relative to the crushed cement paste weight was added. The bottles were sealed with parafilm and cured for another four months at the respective temperatures. After a total of seven months of curing, the bottles were stored at 20 °C for two weeks before starting exposure at 20 °C. This sample preparation led to moist-sand like cement pastes. We chose this way of preparing the samples to maximize the degree of hydration of the binder before exposure and thus minimize any continued hydration during exposure.

2.2 CHLORIDE EXPOSURE

For the exposure, 30 g of the moist-sand-like cement paste was poured into 45 mL centrifuge tubes, to which 15 mL of exposure solution was added using a volumetric pipette. The exposure solutions were solutions of NaCl or $CaCl_2$ with chloride concentrations ranging from 0.25 to 3 mol/L, prepared with deionized water and laboratory-grade salts of NaCl or $CaCl_2 \cdot 2H_2O$ (supplied by Merck). The reference samples of all mixes were exposed to 15 mL of deionized water. The closed centrifuge tubes were shaken weekly and stored at 20 °C for at least one month to reach equilibrium prior to the investigation.

2.3 METHODS

2.3.1 Investigation of the supernatant

The chloride concentration in the supernatant was determined by potentiometric titration. The samples were centrifuged at 4000 rpm for 2.5 min. A known volume (0.2–0.8 mL, depending on the chloride concentration of the exposure solution) of the supernatant was pipetted into a measurement beaker, to which 1 mL of HNO_3 (65% supplied by Merck, and diluted 1:10), 2.5 mL of 0.2% polyvinyl alcohol (supplied by Merck, 2 g was dissolved in 1 L deionized water), and approx. 20 mL of deionized water were added. The chloride content was measured with a Titrando 905 titrator from Metrohm against a 0.1 mol/L $AgNO_3$ solution (Titrisol, supplied by Merck).

During the exposure of the cement paste, chlorides from the solution are taken up by the hydrates of the cement paste. The chloride concentration in the solution will therefore decrease. The amount of bound chlorides ($N_{Cl,bound}$) can be calculated as g/g cement paste using Eq. (1) [21].

$$N_{Cl,bound} = \frac{\left(C_{Cl,free} - C_{Cl,eq}\right) \cdot \left(V_{H_2O} + V_{Cl,added}\right)/1000 \cdot M_{Cl}}{m_{sample} - m_{H_2O}} \quad (1)$$

where $C_{Cl,free}$ is the actual concentration of free chlorides present at the beginning of the exposure, which can be calculated using Eq. (2); $C_{Cl,eq}$ is the chloride concentration of the supernatant measured at equilibrium; V_{H2O} is the volume of free water in 30 g of the moist-sand-like hydrated cement paste before exposure; $V_{Cl,added}$ is the volume of exposure solution added (15 mL); M_{Cl} is the molar mass of chlorine (35.453 g/mol); m_{sample} is the mass of the sample added to the centrifuge tube (30 g); and m_{H2O} is the mass of free water in this 30 g of hydrated cement paste.

$$C_{Cl,free} = \frac{C_{Cl,added} \cdot V_{Cl,added}}{V_{H_2O} + V_{Cl,added}} \quad (2)$$

where $C_{Cl,added}$ is the concentration of chlorides in the exposure solution, which was measured with potentiometric titration prior to exposure. V_{H2O} was assumed to be equal to m_{H2O} and was determined by the weight loss of the moist-sand-like hydrated cement pastes after drying at 40 °C in a TGA until constant weight (Table 3).

A selection of samples was analysed in triplets. The average standard deviation obtained for the titrations of samples exposed to NaCl was approx. 10%. For samples exposed to $CaCl_2$, the average standard deviation of the titration experiments was approx. 5%. The standard deviations are indicated with by the error bars in the respective figures.

The experimental data obtained from the titration experiments with chloride concentrations from 0–3 mol/L were fitted with a Langmuir isotherm as shown in Eq. (3) [24].

$$N_{Cl,bound} = \frac{\alpha \cdot C_{Cl,free}}{(1 + \beta \cdot C_{Cl,free})} \quad (3)$$

where $N_{Cl,bound}$ are the amount of bound chlorides, $C_{Cl,free}$ the concentration of free chlorides before exposure, as described above, and α and β are fitting parameters, which depend on the binder composition [24].

After centrifuging, the pH of the supernatant was measured as well. This was done using a 6.0255.100 Profitrode from Metrohm. The measurements of the pH were performed in the laboratory at 20 °C. The electrode was calibrated on every measurement day with buffer solutions of pH 7, 10 and 13.

2.3.2 Investigation of the solids

The solid fraction was investigated on all samples exposed to a chloride concentration of 2 mol/L for NaCl and $CaCl_2$. The reference samples exposed to deionized water were also investigated. Approx. 6 g of the 30 g of each hydrated cement paste sample was taken out of the centrifuge tube after all the investigations of the liquids had been performed. To stop the hydration and remove the water or chloride solution, the wet hydrated cement paste was immersed in 100 mL isopropanol, shaken for 30 s, and left to rest for 5 min before the isopropanol was decanted. The isopropanol treatment was then repeated. After that, the sample was immersed in 20 mL petroleum ether, stirred for 30 sec, and left to rest again for 5 min. The petroleum ether was

filtrated off using a vacuum filtration unit, and the samples were dried in a desiccator overnight under a slight vacuum (-0.2 bar) applied using a water pump. The dried samples were ground to a particle size <63 µm and then analysed with TGA or XRD.

For the thermogravimetric analysis (TGA), approx. 150 mg of each ground sample was poured into a 600 µl corundum crucible. The weight loss was measured from 40–900 °C, with a heating rate of 10 °C/min in a Mettler Toledo TGA/DSC3+ device. During the experiments, the measurement cell was purged with 50 mL/min N_2 gas. TGA was used to identify changes in the phase assemblage and to quantify the amount of bound water and portlandite in each of the mixes investigated.

The derivate curves of the TG signal, the DTG curves, were used to detect phase changes. The DTG curves can be divided into several temperature intervals, in which the decomposition of specific phases can be detected as a weight loss. These temperature intervals were used to identify various hydration phases as suggested by Lothenbach et al. [25]. The first weight loss peak at around 100 °C is related to the ettringite (Et) decomposition and the beginning of the dehydroxylation of the C-S-H phase. C-S-H decomposes gradually between 40 °C and 600 °C and appears as a polynomial baseline under the other peaks. Hydrotalcite (Ht) shows two mass loss events, the first at approx. 220 °C and the second at around 400 °C. The subsequent sharp peak between approx. 400 °C and 550 °C is related to the decomposition of portlandite (CH). Above 550 °C, carbonates decompose by emitting CO_2. To make it possible to quantify the amount of bound water ($H_{dry\ binder\ weight}$) using Eq. (4) [26], the weight loss between 50 °C and approx. 550 °C was determined with a horizontal step. The weight loss related to the amount of portlandite was measured by integrating the DTG curve between approx. 400 °C and 550 °C with a linear baseline. This method is assumed to give similar results as using a tangential step and excludes the weight loss from the C-S-H decomposition still ongoing in this temperature region [25]. The portlandite content ($CH_{dry\ binder\ weight}$) can be calculated using Eq. (5) [26], where $M(Ca(OH)_2)$=74 g/mol and $M(H_2O)$=18 g/mol. Both quantifications in Eq. (4) and Eq. (5) are normalized to the dry binder weight, which is the sample weight at 550 °C and assumed to remain constant during hydration [26].

$$H_{dry\ binder\ weight} = \frac{w_{50} - w_{550}}{w_{550}} \tag{4}$$

$$CH_{dry\ binder\ weight} = \frac{w_{400} - w_{550}}{w_{550}} \cdot \frac{M(Ca(OH)_2)}{M(H_2O)} \tag{5}$$

The error for the $H_{dry\ binder\ weight}$ and $CH_{dry\ binder\ weight}$ is estimated to be 1% wt. The errors are indicated with the error bars in the respective figures.

To identify the gasses leaving the samples at a certain temperature interval, another TGA device (STA 449 C Jupiter from Netzsch) coupled with a quadrupole mass spectrometer unit (QMS 403 C Aëolos from Netzsch) was used. For these measurements, approx. 20 mg of selected samples were poured into corundum crucibles. The samples were analysed from 40–900 °C with a heating rate of 10 °C/min. During the measurement, the measurement cell was purged with 30 mL/min N_2 gas.

The X-ray diffraction (XRD) analyses were carried out using a D8 Focus from Bruker built with a Bragg-Brentano θ–2θ geometry, a LynxEye detector, and a goniometer radius of 200.5 mm. The samples were measured between 5 °2θ and 55 °2θ using Cu-Kα radiation with a wavelength of approx. 1.54 Å as X-ray source, a step size of 0.01 °2θ, and a sampling time per step of 0.5 s. The ground samples were front-loaded into the sample holders and queued in a sample changer until measurement (max. 4.5 h). The XRD plots were qualitatively evaluated using DIFFRAC.EVA V4.0 software from Bruker.

For the investigation of the hydrate phase assemblage with scanning electron microscopy (SEM), some of the hydration-stopped and dried but not ground samples were cast in epoxy, polished and carbon-coated. The investigated samples included all samples containing dolomite (60C40D and 60C35D5M) and the samples 60C35L5M exposed to NaCl or $CaCl_2$. Elemental mapping and point analyses were carried out using a Hitachi S-3400N electron microscope equipped with an energy dispersive spectrometer (EDS) from Oxford Instruments. The SEM was operated at an accelerating voltage of 15 keV, a working distance of 5 mm for taking the BSE images, and a working distance of 10 mm for operating the EDS. As reference samples, the results from a previous study [10] were used. In that study, the samples had similar binder compositions and were cured sealed at 100% RH for 360 days at 60 °C or 38 °C and prepared for SEM-EDS analysis in a similar way.

2.3.3 Thermodynamic modelling

The Gibbs free energy minimization program GEMS [27,28] was used to model the activity of CO_3^{2-} ions in the pore solution of a model system with increasing additions of NaCl or $CaCl_2$. The model system used consisted of 100 H_2O and 20 g $CaCO_3$. Because 0.03 g NaOH and 0.06 g KOH were included in the model, the pH at the starting point of the modelling was high (pH 13.9), which is similar to the pH in cementitious systems.

2.3.4 Mass balance calculations

The contribution of the various hydration phases to the chloride binding of the cement pastes was estimated with mass balance calculations for the samples 60C40D (60 °C) and 60C40L (38 °C) exposed to NaCl or $CaCl_2$. We used mass balance calculations instead of the thermodynamic

modelling software GEMS for this due to a lack of thermodynamic data for the chloride-containing hydrotalcite or the chloride uptake of the C-S-H. In a first step, the amount or volume of the various phases present in the system was calculated based on the following assumptions:

- For the cement, the QXRD results of a similar cement clinker and gypsum [10] were used as input for the calculations. The reaction degree of belite was set to 90% and the ferrite and periclase were assumed to not have reacted. All other components of the cement clinker and the gypsum were assumed to have reacted fully. For the dolomite ($CaMg(CO_3)_2$) a reaction degree of 30% was assumed when cured at 60 °C, and for the limestone ($CaCO_3$)a reaction degree of 5% was assumed when cured at 38 °C. The ideal stoichiometric compositions of dolomite and limestone were used as input for the calculations.
- The amount of calcium, aluminium, and sulphur in the C-S-H phase was calculated from the SEM-EDS point analysis results (Table 5), assuming 1 mol of C-S-H contains 1 mol of silicon.
- All the magnesium from the reaction of dolomite is bound in hydrotalcite. The hydrotalcite formula used for the calculations ($Mg_6Al_2(OH)_{18}{\cdot}3(H_2O)$) was taken from [29], because thermodynamic modelling of the reaction of dolomite in cement paste predicted the formation of a hydrotalcite, which does not contain carbonates [30], and the Mg/Al ratio of the hydrotalcite formed in the sample 60C40D was shown to be approx. 3 (Table 6).
- The amount of ettringite formed was calculated by subtracting the amount of sulphate in the C-S-H phase from the total amount of sulphates available in the system.
- The amount of AFm phases was calculated by subtracting the amount of aluminium incorporated in the C-S-H, ettringite, and hydrotalcite from the total amount of aluminium available in the system. The AFm phases taken into account for the calculations were monocarbonate and Friedel's salt. Several mass balance calculations were performed, in which the aluminium available for the formation of AFm phases was distributed in varying ratios to these two AFm phases (from 100% to 0% Friedel's salt and consequently 0% to 100% monocarbonate).
- The amount of secondary calcite, formed by the reaction of dolomite, was calculated by subtracting the amount of carbonates included in the monocarbonate from the total amount of carbonates available in the system.
- The amount of portlandite was calculated by the amount of calcium left in the system after subtracting the calcium incorporated in the C-S-H phase, secondary calcite, ettringite, monocarbonate, and Friedel's salt from the total amount of calcium available in the system.

Subsequently, the amount of chloride bound in the hydrotalcite, Friedel's salt, and C-S-H were calculated with the following steps:

- The amount of chloride in hydrotalcite[1] was calculated by the Mg/Al and Cl/Al ratio of the hydrotalcite determined with SEM-EDS (see Table 6).
- The amount of chloride in the Friedel's salt was calculated with its stoichiometric formula ($3CaO{\cdot}Al_2O_3{\cdot}CaCl_2{\cdot}10H_2O$), by taking into account the various amounts of Friedel's salt calculated, as described above.
- The amount of chloride in the C-S-H was determined by subtracting the amount of bound chlorides in hydrotalcite and Friedel's salt from the total amount of bound chlorides, as determined by potentiometric titration for the samples exposed to a 2 mol/L chloride solution (NaCl or $CaCl_2$) (see Figure 1). With this, the Cl/Si ratio of the C-S-H was calculated and compared to the Cl/Si ratio measured experimentally with SEM-EDS.

3 RESULTS

3.1 Chloride-binding isotherms

The results for the chloride-binding isotherms were plotted as the data points obtained experimentally by chloride titration and their corresponding fitted chloride-binding isotherms.

3.1.1 Chloride-binding isotherms of samples containing dolomite or limestone

Figure 2 shows the chloride-binding isotherms for samples 60C40D and 60C40L cured at 38 °C or 60 °C and exposed to NaCl. When cured at 38 °C, the sample containing limestone shows a similar chloride binding as the sample containing dolomite. However, when cured at 60 °C, the chloride binding of sample 60C40L drops slightly while sample 60C40D shows an increase.

3.1.2 Chloride-binding isotherms of samples containing a combination of dolomite or limestone with metakaolin

Figure 3 shows the chloride-binding isotherms for the samples cured at a) 38 °C and b) 60 °C exposed to NaCl. All samples cured at 38 °C and containing metakaolin, whether in combination with dolomite or limestone, showed a higher chloride binding than the 100C reference sample. Samples containing no metakaolin (60C40D and 60C40L) showed a lower chloride binding than the 100C reference. Moreover, the samples containing a combination of metakaolin and carbonate

[1]Due to the lack of an exact chemical formula for the chloride-containing hydrotalcite, we calculated its molar mass from the formula: $Mg_6Al_2(OH)_{18}{\cdot}3H_2O$.

(dolomite or limestone) did not seem to reach a plateau when they were exposed to chloride solutions with high concentrations, whereas the reference 100C and the samples 60C40D and 60C40L did.

When cured at 60 °C, the chloride binding of sample 60C40D was higher compared to 38 °C. Whereas for all other samples the chloride binding was lower at 60 °C compared to 38 °C. Sample 60C40D showed the highest chloride binding of the samples cured at 60 °C. Sample 60C35D5M showed a significantly lower chloride binding than sample 60C40D when cured at 60 °C.

3.1.3 Chloride-binding isotherms of samples exposed to $CaCl_2$

Figure 4 shows the chloride-binding isotherms for the samples exposed to various concentrations of $CaCl_2$ solution. The chloride-binding capacities were considerably higher for all samples exposed to $CaCl_2$ than for those exposed to NaCl (by a factor of 5–10).

Samples cured at 38 °C (Figure 4a) showed trends similar to those of the samples exposed to NaCl. Samples containing a combination of metakaolin and either dolomite or limestone showed a higher chloride binding than the 100C reference and gave the overall highest chloride binding of all samples investigated. Samples 60C40D and 60C40L showed a similar and low chloride binding.

For the samples cured at 60 °C (Figure 4b), however, the trends observed for the $CaCl_2$ exposure were different from those for NaCl. With $CaCl_2$ exposure, the samples containing dolomite, with or without metakaolin, showed very similar and the highest chloride binding of all samples cured at 60 °C. The reference sample 100C showed, as for NaCl exposure, a lower chloride binding than when cured at 38 °C. The samples containing limestone (60C40L, 60C35L5M) cured at 60 °C showed similar chloride binding and the lowest chloride binding of all the samples exposed to $CaCl_2$.

3.2 pH measurements

Figure 5 shows the results of the pH measurements of the supernatant of the various binder compositions cured at 38 °C and 60 °C and exposed to NaCl (Figure 5 a and b) and to $CaCl_2$ (Figure 5 c and d). The results of the pH measurements of the reference samples exposed to deionized water are plotted as the points for 0 mol/L added chloride concentration in all graphs.

All the samples containing SCMs that were exposed to NaCl showed a lower pH than the Portland cement sample 100C. This effect of SCMs on the pH of the pore solution has been described previously [31]. All samples containing SCMs and cured at 38 °C showed a very similar pH at all

concentrations of added chloride solution. The pH seemed to decrease only slightly with increasing chloride concentrations. The samples containing dolomite (60C40D and 60C35D5M) and cured at 60 °C, showed a lower pH than the samples containing limestone. This might be explained by the enhanced dolomite reaction at 60 °C, which has been shown to reduce the pH in a model system [32].

For $CaCl_2$ exposure, the 100C sample again showed a higher pH for all added chloride concentrations added than for the samples, in which 40%wt of the Portland cement was replaced with SCMs. The drop in the pH with increasing chloride concentrations was much greater than in the samples exposed to NaCl. This is attributed partly to the adsorption of calcium on silanol groups, which releases H^+-ions in the pore solution, and the common ion effect of portlandite (calcium hydroxide), as reported in the literature [3,20,22,23,33]. The decrease in the pH upon $CaCl_2$ addition results in a partial dissolution of the portlandite as experimentally observed in Figure 9.

There were no differences in the pH between the samples containing dolomite or limestone at either curing temperature when exposed to $CaCl_2$. This indicates that in the case of $CaCl_2$ exposure, the Ca^{2+} ions dominate the pH in contrast to the NaCl exposure, where the reaction of dolomite dominates the pH.

3.3 Thermodynamic modelling

Figure 6 shows the development of the activity of CO_3^{2-} ions in the solution and the amount of $CaCO_3$ present in the system with increasing additions of NaCl and $CaCl_2$ to the model system H_2O-$CaCO_3$ at a high pH. It can be seen that the activity of the carbonate ions is decreasing with increasing amounts of $CaCl_2$ added. First, the activity drops very rapidly and at free chloride concentrations higher than approx. 1.2 mol/L, the activity decreases with a smaller slope. The decrease in the carbonate ion activity is due to higher calcium concentration in the solution and the common ion effect, which is visible by the precipitation of small amounts of $CaCO_3$ in Figure 6. In the model system exposed to NaCl, however, there is no drop in the activity of carbonate ions within the range of the free chloride concentration modelled.

3.4 Hydrate phase assemblage of exposed samples determined with TGA and XRD

Table 4 gives a qualitative comparison of the phase assemblages observed with TGA or XRD in the various binder compositions cured at 38 °C or 60 °C and exposed to H_2O, NaCl or $CaCl_2$. In general, the results for TGA and XRD correlate well. In samples where we could only identify a phase with TGA but not with XRD, we assumed the phases to be poorly crystallized or amorphous. A detailed

description of the phase assemblages of the various samples and their associated TGA and XRD plots are given in the Appendix.

In the reference samples exposed to water, hydrotalcite formed in samples containing dolomite as detected with TGA and XRD. The weight loss peak of hydrotalcite increased with the curing temperature from 38 °C to 60 °C, for the samples containing dolomite. The samples containing limestone also showed a small weight loss in the temperature region of hydrotalcite. This weight loss in the samples could be associated with the decomposition of a siliceous hydrogarnet, because small peaks of this phase were observed with XRD in all the samples cured at 60 °C (not shown here). Monocarbonate was observed in all samples cured at 38 °C except 60C40D.

In samples exposed to NaCl or $CaCl_2$, chloride-containing phases were observed instead of monocarbonate or normal hydrotalcite. In samples containing dolomite, chloride-containing hydrotalcite, and in samples containing limestone, Friedel's salt was common. The chloride-containing hydrotalcite can be identified with XRD, as reported by Ke et al., by its the shift in the peak position to lower angles, as shown in Figure 7 [13]. Moreover, the signal in TGA also changed. The first peak of hydrotalcite (approx. 220 °C) decreased or completely disappeared and the second peak (approx. 400 °C) shifted to lower temperatures (approx. 370 °C) (Figure A1). The chloride-containing hydrotalcite was observed in chloride-exposed samples containing dolomite cured at both curing temperatures. A possible intermixing with Friedel's salt cannot be excluded, as the peaks of the chloride-containing hydrotalcite show a slightly asymmetric peak, which could indicate the presence of small amounts of Friedel's salt. Clear peaks of Friedel's salt were only visible in samples cured at 38 °C in the XRD and TGA graphs, though there was a small peak of Friedel's salt in sample 60C35L5M cured at 60 °C. In all samples exposed to $CaCl_2$, except sample 60C40D cured at 60 °C, a small hump of what was probably monosulphate-14H was observed. We could not identify this phase with TGA, probably due to its very small amounts and the overlapping of AFm decomposition peaks in the DTH curve. This indicates that the presence of calcium ions is also influencing the balance between monosulphate and ettringite, and not only the SO_3^{2-}/Al_2O_3 ratio of the pore solution. Sample 60C40D cured at 60 °C showed a monocarbonate peak instead of the monosulphate peak when exposed to $CaCl_2$.

It is important to note that, even though the TGA and XRD results correlate qualitatively very well, the ettringite peak in XRD seemed to be higher for the samples cured at 60 °C than for the samples cured at 38 °C. This increase was not observed with TGA. The reason for this is not clear, but it could be due to the sample preparation, in which the ettringite might have been severely

decomposed during the curing at 60 °C and re-crystallized later at 20 °C, potentially resulting in a higher degree of crystallinity.

There were several peaks observed in the carbonate weight loss region of samples exposed to either NaCl or $CaCl_2$. TGA-MS investigations of the sample 60C35D5M cured at 38 °C and exposed to $CaCl_2$, showed that these peaks are related to the release of CO_2 (Figure 8). We expect the degree of carbonation due to sample preparation to be similar in all samples, because they were all prepared in the same way. The evaporation of chlorine, as reported for chloride-containing hydrotalcite [13], is indicated by the increasing ion current for the chlorine (H-^{35}Cl, H-^{37}Cl, ^{35}Cl) at temperatures >800 °C.

3.5 Portlandite and bound water content

Figure 9 shows the portlandite content normalized to the dry binder weight of the various mixes investigated. The portlandite content was lower in samples containing a combination of metakaolin and carbonate (whether dolomite or limestone) than in samples containing only carbonates as SCMs. Moreover, all samples containing dolomite and/or metakaolin showed a lower portlandite content when cured at 60 °C than when cured at 38 °C. This can be explained by the pozzolanic reaction of metakaolin to form additional C-S-H, and the reaction of dolomite to form hydrotalcite and calcite, which both consume portlandite and are accelerated at elevated curing temperatures. Only sample 60C40L exposed to $CaCl_2$ showed a higher portlandite content when cured at 60 °C than when cured at 38 °C.

All samples exposed to chloride solutions showed a lower portlandite content than their reference samples exposed to deionized water. This difference was greater for the exposure to $CaCl_2$ than to NaCl. This was also experimentally observed in [22].

Figure 10 shows the amount of bound water in the various mixes investigated. The samples containing dolomite or limestone show very similar results. The samples containing metakaolin had a higher or similar bound water content compared to the 100C reference for both curing temperatures. This indicates that the pozzolanic reaction of metakaolin, which forms additional C-S-H and AFm phases, is able to compensate for the smaller amount of Portland cement in these samples. The samples cured at 60 °C showed a lower bound water content than the samples cured at 38 °C, even though, the clinker hydration and the pozzolanic reaction of metakaolin are accelerated at elevated curing temperatures, and should thus lead to an increase in the bound water content. The lower bound water content in samples cured at 60 °C compared to samples

cured at 38 °C might, however, be explained by the densification of the C-S-H at such high temperatures, which is associated with a loss of its structural water [34,35].

The bound water content changes for the various exposures. Samples exposed to NaCl showed a lower bound water content than their reference samples exposed to deionized water. Samples exposed to $CaCl_2$ showed a higher bound water content than samples exposed to NaCl, and in some cases a higher bound water content than samples exposed to deionized water.

Samples exposed to $CaCl_2$ show a lower portlandite and higher bound water content, than samples with the same composition exposed to NaCl. We, therefore, assume that the $CaCl_2$ reacted with the cementitious system to form additional phases. One possible reaction is the formation of calcium oxychloride phases from the reaction of $CaCl_2$ with water and portlandite [36–42]. However, we did not observe peaks of calcium oxychloride with XRD. This might be explained by the complexity of these salts, which were reported to decompose or carbonate easily during sample preparation [37,43].

3.6 Composition of the C-S-H and hydrotalcite in exposed samples measured with SEM-EDS

3.6.1 BSE imaging and elemental mapping

As an example of back-scattered electron (BSE) imaging, Figure 11 shows the BSE image and elemental maps of magnesium, aluminium, calcium, silicon and chlorine for sample 60C40D cured at 60 °C and exposed to NaCl. We chose this composition, because it showed the highest degree of dolomite reaction in a previous study [10]. The samples exposed to $CaCl_2$, as well as the samples 60C35D5M showed similar results. The up to 60 µm large uniformly grey particles are the unreacted parts of the dolomite particles. This is confirmed by the elemental maps, which show that these particles contain only magnesium and calcium. Around these particles, the original grain boundaries of the dolomite particles are still visible due to a thin layer of C-S-H that probably precipitated at early ages and persisted after the dolomite started to react. Between the original grain boundaries of dolomite and the boundary of the still unreacted dolomite particles, dark reaction rims are visible (highlighted with small arrows). These rims are rich in magnesium and aluminium but poor in calcium and silicon. Moreover, the rims seem to show a slightly higher chloride content than the matrix. The matrix shows a generally homogeneous chloride content. The small points of very high chlorine content in the last map are most probably crystals of NaCl that precipitated during drying in the samples. Point analyses of the samples exposed to NaCl or $CaCl_2$ were taken in the matrix of the samples and inside the reaction rims around the dolomite particles.

3.6.2 Effect of curing temperature, metakaolin addition and exposure solution on the composition of the C-S-H

Table 5 shows the results for the SEM-EDS point analyses of the matrix of selected samples exposed to NaCl or $CaCl_2$. The results given in Table 5 were determined by plotting the atomic ratios (e.g. Al/Ca over Si/Ca), in 2D diagrams. Tangents framing the C-S-H data cloud were used to discriminate the intermixed phases and determine the atomic ratios of the C-S-H phase.

The results for samples 60C40D exposed to NaCl show that the Si/Ca ratio and the Al/Si ratio of the C-S-H were lower in samples cured at 60 °C than in samples cured at 38 °C. This might be explained by the enhanced reaction of clinker and dolomite at 60 °C. Zajac et al. reported a lower aluminium content of the C-S-H in samples where dolomite reacted to hydrotalcite, which incorporates the aluminium instead [9].

In most of the samples containing metakaolin (60C35D5M and 60C35L5M) that were exposed to NaCl, the Al/Si and the Si/Ca ratio of the C-S-H is higher than in the samples containing no metakaolin (60C40D). This effect of the addition of metakaolin on the Si/Ca ratio of the C-S-H is qualitatively in agreement with literature [44,45]. However, it should be noted that the Si/Ca ratio of 0.9 for the sample 60C35L5M cured at 38 °C and exposed to NaCl is much higher than reported for the addition of 5%wt metakaolin [45]. The Si/Ca ratios of the other samples containing limestone and metakaolin are relatively similar. The reason for the high values for the sample 60C35L5M 38 °C NaCl are unclear. In samples exposed to $CaCl_2$, the Si/Ca ratio of the C-S-H was lower than in the samples exposed to NaCl for all samples except the sample 60C40D 38 °C.

To illustrate the chloride uptake of the C-S-H in these samples, Table 5 also shows the Cl/Si ratio of the point analyses of the matrix. For most of the samples, the Cl/Si ratio of the C-S-H is higher at 60 °C than at 38 °C. Exposure to $CaCl_2$ also increased the chloride content in the C-S-H compared to NaCl.

Table 5 also shows the S/Si ratio of the C-S-H in the various samples investigated. It can be seen that contradictive to the commonly observed higher sulphate content of C-S-H at higher curing temperatures, the S/Si ratio of the C-S-H in the samples cured at 60 °C was similar or lower than in the samples cured at 38 °C. This can be explained by the sample preparation, where the samples were cured at 60 °C or 38 °C, but exposed at 20 °C. This indicates that the C-S-H in the samples cured at 60 °C released a considerable amount of sulphate during the exposure at 20 °C, and can

explain the formation of ettringite or monosulphate in samples cured at 60 °C, as observed in with XRD.

3.6.3 Effect of metakaolin addition and exposure solution on the composition of hydrotalcite

The results for the point analyses taken in the reaction rims inside the original dolomite grains are shown in Figure 12 as the Mg/Ca ratio over the Al/Ca ratio. The results follow two linear lines, one for the hydrotalcite formed in samples containing dolomite (60C40D), and the other for the hydrotalcite formed in samples containing a combination of dolomite and metakaolin (60C35D5M). This indicates that no other aluminium-containing hydration products, such as Friedel's salt, were present in the reaction rims, as they would cause a spread of the result towards lower Mg/Al ratios. The different slopes of these lines indicate a decrease in the Mg/Al ratio of the hydrotalcite formed from approx. 3.2 in sample 60C40D to approx. 2.4 in sample 60C35D5M. The Mg/Al ratio does not seem to be affected by the exposure solution, but only by the presence of metakaolin.

Figure 13 shows the Cl/Ca over the Al/Ca ratio of the point analysis results in rims around the dolomite grains, which are filled with hydrotalcite. The slope of the lines indicated in Figure 13, presents the Cl/Al ratio of the hydrotalcite in the various samples, which is summarized for the various samples in Table 6. Hydrotalcite is reported to contain a constant amount of aluminium, but varying amounts of magnesium [46]. In this study we assumed hydrotalcite to always contain 2 mol of aluminium. Therefore, the results of the calculation of the amount of chloride ions in 1 mol of hydrotalcite show a lower chloride content in the hydrotalcite formed in samples containing metakaolin (Table 6).

3.7 Mass balance calculations

The amount of chloride bound in the C-S-H phase, Friedel's salt, and hydrotalcite per gram of cement paste in the samples 60C40D (60 °C) and 60C40L (38 °C) was calculated by a mass balance approach for exposure to either NaCl or $CaCl_2$. It is reported that with increasing concentrations of chlorides in the pore solution, monocarbonate transforms gradually to Friedel's salt [47]. With TGA and XRD it is not possible to distinguish Friedel's salt, hydrotalcite and monocarbonate completely. Especially, if little amounts of one of them are present in the samples. Due to the asymmetric peak of the chloride-containing hydrotalcite, the presence of Friedel's salt in samples containing dolomite cannot be excluded. Therefore, the aluminium available for the formation of AFm phases from the mass balance calculation was distributed in various ratios between monocarbonate and Friedel's salt (from 100% to 0% Friedel's salt and consequently 0% to 100%

monocarbonate). Figure 14 shows the amount of chloride bound in the various hydrates calculated by mass balance for the various combinations of monocarbonate and Friedel's salt.

For the high amounts of Friedel's salt assumed to be present, the calculated chloride content in the C-S-H phase shows negative values in case of exposure to NaCl. This is because the Cl/Si ratio of the C-S-H was calculated by subtracting the calculated amount of chloride bound in Friedel's salt and hydrotalcite from the total amount of chloride bound in the system measured. At high amounts of Friedel's salt present, more chlorides are calculated to be bound in the Friedel's salt than measured for the samples exposed to NaCl. We, therefore, assume these high Friedel's salt amounts to be an overestimation and concentrate in the following on the calculations where the aluminium available for the formation of AFm phases was distributed max. 30% to Friedel's salt (as indicated by the dashed rectangles). Because the hydrotalcite formed contains aluminium, less aluminium is available for the formation of AFm phases in the samples containing dolomite than in the sample containing limestone. This results in a smaller variation in the amount of chloride bound in the C-S-H or in the Friedel's salt in the sample 60C40D than in the sample 60C40L.

For the sample 60C40D, it was calculated that approx. 0.003 g of chlorides/g hydrated binder for NaCl exposure and approx. 0.006 g chlorides/g hydrated binder for $CaCl_2$ exposure were bound in hydrotalcite. For the sample 60C40L, where no hydrotalcite was formed, the maximum amount of chloride bound by Friedel's salt were approx. 0.003 g chlorides/g hydrated binder for NaCl exposure and approx. 0.002 g chlorides/g hydrated binder for $CaCl_2$ exposure.

We also used mass balance to calculate the Cl/Si ratio of the C-S-H, as described in 2.3.4. The highest Cl/Si ratios calculated for the C-S-H phase in sample 60C40D for NaCl or $CaCl_2$ exposure were approx. 0.03 and 0.15 respectively, which is considerably lower than the measured Cl/Si ratios of 0.1 and 0.24 for sample 60C40D cured at 60 °C (Table 5). This difference between measured and calculated Cl/Si ratios might be explained by the inability of the used solvents (isopropanol and petroleum ether) to penetrate the gel porosity of the C-S-H phase during the solvent exchange and replace the pore solution between the C-S-H sheets. This was explained by the big molecular size of alcohols compared to water, which inhibits the replacement of the water in very small pores [48]. Similarly, Plusquellec et al. showed that even methanol, which has a smaller molecular size than isopropanol, is unable to replace all the pore solution in ground concrete samples, leading to a lower amount of alkalis extracted from these samples [49]. In the present study, consequently, some of the chloride-rich solution would be trapped in the gel porosity and create an artificially high Cl/Si ratio in the point measurements with SEM-EDS.

Another possible explanation might be that the solubility of e.g. NaCl is much smaller in solvents than in water. Therefore, chloride salts, which might have precipitated in the sample during the solvent exchange, cannot be dissolved by the solvents.

The differences between the measured and calculated Cl/Si ratios of the C-S-H indicate that the solvent exchange treatment applied in this study is not a reliable method for sample preparation for SEM-EDS when the chloride content of the C-S-H needs to be measured. This is also indicated by the small points of very high chlorine content in the elemental map of chlorine (Figure 11), which are most probably crystals of NaCl that precipitated during the sample preparation.

The sample 60C40L was not investigated with SEM-EDS, and we can therefore not discuss on possible differences between the measured and calculated Cl/Si ratios in this samples.

We also calculated the portlandite content normalized to the dry binder weight of the samples 60C40D (60C40D-NaCl: 12 %wt, 60C40D-$CaCl_2$: 10 %wt) and 60C40L (60C40L-NaCl: 14 %wt, 60C40L-$CaCl_2$: 9 %wt) with the mass balance approach. We compared these values with the portlandite content normalized to the dry binder weight obtained experimentally with TGA (see Figure 9). Except for the sample 60C40L-$CaCl_2$, the portlandite content calculated with mass balance is larger than calculated with TGA. This indicates the formation of a calcium-containing phase in the samples exposed to the chloride solutions, which we did not account for in mass balance.

4 DISCUSSION

4.1 Chloride-binding isotherms for the samples containing limestone and metakaolin

The chloride binding of the samples containing limestone (60C40L and 60C35L5M) and the reference sample 100C was lower for the samples cured at 60 °C than of those cured at 38 °C (Figure 3 & Figure 4). This confirms the observations of other authors [50,51]. The increase in curing temperature from 38 °C to 60 °C changed the stability of some phases. This is visible in the XRD and TGA plots (results summarized in Table 4), where no or only small amounts of Friedel's salt can be observed with XRD and TGA in the samples cured at 60 °C. We, therefore, conclude that the lower chloride binding of samples containing limestone cured at 60 °C is due to the lower amount of chloride-containing hydrates in these samples.

When cured at 38 °C, where phases like Friedel's salt are observed with XRD and TGA, samples containing metakaolin show a higher chloride binding than samples without metakaolin (Figure 3a & Figure 4a). This effect has been explained by the additional aluminium delivered by the metakaolin [2,3]. The addition of aluminium enables the formation of more Friedel's salt and thereby increases the chloride-binding capacity of cement pastes. This is confirmed by our results, because we also observe an increase in the Friedel's salt with TGA in samples containing metakaolin (e.g. Figure A3).

4.2 Effect of hydrotalcite on the chloride binding in samples containing dolomite without metakaolin addition

Figure 2 shows the chloride-binding isotherms for the samples 60C40D and 60C40L cured at 38 °C, and 60 °C exposed to NaCl solutions. The sample 60C40D cured at 60 °C showed considerably greater chloride binding compared to the other samples. Assuming that the chloride content of the C-S-H is similar for the sample 60C40D and 60C40L, the increased chloride binding of the sample 60C40D cured at 60 °C will be due to the chloride binding in other hydrates than C-S-H. When cured at 60 °C, the dolomite in the samples has been shown to react significantly more than when cured at 38 °C and to form more hydrotalcite [9,10].

In the samples containing dolomite exposed to deionized water hydrotalcite formed, and in the samples exposed to a chloride solution a chloride-containing hydrotalcite was observed. This can be seen by the shift in the peak position of the hydrotalcite in XRD between the samples exposed to deionized water and those exposed to NaCl (Figure 7). A similar shift was observed previously by Ke et al. [13]. The peak position in XRD strongly depends on the c-parameter of the crystal lattice [52]. With the incorporation of chloride ions in the interlayer of the hydrotalcite the interlayer spacing is increased, because chloride ions have a larger ionic radius than hydroxide ions [11,13,16,53]. An increase in the c-parameter results in a lower angle for the diffraction peak of the phases. Moreover, the signal in TGA also changed, because the first peak of hydrotalcite (approx. 220 °C) decreased or completely disappeared and the second peak (approx. 400 °C) shifted to lower temperatures (approx. 370 °C) (Figure A1). Similar changes in the TGA signal upon the formation of a chloride-containing hydrotalcite were reported by Ke et al. [13]. However, the temperatures of these peaks in the present study vary from the temperatures reported by Ke et al. [13], probably because the hydrotalcite in this study was formed in a cementitious system rather than synthesised as a pure phase. The SEM-EDS point analyses (Figure 13) also showed a chloride uptake of the hydrotalcite in the samples exposed to NaCl. It should be noted that the amount of chloride in the hydrotalcite will be discussed in the following. Moreover, we do not observe clear peaks of Friedel's salt in sample 60C40D exposed to NaCl (Table 4). We, therefore,

conclude that the samples containing dolomite cured at 60 °C showed an increased chloride binding due to the formation of hydrotalcite, which is able to bind significant amounts of chloride. To which extent these chlorides are bound in the interlayer of the hydrotalcite or adsorbed on its surface could not be evaluated in with the experimental set-up in this study.

It should be noted that amongst the samples cured at 38 °C and exposed to NaCl, the reference sample 100C shows the highest chloride binding in the concentration range of a classic ponding test (0.5 mol/L). However, when cured at 60 °C, the sample 60C40D shows the highest chloride binding, also in this concentration range. As the curing at 60 °C was applied to accelerate the dolomite reaction, we assume the chloride binding of the sample 60C40D cured at 38 °C to increase with the increasing reaction degree of dolomite over time.

4.3 Effect of additional metakaolin on the composition and chloride-binding capacity of hydrotalcite

The Mg/Al ratio of hydrotalcite is known to be dependent on the availability of aluminium [17,18], and therefore on the addition of metakaolin [10]. The samples containing metakaolin cured at 60 °C showed a lower Mg/Al ratio of the hydrotalcite than in samples without metakaolin (Figure 12). The change in the Mg/Al ratio is also indirectly visible with XRD, where the hydrotalcite formed showed a peak at slightly higher angles in sample 60C35D5M than the sample 60C40D (Figure 7). This can be explained by the lower Mg/Al ratio of the hydrotalcite in the sample 60C35D5M, which increases the positive charge of the main layer [16]. Therefore, more anions are needed in the interlayer to compensate for the higher charge in the main layer, which reduced the c-parameter because of a shortening in the hydrogen bonds [54].

The calculations of the amount of chloride in 1 mol of hydrotalcite based on the SEM-EDS show a lower chloride content of the hydrotalcite in the samples 60C35D5M than in the samples 60C40D (Table 6). This is not in agreement with the literature, where it was reported that a lower Mg/Al ratio results in an increased uptake of chloride ions in the interlayer of hydrotalcite [16]. This was explained by the increased positive charge of the main layer due to aluminium having a higher charge than magnesium. Because the interlayer seeks electrical neutrality, more anions, in this case chlorides, should be taken up by the interlayer in the case of a decreased Mg/Al ratio [16]. The reason for the contradictive results in the present study are unknown.

The chloride-binding isotherms showed a lower chloride binding for the sample 60C35D5M cured at 60 °C and exposed to NaCl than for the sample 60C40D (Figure 3). Assuming that the apparent lower chloride-content of the hydrotalcite in the samples containing metakaolin is an artefact, one

possible explanation for this could be the lower amount of hydrotalcite in the sample 60C35D5M compared to 60C40D. In a previous study, we showed that the amount of hydrotalcite formed strongly depends on the availability of portlandite in the system, which decreased with the amount of metakaolin added [10].

4.4 Effect of the exposure solution on the chloride binding of the cement paste

4.4.1 Effect of the exposure solution on the chloride-binding capacity of C-S-H

Samples exposed to $CaCl_2$ show a greater chloride binding than samples exposed to NaCl (Figure 3 and Figure 4). Several authors have described increased chloride binding when samples are exposed to $CaCl_2$ rather than NaCl [1,3,19–23]. The difference might be due to the ability of samples to accumulate chloride ions in the diffuse layer of the C-S-H in the case of $CaCl_2$ exposure (Table 5). This has previously been explained by the overcompensation of the originally negative surface charge of the C-S-H by the adsorption of divalent calcium ions in the Stern layer of the C-S-H [55]. This overcompensation reverses the surface charge and turns it positive [55], which means negatively charged chloride ions can accumulate in the diffuse layer of the C-S-H [8,23]. This is qualitatively in accordance with our results, as a higher Cl/Si ratio of the C-S-H phase was measured in samples exposed to $CaCl_2$ compared to NaCl (see Table 5).

4.4.2 Effect of the exposure solution on the chloride-binding capacity of hydrotalcite

A higher chloride uptake in hydrotalcite was observed in the case of $CaCl_2$ exposure compared to NaCl (Table 6). This could be explained using thermodynamic modelling, which showed that the activity of the carbonate ions in the pore solution of a model system is decreased for $CaCl_2$ exposure, while it was not affected by NaCl exposure (Figure 6). Generally, divalent ions, such as CO_3^{2-}, are more preferably incorporated in the interlayer of hydrotalcite than monovalent ions, e.g. Cl^-. Due to the decrease of the activity of carbonate ions when exposed to $CaCl_2$, less carbonate and more chloride ions might be accommodated in the interlayer of hydrotalcite in the case of $CaCl_2$ exposure than in the case of NaCl exposure. The Mg/Al ratio of the hydrotalcite did not seem to be affected by the exposure solution (Figure 12).

An additional explanation for the increased chloride uptake of hydrotalcite upon exposure to $CaCl_2$ compared to NaCl, is the decrease in the pH of the pore solution for $CaCl_2$ exposure, as shown in Figure 5. Ke et al. highlighted the importance of the $[Cl^-]/[OH^-]$ ratio in the pore solution, which can have a significant effect on the adsorption of chlorides on hydrotalcite. At a lower pH, the concentration of OH^- ions is decreased, which might lead to the adsorption of chlorides rather than

hydroxides on the hydrotalcite [13]. In this study, we did however not differentiate between surface adsorption and incorporation of chlorides in the interlayer of hydrotalcite.

4.5 Comparison of the contribution of hydrotalcite and Friedel's salt to the chloride binding of the cement pastes

The amount of chloride bound in the C-S-H phase, Friedel's salt, and hydrotalcite per gram of cement paste in the samples 60C40D (60 °C) and 60C40L (38 °C) exposed to either NaCl or $CaCl_2$ was calculated by a mass balance approach. The two different temperatures for the samples were chosen, because considerable amounts of hydrotalcite were detected only in the samples containing dolomite cured at 60 °C, whereas clear peaks of Friedel's salt were detected only in the samples containing limestone cured at 38 °C.

The contribution of hydrotalcite, Friedel's salt and the C-S-H to the chloride binding of the cement pastes exposed to a 2 mol/L chloride solution was estimated from the results of the mass balance calculations shown in Figure 14. For the calculations where more than 30% of the aluminium available for the formation of AFm phases is distributed to Friedel's salt, the Cl/Si ratio of the C-S-H, and therefore its contribution to the chloride binding, is negative for the samples 60C40D and 60C40L exposed to NaCl, as described in 3.7. Negative values for the Cl/Si ratios are impossible, and these calculations were not considered further. For the comparison between the contribution of the chloride-containing hydrotalcite and the Friedel's salt to the chloride binding of the cement paste, we chose the calculations were 25% of the aluminium is distributed to the formation of Friedel's salt, as shown in Figure 15. This was done because the calculated Cl/Si ratio of the C-S-H was similar between samples 60C40D an 60C40L in these calculations. The amount of chloride bound in the hydrotalcite is unaffected by the combination of monocarbonate and Friedel's salt, because the amount of hydrotalcite formed was assumed to depend solely on the reaction degree of the dolomite.

The results of the mass balance calculations shown in Figure 15 indicate that the contribution of hydrotalcite to the chloride binding of the sample 60C40D (60 °C) is in the range of Friedel's salt in the sample 60C40L (38 °C) for both exposures.

However, the results of the mass balance calculations in this study are dependent on the amount of hydrotalcite present, and therefore on the reaction degree of dolomite, which in this case is assumed. Therefore, we also calculated the amount of chloride (N_{Cl}) in 1 mol of hydrotalcite (Table 6). We assumed hydrotalcite to contain always 2 mol of aluminium and varying amounts of magnesium in the main layer. The Mg/Al and Cl/Al ratio of the hydrotalcite in sample 60C40D

were determined with SEM-EDS point analyses (Table 6). In case of NaCl exposure, 1 mol of the hydrotalcite formed contained approx. 0.8 moles of chlorides and in case of $CaCl_2$ exposure, approx. 1.8 mol of chlorides. For Friedel's salt, this value equals 2 according to its stoichiometric formula ($3CaO{\cdot}Al_2O_3{\cdot}CaCl_2{\cdot}10H_2O$). This indicates that the hydrotalcite formed due to the reaction of dolomite is able to bind similar amounts of chlorides compared to Friedel's salt when exposed to $CaCl_2$, and can, depending on the amount of hydrotalcite formed, contribute considerably to the chloride binding of the cement paste.

5 CONCLUSIONS

We investigated well-hydrated cement pastes in which 40%wt of the Portland cement was replaced with dolomite or a combination of dolomite and metakaolin cured at 38 °C or 60 °C. The pastes were exposed to NaCl, $CaCl_2$ or deionized water and the chloride binding, pH, phase assemblage and phase composition were determined. From the results the following conclusions can be drawn:

- The hydrotalcite that formed in samples containing dolomite contributed considerably to the chloride binding of these samples. This is especially visible in the samples containing dolomite cured at 60 °C, because higher curing temperatures resulted in an acceleration of the dolomite and reaction.
- In samples exposed to $CaCl_2$, hydrotalcite showed a higher chloride binding capacity than in samples exposed to NaCl. This can probably be explained by the decrease in the carbonate ion activity when the samples are exposed to $CaCl_2$, which might increase the uptake of chlorides instead of carbonates in the interlayer of hydrotalcite.
- With mass balance calculations, it was shown that the hydrotalcite in samples containing dolomite can contribute to the chloride binding of the cement pastes to a similar extent as the Friedel's salt formed in samples containing limestone.

6 Acknowledgements

The authors would like to thank the industrial PhD programme of the Norwegian Research Council (Project: 241637) and the Heidelberg Technology Center for their financial support. We are also grateful for the help and assistance of Tone Anita Østnor and Anne-Kristin Mjøen from SINTEF and the student assistants Petter Hemstad, Kristine Nøttveit, and Oda Tjeland from NTNU with the sample preparation and the chloride titration experiments.

7 References

[1] C. Arya, N.R. Buenfeld, J.B. Newman, Factors influencing chloride-binding in concrete, Cem Concr Res 20 (1990) 291–300.

[2] M.D.A. Thomas, R.D. Hooton, A. Scott, H. Zibara, The effect of supplementary cementitious materials on chloride binding in hardened cement paste, Cem Concr Res 42 (2012) 1–7.

[3] Z. Shi, M.R. Geiker, K. De Weerdt, T.A. Østnor, B. Lothenbach, F. Winnefeld, J. Skibsted, Role of calcium on chloride binding in hydrated Portland cement–metakaolin–limestone blends, Cem Concr Res 95 (2017) 205–216.

[4] C. Arya, Y. Xu, Effect of cement type on chloride binding and corrosion of steel in concrete, Cem Concr Res 25 (1995) 893–902.

[5] R.K. Dhir, M.A.K. El-Mohr, T.D. Dyer, Developing chloride resisting concrete using PFA, Cem Concr Res 27 (1997) 1633–1639.

[6] A. Ipavec, T. Vuk, R. Gabrovšek, V. Kaučič, Chloride binding into hydrated blended cements: The influence of limestone and alkalinity, Cem Concr Res 48 (2013) 74–85.

[7] O.R. Ogirigbo, L. Black, Chloride binding and diffusion in slag blends: Influence of slag composition and temperature, Constr Build Mater 149 (2017) 816–825.

[8] G. Plusquellec, A. Nonat, Interactions between calcium silicate hydrate (C-S-H) and calcium chloride, bromide and nitrate, Cem Concr Res 90 (2016) 89–96.

[9] M. Zajac, S.K. Bremseth, M. Whitehead, M. Ben Haha, Effect of $CaMg(CO_3)_2$ on hydrate assemblages and mechanical properties of hydrated cement pastes at 40 °C and 60 °C, Cem Concr Res 65 (2014) 21–29.

[10] A. Machner, M. Zajac, M. Ben Haha, K.O. Kjellsen, M.R. Geiker, K. De Weerdt, Limitations of the hydrotalcite formation in Portland composite cement pastes containing dolomite and metakaolin, Manuscript submitted for publication (2017).

[11] S. Miyata, Anion-Exchange Properties of Hydrotalcite-Like Compounds, Clays and Clay Minerals 31 (1983) 305–311.

[12] L. Châtelet, J.Y. Bottero, J. Yvon, A. Bouchelaghem, Competition between monovalent and divalent anions for calcined and uncalcined hydrotalcite: anion exchange and adsorption sites, Colloids and Surfaces A 111 (1996) 167–175.

[13] X. Ke, S.A. Bernal, J.L. Provis, Uptake of chloride and carbonate by Mg-Al and Ca-Al layered double hydroxides in simulated pore solutions of alkali-activated slag cement, Cem Concr Res 100 (2017) 1–13.

[14] O. Kayali, M.S.H. Khan, M. Sharfuddin Ahmed, The role of hydrotalcite in chloride binding and corrosion protection in concretes with ground granulated blast furnace slag, Cement and Concrete Composites 34 (2012) 936–945.

[15] H. Ye, X. Jin, W. Chen, C. Fu, N. Jin, Prediction of chloride binding isotherms for blended cements, Computers and Concrete 17 (2016) 655–672.

[16] S. Miyata, The Syntheses of Hydrotalcite-Like Compounds and Their Structures and Physico-Chemical Properties I: The Systems Mg^{2+}-Al^{3+}-NO_3^-, Mg^{2+}-Al^{3+}-Cl^-, Mg^{2+}-Al^{3+}-ClO_4^-, Ni^{2+}-Al^{3+}-Cl^- and Zn^{2+}-Al^{3+}-Cl^-, Clays and Clay Minerals 23 (1975) 369–375.

[17] R. Taylor, I.G. Richardson, R.M.D. Brydson, Composition and microstructure of 20-year-old ordinary Portland cement–ground granulated blast-furnace slag blends containing 0 to 100% slag, Cem Concr Res 40 (2010) 971–983.

[18] M. Ben Haha, B. Lothenbach, G. Le Saout, F. Winnefeld, Influence of slag chemistry on the hydration of alkali-activated blast-furnace slag – Part II: Effect of Al_2O_3, Cem Concr Res 42 (2012) 74–83.

[19] A. Delagrave, J. Marchand, J.-P. Ollivier, S. Julien, K. Hazrati, Chloride Binding Capacity of Various Hydrated Cement Paste Systems, Advanced Cement Based Materials 6 (1997) 28–35.

[20] Q. Zhu, L. Jiang, Y. Chen, J. Xu, L. Mo, Effect of chloride salt type on chloride binding behavior of concrete, Construction and Building Materials 37 (2012) 512–517.

[21] K. De Weerdt, D. Orsáková, M.R. Geiker, The impact of sulphate and magnesium on chloride binding in Portland cement paste, Cem Concr Res 65 (2014) 30–40.

[22] K. De Weerdt, A. Colombo, L. Coppola, H. Justnes, M.R. Geiker, Impact of the associated cation on chloride binding of Portland cement paste, Cem Concr Res 68 (2015) 196–202.

[23] O. Wowra, M.J. Setzer, Sorption of chlorides on hydrated cement and C_3S pastes, in: M.J. Setzer, R. Auberg (Eds.), Frost Resistance of Concrete, E & FN Spon, London, 1997, pp. 147–153.

[24] Q. Yuan, C. Shi, G. de Schutter, K. Audenaert, D. Deng, Chloride binding of cement-based materials subjected to external chloride environment – A review, Constr Build Mater 23 (2009) 1–13.

[25] B. Lothenbach, P. Durdzinski, K. De Weerdt, Thermogravimetric Analysis, in: K.L. Scrivener, R. Snellings, B. Lothenbach (Eds.), A Practical Guide to Microstructural Analysis of Cementitious Materials, CRC Press Taylor & Francis Group, Boca Raton, 2015, pp. 177–211.

[26] K. De Weerdt, E. Sellevold, K.O. Kjellsen, H. Justnes, Fly ash–limestone ternary cements: effect of component fineness, Advances in Cement Research 23 (2011) 203–214.

[27] D. Kulik, GEM-Selektor v.3.3, available at: http://gems.web.psi.ch/.

[28] B. Lothenbach, F. Winnefeld, Thermodynamic modelling of the hydration of Portland cement, Cem Concr Res 36 (2006) 209–226.

[29] R.J. Myers, B. Lothenbach, S.A. Bernal, J.L. Provis, Thermodynamic modelling of alkali-activated slag cements, Applied Geochemistry 61 (2015) 233–247.

[30] A. Machner, M. Zajac, M. Ben Haha, K.O. Kjellsen, M.R. Geiker, K. De Weerdt, Portland metakaolin cement containing dolomite or limestone – Similarities and differences in phase assemblage and compressive strength, Constr Build Mater 157 (2017) 214–225.

[31] B. Lothenbach, K.L. Scrivener, R.D. Hooton, Supplementary cementitious materials, Cem Concr Res 41 (2011) 1244–1256.

[32] E. Garcia, P. Alfonso, M. Labrador, S. Galí, Dedolomitization in different alkaline media: Application to Portland cement paste., Cem Concr Res 33 (2003) 1443–1448.

[33] J. Tritthart, Chloride binding in cement - II. The influence of the hydroxide concentration in the pore solution of hardened cement paste on chloride binding, Cem Concr Res 19 (1989) 683–691.

[34] B. Lothenbach, F. Winnefeld, C. Alder, E. Wieland, P. Lunk, Effect of temperature on the pore solution, microstructure and hydration products of Portland cement pastes, Cem Concr Res 37 (2007) 483–491.

[35] E. Gallucci, X. Zhang, K.L. Scrivener, Effect of temperature on the microstructure of calcium silicate hydrate (C-S-H), Cem Concr Res 53 (2013) 185–195.

[36] L. Berntsson, S. Chandra, Damage of concrete sleepers by calcium chloride, Cement and Concrete Research 12 (1982) 87–92.

[37] K. Peterson, G. Julio-Betancourt, L. Sutter, R.D. Hooton, D. Johnston, Observations of chloride ingress and calcium oxychloride formation in laboratory concrete and mortar at 5°C, Cement and Concrete Research 45 (2013) 79–90.

[38] L. Sutter, K. Peterson, S. Touton, T. van Dam, D. Johnston, Petrographic evidence of calcium oxychloride formation in mortars exposed to magnesium chloride solution, Cement and Concrete Research 36 (2006) 1533–1541.

[39] H.G. Smolczyk, Chemical reactions of strong chloride-solutions with concrete, in: S. Kyōkai (Ed.), Proceedings of the 5th International Symposium on the Chemistry of Cement, 1968.

[40] M. Collepardi, L. Coppola, C. Pistolesi, Durability of concrete structures exposed to $CaCl_2$ based de-icing salts, in: V.M. Malhotra (Ed.), Proceedings of the third CANMET/ACI International Conference of Durability of Concrete, American Concrete Institute, 1994.

[41] H. Justnes, K. De Weerdt, M.R. Geiker, Chloride binding in concrete exposed to sea water and salt solutions, in: Z.J. Li, C.W. Miao, O.E. Gjørv, W. Sun, K. Sakai, N. Banthia (Eds.), Seventh International Conference on Concrete under Severe Conditions (CONSEC13) Nanjing, China, 23-25 September 2013, RILEM proceedings PRO, 2013, pp. 647–659.

[42] G. Julio-Betancourt, Effect of de-icer and anti-icer chemicals on the durability, microstructure, and properties of cement-based materials. Ph.D. Thesis, University of Toronto, 2009.

[43] C. Shi, Formation and stability of $3CaO{\cdot}CaCl_2{\cdot}12H_2O$, Cement and Concrete Research 31 (2001) 1373–1375.

[44] Z. Dai, T.T. Tran, J. Skibsted, H. Jennings, Aluminum Incorporation in the C-S-H Phase of White Portland Cement-Metakaolin Blends Studied by ^{27}Al and ^{29}Si MAS NMR Spectroscopy, J. Am. Ceram. Soc. 97 (2014) 2662–2671.

[45] W. Kunther, Z. Dai, J. Skibsted, Thermodynamic modeling of hydrated white Portland cement–metakaolin–limestone blends utilizing hydration kinetics from ^{29}Si MAS NMR spectroscopy, Cem Concr Res 86 (2016) 29–41.

[46] K. Morimoto, S. Anraku, J. Hoshino, T. Yoneda, T. Sato, Surface complexation reactions of inorganic anions on hydrotalcite-like compounds, Journal of Colloid and Interface Science 384 (2012) 99–104.

[47] M. Balonis, B. Lothenbach, G. Le Saout, F.P. Glasser, Impact of chloride on the mineralogy of hydrated Portland cement systems, Cem Concr Res 40 (2010) 1009–1022.

[48] J. Zhang, G.W. Scherer, Comparison of methods for arresting hydration of cement, Cem Concr Res 41 (2011) 1024–1036.

[49] G. Plusquellec, M.R. Geiker, J. Lindgård, J. Duchesne, B. Fournier, K. De Weerdt, Determination of the pH and the free alkali metal content in the pore solution of concrete: Review and experimental comparison, Cement and Concrete Research 96 (2017) 13–26.

[50] M.H. Roberts, Effect of calcium chloride on the durability of pre-tensioned wire in prestressed concrete, Magazine of Concrete Research 14 (1962) 143–154.

[51] S.E. Hussain, Rasheeduzzafar, Effect of temperature on pore solution composition in plain cements, Cem Concr Res 23 (1993) 1357–1368.

[52] T. Witzke, L. Torres-Dorante, F. Bullerjahn, H. Pöllmann, Use of Layered Double Hydroxides (LDH) of the Hydrotalcite Group as Reservoir Minerals for Nitrate in Soils – Examination of the Chemical and Mechanical Stability, in: S.V. Krivovichev (Ed.), Minerals as Advanced Materials II, Springer Berlin Heidelberg, Berlin, Heidelberg, 2012, pp. 131–145.

[53] A. de Roy, Lamellar Double Hydroxides, Molecular Crystals and Liquid Crystals Science and Technology. Section A. Molecular Crystals and Liquid Crystals 311 (1998) 173–193.

[54] G. Mascolo, O. Marino, A new synthesis and characterization of magnesium-aluminium hydroxides, Mineral. Mag. 43 (1980) 619–621.

[55] C. Labbez, A. Nonat, I. Pochard, B. Jönsson, Experimental and theoretical evidence of overcharging of calcium silicate hydrate, Journal of Colloid and Interface Science 309 (2007) 303–307.

Tables

Table 1: Chemical composition of the Portland cement, dolomite, limestone and metakaolin used, as determined by XRF [%wt] and their Blaine surface areas [m^2/kg].

Oxide	Portland cement	Dolomite	Limestone	Metakaolin
SiO_2	19.91	0.52	0.12	52.18
Al_2O_3	5.15	0.01	0.06	44.92
TiO_2	0.282	0.00	0.00	1.14
MnO	0.062	0.00	0.00	0.00
Fe_2O_3	3.42	0.04	0.03	0.62
CaO	62.73	31.52	55.12	0.12
MgO	2.34	20.14	0.41	0.04
K_2O	1.09	0.00	0.01	0.18
Na_2O	0.48	0.00	0.00	0.17
SO_3	3.16	0.00	0.02	0.14
P_2O_5	0.109	0.01	0.00	0.07
LOI	1.07	46.79	43.57	0.29
Sum (1050 °C)	**99.80**	**99.03**	**99.34**	**99.87**
Blaine [m^2/kg]	**416**	**340**	**370**	**987**

Table 2: Matrix for the mixes [%wt]. The sulphate content of the Portland cement was set to 3.2%wt.

Name	C Portland cement	D Dolomite	L Limestone	M Metakaolin
100C	100	-	-	-
60C40D	60	40	-	-
60C35D5M	60	35	-	5
60C40L	60	-	40	-
60C35L5M	60	-	35	5

Table 3: Overview of the weight losses of the various well-hydrated samples before exposure during drying at 40 °C until constant weight [%wt]. The accuracy was estimated to 1%wt.

Sample name	Curing temperature [°C]	Weight loss drying at 40 °C [%wt]
100C	38 °C	33
60C40D	38 °C	35
60C35D5M	38 °C	35
60C40L	38 °C	39
60C35L5M	38 °C	37
100C	60 °C	32
60C40D	60 °C	35
60C35D5M	60 °C	35
60C40L	60 °C	37
60C35L5M	60 °C	38

Table 4: Phase assemblage of ettringite (Et), monosulphate-14H (Ms), monocarbonate (Mc), Friedel's salt (Fs), chloride-containing hydrotalcite (Ht_{Cl}), and hydrotalcite (Ht) observed with TGA or XRD in the various mixes for various curing temperatures (38 °C, 60 °C) and exposures (H_2O, NaCl, $CaCl_2$). The text in brackets indicates a low signal of that phase or an overlap with another peak so that its presence could not be confirmed nor excluded.

Sample	Exposure	Temp.	Et	Ms-14	Mc	Fs	Ht_{Cl}	Ht
60C40D	H_2O	38 °C	TGA|XRD					TGA|XRD
		60 °C						TGA|XRD
60C35D5M	H_2O	38 °C	TGA|XRD		TGA|XRD			TGA|(XRD)
		60 °C	(TGA)|XRD					TGA|XRD
60C40L	H_2O	38 °C	TGA|XRD		TGA|XRD			(TGA)
		60 °C	TGA|XRD					(TGA)
60C35L5M	H_2O	38 °C	TGA|XRD		TGA|XRD			(TGA)
		60 °C	TGA|XRD					(TGA)
60C40D	NaCl	38 °C	TGA			(XRD)	TGA|XRD	
		60 °C				(XRD)	TGA|XRD	
60C35D5M	NaCl	38 °C	TGA		(TGA)	(TGA)|XRD	TGA|(XRD)	
		60 °C	(TGA)|XRD			(XRD)	TGA|XRD	(TGA)
60C40L	NaCl	38 °C	TGA		(TGA)	TGA|XRD	(TGA)	
		60 °C	TGA|XRD			(TGA)	(TGA)	
60C35L5M	NaCl	38 °C	TGA		TGA	TGA|XRD	(TGA)	
		60 °C	(TGA)			(TGA)|XRD	(TGA)	
60C40D	$CaCl_2$	38 °C	TGA	(XRD)		TGA|(XRD)	TGA|XRD	
		60 °C			TGA|XRD	(XRD)	TGA|XRD	
60C35D5M	$CaCl_2$	38 °C	TGA	(XRD)		TGA|XRD	TGA	
		60 °C	TGA	(XRD)		(XRD)	TGA|XRD	
60C40L	$CaCl_2$	38 °C	TGA	(XRD)		TGA|XRD	(TGA)	
		60 °C	TGA|XRD	(XRD)			(TGA)	
60C35L5M	$CaCl_2$	38 °C	TGA	(XRD)		TGA|XRD	(TGA)	
		60 °C	TGA	(XRD)		TGA|XRD	(TGA)	

Table 5: Overview of the C-S-H composition of the samples 60C40D, 60C35D5M, and 60C35L5M cured at 38 °C or 60 °C and exposed to NaCl or $CaCl_2$.

Sample			Si/Ca	Al/Si	Cl/Si	S/Si
60C40D	38 °	NaCl	0.68	0.03	0.05	0.03
		$CaCl_2$	0.78	0.04	0.24	0.03
	60 °	NaCl	0.58	0	0.1	0.04
		$CaCl_2$	0.55	0	0.24	0.04
60C35D5M	38 °	NaCl	0.78	0.04	0.05	0.04
		$CaCl_2$	0.75	0.06	0.19	0.03
	60 °	NaCl	0.73	0.04	0.16	0.02
		$CaCl_2$	0.65	0.04	0.24	0.02
60C35L5M	38 °	NaCl	0.9	0.08	0.05	0.04
		$CaCl_2$	0.65	0.08	0.2	0.03
	60 °	NaCl	0.65	0.04	0.16	0.008
		$CaCl_2$	0.56	0.04	0.24	0.008

Table 6: Overview of the Mg/Al and Cl/Al ratio of the hydrotalcite in the various samples, and the amount of chloride calculated [mol] per 1 mol of hydrotalcite (N_{Cl}).

Sample			Mg/Al	Cl/Al	N_{Cl}
Hydrotalcite	60C40D	NaCl	3.2	0.4	0.8
		$CaCl_2$	3.2	0.9	1.8
	60C35D5M	NaCl	2.4	0.2	0.4
		$CaCl_2$	2.4	0.7	1.4

Figures

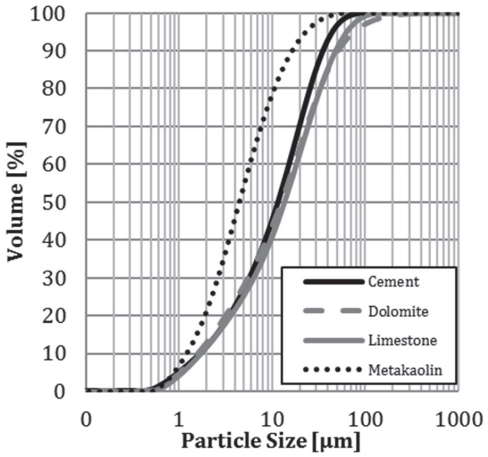

Figure 1: Particle size distribution of the materials used determined by laser diffraction.

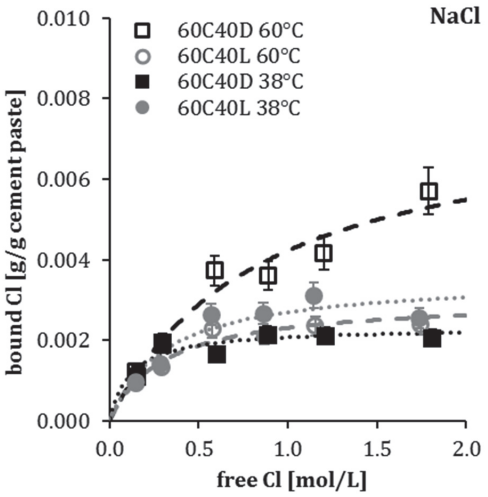

Figure 2: Experimental data and fitted curves of the chloride-binding isotherms for the samples 60C40D (*black squares*) and 60C40L (*grey spheres*) cured at 38 °C (*filled icons, dotted lines*) or 60 °C (*hollow icons, dashed lines*) and exposed to NaCl.

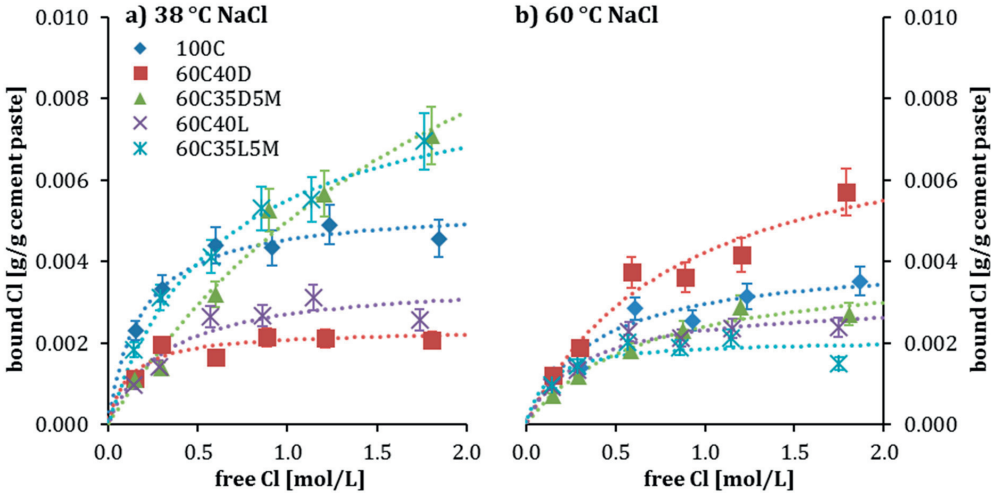

Figure 3: Experimental data and fitted curves of the chloride-binding isotherms for all the mixes investigated that were cured at a) 38 °C or b) 60 °C and exposed to NaCl.

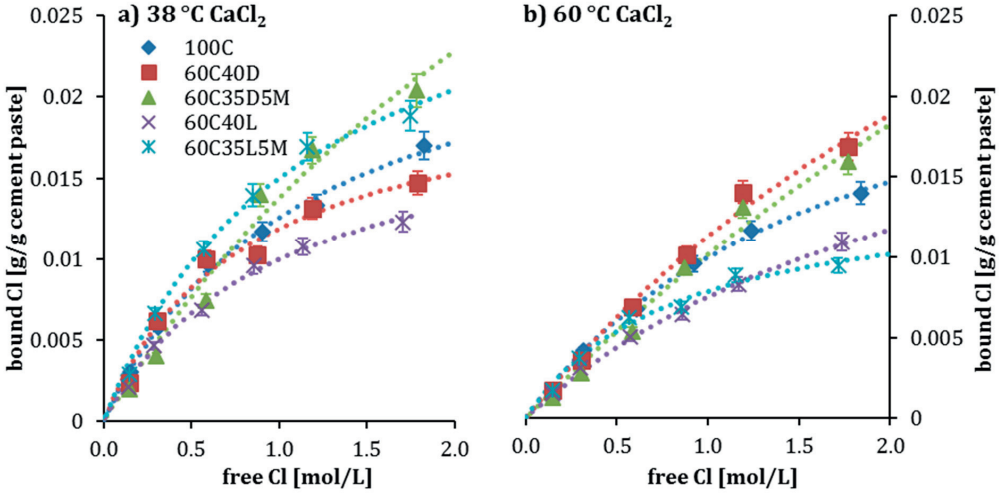

Figure 4: Experimental data and fitted curves of the chloride-binding isotherms for all the mixes investigated that were cured at a) 38 °C or b) 60 °C and exposed to $CaCl_2$. Note that the scale of the y-axis is different compared to Figure 2 and Figure 3.

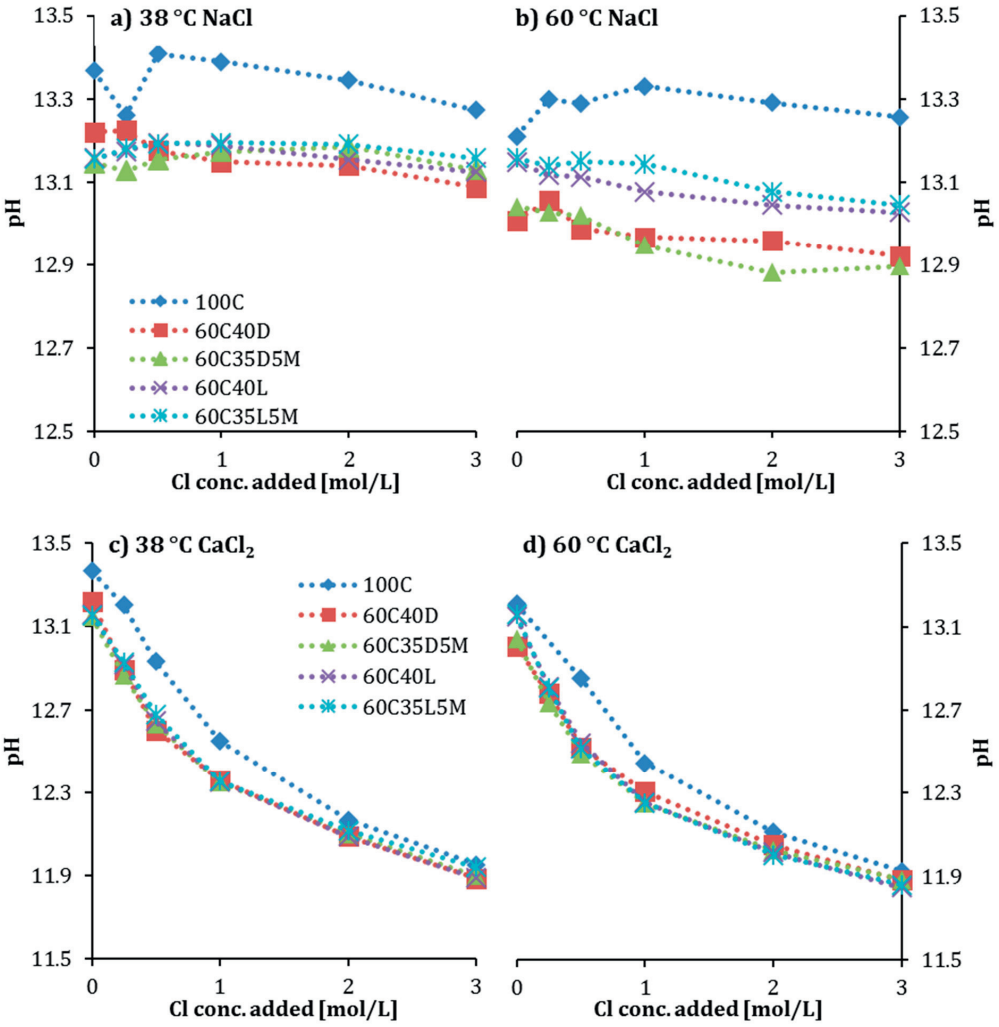

Figure 5: pH measurements of the supernatant of the various binder compositions cured at 38 °C or 60 °C and exposed to various concentrations of NaCl or $CaCl_2$. The measurements were performed at 20 °C. The points at 0 mol/L refer to the pH measurements of the reference samples exposed to deionized water.

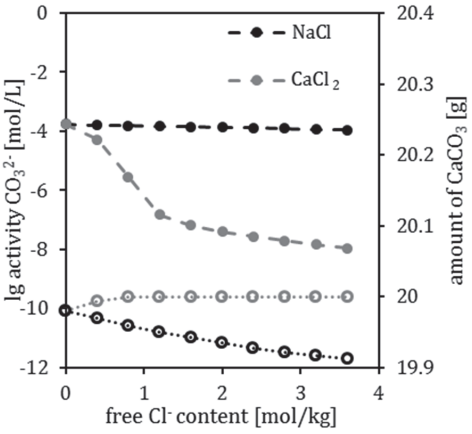

Figure 6: Results of the thermodynamic modelling of the activity of CO_3^{2-} ions (*filled icons, dashed lines, plotted as* log_{10}) in the pore solution and the amount of $CaCO_3$ present in the system (*hollow icons, dotted lines*) with increasing additions of NaCl or $CaCl_2$.

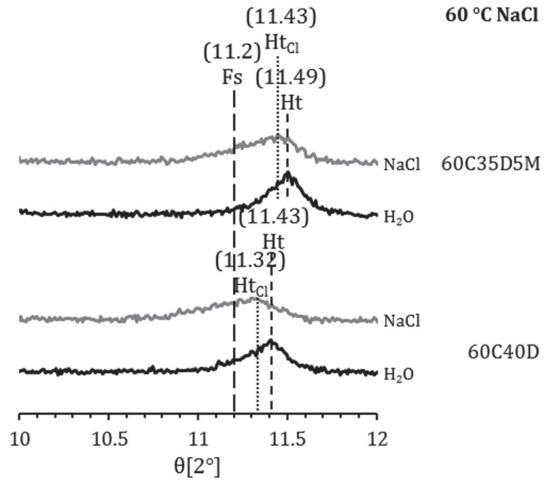

Figure 7: Zoomed in XRD patterns between 10 and 12 °2θ of the samples 60C40D and 60C35D5M cured at 60 °C that were exposed to NaCl compared with their reference samples exposed to deionized water.

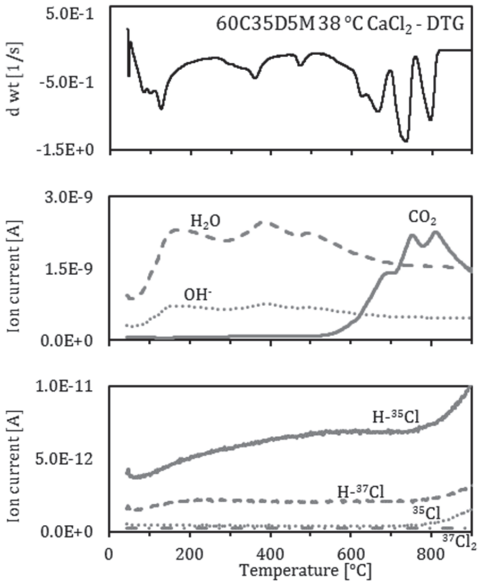

Figure 8: Mass spectra of the various components released during TGA-MS investigations of sample 60C35D5M cured at 38 °C and exposed to $CaCl_2$. Note the different scaling on the y-axes.

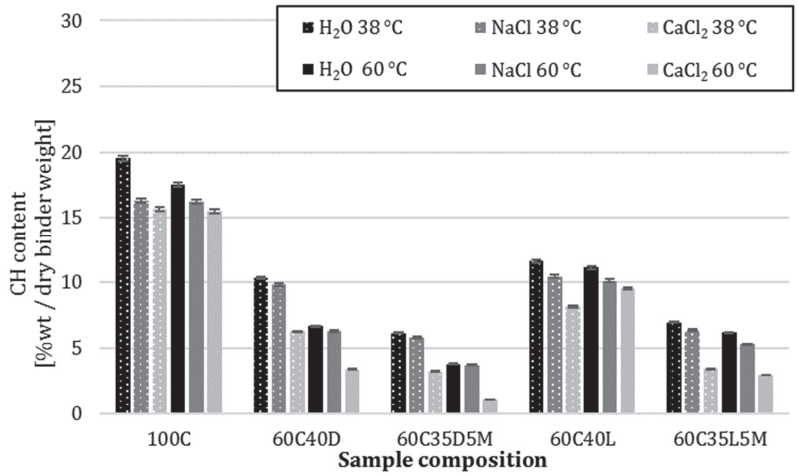

Figure 9: Portlandite content normalized to the dry binder weight for the various samples cured at 38 °C or 60 °C that were exposed to H_2O, NaCl or $CaCl_2$.

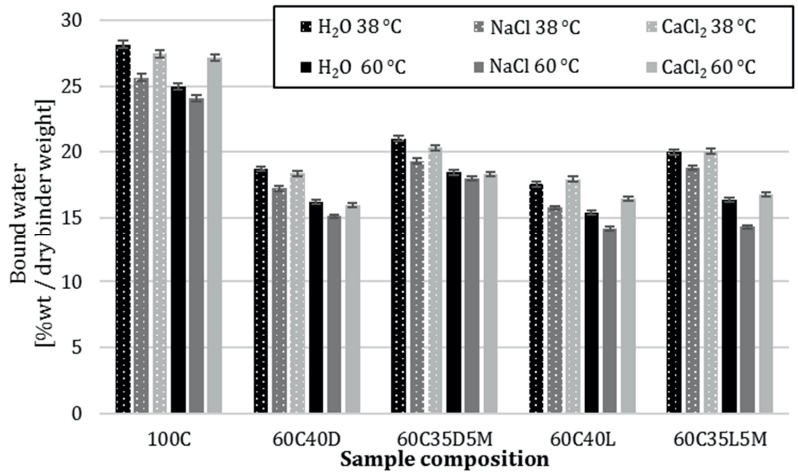

Figure 10: Bound water content normalized to the dry binder weight for the various samples cured at 38 °C or 60 °C that were exposed to H_2O, NaCl or $CaCl_2$.

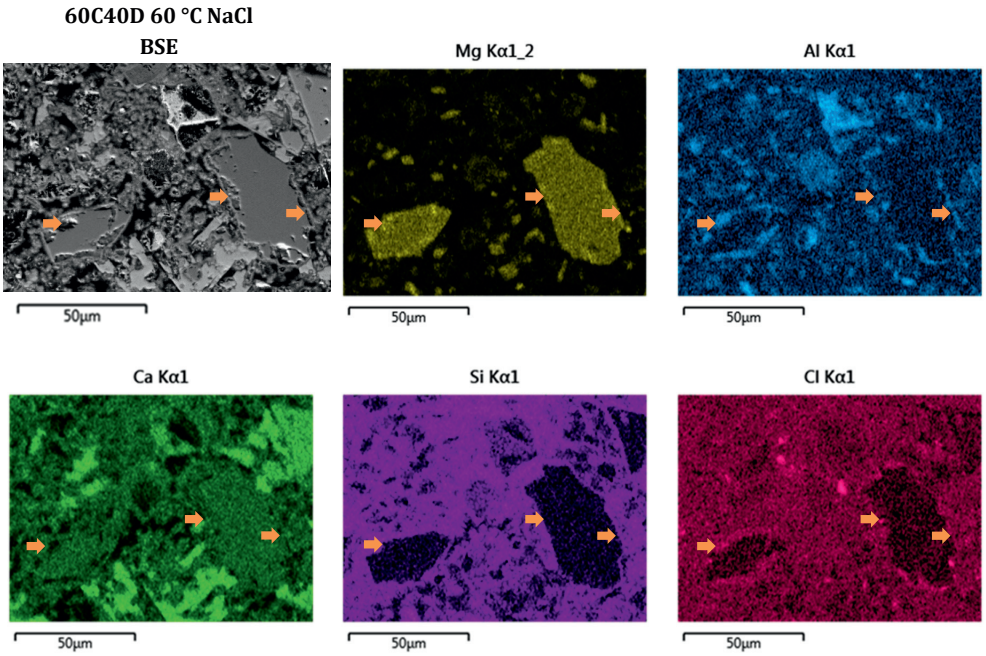

Figure 11: BSE image and elemental maps of magnesium, aluminium, calcium, silicon and chlorine for sample 60C40D cured at 60 °C and exposed to a 2 mol/L NaCl solution.

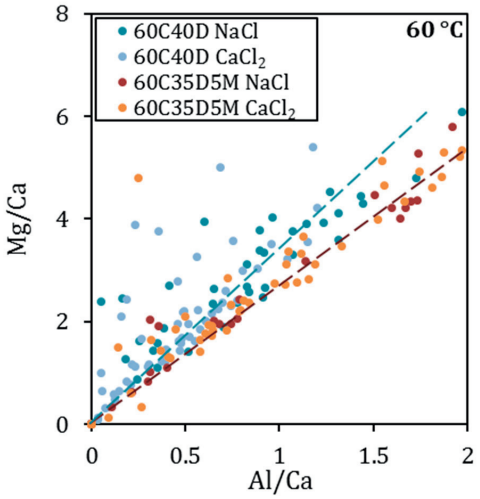

Figure 12: Mg/Ca ratio over the Al/Ca ratio for the point analyses of the reaction rims around the dolomite grains in samples 60C40D and 60C35D5M, which were cured at 60 °C and exposed to NaCl or $CaCl_2$.

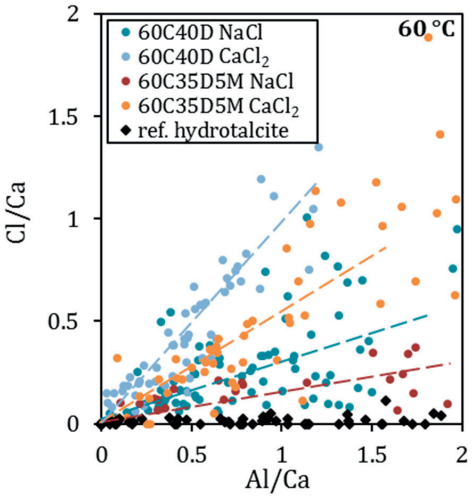

Figure 13: Cl/Ca ratio over the Al/Ca ratio for the point analyses of the reaction rims around the dolomite grains in samples 60C40D and 60C35D5M, which were cured at 60 °C and exposed to NaCl or $CaCl_2$. In addition, the results for the point analyses in such reaction rims from a previous study [10] are shown as a reference for not-exposed samples.

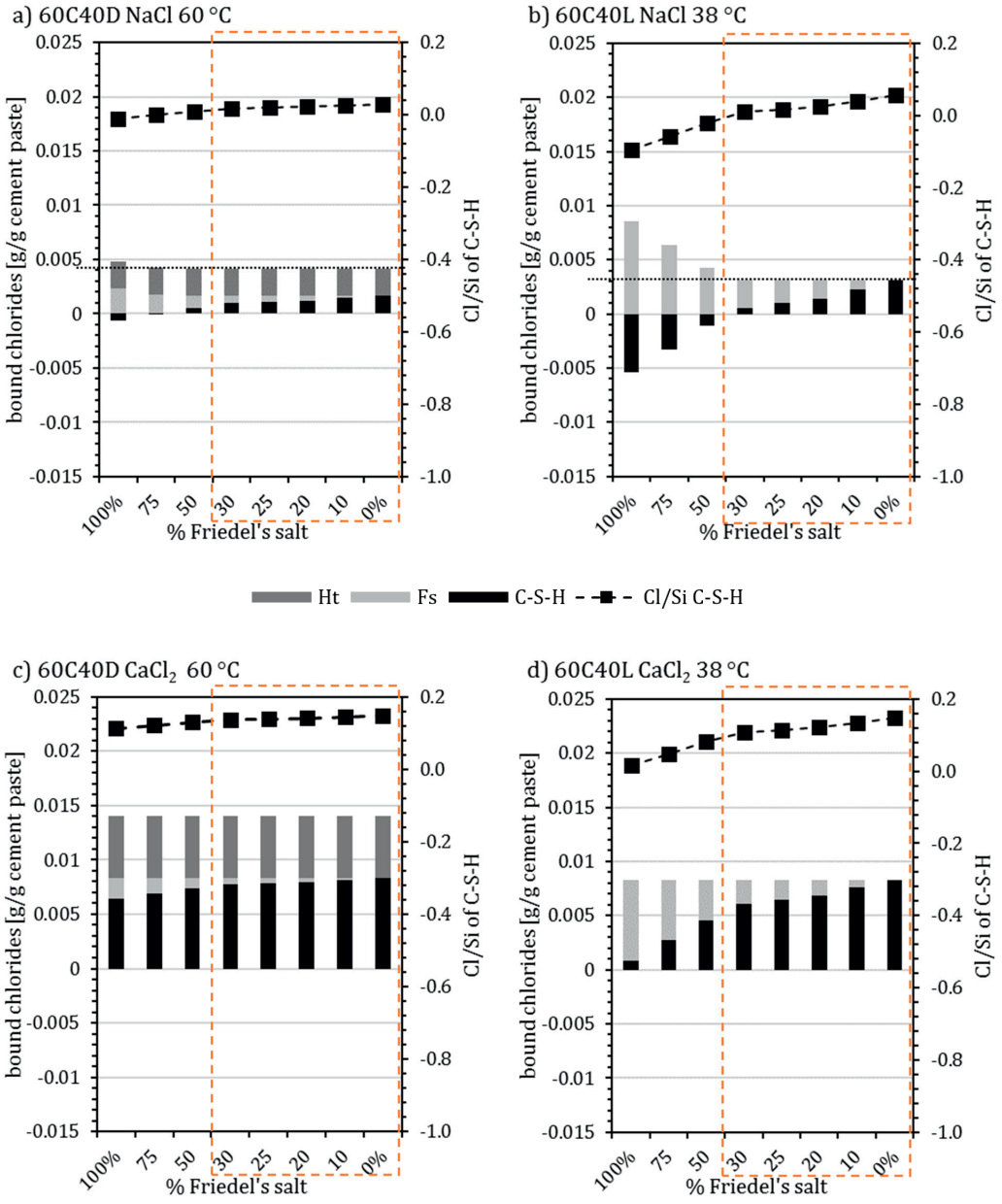

Figure 14: Calculated Cl/Si ratio of the C-S-H and amount of chloride bound in C-S-H, Friedel's salt, and hydrotalcite calculated for the samples 60C40D (60 °C) and 60C40L (38 °C) exposed to NaCl or $CaCl_2$ depending on the distribution of the aluminium between Friedel's salt and monocarbonate. The dotted lines in a) and b) indicate the amount of bound chlorides determined with potentiometric titration (see Figure 3).

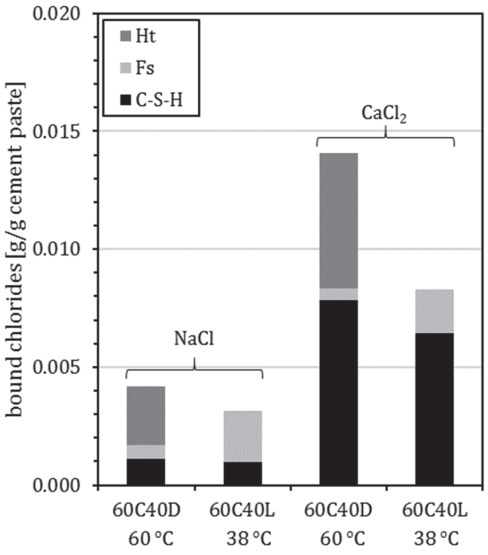

Figure 15: Amount of chloride bound in C-S-H, Friedel's salt, and hydrotalcite calculated for the samples 60C40D (60 °C) and 60C40L (38 °C) exposed to NaCl or $CaCl_2$, when 25% of the aluminium available for the formation of AFm phases is distributed to Friedel's salt (and 75% to monocarbonate).

8 Appendix

8.1 Hydrate phase assemblage in the exposed samples

8.1.1 XRD

Figure A1 a), b) and Figure A2 a), b) show the XRD patterns between 8 and 13 °2θ for the samples containing dolomite exposed to NaCl or $CaCl_2$ and their reference samples exposed to deionized water. The peak positions of ettringite (Et – 9.1 °2θ), monosulphate (Ms – 9.9 °2θ), Friedel's salt (Fs – 11.2 °2θ), monocarbonate (Mc – 11.7 °2θ), hydrotalcite (Ht – approx. 11.4 °2θ) and the chloride-containing hydrotalcite (Ht_{Cl} – approx. 11.1–11.3 °2θ) are also indicated.

Whether exposed to NaCl or $CaCl_2$, the samples show very similar qualitative phase assemblages, so they are described together in the following, with differences highlighted.

Sample 60C40D shows a qualitatively similar phase assemblage whether cured at 38 °C or 60 °C. In both cases, hydrotalcite was observed in the reference samples exposed to water and, with chloride exposure, this peak shifted to lower angles. This shift was reported to be due to the formation of a chloride-containing hydrotalcite-like phase [13]. The peaks of hydrotalcite and chloride-containing hydrotalcite were both higher in samples cured at 60 °C than in samples cured at 38 °C. In samples with metakaolin added in combination with dolomite (60C35D5M), monocarbonate was observed as well as a small peak of hydrotalcite in the reference samples cured at 38 °C. In the samples exposed to chloride solutions, the monocarbonate transformed to Friedel's salt. The Friedel's salt and chloride-containing hydrotalcite peaks overlap, so no conclusion on the presence of small amounts of chloride-containing hydrotalcite can be drawn for this sample with XRD. Cured at 60 °C, sample 60C35D5M showed no peaks of monocarbonate or Friedel's salt. As with sample 60C40D only hydrotalcite, in the case of water exposure, or the chloride-containing hydrotalcite, in the case of chloride exposure, were observed. The ettringite observed in the reference samples seemed to be reduced by the exposure to chloride solutions or to disappear completely. The only exception was sample 60C35D5M, which also showed an increase in the ettringite peak when originally cured at 60 °C as opposed to 38 °C. For the compositions for which ettringite could be observed when exposed to deionized water, a monosulphate-14H peak was observed instead of ettringite when exposed to $CaCl_2$.

Figure A3 a), b) and Figure A4 a), b) show the XRD patterns of the samples containing limestone exposed to NaCl or $CaCl_2$ and their reference samples exposed to deionized water. In samples containing limestone cured at 38 °C, the AFm phase observed in water-exposed samples was monocarbonate, while in chloride-exposed samples the AFm phase was mainly Friedel's salt. No

monocarbonate peak was observed in any of the samples cured at 60 °C, and only a small hump of Friedel's salt was detected in sample 60C35L5M (60 °C) exposed to NaCl. As with the samples containing dolomite, the ettringite peak seemed to be reduced by exposure to chloride solutions and a monosulphate-14H peak was observed in the samples exposed to $CaCl_2$. Sample 60C40L showed an especially high ettringite peak in the samples cured at 60 °C compared to 38 °C.

8.1.2 TGA

The TGA results for the samples exposed to NaCl or $CaCl_2$ were generally quite similar so they are described together in the following, with differences highlighted.

Figure A1 c), d) and Figure A2 c), d) show the DTG curves of the samples containing dolomite exposed to NaCl or $CaCl_2$ and their reference samples, which were exposed to deionized water. Samples containing dolomite and cured at 38 °C showed a clear ettringite peak in samples exposed to deionized water, and to a lesser degree in the samples exposed to NaCl or $CaCl_2$. The samples containing a combination of metakaolin and dolomite showed a clear peak of monocarbonate where exposed to water, and of Friedel's salt were exposed to chloride solution. Neither monocarbonate nor Friedel's salt were observed with TGA in samples containing dolomite that did not contain metakaolin, indicating that most of the aluminium is bound in the hydrotalcite. The only exception to this was sample 60C40D exposed to $CaCl_2$, which showed a small peak of Friedel's salt. Due to the overlap of the second peak of Friedel's salt (approx. 370 °C) with the decomposition temperature of chloride-containing hydrotalcite, the appearance of the first peak (approx. 150 °C) was used to identify Friedel's salt in the sample. This first Friedel's salt peak was more pronounced in samples exposed to $CaCl_2$ than in samples exposed to NaCl. This observation confirms the findings of Shi et al., who reported additional formation of Friedel's salt in samples exposed to $CaCl_2$ due to the increased availability of calcium ions [3]. Hydrotalcite also showed two peaks in TGA, the first of which (approx. 220 °C) was significantly reduced or completely vanished in the samples exposed to chloride solutions instead of deionized water. The second peak of hydrotalcite (approx. 400 °C) shifted to lower temperatures (approx. 370 °C) in samples exposed to chloride solutions. On this peak, the shoulder of a Friedel's salt peak at even lower temperatures was observed in samples that also showed the first Friedel's salt peak. The portlandite peak seemed little affected by exposure to NaCl, but it was significantly lower in samples containing metakaolin or exposed to $CaCl_2$.

In samples containing dolomite cured at 60 °C, the ettringite peak was significantly lower compared to 38 °C, especially in samples containing no metakaolin. AFm phases like monocarbonate or Friedel's salt were no longer observed. Only sample 60C40D cured at 60 °C and

exposed to $CaCl_2$ showed a peak of monocarbonate. The peaks related to hydrotalcite or chloride-containing hydrotalcite were higher than in samples cured at 38 °C. In both cases, the chloride-containing hydrotalcite could be distinguished by the significantly lower or missing first peak and the shift to lower temperatures of the second peak compared to the normal hydrotalcite. This was observed in all samples except sample 60C35D5M cured at 60 °C exposed to NaCl, which showed only a slight decrease in the first peak and no shift for the second peak. In samples cured at 60 °C, the portlandite content seemed lower in samples with NaCl exposure, metakaolin addition and especially with $CaCl_2$ exposure.

The DTG curves for the samples containing limestone exposed to NaCl or $CaCl_2$ and their reference samples exposed to deionized water are shown in Figure A3 c), d) and Figure A4 c), d). Like the samples containing dolomite, the samples containing limestone cured at 38 °C, showed a clear ettringite peak at low temperatures that seemed to decrease when exposed to NaCl or $CaCl_2$ compared to the references exposed to water. In the latter case, there was a clear peak of monocarbonate, which was even greater for samples containing metakaolin. In samples exposed to $CaCl_2$, a clear Friedel's salt peak was observed instead of monocarbonate. This was also the case in samples exposed to NaCl, but it was less clear and combined with a monocarbonate peak. The reference samples containing limestone exposed to deionized water also showed very small peaks in the temperature region of hydrotalcite. This weight loss might be caused by hydrotalcite formed due to the large amount of magnesium present in the cement (Table 1). In the samples containing limestone exposed to NaCl or $CaCl_2$, a clear peak of Friedel's salt and what was probably a small peak of chloride-containing hydrotalcite was observed. As with the samples containing dolomite, the portlandite peak was only affected by the presence of metakaolin or the exposure to $CaCl_2$.

In samples containing limestone cured at 60 °C, the ettringite peak was again lower than in those cured at 38 °C, though the decrease was not as great as in the samples containing dolomite. No AFm phases were observed with TGA, except for a small peak of Friedel's salt in sample 60C35L5M exposed to $CaCl_2$. As in the samples containing dolomite, the peaks related to hydrotalcite were higher in samples cured at 60 °C than in samples cured at 38 °C. The Friedel's salt peak in the chloride-exposed samples showed a clear asymmetry or a double peak, indicating also an increase in the amount of chloride-containing hydrotalcite. The portlandite peak was reduced by both chloride exposures, but especially by exposure to $CaCl_2$, and in samples with metakaolin.

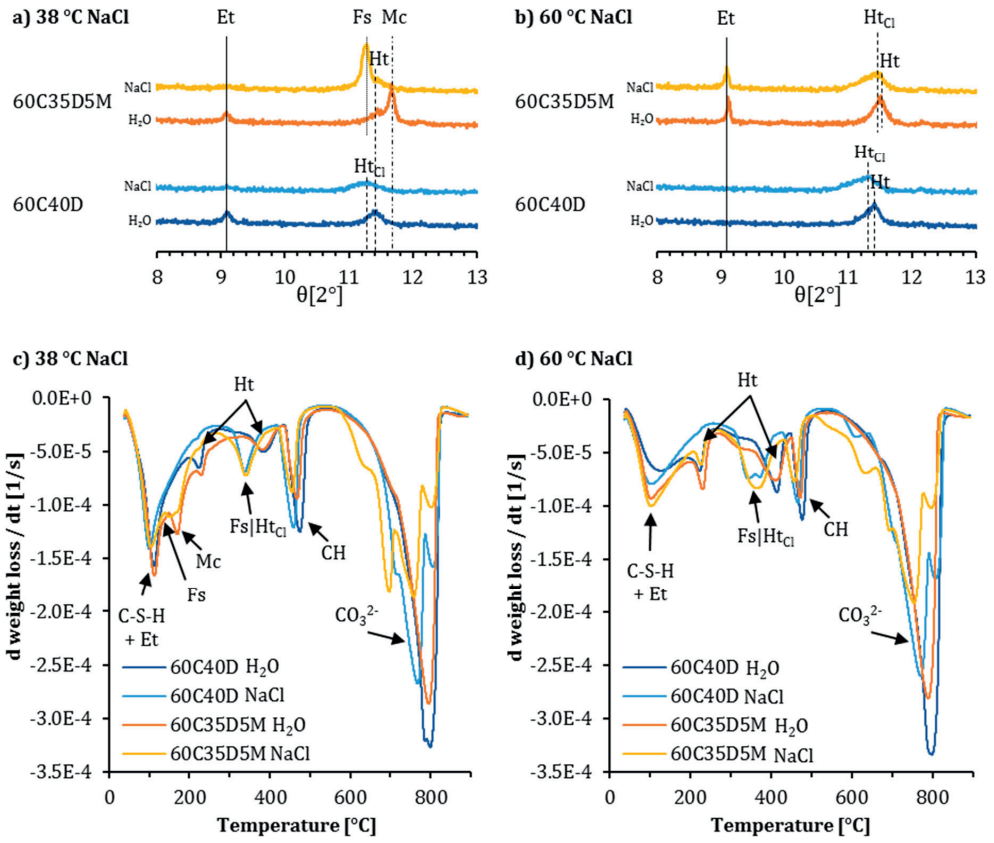

Figure A1: Phase assemblage of the samples containing dolomite cured at 38 °C or 60 °C that were exposed to 2 mol/L NaCl compared with their reference samples exposed to deionized water. a) and b) show the XRD patterns of these samples between 8 and 13 °2θ, and c) and d) show the DTG curves of these samples from 40–900 °C.

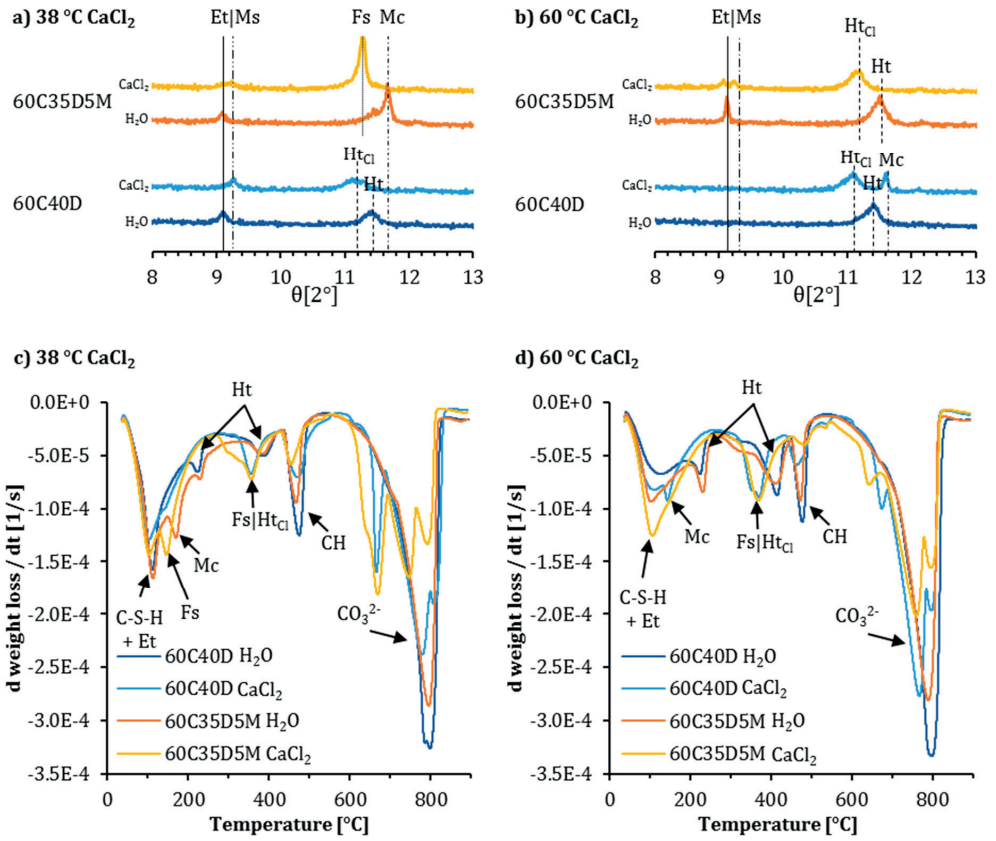

Figure A2: Phase assemblage of the samples containing dolomite cured at 38 °C or 60 °C that were exposed to 2 mol/L $CaCl_2$ compared with their reference samples exposed to deionized water. a) and b) show the XRD patterns of these samples between 8 and 13 °2θ, c) and d) show the DTG curves of these samples from 40–900 °C.

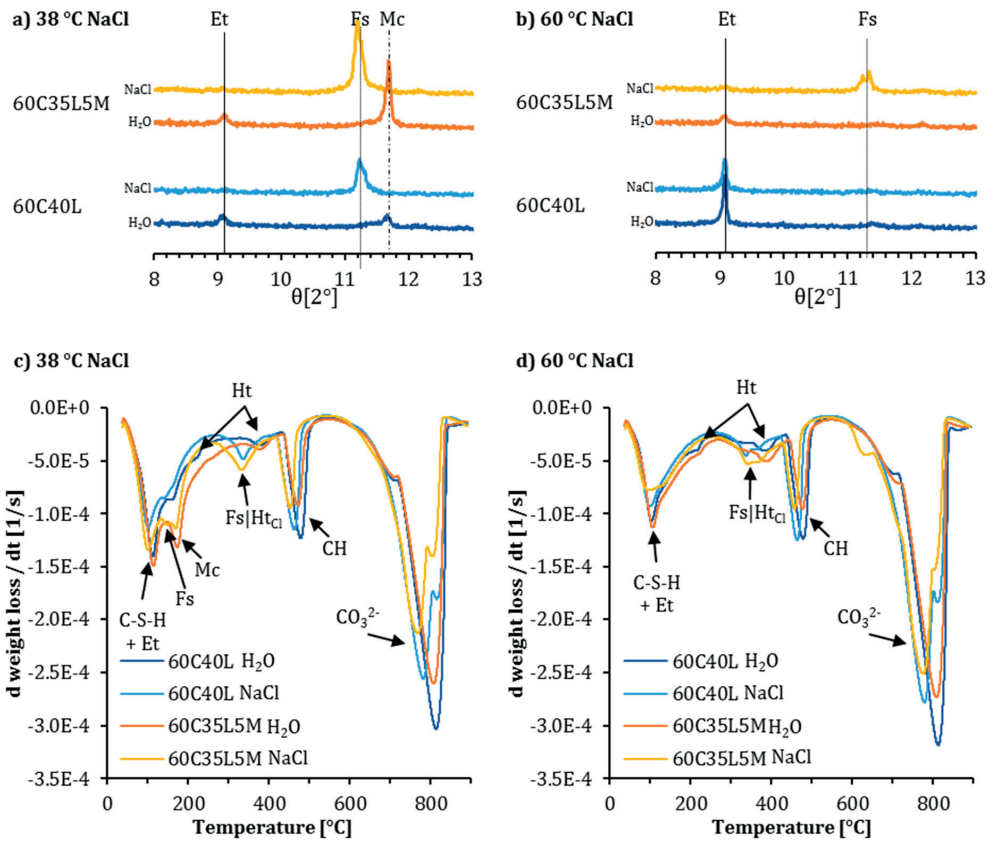

Figure A3: Phase assemblage of the samples containing limestone cured at 38 °C or 60 °C that were exposed to 2 mol/L NaCl compared with their reference samples exposed to deionized water. a) and b) show the XRD patterns of these samples between 8 and 13 °2θ, c) and d) show the DTG curves of these samples from 40–900 °C.

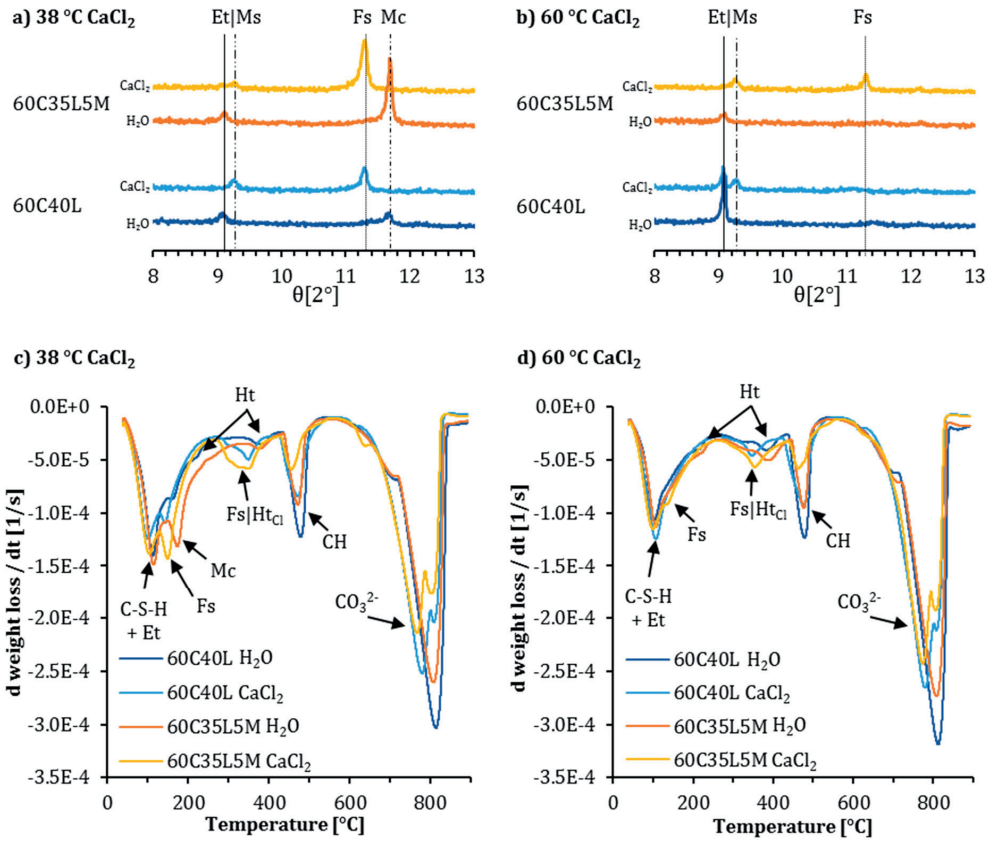

Figure A4: Phase assemblage of the samples containing limestone cured at 38 °C or 60 °C that were exposed to 2 mol/L $CaCl_2$ compared with their reference samples exposed to deionized water. a) and b) show the XRD patterns of these samples between 8 and 13 °2θ, c) and d) show the DTG curves of these samples from 40–900 °C.

Appendix

Investigation of the products of the dolomite reaction in Portland cement pastes

Machner, A., Zajac, M., Ben Haha, M., Kjellsen, K.O., Geiker, M.R., De Weerdt, K.
Proceedings of the XXIII Nordic Concrete Research Symposium, Aalborg (Denmark),
August 21th–23rd 2017.

Investigation of the products of the dolomite reaction in Portland cement pastes

Alisa Machner
Industrial PhD student
Norcem AS
NTNU Department of Structural Engineering
NO – 7034 Trondheim
alisa.machner@ntnu.no

Maciej Zajac
Mohsen Ben Haha
Heidelberg Technology Center
DE – 69181 Leimen
maciej.zajac@htc-gmbh.com
mohsen.ben.haha@htc-gmbh.com

Knut O. Kjellsen
R&D Manager
Norcem AS
FoU
NO – 3991 Brevik
knut.kjellsen@norcem.no

Mette R. Geiker
Klaartje De Weerdt
Professors
NTNU Department of Structural Engineering
NO – 7034 Trondheim
klaartje.d.weerdt@ntnu.no
mette.geiker@ntnu.no

ABSTRACT

The formation of potentially deleterious reaction products from the reaction of dolomite fines in Portland cement pastes was investigated. It was shown that the reaction of dolomite fines did not follow the commonly accepted dedolomitization reaction. Instead, similar hydration phases as reported for the Portland cement containing limestone are observed, with the exception that also hydrotalcite is formed. It was shown with SEM-EDS and XRD that hydrotalcite is the only magnesium containing hydration product of the dolomite reaction, as no brucite or M-S-H were detected. In the next step of this study this reaction will be investigated in Al-rich systems.

Keywords: Supplementary cementitious materials (SCM)

1. INTRODUCTION

Due to the scarceness of high-quality limestone as required for CEM II Portland-limestone cements, other carbonate sources, like dolomite ($CaMg(CO_3)_2$), are in the focus as alternative mineral replacement for cement clinker. However, dolomite is assumed to undergo the so-called dedolomitization reaction in high-pH environments. In this reaction, dolomite reacts with calcium hydroxide (portlandite) to form calcium carbonate (calcite) and magnesium hydroxide (brucite) [1-3], as shown in equation 1.

$$CaMg(CO_3)_2 + Ca(OH)_2 \rightarrow 2CaCO_3 + Mg(OH)_2 \quad (1)$$

There is still an ongoing discussion whether this reaction is harmful to concrete made with dolomitic aggregates. It was recently shown, that in cementitious systems, where other ions are present (Al, Si), the reaction of dolomite results in products similar to those of hydrating Portland-limestone cement with the exception of additional hydrotalcite [4]. The aim of this study was to investigate the influence of replacement of Portland cement clinker by dolomite on the phase assemblage. This was done with focus on whether other magnesium-containing and potentially harmful phases are formed during the reaction of dolomite i.e. brucite (expansive) or

M-S-H (low cementing properties). In a next step of this study the influence of additional aluminium by the addition of metakaolin on the dolomite reaction will be investigated.

2. EXPERIMENTAL

The cement pastes investigated in this study were prepared by replacing 40 %wt of a Portland cement clinker by natural dolomite. Precipitated gypsum was added, when mixing, in order to achieve a sulphate content of 2.5 %wt per gram of binder. The cement clinker was ground in a laboratory ball mill until a Blaine surface of approx. 400 m^2/kg was achieved. The dolomite was used as received (Blaine surface: 340 m^2/kg). The chemical compositions of the major elements of the materials used are given in Table 1. The paste samples were prepared with a w/b ratio of 0.45 and were stored under sealed conditions at a relative humidity of 100% at 38 °C or 60 °C for 360 days.

Table 1 – Chemical composition of the clinker and dolomite used.

	SiO_2	Al_2O_3	Fe_2O_3	CaO	MgO	K_2O	Na_2O	SO_3	LOI
Clinker	20.6	5.6	3.12	63.26	2.66	1.23	0.51	1.37	-
Dolomite	0.52	0.01	0.04	31.52	20.14	0.00	0.00	0.00	46.79

In order to investigate the phase assemblage and microstructure of the samples with scanning electron microscopy (SEM), a 3 mm slice was cut off the cured cement paste and immersed in isopropanol for min. 1 week. Polished and carbon coated sections of the paste samples were prepared for SEM analysis. Elemental mapping and spot analyses were carried out using a Hitachi S-3400N microscope equipped with an energy dispersive spectrometer (EDS) from Oxford. Prior to X-ray diffraction (XRD) analyses, the hydration of the cement pastes was stopped by double solvent exchange using isopropanol and petroleum ether. For the XRD analyses a D8 Focus diffractometer from Bruker was used for the measurements with a Bragg-Brentano $\theta - \theta$ geometry and Cu-Kα radiation (approx. 1.54 Å).

3. RESULTS AND DISCUSSION

Figure 1 shows the BSE images and the elemental maps of magnesium, aluminium, oxygen, calcium and silicon for the investigated sample cured at 38 °C and 60 °C. The large uniform grains (length up to 70 µm) in both images contain magnesium and calcium and are poor in silicon and aluminium. These particles are unreacted dolomite grains. For the sample cured at 60 °C (Figure 1 – upper row) a darker reaction rim can be observed within the original grain boundaries of the dolomite grains. These rims appear to be enriched in magnesium compared to the original dolomite grains. Additionally they contain high amounts of aluminium but are poor in silicon and calcium. High oxygen levels were measured in these rims, indicating that the products formed in them are hydrates. The original grain boundaries of the dolomite grains are still visible because a bright thin layer of C-S-H phase has precipitated around them at early ages. This layer then persisted even after the dolomite started to react at later ages. The dark thick reaction rims within the former dolomite grain boundaries indicate a high reaction degree of the dolomite at 60 °C, which results in complete reaction of the smaller dolomite particles. The sample cured at 38 °C shows almost no reaction of the dolomite (Figure 2 – lower row). Only around small cracks in the dolomite particles and directly at the surface, aluminium and oxygen are slightly increased. This is in-line with the findings of Zajac et al. [4], who reported a notably higher reaction degree for dolomite in a composite cement when cured at 60 °C compared to 38 °C. Also other authors reported an increased dissolution rate of dolomite at

elevated curing temperatures [2,3]. From the elemental map of magnesium it can be seen, that magnesium is present only inside the former dolomite grain boundaries. This is probably due to the low mobility of magnesium in high pH environment. The results of the SEM-EDS point analyses of the reaction rims are plotted in Figure 2 as the Mg/Si over the Al/Si ratio. The data points for the sample cured at 38 °C coincide with the y-axis. This is probably due to the limited rim thickness, which results in the measurement of the unreacted dolomite rather than an actual reaction product. In the case of the sample cured at 60 °C, the data points describe a linear line. This indicates that the reaction product has a fixed Mg/Al ratio and does not contain silicon. It can therefore be concluded, that no M-S-H has formed during the reaction of dolomite. The reaction product can be identified as hydrotalcite ($Mg_{4+x}Al_2(CO_3)_y(OH)_{16}\cdot 4(H_2O)$) [5]. The Mg/Al ratio of the hydrotalcite formed was 3.2 in this study. Zajac et al [4] measured a lower Mg/Al ratio of approx. 2 in their samples, probably due to the lower dolomite addition they used in their mixes as they used a similar clinker.

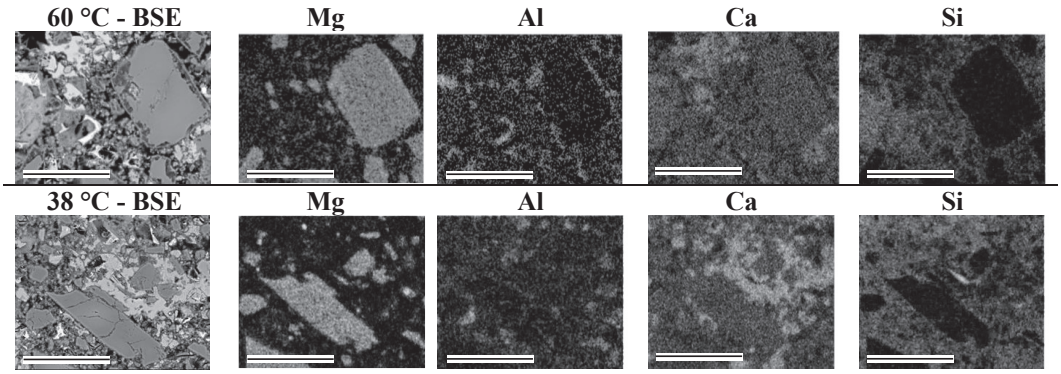

Figure 1 – BSE image and elemental maps of Mg, Al, O, Ca and Si of the sample 60C40D cured at 60 °C (upper row) and 38 °C (lower row) for 360 days. The scales (white bars) represent a length of 50 µm.

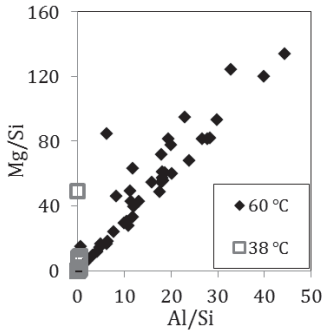

Figure 2 – Mg/Si over Al/Si ratio of the reaction rim in the samples cured at 60 °C or 38 °C.

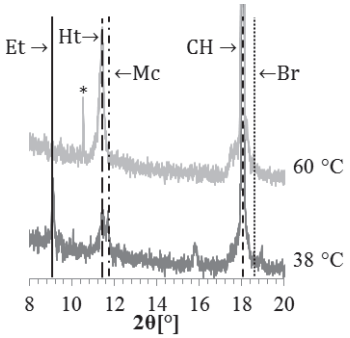

Figure 3 – XRD plots of the samples cured at 60 °C or 38 °C for 360 days. (indicates a peak of unknown origin)*

Figure 3 shows the XRD plots for the samples cured at 38 °C and 60 °C in the range of 8 to 20 °2θ. The main reflections of ettringite (Et) (9.1 °2θ), hydrotalcite (Ht) (11.4 °2θ), monocarbonate (Mc) (11.7 °2θ), portlandite (CH) (18.1 °2θ) and brucite (Br) (18.6 °2θ) are indicated. The sample cured at 38 °C, shows a clear ettringite peak and small peaks of hydrotalcite and monocarbonate. The reaction of dolomite delivers CO_2 to the system, which

can stabilize ettringite by the formation of monocarbonate at 38 °C. This is in agreement with the findings of Zajac et al. [4]. At 60 °C, the stable phases differ significantly from those at 38 °C. The ettringite peak is not observed as this phase is not stable at 60 °C [6]. Moreover, monocarbonate is not detected. The main diffraction peak observed is hydrotalcite, which shows a notably higher and sharper peak at 60 °C compared to the sample cured at 38 °C. This is in good agreement with the observations made by SEM-EDS, which showed a notably higher reaction degree of dolomite at 60 °C compared to 38 °C. In both samples no clear brucite peaks could be observed by XRD. Hydrotalcite is therefore assumed to be the only magnesium-containing reaction product of the dolomite reaction. The proposed reaction based on our observations of dolomite in a cementitious system is given in equation 2.

$$CaMg(CO_3)_2+Ca(OH)_2+[Al(OH)_4]^- \rightarrow Mg_{4+x}Al_2(CO_3)_y(OH)_{16}\cdot 4(H_2O) + CaCO_3 + CO_3^{2-} \quad (2)$$

The dolomite will react with portlandite and alumina in the pore solution to form hydrotalcite and provides carbonate ions to the system which might partially react further to calcite or carbonate AFm. No potentially harmful phases such as brucite or M-S-H were observed.

4. CONCLUSION

It has been shown that the reaction of dolomite fines, when used as replacement for Portland cement clinker, results in the formation of hydrotalcite, especially at 60 °C. Additionally, at 38 °C the stabilization of ettringite due to the formation of monocarbonate can be observed. Contrary to the commonly assumed reaction of dolomite in high-pH environments no brucite was detected. Hydrotalcite was the only magnesium containing product of the dolomite reaction. The reaction of dolomite fines in cementitious systems is therefore not assumed to form any deleterious hydration products. In a next step of this study we will investigate the influence of additional aluminium by the addition of metakaolin on the dolomite reaction.

5. ACKNOWLEDGEMENTS

We acknowledge the industrial Ph.D. programme (project-nr: 241637) of the Norwegian Research Council and the Heidelberg Technology Center for their financial support.

REFERENCES

1. E. Garcia, P. Alfonso, M. Labrador, S. Galí, Dedolomitization in different alkaline media: Application to Portland cement paste, Cem Concr Res 33 (2003) 1443–1448.
2. S. Galí, C. Ayora, P. Alfonso, E. Tauler, M. Labrador, Kinetics of dolomite-portlandite reaction - Application to Portland cement concrete, Cem Concr Res 31 (2001) 933–939.
3. X. Zhang, F.P. Glasser, K.L. Scrivener, Reaction kinetics of dolomite and portlandite, Cem Concr Res 66 (2014) 11–18.
4. M. Zajac, S.K. Bremseth, M. Whitehead, M. Ben Haha, Effect of $CaMg(CO_3)_2$ on hydrate assemblages and mechanical properties of hydrated cement pastes at 40 °C and 60 °C., Cem Concr Res 65 (2014) 21–29.
5. M. Ben Haha, B. Lothenbach, G. Le Saout, F. Winnefeld, Influence of slag chemistry on the hydration of alkali-activated blast-furnace slag — Part I: Effect of MgO, Cem Concr Res 41 (2011) 955–963.
6. B. Lothenbach, F. Winnefeld, C. Alder, E. Wieland, P. Lunk, Effect of temperature on the pore solution, microstructure and hydration products of Portland cement pastes, Cem Concr Res 37 (2007) 483–491.

Bedre egenskaper med dolomitt i sement

Machner, A., Geiker, M.R., De Weerdt, K., Kjellsen, K.O.
Byggeindustrien, 2017, Nr. 16, p. 76

NYTT FRA NTNU

Bedre egenskaper med dolomitt i sement

Komposittsementer kan ha tilsvarende eller til og med bedre egenskaper enn ren Portland sement. På grunn av den økende etterspørselen etter betong, og dermed sement, er tradisjonelle supplerende sementmaterialer en mangelvare. Alternative sementmaterialer har derfor fokus i dagens forskning. Resultatene fra DOLCEM-prosjektet viser at bruk av dolomitt kan gi økt bestandighet til betong.

Alisa Machner, Mette R. Geiker og Klaartje De Weerdt
Institutt for konstruksjonsteknikk

Knut O. Kjellsen
Norcem HeidelbergCement

Lav CO2 utslippsement produseres ved å bruke lokale substituttmaterialer som dolomitt og kalsinerte leire.
Foto: Norcem

Bruk av dolomitt som et alternativ til kalkstein som substituttmateriale til Portland klinker, gir sementindustrien bedre mulighet til å utnytte lokale råstoffer. Dette vil ofte medføre lavere kostnader og lavere CO2 utslipp pga. redusert transport. Også bruk av kalsinert leire kan være interessant for sementindustrien i framtiden for å redusere CO2 utslipp. Enten fordi alternative pozzolaniske materialer ikke finnes lokalt, eller fordi tilgangen til de gode pozzolaniske materialene som i dag brukes av sementindustrien i stor skala (flygeaske fra kullfyrte kraftverk og granulert jernovnsslag), blir dårligere.

Dolomitt og kalsinert leire som supplerende sementmaterialer

I DOLCEM-prosjektet har vi fokusert på komposittsementer som inneholder både kalsinert leire og dolomitt som substituttmaterialer. Omfattende forskning innenfor blant annet COIN-prosjektet har vist at kalsinert leire er en veldig lovende pozzolan for sementproduksjon. Utfordringen er at dolomitt ikke kan brukes i følge regelverket som kun tillater ren kalkstein. Men ren kalkstein, slik det kreves i den europeiske standarden, er ikke tilgjengelig i alle deler av verden i tilstrekkelige mengder. Vi har derfor fokusert på dolomitt som et alternativ til konvensjonelt anvendt kalkstein for komposittsementer med kalsinert leire.

Effekt av dolomitt på sementreaksjonen

Vi har vist at det er mulig å erstatte tilsvarende mengde kompositsement med enten dolomitt eller kalkstein uten å redusere trykkfastheten. Ved bruk av dolomitt eller kalsinert leire dannes det andre typer hydratasjonsfaser enn i ren Portland sement. Karbonatene fra dolomitt reagerer på lignende måte som karbonatene fra kalkstein, og stabiliserer ettringitt ved dannelse av karbonat-AFm-fasene. De ekstra magnesiumionene som introduseres med dolomitt i systemet, fører til dannelse av en ny fase kalt hydrotalkitt.

Forholdet mellom dolomitt og kalsinert leire er viktig

PhD kandidat Alisa Machner har i sitt doktorarbeid testet forskjellige kombinasjoner av dolomitt og kalsinert leire som supplerende sementmaterialer for sement. Forskningen viser at for å få dolomitt til å reagere, bør man bruke begrensede mengder kalsinert leire. Dette fordi kalsinert leire vil vinne kampen om Portlanditt som både dolomitt og kalsinert leire trenger for å kunne reagere.

Økt bestandighet av sementen

Hydrotalkitt, hovedhydratasjonsfasen til dolomitt, viser seg å være veldig stabil i aggressive miljøer som karbonatisering, utluting eller kloridholdige løsninger. Hydrotalkitt viser seg å kunne binde klorider. Høyere kloridbinding av betongen resulterer i en mindre andel frie klorider, og dermed forsinket kloridinntrenging og utsatt armeringskorrosjon. Dolomitt i kompositsement kan altså være en fordel for betong som skal være i kontakt med sjøvann eller tinesalter.

Forskningen innenfor DOLCEM-prosjektet er utført av Alisa Machner. Hun jobber som nærings-PhD ved NTNU, og er ansatt ved Norcem. På grunn av det tette samarbeidet med eksperter fra HeidelbergCement Technology Center i Tyskland, vil resultatene fra prosjektet påvirke sementproduksjonen også utenfor Norges grenser. Foto: Giedrius Zirgulis.

Doctoral Theses at the Department of Structural Engineering
at the Norwegian University of Science and Technology

DEPARTMENT OF STRUCTURAL ENGINEERING
NORWEGIAN UNIVERSITY OF SCIENCE AND TECHNOLOGY

N–7491 TRONDHEIM, NORWAY
Telephone: +47 73 59 47 00 Telefax: +47 73 59 47 01

"Reliability Analysis of Structural Systems using Nonlinear Finite Element Methods",
C. A. Holm, 1990:23, ISBN 82-7119-178-0.

"Uniform Stratified Flow Interaction with a Submerged Horizontal Cylinder",
Ø. Arntsen, 1990:32, ISBN 82-7119-188-8.

"Large Displacement Analysis of Flexible and Rigid Systems Considering
Displacement-Dependent Loads and Nonlinear Constraints",
K. M. Mathisen, 1990:33, ISBN 82-7119-189-6.

"Solid Mechanics and Material Models including Large Deformations",
E. Levold, 1990:56, ISBN 82-7119-214-0, ISSN 0802-3271.

"Inelastic Deformation Capacity of Flexurally-Loaded Aluminium Alloy Structures",
T. Welo, 1990:62, ISBN 82-7119-220-5, ISSN 0802-3271.

"Visualization of Results from Mechanical Engineering Analysis",
K. Aamnes, 1990:63, ISBN 82-7119-221-3, ISSN 0802-3271.

"Object-Oriented Product Modeling for Structural Design",
S. I. Dale, 1991:6, ISBN 82-7119-258-2, ISSN 0802-3271.

"Parallel Techniques for Solving Finite Element Problems on Transputer Networks",
T. H. Hansen, 1991:19, ISBN 82-7119-273-6, ISSN 0802-3271.

"Statistical Description and Estimation of Ocean Drift Ice Environments",
R. Korsnes, 1991:24, ISBN 82-7119-278-7, ISSN 0802-3271.

“Properties of concrete related to fatigue damage: with emphasis on high strength
concrete”,
G. Petkovic, 1991:35, ISBN 82-7119-290-6, ISSN 0802-3271.

"Turbidity Current Modelling",
B. Brørs, 1991:38, ISBN 82-7119-293-0, ISSN 0802-3271.

"Zero-Slump Concrete: Rheology, Degree of Compaction and Strength. Effects of
Fillers as Part Cement-Replacement",
C. Sørensen, 1992:8, ISBN 82-7119-357-0, ISSN 0802-3271.

"Nonlinear Analysis of Reinforced Concrete Structures Exposed to Transient Loading",
K. V. Høiseth, 1992:15, ISBN 82-7119-364-3, ISSN 0802-3271.

"Finite Element Formulations and Solution Algorithms for Buckling and Collapse Analysis of Thin Shells",
R. O. Bjærum, 1992:30, ISBN 82-7119-380-5, ISSN 0802-3271.

"Response Statistics of Nonlinear Dynamic Systems",
J. M. Johnsen, 1992:42, ISBN 82-7119-393-7, ISSN 0802-3271.

"Digital Models in Engineering. A Study on why and how engineers build and operate digital models for decisison support",
J. Høyte, 1992:75, ISBN 82-7119-429-1, ISSN 0802-3271.

"Sparse Solution of Finite Element Equations",
A. C. Damhaug, 1992:76, ISBN 82-7119-430-5, ISSN 0802-3271.

"Some Aspects of Floating Ice Related to Sea Surface Operations in the Barents Sea",
S. Løset, 1992:95, ISBN 82-7119-452-6, ISSN 0802-3271.

"Modelling of Cyclic Plasticity with Application to Steel and Aluminium Structures",
O. S. Hopperstad, 1993:7, ISBN 82-7119-461-5, ISSN 0802-3271.

"The Free Formulation: Linear Theory and Extensions with Applications to Tetrahedral Elements
with Rotational Freedoms",
G. Skeie, 1993:17, ISBN 82-7119-472-0, ISSN 0802-3271.

"Høyfast betongs motstand mot piggdekkslitasje. Analyse av resultater fra prøving i Veisliter'n",
T. Tveter, 1993:62, ISBN 82-7119-522-0, ISSN 0802-3271.

"A Nonlinear Finite Element Based on Free Formulation Theory for Analysis of Sandwich Structures",
O. Aamlid, 1993:72, ISBN 82-7119-534-4, ISSN 0802-3271.

"The Effect of Curing Temperature and Silica Fume on Chloride Migration and Pore Structure of High Strength Concrete",
C. J. Hauck, 1993:90, ISBN 82-7119-553-0, ISSN 0802-3271.

"Failure of Concrete under Compressive Strain Gradients",
G. Markeset, 1993:110, ISBN 82-7119-575-1, ISSN 0802-3271.

"An experimental study of internal tidal amphidromes in Vestfjorden",
J. H. Nilsen, 1994:39, ISBN 82-7119-640-5, ISSN 0802-3271.

"Structural analysis of oil wells with emphasis on conductor design",
H. Larsen, 1994:46, ISBN 82-7119-648-0, ISSN 0802-3271.

"Adaptive methods for non-linear finite element analysis of shell structures",
K. M. Okstad, 1994:66, ISBN 82-7119-670-7, ISSN 0802-3271.

"On constitutive modelling in nonlinear analysis of concrete structures",
O. Fyrileiv, 1994:115, ISBN 82-7119-725-8, ISSN 0802-3271.

"Fluctuating wind load and response of a line-like engineering structure with emphasis on motion-induced wind forces",
J. Bogunovic Jakobsen, 1995:62, ISBN 82-7119-809-2, ISSN 0802-3271.

"An experimental study of beam-columns subjected to combined torsion, bending and axial actions",
A. Aalberg, 1995:66, ISBN 82-7119-813-0, ISSN 0802-3271.

"Scaling and cracking in unsealed freeze/thaw testing of Portland cement and silica fume concretes",
S. Jacobsen, 1995:101, ISBN 82-7119-851-3, ISSN 0802-3271.

"Damping of water waves by submerged vegetation. A case study of laminaria hyperborea",
A. M. Dubi, 1995:108, ISBN 82-7119-859-9, ISSN 0802-3271.

"The dynamics of a slope current in the Barents Sea",
Sheng Li, 1995:109, ISBN 82-7119-860-2, ISSN 0802-3271.

"Modellering av delmaterialenes betydning for betongens konsistens",
Ernst Mørtsell, 1996:12, ISBN 82-7119-894-7, ISSN 0802-3271.

"Bending of thin-walled aluminium extrusions",
Birgit Søvik Opheim, 1996:60, ISBN 82-7119-947-1, ISSN 0802-3271.

"Material modelling of aluminium for crashworthiness analysis",
Torodd Berstad, 1996:89, ISBN 82-7119-980-3, ISSN 0802-3271.

"Estimation of structural parameters from response measurements on submerged floating tunnels",
Rolf Magne Larssen, 1996:119, ISBN 82-471-0014-2, ISSN 0802-3271.

“Numerical modelling of plain and reinforced concrete by damage mechanics”,
Mario A. Polanco-Loria, 1997:20, ISBN 82-471-0049-5, ISSN 0802-3271.

“Nonlinear random vibrations - numerical analysis by path integration methods”,
Vibeke Moe, 1997:26, ISBN 82-471-0056-8, ISSN 0802-3271.

"Numerical prediction of vortex-induced vibration by the finite element method",
Joar Martin Dalheim, 1997:63, ISBN 82-471-0096-7, ISSN 0802-3271.

"Time domain calculations of buffeting response for wind sensitive structures",
Ketil Aas-Jakobsen, 1997:148, ISBN 82-471-0189-0, ISSN 0802-3271.

"A numerical study of flow about fixed and flexibly mounted circular cylinders",
Trond Stokka Meling, 1998:48, ISBN 82-471-0244-7, ISSN 0802-3271.

"Estimation of chloride penetration into concrete bridges in coastal areas",
Per Egil Steen, 1998:89, ISBN 82-471-0290-0, ISSN 0802-3271.

"Stress-resultant material models for reinforced concrete plates and shells",
Jan Arve Øverli, 1998:95, ISBN 82-471-0297-8, ISSN 0802-3271.

"Chloride binding in concrete. Effect of surrounding environment and concrete composition",
Claus Kenneth Larsen, 1998:101, ISBN 82-471-0337-0, ISSN 0802-3271.

"Rotational capacity of aluminium alloy beams",
Lars A. Moen, 1999:1, ISBN 82-471-0365-6, ISSN 0802-3271.

"Stretch Bending of Aluminium Extrusions",
Arild H. Clausen, 1999:29, ISBN 82-471-0396-6, ISSN 0802-3271.

"Aluminium and Steel Beams under Concentrated Loading",
Tore Tryland, 1999:30, ISBN 82-471-0397-4, ISSN 0802-3271.

"Engineering Models of Elastoplasticity and Fracture for Aluminium Alloys",
Odd-Geir Lademo, 1999:39, ISBN 82-471-0406-7, ISSN 0802-3271.

"Kapasitet og duktilitet av dybelforbindelser i trekonstruksjoner",
Jan Siem, 1999:46, ISBN 82-471-0414-8, ISSN 0802-3271.

"Etablering av distribuert ingeniørarbeid; Teknologiske og organisatoriske erfaringer fra en norsk ingeniørbedrift",
Lars Line, 1999:52, ISBN 82-471-0420-2, ISSN 0802-3271.

"Estimation of Earthquake-Induced Response",
Símon Ólafsson, 1999:73, ISBN 82-471-0443-1, ISSN 0802-3271.

"Coastal Concrete Bridges: Moisture State, Chloride Permeability and Aging Effects"
Ragnhild Holen Relling, 1999:74, ISBN 82-471-0445-8, ISSN 0802-3271.

"Capacity Assessment of Titanium Pipes Subjected to Bending and External Pressure",
Arve Bjørset, 1999:100, ISBN 82-471-0473-3, ISSN 0802-3271.

“Validation of Numerical Collapse Behaviour of Thin-Walled Corrugated Panels”,
Håvar Ilstad, 1999:101, ISBN 82-471-0474-1, ISSN 0802-3271.

“Strength and Ductility of Welded Structures in Aluminium Alloys”,
Miroslaw Matusiak, 1999:113, ISBN 82-471-0487-3, ISSN 0802-3271.

“Thermal Dilation and Autogenous Deformation as Driving Forces to Self-Induced Stresses in High Performance Concrete”,
Øyvind Bjøntegaard, 1999:121, ISBN 82-7984-002-8, ISSN 0802-3271.

“Some Aspects of Ski Base Sliding Friction and Ski Base Structure”,
Dag Anders Moldestad, 1999:137, ISBN 82-7984-019-2, ISSN 0802-3271.

"Electrode reactions and corrosion resistance for steel in mortar and concrete",
Roy Antonsen, 2000:10, ISBN 82-7984-030-3, ISSN 0802-3271.

"Hydro-Physical Conditions in Kelp Forests and the Effect on Wave Damping and Dune Erosion. A case study on Laminaria Hyperborea",
Stig Magnar Løvås, 2000:28, ISBN 82-7984-050-8, ISSN 0802-3271.

"Random Vibration and the Path Integral Method",
Christian Skaug, 2000:39, ISBN 82-7984-061-3, ISSN 0802-3271.

"Buckling and geometrical nonlinear beam-type analyses of timber structures",
Trond Even Eggen, 2000:56, ISBN 82-7984-081-8, ISSN 0802-3271.

”Structural Crashworthiness of Aluminium Foam-Based Components”,
Arve Grønsund Hanssen, 2000:76, ISBN 82-7984-102-4, ISSN 0809-103X.

“Measurements and simulations of the consolidation in first-year sea ice ridges, and some aspects of mechanical behaviour”,
Knut V. Høyland, 2000:94, ISBN 82-7984-121-0, ISSN 0809-103X.

”Kinematics in Regular and Irregular Waves based on a Lagrangian Formulation”,
Svein Helge Gjøsund, 2000-86, ISBN 82-7984-112-1, ISSN 0809-103X.

”Self-Induced Cracking Problems in Hardening Concrete Structures”,
Daniela Bosnjak, 2000-121, ISBN 82-7984-151-2, ISSN 0809-103X.

"Ballistic Penetration and Perforation of Steel Plates",
Tore Børvik, 2000:124, ISBN 82-7984-154-7, ISSN 0809-103X.

"Freeze-Thaw resistance of Concrete. Effect of: Curing Conditions, Moisture Exchange and Materials",
Terje Finnerup Rønning, 2001:14, ISBN 82-7984-165-2, ISSN 0809-103X

"Structural behaviour of post tensioned concrete structures. Flat slab. Slabs on ground",
Steinar Trygstad, 2001:52, ISBN 82-471-5314-9, ISSN 0809-103X.

"Slipforming of Vertical Concrete Structures. Friction between concrete and slipform panel",
Kjell Tore Fosså, 2001:61, ISBN 82-471-5325-4, ISSN 0809-103X.

"Some numerical methods for the simulation of laminar and turbulent incompressible flows",
Jens Holmen, 2002:6, ISBN 82-471-5396-3, ISSN 0809-103X.

“Improved Fatigue Performance of Threaded Drillstring Connections by Cold Rolling”,
Steinar Kristoffersen, 2002:11, ISBN: 82-421-5402-1, ISSN 0809-103X.

"Deformations in Concrete Cantilever Bridges: Observations and Theoretical Modelling",
Peter F. Takâcs, 2002:23, ISBN 82-471-5415-3, ISSN 0809-103X.

"Stiffened aluminium plates subjected to impact loading",
Hilde Giæver Hildrum, 2002:69, ISBN 82-471-5467-6, ISSN 0809-103X.

"Full- and model scale study of wind effects on a medium-rise building in a built up area",
Jónas Thór Snæbjørnsson, 2002:95, ISBN82-471-5495-1, ISSN 0809-103X.

“Evaluation of Concepts for Loading of Hydrocarbons in Ice-infested water”,
Arnor Jensen, 2002:114, ISBN 82-417-5506-0, ISSN 0809-103X.

”Numerical and Physical Modelling of Oil Spreading in Broken Ice”,
Janne K. Økland Gjøsteen, 2002:130, ISBN 82-471-5523-0, ISSN 0809-103X.

”Diagnosis and protection of corroding steel in concrete”,
Franz Pruckner, 20002:140, ISBN 82-471-5555-4, ISSN 0809-103X.

“Tensile and Compressive Creep of Young Concrete: Testing and Modelling”,
Dawood Atrushi, 2003:17, ISBN 82-471-5565-6, ISSN 0809-103X.

“Rheology of Particle Suspensions. Fresh Concrete, Mortar and Cement Paste with Various Types of Lignosulfonates”,
Jon Elvar Wallevik, 2003:18, ISBN 82-471-5566-4, ISSN 0809-103X.

“Oblique Loading of Aluminium Crash Components”,
Aase Reyes, 2003:15, ISBN 82-471-5562-1, ISSN 0809-103X.

“Utilization of Ethiopian Natural Pozzolans”,
Surafel Ketema Desta, 2003:26, ISSN 82-471-5574-5, ISSN:0809-103X.

“Behaviour and strength prediction of reinforced concrete structures with discontinuity regions”, Helge Brå, 2004:11, ISBN 82-471-6222-9, ISSN 1503-8181.

“High-strength steel plates subjected to projectile impact. An experimental and numerical study”, Sumita Dey, 2004:38, ISBN 82-471-6282-2 (printed version), ISBN 82-471-6281-4 (electronic version), ISSN 1503-8181.

“Alkali-reactive and inert fillers in concrete. Rheology of fresh mixtures and expansive reactions.”
Bård M. Pedersen, 2004:92, ISBN 82-471-6401-9 (printed version), ISBN 82-471-6400-0 (electronic version), ISSN 1503-8181.

“On the Shear Capacity of Steel Girders with Large Web Openings”.
Nils Christian Hagen, 2005:9 ISBN 82-471-6878-2 (printed version), ISBN 82-471-6877-4 (electronic version), ISSN 1503-8181.

”Behaviour of aluminium extrusions subjected to axial loading”.
Østen Jensen, 2005:7, ISBN 82-471-6873-1 (printed version), ISBN 82-471-6872-3 (electronic version), ISSN 1503-8181.

”Thermal Aspects of corrosion of Steel in Concrete”.
Jan-Magnus Østvik, 2005:5, ISBN 82-471-6869-3 (printed version), ISBN 82-471-6868 (electronic version), ISSN 1503-8181.

”Mechanical and adaptive behaviour of bone in relation to hip replacement.” A study of bone remodelling and bone grafting.
Sébastien Muller, 2005:34, ISBN 82-471-6933-9 (printed version), ISBN 82-471-6932-0 (electronic version), ISSN 1503-8181.

“Analysis of geometrical nonlinearities with applications to timber structures”.
Lars Wollebæk, 2005:74, ISBN 82-471-7050-5 (printed version), ISBN 82-471-7019-1 (electronic version), ISSN 1503-8181.

“Pedestrian induced lateral vibrations of slender footbridges”,
Anders Rönnquist, 2005:102, ISBN 82-471-7082-5 (printed version), ISBN 82-471-7081-7 (electronic version), ISSN 1503-8181.

“Initial Strength Development of Fly Ash and Limestone Blended Cements at Various Temperatures Predicted by Ultrasonic Pulse Velocity”,
Tom Ivar Fredvik, 2005:112, ISBN 82-471-7105-8 (printed version), ISBN 82-471-7103-1 (electronic version), ISSN 1503-8181.

“Behaviour and modelling of thin-walled cast components”,
Cato Dørum, 2005:128, ISBN 82-471-7140-6 (printed version), ISBN 82-471-7139-2 (electronic version), ISSN 1503-8181.

“Behaviour and modelling of selfpiercing riveted connections”,
Raffaele Porcaro, 2005:165, ISBN 82-471-7219-4 (printed version), ISBN 82-471-7218-6 (electronic version), ISSN 1503-8181.

”Behaviour and Modelling og Aluminium Plates subjected to Compressive Load”,
Lars Rønning, 2005:154, ISBN 82-471-7169-1 (printed version), ISBN 82-471-7195-3 (electronic version), ISSN 1503-8181.

”Bumper beam-longitudinal system subjected to offset impact loading”,
Satyanarayana Kokkula, 2005:193, ISBN 82-471-7280-1 (printed version), ISBN 82-471-7279-8 (electronic version), ISSN 1503-8181.

“Control of Chloride Penetration into Concrete Structures at Early Age”,
Guofei Liu, 2006:46, ISBN 82-471-7838-9 (printed version), ISBN 82-471-7837-0 (electronic version), ISSN 1503-8181.

“Modelling of Welded Thin-Walled Aluminium Structures”,
Ting Wang, 2006:78, ISBN 82-471-7907-5 (printed version), ISBN 82-471-7906-7 (electronic version), ISSN 1503-8181.

”Time-variant reliability of dynamic systems by importance sampling and probabilistic analysis of ice loads”,
Anna Ivanova Olsen, 2006:139, ISBN 82-471-8041-3 (printed version), ISBN 82-471-8040-5 (electronic version), ISSN 1503-8181.

“Fatigue life prediction of an aluminium alloy automotive component using finite element analysis of surface topography”.
Sigmund Kyrre Ås, 2006:25, ISBN 82-471-7791-9 (printed version), ISBN 82-471-7791-9 (electronic version), ISSN 1503-8181.

”Constitutive models of elastoplasticity and fracture for aluminium alloys under strain path change”,
Dasharatha Achani, 2006:76, ISBN 82-471-7903-2 (printed version), ISBN 82-471-7902-4 (electronic version), ISSN 1503-8181.

“Simulations of 2D dynamic brittle fracture by the Element-free Galerkin method and linear fracture mechanics”,
Tommy Karlsson, 2006:125, ISBN 82-471-8011-1 (printed version), ISBN 82-471-8010-3 (electronic version), ISSN 1503-8181.

“Penetration and Perforation of Granite Targets by Hard Projectiles”,
Chong Chiang Seah, 2006:188, ISBN 82-471-8150-9 (printed version), ISBN 82-471-8149-5 (electronic version), ISSN 1503-8181.

"Deformations, strain capacity and cracking of concrete in plastic and early hardening phases",
Tor Arne Hammer, 2007:234, ISBN 978-82-471-5191-4 (printed version), ISBN 978-82-471-5207-2 (electronic version), ISSN 1503-8181.

"Crashworthiness of dual-phase high-strength steel: Material and Component behaviour", Venkatapathi Tarigopula, 2007:230, ISBN 82-471-5076-4 (printed version), ISBN 82-471-5093-1 (electronic version), ISSN 1503-8181.

"Fibre reinforcement in load carrying concrete structures",
Åse Lyslo Døssland, 2008:50, ISBN 978-82-471-6910-0 (printed version), ISBN 978-82-471-6924-7 (electronic version), ISSN 1503-8181.

"Low-velocity penetration of aluminium plates",
Frode Grytten, 2008:46, ISBN 978-82-471-6826-4 (printed version), ISBN 978-82-471-6843-1 (electronic version), ISSN 1503-8181.

"Robustness studies of structures subjected to large deformations",
Ørjan Fyllingen, 2008:24, ISBN 978-82-471-6339-9 (printed version), ISBN 978-82-471-6342-9 (electronic version), ISSN 1503-8181.

"Constitutive modelling of morsellised bone",
Knut Birger Lunde, 2008:92, ISBN 978-82-471-7829-4 (printed version), ISBN 978-82-471-7832-4 (electronic version), ISSN 1503-8181.

"Experimental Investigations of Wind Loading on a Suspension Bridge Girder",
Bjørn Isaksen, 2008:131, ISBN 978-82-471-8656-5 (printed version), ISBN 978-82-471-8673-2 (electronic version), ISSN 1503-8181.

"Cracking Risk of Concrete Structures in The Hardening Phase",
Guomin Ji, 2008:198, ISBN 978-82-471-1079-9 (printed version), ISBN 978-82-471-1080-5 (electronic version), ISSN 1503-8181.

"Modelling and numerical analysis of the porcine and human mitral apparatus",
Victorien Emile Prot, 2008:249, ISBN 978-82-471-1192-5 (printed version), ISBN 978-82-471-1193-2 (electronic version), ISSN 1503-8181.

"Strength analysis of net structures",
Heidi Moe, 2009:48, ISBN 978-82-471-1468-1 (printed version), ISBN 978-82-471-1469-8 (electronic version), ISSN1503-8181.

"Numerical analysis of ductile fracture in surface cracked shells",
Espen Berg, 2009:80, ISBN 978-82-471-1537-4 (printed version), ISBN 978-82-471-1538-1 (electronic version), ISSN 1503-8181.

"Subject specific finite element analysis of bone – for evaluation of the healing of a leg lengthening and evaluation of femoral stem design",
Sune Hansborg Pettersen, 2009:99, ISBN 978-82-471-1579-4 (printed version), ISBN 978-82-471-1580-0 (electronic version), ISSN 1503-8181.

"Evaluation of fracture parameters for notched multi-layered structures",
Lingyun Shang, 2009:137, ISBN 978-82-471-1662-3 (printed version), ISBN 978-82-471-1663-0 (electronic version), ISSN 1503-8181.

"Modelling of Dynamic Material Behaviour and Fracture of Aluminium Alloys for Structural Applications"
Yan Chen, 2009:69, ISBN 978-82-471-1515-2 (printed version), ISBN 978-82 471-1516-9 (electronic version), ISSN 1503-8181.

"Nanomechanics of polymer and composite particles"
Jianying He 2009:213, ISBN 978-82-471-1828-3 (printed version), ISBN 978-82-471-1829-0 (electronic version), ISSN 1503-8181.

"Mechanical properties of clear wood from Norway spruce"
Kristian Berbom Dahl 2009:250, ISBN 978-82-471-1911-2 (printed version) ISBN 978-82-471-1912-9 (electronic version), ISSN 1503-8181.

"Modeling of the degradation of TiB_2 mechanical properties by residual stresses and liquid Al penetration along grain boundaries"
Micol Pezzotta 2009:254, ISBN 978-82-471-1923-5 (printed version) ISBN 978-82-471-1924-2 (electronic version) ISSN 1503-8181.

"Effect of welding residual stress on fracture"
Xiabo Ren 2010:77, ISBN 978-82-471-2115-3 (printed version) ISBN 978-82-471-2116-0 (electronic version), ISSN 1503-8181.

"Pan-based carbon fiber as anode material in cathodic protection system for concrete structures"
Mahdi Chini 2010:122, ISBN 978-82-471-2210-5 (printed version) ISBN 978-82-471-2213-6 (electronic version), ISSN 1503-8181.

"Structural Behaviour of deteriorated and retrofitted concrete structures"
Irina Vasililjeva Sæther 2010:171, ISBN 978-82-471-2315-7 (printed version) ISBN 978-82-471-2316-4 (electronic version) ISSN 1503-8181.

"Prediction of local snow loads on roofs"
Vivian Meløysund 2010:247, ISBN 978-82-471-2490-1 (printed version) ISBN 978-82-471-2491-8 (electronic version) ISSN 1503-8181.

"Behaviour and modelling of polymers for crash applications"
Virgile Delhaye 2010:251, ISBN 978-82-471-2501-4 (printed version) ISBN 978-82-471-2502-1 (electronic version) ISSN 1503-8181.

"Blended cement with reducted CO_2 emission – Utilizing the Fly Ash-Limestone Synergy",
Klaartje De Weerdt 2011:32, ISBN 978-82-471-2584-7 (printed version) ISBN 978-82-471-2584-4 (electronic version) ISSN 1503-8181.

"Chloride induced reinforcement corrosion in concrete" Concept of critical chloride content – methods and mechanisms.
Ueli Angst 2011:113, ISBN 978-82-471-2769-9 (printed version) ISBN 978-82-471-2763-6 (electronic version) ISSN 1503-8181.

"A thermo-electric-Mechanical study of the carbon anode and contact interface for Energy savings in the production of aluminium".
Dag Herman Andersen 2011:157, ISBN 978-82-471-2859-6 (printed version) ISBN 978-82-471-2860-2 (electronic version) ISSN 1503-8181.

"Structural Capacity of Anchorage Ties in Masonry Veneer Walls Subjected to Earthquake". The implications of Eurocode 8 and Eurocode 6 on a typical Norwegain veneer wall.
Ahmed Mohamed Yousry Hamed 2011:181, ISBN 978-82-471-2911-1 (printed version) ISBN 978-82-471-2912-8 (electronic ver.) ISSN 1503-8181.

"Work-hardening behaviour in age-hardenable Al-Zn-Mg(-Cu) alloys".
Ida Westermann , 2011:247, ISBN 978-82-471-3056-8 (printed ver.) ISBN 978-82-471-3057-5 (electronic ver.) ISSN 1503-8181.

"Behaviour and modelling of selfpiercing riveted connections using aluminium rivets".
Nguyen-Hieu Hoang, 2011:266, ISBN 978-82-471-3097-1 (printed ver.) ISBN 978-82-471-3099-5 (electronic ver.) ISSN 1503-8181.

"Fibre reinforced concrete".
Sindre Sandbakk, 2011:297, ISBN 978-82-471-3167-1 (printed ver.) ISBN 978-82-471-3168-8 (electronic ver) ISSN 1503:8181.

"Dynamic behaviour of cablesupported bridges subjected to strong natural wind".
Ole Andre Øiseth, 2011:315, ISBN 978-82-471-3209-8 (printed ver.) ISBN 978-82-471-3210-4 (electronic ver.) ISSN 1503-8181.

"Constitutive modeling of solargrade silicon materials"
Julien Cochard, 2011:307, ISBN 978-82-471-3189-3 (printed ver). ISBN 978-82-471-3190-9 (electronic ver.) ISSN 1503-8181.

"Constitutive behavior and fracture of shape memory alloys"
Jim Stian Olsen, 2012:57, ISBN 978-82-471-3382-8 (printed ver.) ISBN 978-82-471-3383-5 (electronic ver.) ISSN 1503-8181.

“Field measurements in mechanical testing using close-range photogrammetry and digital image analysis”
Egil Fagerholt, 2012:95, ISBN 978-82-471-3466-5 (printed ver.) ISBN 978-82-471-3467-2 (electronic ver.) ISSN 1503-8181.

“Towards a better under standing of the ultimate behaviour of lightweight aggregate concrete in compression and bending”,
Håvard Nedrelid, 2012:123, ISBN 978-82-471-3527-3 (printed ver.) ISBN 978-82-471-3528-0 (electronic ver.) ISSN 1503-8181.

“Numerical simulations of blood flow in the left side of the heart”
Sigrid Kaarstad Dahl, 2012:135, ISBN 978-82-471-3553-2 (printed ver.) ISBN 978-82-471-3555-6 (electronic ver.) ISSN 1503-8181.

“Moisture induced stresses in glulam”
Vanessa Angst-Nicollier, 2012:139, ISBN 978-82-471-3562-4 (printed ver.) ISBN 978-82-471-3563-1 (electronic ver.) ISSN 1503-8181.

“Biomechanical aspects of distraction osteogensis”
Valentina La Russa, 2012:250, ISBN 978-82-471-3807-6 (printed ver.) ISBN 978-82-471-3808-3 (electronic ver.) ISSN 1503-8181.

“Ductile fracture in dual-phase steel. Theoretical, experimental and numerical study”
Gaute Gruben, 2012:257, ISBN 978-82-471-3822-9 (printed ver.) ISBN 978-82-471-3823-6 (electronic ver.) ISSN 1503-8181.

“Damping in Timber Structures”
Nathalie Labonnote, 2012:263, ISBN 978-82-471-3836-6 (printed ver.) ISBN 978-82-471-3837-3 (electronic ver.) ISSN 1503-8181.

“Biomechanical modeling of fetal veins: The umbilical vein and ductus venosus bifurcation”
Paul Roger Leinan, 2012:299, ISBN 978-82-471-3915-8 (printed ver.) ISBN 978-82-471-3916-5 (electronic ver.) ISSN 1503-8181.

“Large-Deformation behaviour of thermoplastics at various stress states”
Anne Serine Ognedal, 2012:298, ISBN 978-82-471-3913-4 (printed ver.) ISBN 978-82-471-3914-1 (electronic ver.) ISSN 1503-8181.

“Hardening accelerator for fly ash blended cement”
Kien Dinh Hoang, 2012:366, ISBN 978-82-471-4063-5 (printed ver.) ISBN 978-82-471-4064-2 (electronic ver.) ISSN 1503-8181.

“From molecular structure to mechanical properties”
Jianyang Wu, 2013:186, ISBN 978-82-471-4485-5 (printed ver.) ISBN 978-82-471-4486-2 (electronic ver.) ISSN 1503-8181.

“Experimental and numerical study of hybrid concrete structures”
Linn Grepstad Nes, 2013:259, ISBN 978-82-471-4644-6 (printed ver.) ISBN 978-82-471-4645-3 (electronic ver.) ISSN 1503-8181.

“Mechanics of ultra-thin multi crystalline silicon wafers”
Saber Saffar, 2013:199, ISBN 978-82-471-4511-1 (printed ver.) ISBN 978-82-471-4513-5 (electronic ver). ISSN 1503-8181.

“Through process modelling of welded aluminium structures”
Anizahyati Alisibramulisi, 2013:325, ISBN 978-82-471-4788-7 (printed ver.) ISBN 978-82-471-4789-4 (electronic ver.) ISSN 1503-8181.

“Combined blast and fragment loading on steel plates”
Knut Gaarder Rakvåg, 2013:361, ISBN978-82-471-4872-3 (printed ver.) ISBN 978-82-4873-0 (electronic ver.). ISSN 1503-8181.

“Characterization and modelling of the anisotropic behaviour of high-strength aluminium alloy”
Marion Fourmeau, 2014:37, ISBN 978-82-326-0008-3 (printed ver.) ISBN 978-82-326-0009-0 (electronic ver.) ISSN 1503-8181.

“Behaviour of threated steel fasteners at elevated deformation rates”
Henning Fransplass, 2014:65, ISBN 978-82-326-0054-0 (printed ver.) ISBN 978-82-326-0055-7 (electronic ver.) ISSN 1503-8181.

“Sedimentation and Bleeding”
Ya Peng, 2014:89, ISBN 978-82-326-0102-8 (printed ver.) ISBN 978-82-326-0103-5 (electric ver.) ISSN 1503-8181.

“Impact against X65 offshore pipelines”
Martin Kristoffersen, 2014:362, ISBN 978-82-326-0636-8 (printed ver.) ISBN 978-82-326-0637-5 (electronic ver.) ISSN 1503-8181.

“Formability of aluminium alloy subjected to prestrain by rolling”
Dmitry Vysochinskiy, 2014:363,, ISBN 978-82-326-0638-2 (printed ver.) ISBN 978-82-326-0639-9 (electronic ver.) ISSN 1503-8181.

“Experimental and numerical study of Yielding, Work-Hardening and anisotropy in textured AA6xxx alloys using crystal plasticity models”
Mikhail Khadyko, 2015:28, ISBN 978-82-326-0724-2 (printed ver.) ISBN 978-82-326-0725-9 (electronic ver.) ISSN 1503-8181.

“Behaviour and Modelling of AA6xxx Aluminium Alloys Under a Wide Range of Temperatures and Strain Rates”
Vincent Vilamosa, 2015:63, ISBN 978-82-326-0786-0 (printed ver.) ISBN 978-82-326-0787-7 (electronic ver.) ISSN 1503-8181.

“A Probabilistic Approach in Failure Modelling of Aluminium High Pressure Die-Castings”
Octavian Knoll, 2015:137, ISBN 978-82-326-0930-7 (printed ver.) ISBN 978-82-326-0931-4 (electronic ver.) ISSN 1503-8181.

“Ice Abrasion on Marine Concrete Structures”
Egil Møen, 2015:189, ISBN 978-82-326-1034-1 (printed ver.) ISBN 978-82-326-1035-8 (electronic ver.) ISSN 1503-8181.

“Fibre Orientation in Steel-Fibre-Reinforced Concrete”
Giedrius Zirgulis, 2015:229, ISBN 978-82-326-1114-0 (printed ver.) ISBN 978-82-326-1115-7 (electronic ver.) ISSN 1503-8181.

“Effect of spatial variation and possible interference of localised corrosion on the residual capacity of a reinforced concrete beam”
Mohammad Mahdi Kioumarsi, 2015:282, ISBN 978-82-326-1220-8 (printed ver.) ISBN 978-82-1221-5 (electronic ver.) ISSN 1503-8181.

“The role of concrete resistivity in chloride-induced macro-cell corrosion”
Karla Horbostel, 2015:324, ISBN 978-82-326-1304-5 (printed ver.) ISBN 978-82-326-1305-2 (electonic ver.) ISSN 1503-8181.

“Flowable fibre-reinforced concrete for structural applications”
Elena Vidal Sarmiento, 2015-335, ISBN 978-82-326-1324-3 (printed ver.) ISBN 978-82-326-1325-0 (electronic ver.) ISSN 1503-8181.

“Development of chushed sand for concrete production with microproportioning”
Rolands Cepuritis, 2016:19, ISBN 978-82-326-1382-3 (printed ver.) ISBN 978-82-326-1383-0 (electronic ver.) ISSN 1503-8181.

“Withdrawal properties of threaded rods embedded in glued-laminated timer elements”
Haris Stamatopoulos, 2016:48, ISBN 978-82-326-1436-3 (printed ver.) ISBN 978-82-326-1437-0 (electronic ver.) ISSN 1503-8181.

“An Experimental and numerical study of thermoplastics at large deformation”
Marius Andersen, 2016:191, ISBN 978-82-326-1720-3 (printed ver.) ISBN 978-82-326-1721-0 (electronic ver.) ISSN 1503-8181.

“Modeling and Simulation of Ballistic Impact”
Jens Kristian Holmen, 2016:240, ISBN 978-82-326-1818-7 (printed ver). ISBN 978-82-326-1819-4 (electronic ver.) ISSN 1503-8181.

“Early age crack assessment of concrete structures”
Anja B. Estensen Klausen, 2016:256, ISBN 978-82-326-1850-7 (printed ver). ISBN 978-82-326-1851-4 (electronic ver.) ISSN 1503-8181.

“Uncertainty quantification and sensitivity analysis for cardiovascular models”
Vinzenz Gregor Eck, 2016:234, ISBN 978-82-326-1806-4 (printed ver.) ISBN 978-82-326-1807-1 (electronic ver.) ISSN 1503-8181.

“Dynamic behaviour of existing and new railway catenary systems under Norwegain conditions”
Petter Røe Nåvik, 2016:298, ISBN 978-82-326-1935-1 (printed ver.) ISBN 978-82-326-1934-4 (electronic ver.) ISSN 1503-8181.

“Mechanical behaviour of particle-filled elastomers at various temperatures”
Arne Ilseng, 2016-295, ISBN978-82-326-1928-3 (printed ver.) ISBN 978-82-326-1929-0 (electronic ver.) ISSN 1503-8181.

“Nanotechnology for Anti-Icing Application”
Zhiwei He, 2016:348, ISBN 978-82-326-2038-8 (printed ver.) ISBN 978-82-326-2019-5 (electronic ver.) ISSN 1503-8181.

“Conduction Mechanisms in Conductive Adhesives with Metal-Coated Polyer Spheres”
Sigurd Rolland Pettersen, 2016:349, ISBN 978-326-2040-1 (printed ver,) ISBN 978-82-326-2041-8 (electronic ver.) ISSN 1503-8181.

“The interaction between calcium lignosulfonate and cement”
Alessia Colombo, 2017:20, ISBN 978-82-326-2122-4 (printed ver.) ISBN 978-82-326-2123-1 (electronic ver.) ISSN 1503-8181.

“Behaviour and Modelling of Flexible Structures Subjected to Blast Loading”
Vegard Aune, 2017:101, ISBN 978-82-326-2274-0 (printed ver.) ISBN 978-82-326-2275-7 (electronic ver.) ISSN 1503-8181.

“Behaviour of steel connections under quasi-static and impact loading”
Erik Løhre Grimsmo, 2017:159, ISBN 978-82-326-2390-7 (printed ver.) ISBN 978-82-326-2391-4 (electronic ver.) ISSN 1503-8181.

“An experimental and numerical study of cortical bone at he macro and Nano-scale”
Masoud Ramenzanzadehkoldeh,, 2017:208, ISBN 978-82-326-2488-1 (printed ver.) ISBN 978-82-326-2489-8 (electronic ver.) ISSN 1503-8181.

“Optoelectrical Properties of a Novel Organic Semiconductor: 6,13-Dichloropentacene”
Mao Wang, 2017:130, ISBN 978-82-326-2332-7 (printed ver.) ISBN 978-82-326-2333-4) (electronic ver.) ISSN 1503-8181.

“Core-shell structured microgels and their behavior at oil and water interface”
Yi Gong, 2017:182, ISBN 978-82-326-2436-2 (printed. ver.) ISBN 978-82-326-2437-9 (electronic ver.) ISSN 1503-8181.

“Aspects of design of reinforced concrete structures using nonliear finite element analyses”
Morten Engen, 2017:149, ISBN 978-82-326-2370-9 (printed ver.) ISBN 978-82-326-2371-6 (electronic ver.) ISSN 1503-8181.

“Numerical studies on ductile failure of aluminium alloys”
Lars Edvard Dæhli, 2017:284, ISBN 978-82-326-2636-6 (printed ver.) ISBN 978-82-326-2637-3 (electronic ver.) ISSN 1503-8181.

“Modelling and Assessment of Hydrogen Embrittlement in Steels and Nickel Alloys”
Haiyang Yu, 2017:278, ISBN 978-82-326-2624-3 (printed. ver.) ISBN 978-82-326-2625-0 (electronic ver.) ISSN 1503-8181.

“Network arch timber bridges with light timber deck on transverse crossbeams”
Anna Weronika Ostrycharczyk, 2017:318, ISBN 978-82-326-2704-2 (printed ver.) ISBN 978-82-326-2705-9 (electronic ver.) ISSN 1503-8181.

“Splicing of Large Glued Laminated Timber Elements by Use of Long Threated Rods”
Martin Cepelka, 2017:320, ISBN 978-82-326-2708-0 (printed ver.) ISBN 978-82-326-2709-7 (electronic ver.) ISSN 1503-8181.

“Thermomechanical behaviour of semi-crystalline polymers: experiments, modelling and simulation”
Joakim Johnsen, 2017-317, ISBN 978-82-326-2702-8 (printed ver.) ISBN 978-82-326-2703-5 (electronic ver.) ISSN 1503-8181.

“Small-Scale Plasiticity under Hydrogen Environment”
Kai Zhao, 2017:356, ISBN 978-82-326-2782-0 (printed ver.) ISBN 978-82-326-2783-7 (electronic er.) ISSN 1503-8181.

“Risk and Reliability Based Calibration of Structural Design Codes”
Michele Baravalle, 2017:342, ISBN 978-82-326-2752-3 (printed ver,) ISBN 978-82-326-2753-0 (electronic ver.) ISSN 1503-8181.

“Dynamic behaviour of floating bridges exposed to wave excitation”
Knut Andreas Kvåle, 2017:365, ISBN 978-82-326-2800-1 (printed ver.) ISBN 978-82-326-2801-8 (electronic ver.) ISSN 1503-8181.